Using non-destructive laser backscattering imaging technology for kiwifruit quality assessment

A thesis presented in partial fulfilment of the requirements for the degree of

Doctor of Philosophy
in
Food Technology

at Massey University, Manawatū,
New Zealand

Zhuo Yang

2024

Abstract

Kiwifruit is one of the most important exported horticultural products in New Zealand. The supply of kiwifruit to both national and international markets can be extended by harvesting kiwifruit unripe and storing with proper postharvest practice. During kiwifruit storage, quality monitoring is required for inventory planning and consistent quality maintenance. Currently, the industry is using sampled data to represent a batch of kiwifruit. However, kiwifruit quality is difficult to estimate based on destructively measured samples due to the heterogeneous population quality distribution. Therefore, a non-destructive technology is preferred allowing quality measurement for all kiwifruit prior to and during storage, as well as before exporting and marketing. Commercial spectral-optical devices, such as near-infrared (NIR) spectroscopy, have been employed by the industry for fruit grading and sorting at harvest, and have achieved good performance in total soluble solid content (SSC) and dry matter content (DMC) estimation. However, NIR spectroscopy had a poorer performance in estimating kiwifruit flesh firmness (FF), the primary quality indicator. During light and fruit tissue interaction, those optical devices capture data containing primarily the absorption signal related to kiwifruit's chemical composition. Therefore, the FF estimation is indirect and the accuracy of FF measurement is affected when both textural structures and SSC change during postharvest ripening.

Laser backscattering imaging (LBI) records the backscattered signal after a single laser beam interacts with kiwifruit tissue. These light-tissue interactions include light absorption and scattering. The back-scattered signal could be analysed as an attenuation profile, and this attenuation profile is determined by optical properties of absorption (μ_a) and reduced scattering (μ_s') coefficients, which correlate with fruit chemical compositions and physical

properties, respectively. Therefore, LBI data is potentially helpful for FF estimation and early-stage internal disorder symptoms detection.

This PhD work developed a non-destructive approach based on the LBI technique to segregate kiwifruit with internal disorders [brown marmorated stink bug (BMSB) feeding injury and chilling injury (CI)], as well as soft fruit at FF threshold of 9.8 N. Estimation of μ_a and μ_s' was achieved with 56.6 % and 91.5 % accuracy respectively, using a pre-classification method and validated against optical phantoms of known optical properties. Additionally, LBI parameters directly extracted from the images were utilised to develop segregation models owing to the uncertainties in μ_a and μ_s' estimation.

For internal disorder detection, using the estimated kiwifruit μ_a and μ_s', the segregation accuracy for kiwifruit with BMSB damage was 84 % and 62 % for 'Zesy002' (n=198) and 'Hayward' (n=198). Using extracted kiwifruit LBI parameters, the segregation accuracy for kiwifruit with CI was 92 % and 39 % for 'Zesy002' (n=396) and 'Hayward' (n=400). In addition, 'Zesy002' (n=30) and 'Hayward' (n=30) LBI during the postharvest ripening for kiwifruit were collected through a 15-day shelf life at 20 °C, where extracted LBI parameters were used to develop a time-series model. Absolute values of kiwifruit LBI parameters increased during the kiwifruit ripening process for both cultivars and the trend of LBI parameters may be correlated with kiwifruit softening. For segregating kiwifruit based on FF, the kiwifruit FF segregation model was calibrated, cross-validated and externally tested using kiwifruit LBI and corresponding FF data collected from 2 seasons with varying at-harvest maturity stages and stored at 2 temperatures. The segregation model accuracy for classifying fruit based on the 9.8 N FF threshold was 75 % and 70 % for 'Zesy002' (n=2247) and 'Hayward' (n=3558) in test sets. In conclusion, this work confirms that LBI technology has the potential for segregating soft

kiwifruit or kiwifruit with early internal disorder symptoms and be adapted to the packhouse sorting system. However, in this work, FF segregation uncertainty at the 9.8 N threshold was observed when 'Zesy002' FF (N) ∈ (5,15) and 'Hayward' FF (N) ∈ (5,20) due to LBI parameter overlapping. Improved image analysis and segregation algorithms need to be investigated to enhance the segregation sensitivity for kiwifruit FF in the lower firmness range.

Acknowledgement

The accomplishment of this PhD journey is the outcome of endless support from all the people surrounding me. I would like to thank my supervisors for this unique opportunity and for providing support throughout this journey. To my co-supervisors, Dr. Mo Li and Dr. Manuela Zude-Sasse, I thank you for giving advice and feedback on my project and introducing unique perspectives that have motivated me to think critically and deepen my understanding. Besides, you always stood behind me with endless encouragement and cheered for my progress in both my life and academic journey. I learned from you the attitude required to be successful in science as a woman – passion, curiosity, work, and believing in myself- priceless treasures for my future career and life. To my primary supervisor, Prof Andrew East, thanks for giving me the chance to be part of such an incredible team, the Postharvest Team. Besides, you gave me many suggestions to improve my academic communication skills, including writing and presentation, whilst also teaching me critical thinking, a precious treasure for my future career.

I am grateful to acknowledge the staff members from Massey University and ATB. Special thanks firstly go to my technical support. Thanks to Peter Jeffery for providing me with all kinds of technical support and sourcing kiwifruit and equipment in New Zealand and Europe. Thanks to Christian Regen for training me to use the LBI system and assisting me with setting up the system remotely at Massey, from parts ordering to software maintenance. Special thanks also go to Sue Nicholson for assisting me in consumable acquisition and equipment training and providing feedback on my experimental protocols in the postharvest lab. I want to acknowledge Prof. Laszlo Baranyai, who helped me draft the 1st version of the R script for LBI image analysis. I would also like to thank other technical staff members, Steve Glasgow, Gabriele Wegner, Corinna Rolleczek, David Sakowsky, John Pedley, Ian Thomas, Petru Daniels,

Evelyn Lupton and Yanyu He for providing me with lab training and technical support allowing my experiments to run smoothly.

Big thanks to my fellow postgrad students and colleagues in the Postharvest team at Massey University and Precision Horticulture team at ATB. They are Dr. Sebastian Rivera Smith, Dr. Praveen Veeregowda, Yujie Han, Talon Sneddon, Raquel Lozano, Carlos Lopez-Lozano, Josephine Longuet-Higgins, Abdulquadri Alaka, Dr. Nikos Tsoulias, Kowshik Kumar Saha, Dr. Martin Penzel, An Xue, and Dr. Magdalena Urbanska, thanks for your endless support and being cheerful as my friends.

Acknowledgment also goes to Zespri International, who provided funding for this work. Thanks to the Zespri Innovation team for providing feedback for this research. Thanks to Zespri Italian research team and the Zeebrugge team for sourcing kiwifruit in Europe. Thanks to StartAfresh and ARM for sourcing kiwifruit in New Zealand.

Ultimately, I would like to express my gratitude to my family. Special thanks go to my dear grandparents Aihua Li, Cunxi Yang, Yongzhen Ding and Qicheng Zhang for caring for and loving me. I want to tell my deceased Nainai Aihua that I miss you more and more as time goes on, and I hope you rest in peace. I am grateful to have supportive parents, Xia Zhang and Yuhua Yang, who always have my back and show gracious love. Without them, I would not be able to fulfil my dream and have today's achievement. Special thanks must go to my beloved husband and best friend, Lizhi Zhang, for the endless care and love.

Declaration

The presented thesis is comprised of eight chapters including five research chapters with research work in this study. Partial contents of Chapters 3, 4, 5, 6 and 7 are structured as manuscripts that have either been published or intended to be submitted to a journal.

MASSEY UNIVERSITY
UNIVERSITY OF NEW ZEALAND
GRADUATE RESEARCH SCHOOL

STATEMENT OF CONTRIBUTION
DOCTORATE WITH PUBLICATIONS/MANUSCRIPTS

We, the student and the student's main supervisor, certify that all co-authors have consented to their work being included in the thesis and they have accepted the student's contribution as indicated below in the Statement of Originality.

Student name:	**Zhuo Yang**
Name and title of main supervisor:	**Prof. Andrew East**
In which chapter is the manuscript/published work?	**Chapter 3**
What percentage of the manuscript/published work was contributed by the student?	**80 %**

Describe the contribution that the student has made to the manuscript/published work:
Conceptualization; Formal analysis; Investigation; Methodology; Writing-original draft

Please select one of the following three options:

- (●) **The manuscript/published work is published or in press**
  Please provide the full reference of the research output:
  Yang, Z., Banányai, L., Ragen, C., Li, M., East, A. R., & Zude-Sasse, M. (2019). Non-destructive analysis of absorption and reduced scattering coefficients of green and golden kiwifruit. Acta Horticulturae1314, 499-504.
- ( ) **The manuscript is currently under review for publication**
  Please provide the name of the journal:
- ( ) **It is intended that the manuscript will be published, but it has not yet been submitted to a journal**

Student's signature:	Zhuo Yang Digitally signed by Zhuo Yang Date: 2023.07.28 13:04:46 +12'00'	Main supervisor's signature:	Andrew East Digitally signed by Andrew East Date: 2023.08.07 16:45:41 +12'00'

This form should appear at the end of each thesis chapter/section/appendix submitted as a manuscript/ publication or collected as an appendix at the end of the thesis.

MASSEY UNIVERSITY
TE KUNENGA KI PŪREHUROA
GRADUATE RESEARCH SCHOOL

STATEMENT OF CONTRIBUTION
DOCTORATE WITH PUBLICATIONS/MANUSCRIPTS

We, the student and the student's main supervisor, certify that all co-authors have consented to their work being included in the thesis and they have accepted the student's contribution as indicated below in the Statement of Originality.

Student name:	**Zhuo Yang**
Name and title of main supervisor:	**Prof. Andrew East**
In which chapter is the manuscript/published work?	**Chapter 3 & 5**
What percentage of the manuscript/published work was contributed by the student?	**80 %**

Describe the contribution that the student has made to the manuscript/published work:
Conceptualization; Formal analysis; Investigation; Methodology; Writing-original draft

Please select one of the following three options:

- (●) **The manuscript/published work is published or in press**
  Please provide the full reference of the research output:
  Yang, Z., Li, M., East, A. R., & Zude-Sasse, M. (2021). Application of absorption and scattering properties obtained through image pre-classification method using a laser backscattering imaging system to detect kiwifruit chilling injury. Foods, 10(7), 1446.
- ( ) **The manuscript is currently under review for publication**
  Please provide the name of the journal:
- ( ) **It is intended that the manuscript will be published, but it has not yet been submitted to a journal**

Student's signature:	Zhuo Yang — Digitally signed by Zhuo Yang Date: 2023.07.28 13:04:46 +12'00'	Main supervisor's signature:	Andrew East — Digitally signed by Andrew East Date: 2023.07.31 21:49:07 +12'00'

This form should appear at the end of each thesis chapter/section/appendix submitted as a manuscript/publication or collected as an appendix at the end of the thesis.

MASSEY UNIVERSITY
TE KUNENGA KI PŪREHUROA
NEW ZEALAND'S UNIVERSITY

GRADUATE RESEARCH SCHOOL

STATEMENT OF CONTRIBUTION
DOCTORATE WITH PUBLICATIONS/MANUSCRIPTS

We, the student and the student's main supervisor, certify that all co-authors have consented to their work being included in the thesis and they have accepted the student's contribution as indicated below in the Statement of Originality.

Student name:	**Zhuo Yang**
Name and title of main supervisor:	**Prof. Andrew East**

In which chapter is the manuscript/published work?	**Chapter 6**
What percentage of the manuscript/published work was contributed by the student?	**80 %**

Describe the contribution that the student has made to the manuscript/published work:
Conceptualization; Formal analysis; Investigation; Methodology; Writing-original draft

Please select one of the following three options:

- (●) **The manuscript/published work is published or in press**
  Please provide the full reference of the research output:
  Yang, Z., Li, M., East, A., & Zude-Sasse, M. (2024). Understanding changes of laser backscattering imaging parameters through the kiwifruit softening process using time series analysis. New Zealand Journal of Crop and Horticultural Science, 1-25.
- ( ) **The manuscript is currently under review for publication**
  Please provide the name of the journal:
- ( ) **It is intended that the manuscript will be published, but it has not yet been submitted to a journal**

Student's signature:	Zhuo Yang Digitally signed by Zhuo Yang Date: 2024.12.11 23:26:26 +13'00'	Main supervisor's signature:	Andrew East Digitally signed by Andrew East Date: 2024.12.12 16:52:24 +13'00'

This form should appear at the end of each thesis chapter/section/appendix submitted as a manuscript/ publication or collected as an appendix at the end of the thesis.

MASSEY UNIVERSITY
UNIVERSITY OF NEW ZEALAND
GRADUATE RESEARCH SCHOOL

STATEMENT OF CONTRIBUTION
DOCTORATE WITH PUBLICATIONS/MANUSCRIPTS

We, the student and the student's main supervisor, certify that all co-authors have consented to their work being included in the thesis and they have accepted the student's contribution as indicated below in the Statement of Originality.

Student name:	**Zhuo Yang**
Name and title of main supervisor:	**Prof. Andrew East**
In which chapter is the manuscript/published work?	**Chapter 7**
What percentage of the manuscript/published work was contributed by the student?	**80 %**

Describe the contribution that the student has made to the manuscript/published work:
Conceptualization; Formal analysis; Investigation; Methodology; Writing-original draft

Please select one of the following three options:

- ○ **The manuscript/published work is published or in press**
  Please provide the full reference of the research output:
- ○ **The manuscript is currently under review for publication**
  Please provide the name of the journal:
- ◉ **It is intended that the manuscript will be published, but it has not yet been submitted to a journal**

Student's signature:	Zhuo Yang — Digitally signed by Zhuo Yang Date: 2023.07.28 13:04:46 +12'00'	Main supervisor's signature:	Andrew East — Digitally signed by Andrew East Date: 2023.07.31 21:55:22 +12'00'

This form should appear at the end of each thesis chapter/section/appendix submitted as a manuscript/publication or collected as an appendix at the end of the thesis.

Table of Contents

List of Figures

List of Tables

List of Abbreviations and Symbols

μ_a	Absorption coefficient
μ_s	Scattering coefficient
μ_s'	Reduced scattering coefficient
e_t	residuals
ACF	Autocorrelation Function
AF	acoustic firmness
AIC	Akaike information criterion
AR	Autoregressive
ARIMA	Autoregressive integrated moving average
ATB	Leibniz Institute for Agricultural Engineering and Bioeconomy
BIC	Bayesian information criterion
BMSB	Brown marmorated stink bug
BWFR	Brix when fully ripe
CCD	charge-coupled device
CI	Chilling injury
CT	Computed tomography
d	Differencing coefficient
$Data_{cali}$	Calibration dataset
$Data_{vali}$	Cross-validation dataset
DFM	diffusion approximation model
DMC	Dry matter concentration
DW	Dry weight
ECDF	The empirical cumulative distribution function
FDA	Flexible discriminant analysis
FEA	Finite element analysis
FF	Flesh firmness
FN	False negative
FP	False positive
$Fruit_{BMSB}$	BMSB damaged fruit
$Fruit_{ctr}$	control fruit
$Fruit_{exp}$	BMSB-exposed fruit
$Fruit_{sound}$	Sound fruit without BMSB damage
FW	Fresh weight
FWHM	Full width at half maximum
GL	Grower lines
GNB	Gausses naïve Bayes classifier

HSI	Hyperspectral imaging
HWQM	Half width of quarter maximum
HWS	Holt-Winters smoothing
I	Integration
IS-IAD	Intergrading sphere - inverse adding double method
L	Level
LBI	Laser backscattering imaging
MA	Moving average
MBE	Mean bias error
MCS	Monte Carlo simulation
ME	Modulus of elasticity
MLE	Maximum likelihood estimation
MLR	Multiple linear regression
MRI	Magnetic resonance imaging
MST	Multiple scattering theory
NIR	Near-infrared
NLBI	Normalized LBI parameter
NZD	New Zealand dollar
OCT	Optical coherence tomography
PACF	Partial autocorrelation Function
PCA	Principle component analysis
PCR	Principal components regression
PDW	Photon density wave spectroscopy
PLS	Partial least squares regression
Q1R	Radial distance of 75% intensity value
Q3R	Radial distance of 25% intensity value
R^2	Coefficient of determination
$\bar{R}^2$	Adjusted R^2
RMSE	Root mean square error
RR	Respiration rate
RSS	Residual sum of squares
RTT	Radiation transport theory
SFDIS	Spatial-frequency domain imaging system
SFI	Soft fruit incidence
SLP	Slope of log-transformed LBI profile
SRIS	Spatially resolved imaging system
SSC	Total soluble solids content
SSE	Sum of squared errors

T	Trend
Test	Test set validation
TN	True negative
TP	True positive
TRIS	Time-resolved imaging system
TSS	Total sum of squares
Vis/SWNIR	Visible and shortwave near-infrared
Vis-NIR	Visible-near infrared

Chapter 1 Introduction

The kiwifruit industry is one of the largest exporting industries in New Zealand. For instance, for the 2020-2021 season, a total of 2.7 billion NZD worth of kiwifruit was exported (Aitken & Warrington, 2021). Kiwifruit 'Zesy002' (*Actinidia chinensis var. chinensis*) and 'Hayward' (*A. chinensis var. deliciosa),* are the two most important species and export cultivars in New Zealand. When considering both sales and license release, these two cultivars grossed 4.47 billion NZD in revenue for New Zealand (Zespri International, 2022). Apart from New Zealand, the main kiwifruit-producing countries are China, Italy, and Chile. These four countries produce over 80% of the kiwifruit in the world (Ferguson & Seal, 2008; Burdon & Lallu, 2011).

New Zealand is leading the kiwifruit industry with high-quality kiwifruit whilst maintaining its standing as the second-largest kiwifruit producer (Shahbandeh, 2022). New Zealand kiwifruit industry benefits from its unique location and the physiological characteristics of kiwifruit. Specifically, these factors allow New Zealand to provide off-season kiwifruit in the larger markets in the northern hemisphere. However, New Zealand's isolation also challenges decision-making and supply chain efficiency. Generally, it takes 2-weeks for New Zealand kiwifruit to ship to Asia and at least 4 weeks to Europe (Mills, 2004). Therefore, shipment strategies and storage practices are essential to provide quality fruit while balancing consumer requirements and fruit physiology.

Shipment strategies require an efficient supply chain to manage inventory and supply to overseas markets (Jabbar, 2014). The kiwifruit supply chain is based on many factors, including consumer expectations (such as desired size and taste) and kiwifruit physiology. Harker et al. (2009) and Lallu et al. (1989) reported that consumers prefer to purchase fruit in an optimal eating condition which requires uniform ripeness at the export stage. Thus, determining fruit

quality and its storability is necessary to maintain a consistent quality at the time of distribution.

Commercially, kiwifruit samples are destructively assessed for quality assurance before shipping and on-arrival at the distant market. Flesh firmness (FF) is one of the most important attributes for assessing kiwifruit quality and storability. Specifically, an FF of 9.8 N has been utilised as a minimum export threshold to segregate kiwifruit into soft and firm categories (Li et al., 2022). However, kiwifruit have great variability amongst and within batches (Kader & Rolle, 2004), which is caused by a series of factors, such as orchard location, orchard management, harvest maturity, storage condition, transport and handling (East, 2011; Patterson & Currie, 2011; Ward & Courtney, 2013). This variability could cause inconsistent quality due to the nature of subsampling measurements (Costa et al., 2003; East, 2011), thus creating challenges in delivering fruit of uniform qualities as consumers desire. Furthermore, estimating the FF of the entire population using subsamples could result in poor identification of overripe and damaged fruit. This could result in fruit loss due to sound kiwifruit being contaminated by damaged fruit stored together, leading to an annual revenue loss for the kiwifruit industry.

The limitation of sampling measurements may be reduced with non-destructive assessment or sorting techniques. Non-destructive technologies can potentially benefit the industry by identifying kiwifruit with internal disorders or kiwifruit with low FF. These kiwifruit could be removed at the sorting line, avoiding the contamination of other fruit in storage. Additionally, non-destructive technologies may be useful during repacking to exclude kiwifruit with storage disorders prior to marketing. For example, unacceptable chilling injury or overripe kiwifruit could be identified and removed. Moreover, non-destructive techniques may allow the

industry to make predictions about potential quality outcomes by making grading decisions before problematic quality issues occur, thus supporting decision-making and inventory management within the kiwifruit supply.

This study aims to investigate the feasibility of using non-destructive laser backscattering imaging (LBI) technology to segregate kiwifruit with internal disorders from sound ones and segregate soft kiwifruit from firm ones after storage. When fruit are illuminated by light, multiple absorption and scattering events occur due to various cellular structures and molecular components. These light-tissue interactions are related to kiwifruit physical structures and chemical composition, respectively. LBI records backscattered light at specific wavelengths after interacting with the fruit tissue at selected visible and NIR wavelengths and the recorded LBI signal is determined by optical properties including absorption coefficient (μ_a) and reduced scattering coefficient (μ_s'). Alternatively, the recorded LBI signal can be analysed as attenuation and determined by LBI parameters. As a result, extracted optical properties and LBI parameters may be useful to assess changes in kiwifruit chemical composition and physical properties in the subsurface region, and they may potentially be correlated with kiwifruit internal disorder symptoms and FF changes. Therefore, segregation models of damaged and sound kiwifruit as well as soft and firm kiwifruit may be possible according to kiwifruit optical properties and LBI parameters. Ultimately, the goal is to maintain consistent kiwifruit quality by segregating soft or damaged kiwifruit and reducing fruit loss in the supply chain.

Limited studies have been conducted using LBI to estimate kiwifruit quality and detect internal disorders. McGlone et al. (1997) estimated kiwifruit FF using scattered light intensity extracted from the diffuse reflectance spectra and achieved moderate success (R^2 = 67 %) at a scatter angle of 55°. Baranyai & Zude (2009) demonstrated the ability of LBI to segregate kiwifruit

between premium quality and overripe (soft) samples by analysing the anisotropy factor of the tissue. Hence, the potential for applying LBI for the non-destructive assessment of textural properties of kiwifruit has been demonstrated. Moreover, the estimated μ_s' may be greater in firm kiwifruit and kiwifruit with granular tissue, thus estimates of μ_a and μ_s' may be useful for kiwifruit segregation model development.

A major challenge with LBI data analysis is decoupling fruit absorption and scattering coefficient estimation, and hence extract useful information for quantitative FF estimation and internal disorder detection (Zude-Sasse et al., 2019). Therefore, research is required to develop LBI attenuation analysis methodology. With the resulting LBI attenuation data, research is required to provide correlations between kiwifruit FF and symptoms of internal disorders by developing appropriate segregation modelling techniques. Finally, the feasibility of non-destructive LBI technology and its capability to be implemented in the packhouse sorting line need to be investigated.

This PhD work tested a non-destructive approach based on the LBI technique to analyse changes in estimated optical properties and extracted LBI parameters when the fruit is damaged or during kiwifruit ripening and utilised this data to develop models for segregating damaged or soft fruit from sound fruit.

More specifically, the research objectives of this work are:

(i) To establish an LBI technique methodology, including system setup and attenuation analysis protocol.

(ii) To investigate how LBI parameters and estimated optical properties correlate with kiwifruit quality attributes during ripening and disorder existence.

(iii) To develop appropriate segregation models to enable quality estimation of kiwifruit FF and internal disorder symptoms based on LBI parameters and optical properties.

(iv) To investigate the industrial applicability of the developed techniques and models

To achieve the above objectives, this work used a multispectral spatial LBI system to assess kiwifruit quality of 'Zesy002' and 'Hayward' (Figure 1.1). Kiwifruit samples ($n_{Zesy002}$= 2913, $n_{Hayward}$= 4228) were collected at multiple maturities and at multiple ripeness stages across multiple seasons. Quality segregation models were developed to identify kiwifruit that were soft or had internal disorders. The model performance was assessed and discussed in Chapters 4, 5 and 7. Finally, industrial applicability is discussed, along with potential future research directions.

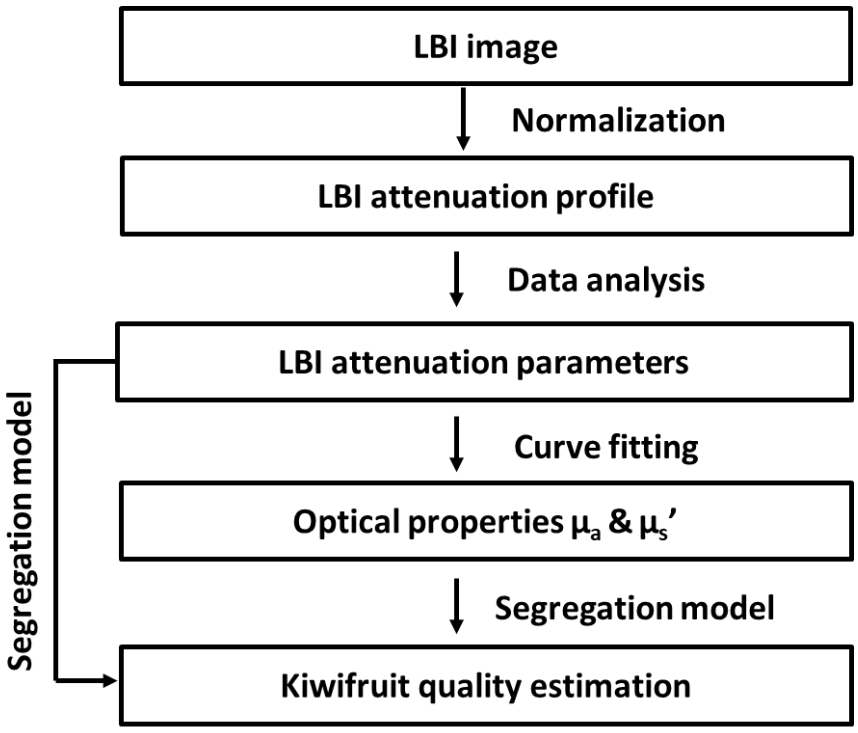

Figure 1.1. Research outline on using laser backscattering imaging (LBI) technology for kiwifruit quality estimation.

The work is presented in the following remaining chapters:

Chapter 2 is a literature review on the topics of kiwifruit physiology during ripening and after internal disorder development, fruit optical properties changes associated with quality changes, methodologies for LBI data analysis, and the applications of optical properties for fruit quality assessment.

Chapter 3 introduces the LBI system used in this work and the consequent signal processing. Manufactured optical phantoms and lab-made optical phantom sets are utilized to develop pre-classification models for μ_a and μ_s' estimation by limiting optical property ranges during calculations.

Chapter 4 presents the estimated kiwifruit optical properties using the developed pre-classification method described in Chapter 3 and the evaluation of using optical properties to segregate kiwifruit with Brown marmorated stink bug (BMSB) damage.

In Chapter 5, kiwifruit LBI parameters are extracted and used to estimate optical properties from an improved pre-classification method described in Chapter 3. Results were evaluated through a case study of segregating kiwifruit with chilling injury from sound ones.

In Chapter 6, kiwifruit LBI parameters were collected throughout the postharvest shelf-life ripening process. LBI parameters were analysed using time-series analysis. The resulting information was investigated for its use in describing and forecasting kiwifruit LBI parameter changes during ripening.

In Chapter 7, the LBI parameters described in Chapter 6 are utilized to develop a kiwifruit FF segregation model for soft and firm kiwifruit at the minimum export criterion (9.8 N) threshold and two alternative thresholds correlating to different softening stages. The model was first internally validated using cross-validation with the subsampling method, and then externally validated using 2 test sets obtained from different seasons and storage methods. In addition,

the segregation model performance was assessed with a 9.8 N FF threshold at different ripening stages.

Chapter 8 provides an overall discussion of the work, including a summary of results from the work, and an evaluation of the current LBI methodology including limitations and possible improvements.

Chapter 2 Literature review

2.1 Kiwifruit physiology changes

2.1.1 Kiwifruit quality changes during ripening

'Zesy002' and 'Hayward' are the two main commercial kiwifruit cultivars in New Zealand. 'Zesy002' is a uniform oval-shaped, yellow-fleshed kiwifruit with relatively-hairless light-brown skin and a 'tropical' flavour (Hallett & Sutherland, 2005; Burdon & Lallu, 2011). Contrastingly, 'Hayward' is a variable-shaped, green-fleshed kiwifruit with brown hairy skin and good postharvest performance (Ferguson, 1984; Burdon & Lallu, 2011). Kiwifruit are climacteric fruit that are often harvested unripe and stored for long periods (6-8 months) in low temperature (0 °C) storage conditions (Schröder & Atkinson, 2006). This long-term storage allows kiwifruit to develop physiologically before becoming suitable for consumption (Beever & Hopkirk, 1990). These physiological changes during ripening can be characterised by flesh softening, flesh colour changes from green to yellow (for 'Zesy002'), starch conversion to soluble simple sugars, acidity reduction, as well as taste and aroma development (Kim et al., 1999; Richardson et al., 2011; McAtee et al., 2015).

Kiwifruit has a complex structure, being comprised of skin, outer pericarp, inner pericarp and core. The kiwifruit skin area contains periderm, trichomes and lenticels which influence gas exchange (Hallett & Sutherland, 2005). Under the skin is the hypodermis region that contains 2-3 layers of closely packed cells with some stone cells (Bauchot et al., 1999). In the outer parenchyma region, there are 2 types of parenchyma cells (small and large), which vary in size and shape. Additionally, the ratio of different cell types affects the dry matter of kiwifruit (Nardozza et al., 2011). Microstructural differences in the sub-surface parenchyma cells are different amongst commercial cultivars (Cantre et al., 2014; Li et al., 2015). Information on fruit microstructure could benefit understanding of fruit softening and quality change processes. In

addition, fruit microstructure information may be considered when making storage decisions. The design of gas composition in modified atmosphere storage could be linked with gas exchange properties, such as porosity (Ho et al., 2010; Bessemans et al., 2016).

During postharvest storage, kiwifruit FF is 60 – 90 N at harvest and decreases to 5 – 8 N at eating ripeness (Beever & Hopkirk, 1990). Kiwifruit FF is also the primary indicator of postharvest ripeness and determines whether fruit can be exported to a distant market. Before exporting, an FF threshold of 9.8 N is commonly used to categorise soft from firm fruit (Pyke et al., 1996; Burdon et al., 2013; Li et al., 2022). A distinct 3-phase curve (Figure 2.1) of FF can be observed during kiwifruit ripening (Schröder & Atkinson, 2006). In the 1st phase, kiwifruit remain relatively firm and close to the at-harvest FF value. Kiwifruit then go through a rapid softening process (2nd phase) and reach 20 % of the initial FF. In the 3rd phase, the FF decreases slowly, and during this period, the internal ethylene production starts and the climacteric burst is triggered (Schröder & Atkinson, 2006). Although initial at-harvest FF is an indicator of kiwifruit storage life, softening speed varies for individual kiwifruit (Feng et al., 2001). In particular, it's well known that kiwifruit softening time is dependent on the at-harvest maturity (Lallu et al., 1989; MacRae et al., 1990). Kiwifruit at later maturity at harvest may be observed to already be in the rapid softening phase (Figure 2.1). Despite this, these fruit tend to progress slower during the final slow-softening phase and can be stored longer (MacRae et al., 1990).

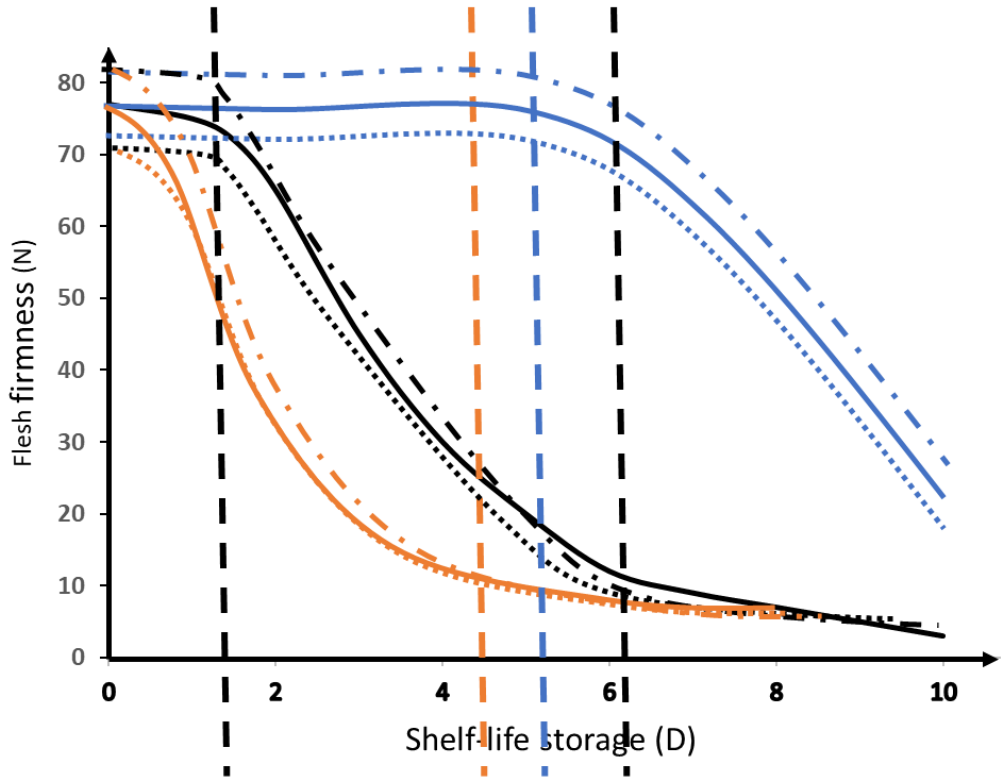

Figure 2.1. Schematic of the kiwifruit softening. (Adapted from MacRae et al., 1992 and Jabbar, 2014). Black curves represent the 3-phase kiwifruit softening curve. Blue curves represent the kiwifruit softening process with the first two phases. Orange curves represent the kiwifruit softening process with the last two phases. Vertical dash lines represent the shifting of the softening phase. Kiwifruit may have different initial firmness. Long dashed, solid and dotted curves represent high, middle and low initial firmness for each type of kiwifruit softening process.

Schröder and Atkinson (2006) discuss kiwifruit softening in relation to physical changes at the cellular level, including cell wall disintegration and particularly emphasize the role of pectin degradation, cell wall swelling and galactose loss. The rapid FF reduction results from pectin solubilisation, wherein water-insoluble pectin becomes soluble (Redgwell & Percy, 1992; Schröder & Atkinson, 2006). Concurrent with pectin degradation, cells begin to swell and separate due to a loss of middle lamellae adhesion, and eventually, the cell walls start to break down (Redgwell et al., 1992).

Besides cell wall degradation, other physical properties, such as water potential, osmotic potential, turgor pressure and tissue density, could also influence FF (Harker & Hallett, 1994).

During softening, kiwifruit turgidity decreases, followed by an increase in air spaces and a decrease in water and osmotic potential (Harker & Hallett, 1994). Ripe kiwifruit with the same turgor pressure as unripe kiwifruit were observed to have lower FF (Rojas et al., 2002). Therefore, both cell wall composition and structural properties contribute to FF change during ripening.

Similarly, total soluble solid content (SSC) is a quality attribute that changes during kiwifruit ripening. During ripening, the SSC increases due to the conversion of starch into sugars through starch solubilisation (Beever & Hopkirk, 1990). The initial starch content is about 5 – 7 % of the fresh weight for 'Hayward' kiwifruit. In kiwifruit, the starch solubilises and the SSC increases (MacRae et al., 1990) until the fruit have less than 0.2% starch content (Macrae et al., 1989). The SSC increases to 14 – 16% when reaching eating ripeness (Beever & Hopkirk, 1990), while consumers have been observed to accept kiwifruit with a SSC of 12% or more (Stec et al., 1989). Kiwifruit dry matter content (DMC) is reasonably constant during ripening, thus, DMC can provide information on the estimation of the final sugar level and assist with the prediction of storage life potential (Burdon et al., 2016). DMC is measured at harvest destructively in the industry to determine kiwifruit quality potential.

In addition to FF and SSC changes, the internal flesh colour of ‘Zesy002’ changes visually from green to yellow – a process known as degreening. For ‘Hayward’, the flesh colour remains green during ripening. The decrease in total chlorophyll content is responsible for this flesh colour change (Fuke et al., 1985).

Traditionally, kiwifruit quality attributes (FF, SSC, DMC and hue) are measured with destructive samples at harvest or during storage. Kiwifruit FF is determined by the maximum force to penetrate the fruit flesh tissue by a distance of 8 mm after 1 mm skin removal (Li et al., 2016).

However, the result of FF measured by penetrometer can vary among different operators (Watkins & Harman, 1981), fruit handling orientation (McGlone & Kawano, 1998) and probe-fruit angle (Davie et al., 1996). Penetrometer measurement is the standard industry method, but it has some inconsistency between multiple measurements per fruit and insensitivity at the softer range. In the industrial postharvest environment, kiwifruit FF is monitored regularly during storage by subsampling, which provides batch performance information but does not enable the identification of individual soft fruit from the highly variable fruit population.

Kiwifruit SSC is measured by collecting juice from the equatorial region or combining juice from the blossom and stem end using a refractometer. The reading of the refractometer can be affected by the speed at which a measurement is done (Magwaza & Opara, 2015) and the region of kiwifruit to sample the juice (Ma et al., 2021).

Kiwifruit DMC is measured by drying a 2-mm slice from the equatorial region at 65 °C for 18 h. Kiwifruit DMC estimation can be affected by water loss from the fresh slice during and before weighing the fresh weight samples or moisture accumulation on dry samples when weighing dry samples.

In addition to assessment errors, kiwifruit samples used for assessment may not represent the total batch. Kiwifruit maturity and quality can vary considerably even from the same orchard and harvest (Costa et al., 2003). The variability in kiwifruit quality is either influenced by variable growing conditions or differences in postharvest handling and storage conditions. The impact of the environment and handling on kiwifruit quality makes it challenging to estimate FF after storage from the at-harvest FF and maturity. Therefore, a reliable and easy-to-operate non-destructive technique is desirable for quality assessment as it enables measurement of the majority or all of kiwifruit.

2.1.2 Kiwifruit disorder and damage development

Postharvest technologies, such as low -temperature storage, minimise postharvest loss and extend fruit storage life. Low temperature effectively decreases respiration, ethylene production and enzymatic reactions, delaying ripening in climacteric fruit (Brizzolara et al., 2020). However, low temperatures can induce chilling injury (CI) in chilling-sensitive fruit because of metabolic imbalances and the loss of cellular compartmentation caused by cold stress (Wills & Golding, 2016). CI is a physiological response causing cell damage during long-term storage at low temperatures (Parkin et al., 1989), so CI could also be defined as low-temperature breakdown and storage breakdown disorder in other works (Table 2.1). The susceptibility of CI is associated with membrane composition and function (Murata & Nishida, 1990). Symptoms of kiwifruit CI are complex and can be observed in the exocarp and mesocarp tissue. In general, the early-stage symptoms are tissue mealiness or corkiness (Figure 2.2 L0-L3 left), then tissue discolouration (Figure 2.2 L4) and later tissue water soaking (Figure 2.2 L3 right) can be observed with higher severity.

The incidence and severity of kiwifruit CI are affected by fruit maturity, with early harvested fruit being more susceptible (Burdon et al., 2014). Moreover, rapid cooling (Zhao et al., 2015), long-term storage at lower temperature (Gwanpua et al., 2018) and ethylene exposure (Jabbar & East, 2016) can exacerbate CI incidence. CI can affect fruit quality, external appearance, respiration rate, and ethylene production (Kader, 2002). Furthermore, kiwifruit with CI have lower resistance to mechanical injury and fungal infection (Sevillano et al., 2009). Wang (1994) discussed that failure to detect kiwifruit CI may result in significant fruit loss during storage and marketing.

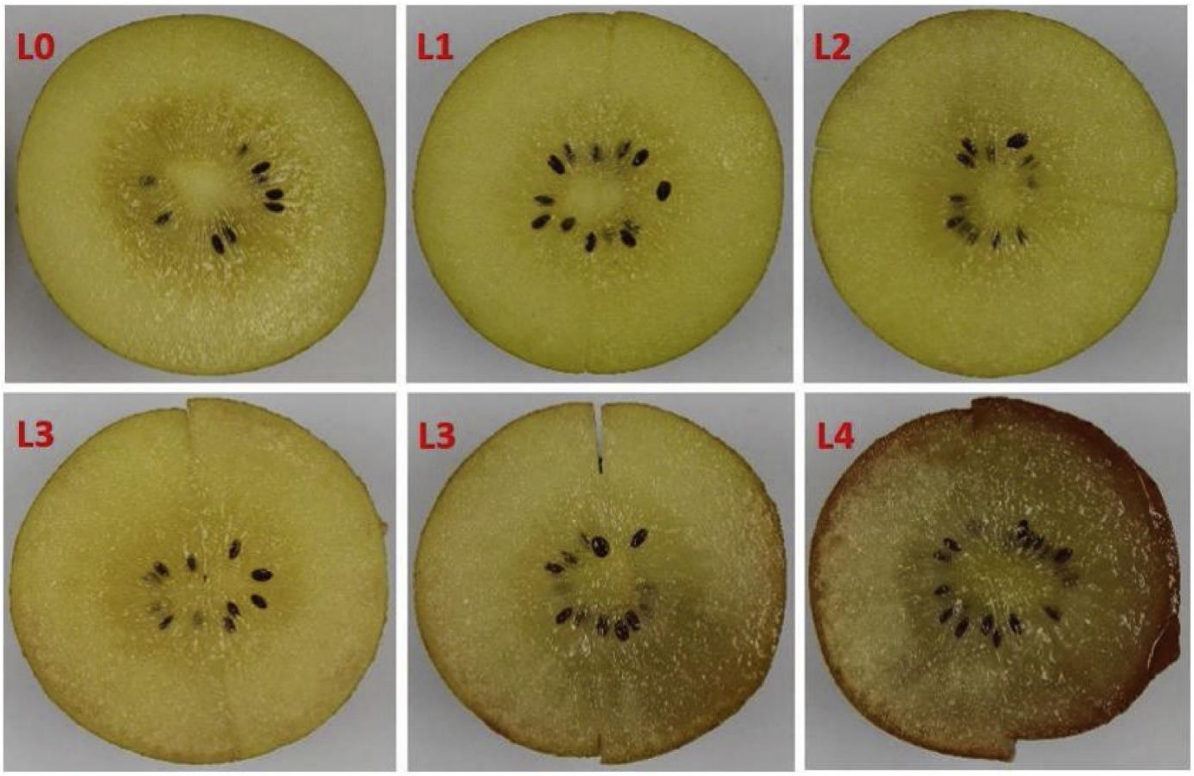

Figure 2.2. Kiwifruit chilling injury symptoms of no symptoms (L0), corkiness (L1, L2, L3 left), water soaking (L3 right), and combined water soaking and discolouration (L4). Retrieved from Wang et al. (2020)with permission.

Kiwifruit CI results in physical property changes, such as skin pitting, granular appearance in the tissue, water-soaked tissue appearance, and tissue disintegration. These CI-related symptoms are due to swelling and disorganization in the chloroplasts and the mitochondria (Burdon & Lallu, 2011a; Wills & Golding, 2016; Kratsch & Wise, 2000). In addition, Kiwifruit CI-related skin and tissue discolouration is caused by changes in chemical composition relating to oxidative damage (Wang, 1989; Burdon & Lallu, 2011a; Burdon, Pidakala, et al., 2014). Those changes can be observed at different CI severities, with the initial CI symptoms only visible internally. Early-stage symptoms of CI can be observed as white specks in the mesocarp tissue at the distal end, while the internal discolouration does not express externally in lower severities. At the microstructure level, Bauchot et al. (1999) reported that the grainy appearance of CI is related to cell porosity. CI tissue presents greater air space and a decreased cell wall material, resulting in white specks and granular tissue spots. Then granular tissue

develops into severe symptoms of granulation and water soaking (Burdon & Lallu, 2011), which isa result of the change in cell membrane permeability.

Table 2.1. Chilling injury symptoms related to changes in physical structure (PS) and chemical composition (CC) for different fruit cultivars.

Fruit	Cultivar	PS symptoms	CC symptoms	examples
Apple	'Granny Smith'	Cell degeneration	Skin discoloration	(Watkins et al., 1995)
Avocado	'Ettinger'	Tissue softening	Mesocarp and skin browning	(Pesis et al., 2002)
Banana	'Brazil'	Pulp rigidity, peel pitting	skin browning	(Luo et al., 2015)
Blood orange	'Sanguinell'	Skin pitting, membrane disintegration	Skin browning	(Habibi et al., 2021)
Cucumber	'Excursion'	Water soaking	Tissue and skin discoloration	(Cen et al., 2016)
Kiwifruit	'Zesy002'	Water soaking	Tissue and skin discoloration	(Wang et al., 2020)
Mango	'Keitt'	Skin pitting, uneven softening	Rind discoloration, poor coloration	(McCollum et al., 1993)
Peaches and nectarines		Tissue mealiness, separation and cavity	Flesh browning, bleeding and internal reddening	(Lurie & Crisosto, 2005)
Tomato	'Rui Xin'	Skin pitting, tissue mealiness	Skin blemished, uneven coloration	(Biswas et al., 2016; Zuo et al., 2016)

However, CI is not the only cause of internal disorder and damage in the kiwifruit industry. Pest-related damage can also become visible in postharvest. In particular, the brown marmorated stink bug (BMSB, *Halyomorpha halys*) is an increasing threat to commercial horticultural crops worldwide. BMSB feed on various crops including kiwifruit and cause substantial economic damage in many countries such as Italy and the USA. Although BMSB hasn't been reported in New Zealand, it raises a high biosecurity risk to key agricultural industries. New Zealand is a suitable region for BMSB establishment, and BMSB could infest kiwifruit quickly if introduced (Lara et al., 2018). NZIER (2017) predicted the exported value of kiwifruit would fall by over NZD 1.8B by 2038 if there were minimal control of BMSB.

The BMSB punctures the skin of the fruit to access food and feed on the abundant sugar supply. Apart from the puncture wound, the damage induced by BMSB can exceed the puncture area during fruit development and postharvest ripening. BMSB damage has been reported to cause kernel abortion and necrotic symptoms in shelled nuts, berries and kiwifruit (Hedstrom et al., 2014; Rice et al., 2014; Lara et al., 2017). Additionally, BMSB damage caused early fruit drop and crop reduction in olives in pre-harvest practices (Zapponi et al., 2022). In postharvest, BMSB damage commonly results in reduced fruit storability (Bergh et al., 2019) and tissue discolouration, as observed in apple (Bergh et al., 2019) and kiwifruit (Andreadis et al., 2018; Lara et al., 2018; Chen et al., 2020). The severity of BMSB damage is affected by the time taken for the damage to develop, as well as fruit cultivar and maturity (Brown & Short, 2010; Bergh et al., 2019). For example, BMSB damage to apples was more severe if the fruit was damaged early in the season when the damage had time to develop prior to harvest (Bergh et al., 2019). Some BMSB wounds are either not visible or only visible as small discoloured dots on the fruit skin (Brown & Short, 2010), and have a delayed impact on fruit quality. Therefore, early detection of BMSB damage is desirable for fruit loss reduction.

In the industry, kiwifruit CI or BMSB damage is assessed visually by cutting a subsample of fruit from a batch before export, assuming that the sample is representative of the entire population. Given the small proportion of fruit disorder or damage can affects, this sampling method can be highly ineffective, and unidentified damaged fruit can result in fruit loss further in the supply chain. A reliable, non-destructive technique is desired for kiwifruit internal disorder detection, enabling inline grading of entire batches of fruit before marketing.

2.2 Fruit and light interaction

2.2.1 Optical properties

Light interacts with fruit tissue in different ways, and those interactions can be characterised as photon propagation inside biological tissues. Light and fruit interactions include reflection (Figure 2.3a), absorption (Figure 2.3b), scattering (Figure 2.3c) and transmission (Figure 2.3d). These interactions are linked with fruit quality attributes and can be interpreted with the results of resolved imaging techniques.

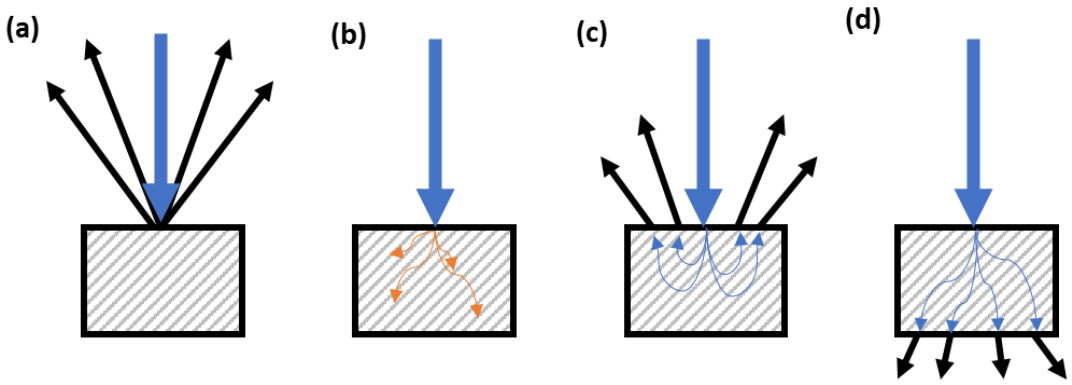

Figure 2.3. Schematic of the potential light and sample interaction (Adapted from Walsh et al., 2020). (a) specular reflection. (b) absorption. (c) scattering. (d) transmitting.

In light propagation, a small portion of the light is directly reflected at the boundary (Figure 2.3a), while the remaining portion of the light enters the medium and is either absorbed or scattered. Figure 2.4 demonstrates how light propagates when it illuminates a turbid medium. A turbid medium is inhomogeneous and causes multiple scattering events when irradiated by light. Fruit tissue can be considered a turbid medium, with light scattering occuring at the cell wall, cell membranes, and nuclei (Esau, 1953). Alternatively, those biological tissues can be considered as homogeneous materials, which are composed of uniform structures and compositions, thus exhibit consistent optical properties, such as refractive index, absorption coefficient and scattering coefficient (Born & Wolf, 2013) to describe light absorption, scattering and reflection. Therefore, when light interacts with fruit tissue, photon activities are

predictable. The changes in optical properties of fruit tissue could be due to multiple environmental factors, such as temperature and pressure (Born & Wolf, 2013).

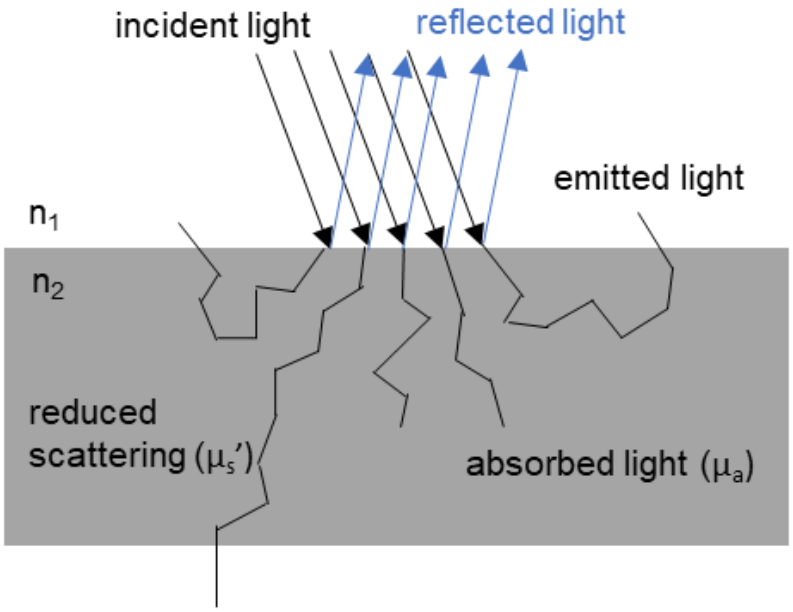

Figure 2.4. Schematic illustration of interactions of light with a turbid sample (adapted from Rowe, 2015).

2.2.1.1 Absorption coefficient

Absorption coefficient (μ_a) describes photons' energy absorbed or decreased by atoms or molecules. Light absorption corresponds to a specific energy level hence absorption changes at different wavelength bands. According to the Beer-Lambert law, the absorption coefficient (μ_a) in a transparent solution of a sample with low or no scattering can be described by Eq. 2.1 (Cen, 2011)

$$I = I_0 exp\,(-\mu_a d) \qquad \text{Eq. 2.1}$$

Where I is the intensity of transmitted light intensity, I_0 is the intensity of incident light intensity, and d is the material thickness.

The absorption of fruit is related to the different chemical compounds inside. In fruit samples, absorption is mainly caused by the C-H, O-H, and N-H bonds in the NIR wavelength bands.

These chemical bonds (excluding N-H) are found in water and sugars (Nicolaï et al., 2014). The absorptions in water, fats, carbohydrates and proteins are mainly at the NIR wavelength (770-2500 nm) due to the rotation or vibration of radiated electrons (Cen, 2011). Absorption in the NIR wavelength region causes rotation or vibration in the irradiated molecules. In liquid water, low-frequency vibrations occur, which involve the stretching or bending of intermolecular hydrogen bonds. Light absorption is also influenced by temperature in the NIR range.

In contrast, the absorption of pigments (Figure 2.5), such as chlorophylls and carotenoids, at the visible wavelength (400-770 nm) is due to the excitation of valence electrons. Absorption at visible wavelength is highly influenced by temperature. The amount of light absorption due to these compounds could be used for fruit and vegetable quality measurement. For instance, Qin and Lu (2008) found the absorption at chlorophyll band (675nm) and anthocyanin band (535nm) could be utilized to classify tomatoes at three maturity stages (green, pink and red).

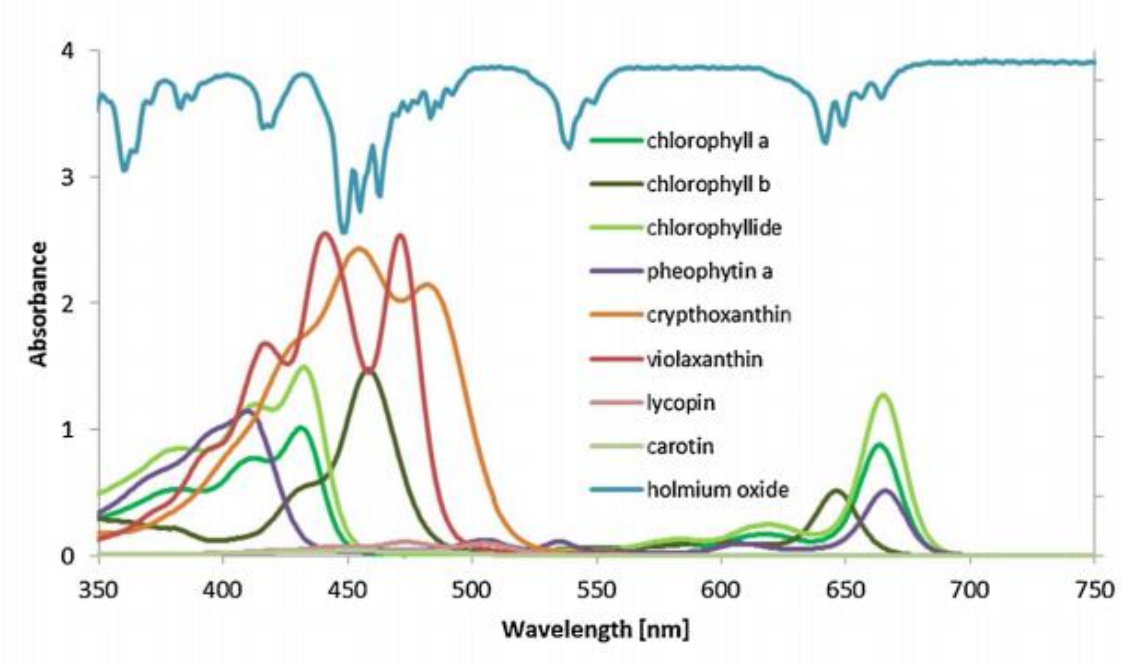

Figure 2.5. Light absorption spectra in the visible region of pigments in fruit. Retrieved from Walsh et al. (2020) with permission.

2.2.1.2 Scattering coefficient

In elastic scattering, the photon interacts with the scatter particle without changing the internal energy. Therefore, the photons have the same kinetic energy after the interaction with possible direction changes. The elastic scattering appears when the photon and the scatter particle have the same wavelength or energy, such as Rayleigh scattering (Miles et al., 2001). In inelastic scattering, the photon transfers some of its energy to the scatter particle, resulting in a decrease in the photon kinetic energy. The wavelength or energy of the scattering particle is different from the photo. The inelastic scattering can result in the excitation of the scatter particle, such as Raman scattering(Long, 2002), where incident photons interact with molecular vibrations. Light scattering in fruit is generally considered inelastic scattering, and can be described as the photon path direction changes when interacting with scattering particles. The angles of the scattering path depend on the refractive indices, scattering material type, scattering particle sizes and light wavelength. Light scattering in biological tissue is denoted by the scattering coefficient scattering coefficient (μ_s), which is defined as the probability of photon scattering in tissue per unit path length. Like the absorption coefficient, μ_s can be described in the following equation (Eq. 2.2, Cen, 2011):

$$I = I_0 exp\,(-\mu_s d) \qquad \text{Eq. 2.2}$$

Where I is the intensity of transmitted light intensity, I_0 is the intensity of incident light intensity, and d is the material thickness.

Light scattering changes with different tissue structures. In fruit samples, scattering is mainly determined by cellular structures and subsurface microstructures. For example, the porosity of apple tissue samples was reported to impact light scattering (Wang et al. 2020). Dintwa et al. (2011) reported that apple FF is related to its microstructure. For example, apple tissue

crispness is related to parenchyma cells with vascular tissue and air spaces (Vanoli et al. 2010). Therefore, μ_s may provide useful information about changes in FF resulting from microstructure changes. Previous research has investigated fruit FF via light scattering. For instance, Rowe (2015) and Vanoli et al. (2010) measured apple FF with a multi-backscattering system and reported correlations between optical properties and FF. Moreover, McGlone et al. (1997) studied kiwifruit FF using a NIR system and found that scattered light intensity increased with decreasing FF. Furthermore, for apple fruit, higher μ_s was found in the skin (around 300 -400 cm^{-1}) than in the cortex (100-130 cm^{-1}). In addition, the μ_s of the apple tissue changed during 70 days of maturation by around 35 cm^{-1} (Van Beers et al., 2017).

2.2.1.3 Anisotropy factor

Anisotropy factor (*g*) measures the number of photons that remain in the same direction after a single occasion of scatter. When a photon is scattered by hitting a particle, its path direction changes with scattering angle θ compared to the original direction. The probability of θ can be described by *g*. According to the Henyey-Greenstein function, *g* could be calculated with the expected value of cosine θ (Cubeddu et al., 2001) as Eq. 2.3

$$g = < cos\,\theta > = \int_0^{\pi} p\,cos\,\theta\,2\pi\,sin\,\theta\,d\,\theta \qquad \text{Eq. 2.3}$$

Where *g* is the anisotropy factor, θ is the scattering angle for each photon, p is the probability of θ, represents the amount of forward direction retained after a single scattering event, and *d* is the material thickness.

The value of *g* ranges from -1 to 1. Photons are backward scattered when *g* = -1 or forward scatted when *g* = 1. For most biological tissues, g ≈ 0.70- 0.99 was reported in the Vis-NIR region

(Cen, 2011). Baranyai & Zude (2009) estimated kiwifruit *g* using a numeric simulation and found that there was a difference ($p < 0.01$) of *g* between firm/ripe and overripe fruit.

2.2.1.4 Reduced scattering coefficient

The reduced scattering coefficient (μ_s') describes the amount of isotropic scattering occurring per unit distance, which is used in the light diffusion theory model. μ_s' is related to the μ_s and *g*, which is calculated as Eq. 2.4 (Graaff et al., 1993):

$$\mu_s' = \mu_s (1 - g) \qquad \text{Eq. 2.4}$$

Where *g* is the anisotropy factor, μ_s is the scattering coefficient.

In many biological materials, photons will be absorbed after several scattering events (Lu & Peng, 2006). Scattering is dominant during the light interaction processes in a turbid medium, and *g* is considered equal to 0. Solutions like milk could be considered isotropic, while the entire fruit cannot be considered as isotropic. Kiwifruit subsurface area may be isotropic, and the light-fruit interaction in this region may be described by μ_a and μ_s'. The μ_s' spectrum of fruit tissues in the Vis-NIR region is relatively flat (Cubeddu et al., 2001; Qin & Lu, 2008), whereas the μ_s' changes during maturation due to accompanied near-surface cellular structural changes of fruit. Seifert et al. (2015) reported a decreased μ_s' at 679 nm during plum and apple fruit development. Therefore, μ_s' obtained from selected wavelengths could be informative without data collection through the entire wavelength band. Values of the kiwifruit μ_s' have been reported that vary at different parts of kiwifruit with seed (0.12 cm^{-1}), flesh (0.39 cm^{-1}) and seed-based part (0.95 cm^{-1}, Fang et al. 2016).

2.2.1.5 Refractive index

The refractive index (*n*) measures light refraction within different materials. According to Snell's law, *n* of two different media can be described as Eq. 2.5:

$$n_1 \sin\theta_1 = n_2 \sin\theta_2 \quad \text{Eq. 2.5}$$

Where n_1 and n_2 are the refractive indices of the different mediums, θ_1 is the incident light angle and θ_2 is the refractive light angle.

The refractive index can change when light travels in multiple layers of biological tissue. The fruit tissue is regarded as a homogenous medium, so an average value of the refractive index is used (Simonenko et al., 2000). Haskell et al. (1994) suggested using an overall fruit relative refractive index (1.35), where the refractive index of water is 1.333, to describe the medium boundary with air. The fruit refractive index is also considered consistent in the vis-NIR region.

2.2.2 Calculation of optical properties

2.2.2.1 Diffusion approximation model of optical properties: multiple scattering theory and radiation transport theory

Two theories could be used to describe light interaction in a turbid medium. The first is the multiple scattering theory (MST) based on Maxwell's equation. MST calculates the results from polarisation, diffraction, and interference (Martelli et al., 2009). However, fruit tissue structures are very complex. Thus, using MST to describe light interactions inside the fruit is very challenging. Alternatively, the second theory, radiation transport theory (RTT), is more suitable to describe light interaction inside the fruit. RTT describes the energy flow changes due to light absorption, scattering or transmission. This section includes a brief introduction of RTT and its mathematical model.

The RTT describes the light energy flow through the medium. The RTT has the assumption that photons do not interact with each other but interact with cell structures or chemical compounds in fruit, resulting in photons being either scattered or absorbed, with —the photon energy changing after scattering and absorption events. The RTT equation (Eq. 2.6) describes that energy reduction is timewise and flow-wise balanced. (Ishimaru, 1978).

$$\frac{1}{c}\frac{\partial L(r,\hat{s},t)}{\partial t} + \nabla \cdot L(r,\hat{s},t)\hat{s} + (\mu_a + \mu_s)L(r,\hat{s},t) = \mu_s \int_{4\pi}^{\infty} L(r,\hat{s}',t)\, p(\hat{s}\cdot\hat{s}')d\Omega' + Q(r,\hat{s},t) \quad \text{Eq. 2.6}$$

Where $L(r,\hat{s},t)$ is the radiant energy (J) with unit solid angle Ω in direction $\hat{s}$ at the position *r* and time *t. The* $p(\hat{s}\cdot\hat{s}')$ is the probability distribution of the scattering angle [$\hat{s}$: $\hat{s}'$]. $Q(r,\hat{s},t)$ is the injection energy. c (m/s) is the velocity of light in the medium, which equates to Eq. 2.7. *n* is the refractive index of the medium.

$$c = (3 \times 10^8)/n \quad \text{Eq. 2.7}$$

Based on the RTT, a diffusion approximation model (DFM) is developed to describe the light propagation in biological materials (Farrell et al., 1992). This DFM model has the following assumptions(Cen, 2011.): Firstly, scattering is dominant (i.e., μ_s' » μ_a). Secondly, the detection distance exceeds the average path length of the photons' free transport. Thirdly, the light propagation is randomized, the light source is isotropic, and lastly, photons travel in an infinite and homogeneous turbid media. Farrell et al. (1992) described the diffusion model equation as Eq. 2.8 and Eq. 2.9:

$$\frac{\partial \Phi(\vec{r},t)}{\partial t} = D\nabla^2\Phi(\vec{r},t) - \mu_a\Phi(\vec{r},t) + S(\vec{r},t) \quad \text{Eq. 2.8}$$

$$D = \frac{1}{3[\mu_a + (1-g)\mu_s]} = \frac{1}{3(\mu_a + \mu_s{}')} \quad \text{Eq. 2.9}$$

Where ∇^2 represents the divergence and gradient spatially, $\Phi(\vec{r}, t)$ is the fluence rate, $\vec{r}$ is the distance, t is time variable, $S(\vec{r}, t)$ is the isotropic source in the medium, and D is the diffusion coefficient. μ_a is the absorption coefficient, and $\mu_s{}'$ is the reduced scattering coefficient.

The DFM equation (Eq. 2.10) can be resolved as follows based on the above equation:

$$R_f(r, \mu_a, \mu_s') = \frac{\mu_s{}'}{4\pi(\mu_a + \mu_s{}')}\left[\frac{1}{\mu_t{}'}\left(\mu_{eff} + \frac{1}{r_1}\right)\frac{exp(-\mu_{eff} r_1)}{r_1{}^2} + \left(\frac{1}{\mu_t{}'} + \frac{4F}{3\mu_t{}'}\right)\left(\mu_{eff} + \frac{1}{r_2}\right)\frac{exp(-\mu_{eff} r_2)}{r_2{}^2}\right] \quad \text{Eq. 2.10}$$

$$\mu_{eff} = [3\mu_a(\mu_a + \mu_s{}')]^{1/2} \quad \text{Eq. 2.11}$$

$$\mu_t{}' = (\mu_a + \mu_s{}') \quad \text{Eq. 2.12}$$

$$r_1 = \left[\left(\frac{1}{\mu_t{}'}\right)^2 + r^2\right]^{1/2} \quad \text{Eq. 2.13}$$

$$r_2 = \left[\left(\frac{1}{\mu_t{}'} + \frac{4F}{3\mu_t{}'}\right)^2 + r^2\right]^{1/2} \quad \text{Eq. 2.14}$$

Where R_f describes the diffusion reflectance on an attenuation profile, r is the distance from the incident point, μ_{eff} is an effective attenuation coefficient (Eq. 2.11), $\mu_t{}'$ is the total attenuation coefficient (Eq. 2.12) and is used for calculating r_1 and r_2 (Eq. 2.13, Eq. 2.14) (Qin & Lu, 2005). F is an internal reflection and Groenhuis et al. (1983) developed an alternative empirical approach to calculate it (Eq. 2.15):

$$F = \frac{1 + r_d}{1 - r_d} \quad \text{Eq. 2.15}$$

Where r_d is the distance of each point on the attenuation profile in the diffusion theory model (Eq. 2.16).

$$r_d \approx -1.440\ {n_r}^{-2} + 0.710{n_r}^{-1} + 0.688 + 0.0636n_r \quad \text{Eq. 2.16}$$

Where n_r is the relative refractive index.

For biological materials, μ_a and μ_s' could be calculated together with a known attenuation profile and refractive index based on DFM equations. Non-destructive techniques based on DFM, including time-resolved, frequency-domain, and spatial-resolved imaging techniques, have been utilised to estimated μ_a and μ_s' (Section 2.2.3). Alternatively, μ_a and μ_s' could be measured destructively using a single-sphere integrating sphere-inverse adding double method (IS-IAD), double-sphere IS-IAD and photon density wave (PDW) spectroscopy (Section 2.2.2.2). Moreover, Zude-Sasse et al. (2019) employed the PDW method as the reference to validate the calculation of μ_a and μ_s'. In addition, numeric simulation methods have been applied for calculating μ_a and μ_s' (Section 2.2.2.3), and Watté et al. (2015) developed a metamodel combining the diffusion theory to extract μ_a and μ_s' separately.

2.2.2.2 Destructive measurement of optical properties

The original double-sphere IS-IAD is presented in Figure 2.6, which has the sample placed between two spheres. The double-sphere IS-IAD system increased signal in both spheres and permitted unscattered light to leave the system (Pickering et al., 1993). To simplify the system in Figure 2.6, single-sphere IS-IAD was developed by reducing one sphere. However, less accurate results were produced than a double-sphere system.

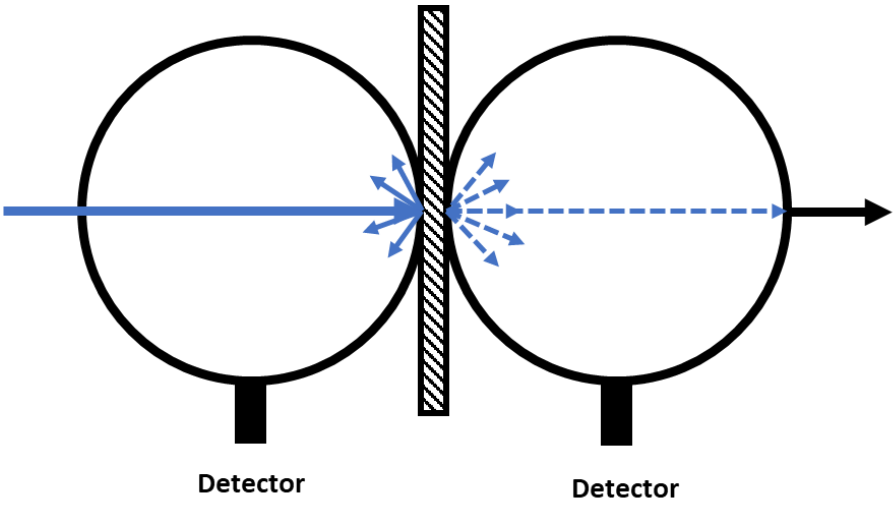

Figure 2.6. The double-sphere sphere Intergrading sphere system measures a sample (grid) (Adapted from Pickering et al., 1993). Blue solid lines represent light beams, blue dashed lines represent transmitted light, blue arrows represent scattered light, and the black arrow represents the escaped light.

The IS-IAD measures optical properties and is used as an optical calibration tool for non-destructive methods that measure the optical properties of tissues (Jacquez & Kuppenheim, 1955; Tuchin, 2007). The inner surface of an integrating sphere is uniformly coated with highly reflective diffuse materials (e.g., reflectivity ρ=0.98) to achieve homogenous distributions of light radiation. A standard IS-IAD process is described by Wang et al. (2014) to measure total transmittance (T) and total reflectance (R). The T and R measured using the integrating sphere can usually be processed using the integrating adding double method (IAD). Lu et al. (2020) described the IAD procedure and how to calculate μ_a and μ_s' (Figure 2.7) and claimed that the results obtained from the IS-IAD method could be used for most fruits and vegetables. Prahl et al. (1993) gave the assumptions for the optical property calculation using IS-IAD, which are that light distribution is not time-dependent, tissue structure is homogenous, sample slab is infinite, and illumination is uniform. However, none of those assumptions can be confirmed in the fruit sample.

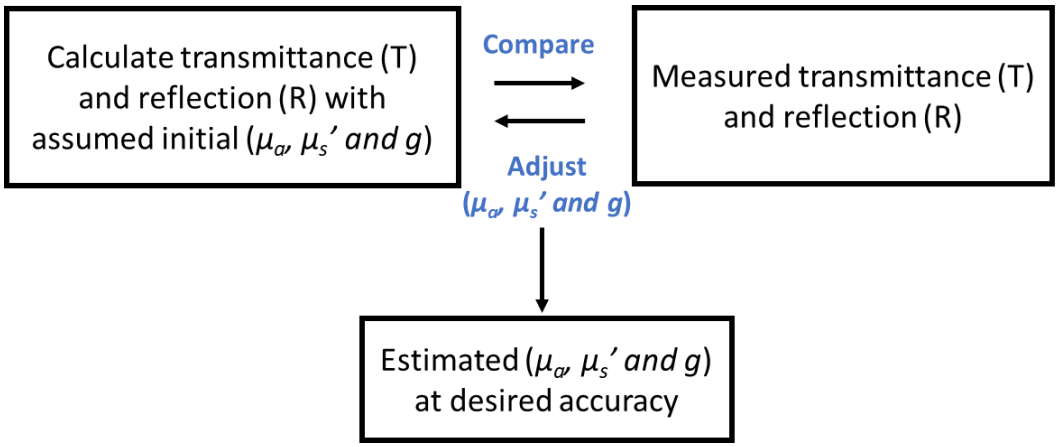

Figure 2.7. Flowchart of the inverse adding double procedure to calculate μ_a and μ_s'.(Adapted from Lu et al 2020)

The IS-IAD method is primarily used at the research scale for data validation. Saeys et al. (2008) investigated apple tissue optical properties using the IS-IAD method at 350-2200 nm for three cultivars and found skin tissue had three times more scattering than flesh tissue. Rowe (2015) employed this technique to validate the Intralipid® optical phantoms for calculating apple μ_a and μ_s'. Fang et al. (2016) reported that kiwifruit's optical properties were different at different subsurface layers using the IS-IAD method. The limitations of applying IS-IAD in the industry are that the IS-IAD method is destructive and has not been proven sufficiently; as a result, large computational power and heavy calculation are required.

Photon density wave (PDW) spectroscopy is another destructive instrument to measure fruit μ_a and μ_s' independently. The setup of a PDW spectrometer is presented in *Figure* 2.8. The PDW system emits photons into the turbid medium along the first optical fibre, and the photons are then transmitted out of the medium with a second fibre of a set length. The PDW spectroscopy calculates optical properties based on the modulation frequency and distance between emission and detection fibres. The advantage of PDW is measuring μ_a and μ_s' independently without calibration inside a multiple light scattering environment. However, there are assumptions about the medium using PDW, which are that the scattering of the medium is

strong, but the absorption is very weak (Hass et al., 2015), and the sample is infinite. Adebayo et al. (2017) and Zude-Sasse et al. (2019) employed PDW spectroscopy to measure the optical properties of pear and utilized solid optical phantoms to validate the resulting optical properties. Compared with the IS-IAD method, PDW has the advantage of measuring a larger area without laborious and destructive sample manipulation. However, PDW is time-consuming and destructive with puncturing holes in the sample, thus, PDW is not ideal for industrial practice either.

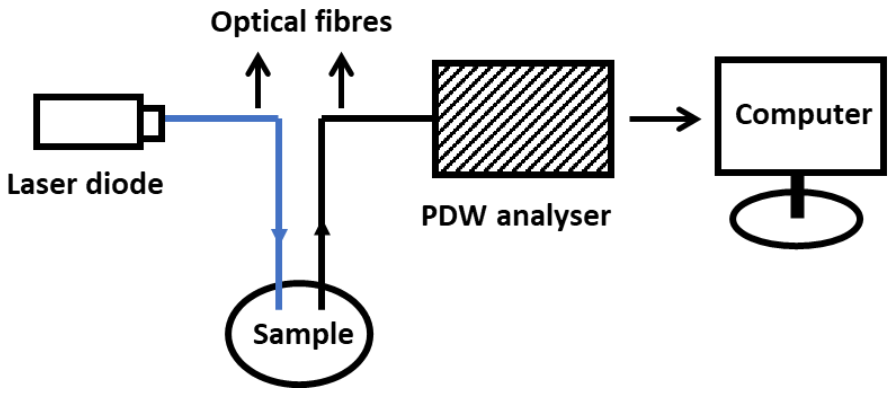

Figure 2.8. Schematic of the photon density wave (PDW) spectrometer (Adapted from Bressel et al., 2013)

2.2.2.3 Simulation of optical properties

Estimating fruit optical properties is very challenging using DFM as fruit samples cannot meet all the assumptions with their heterogeneous and irregular characters. Numeric simulations, including Monte Carlo simulation (MCS) and finite element analysis (FEA), are often applied to extract optical properties from the inverse algorithm. These numerical simulations are utilized to describe the light propagation in a turbid medium under certain conditions.

The MCS method physically determines the expected photon random walk in a turbid medium (Wang et al., 1995) and is served as the inverse validation method of the RTT equation. When a photon is emitted onto the sample, MCS estimates the single interaction of the photon, whether absorbed or scattered. The MCS method requires many photons to simulate

reasonable light propagation paths. Therefore, MCS requires a lot of computing power to achieve accurate simulation. Several programs ('MCML' and 'CONV') developed by Wang et al. (1995) and an R package ('MCBackscattering') written by Baranyai (2020) were created to estimate light paths using MCS. For the fruit quality assessment, MCS could be appropriate as fruit are usually inhomogeneous and multilayered. MCS has been implemented to detect bruising in apples (Baranyai & Zude, 2008) and classify ripe and overripe fruit in kiwifruit maturity studies (Baranyai & Zude, 2009). Postelmans et al. (2018) found that it's critical to identify the refractive index change between particles when using MCS as inverse validation. Although MCS requires intensive computation, MCS can be easily implemented for complex sample estimation and is not limited by the assumption that scattering is dominant. Thus, the MCS method with validation may accurately estimate optical properties in fruits and vegetables (Baranyai & Zude, 2008).

The FEA is another numerical solution to calculate the optical properties of irregular geometrical samples. In the FEA process, continuous functions to define over a finite number of elements (Zulkifli et al., 2020) and continuous quantities (such as μ_a and μ_s') are assumed as discrete particle interactions. In FEA model, a complex physical structure is break down into smaller, simpler parts called finite elements. By analyzing these elements individually, the model can predict the behaviour of the entire structure. Inside the fruit, the absorption and scattering can be predicted by those elements' activities. Therefore, a large number of (infinite) photon propagations can be described physically with finite mathematical properties for the estimation of optical properties (Dintwa et al., 2011). Research has been conducted implementing the FEA method to analyse fruit stress-strain and moisture loss (Janjai et al., 2008). Mohammed & Verhey (2005) added the damage function into the FEA modelling process to predict tissue damage zone geometry. Although FEA models can be analysed using

various software, such as COMSOL, to estimate fruit optical properties, it's difficulted to link simulated optical properties with a real case due to fruit cell interactions.

Metamodeling is another approach to estimating the optical properties of a turbid medium based on scattering particle distribution. Metamodels are created with a set of optical phantoms that serve as a matching standard for the sample medium. Optical phantoms can be manufactured with design μ_a and μ_s' as solid phantoms (Zude-Sasse et al., 2019) or manually made in the lab as liquid phantoms (Aernouts et al., 2013). Aernouts et al. (2013) used a Metamodel with 57 liquid phantoms, 8 known scattering and 8 absorption levels by mixing Methylene Blue ink, Intralipid® 20% and water at different concentrations. In Aernouts et al. (2013) work, the images of liquid phantoms obtained from the optical system were linked to solutions' optical properties measured by the IS-IAD method with quantitative models. In addition, the performance of the Metamodel was validated with 8 additional phantoms at a wavelength range of 550 nm to 1000 nm and achieved a good model performance, where μ_a and μ_s' had a high R^2 (0.980 and 0.998) and low RMSE (0.032 and 0.197 cm^{-1}). In the end, the independent inverse validation is suggested to improve the μ_s' prediction (Aernouts et al., 2015). In conclusion, the Metamodel method has the potential to provide references for estimating the optical properties of turbid samples and is more feasible and less complex compared with the other two numerical simulations

2.2.3 Non-destructive methods for fruit quality measurement

2.2.3.1 Non-destructive technology introduction

Non-destructive techniques have been developed over the past 30 years. Compared with destructive techniques, non-destructive techniques have many advantages. Firstly, non-destructive techniques allow the majority (or all) of fruit to be assessed without damaging the

fruit. Secondly, nondestructive analysis can be conducted on the same fruit over time, capturing more information about the physiological development of the same fruit without introducing the effect of variation among fruit. Thirdly, some optical techniques could potentially be applied in packhouse sorting lines with the spatially resolved set-up, making the quality assessment available in industrial situations.

Many studies have investigated the use of non-destructive techniques to predict quality attributes. However, fruit are biologically complex, so it is difficult to obtain accurate information on internal quality attributes using non-destructive techniques. Despite challenges with the adoption of non-destructive techniques in practice, such as set-up and data analysis, there is potential for non-destructive techniques to be used throughout the supply chain. Examples of industrial-scale and lab-scale non-destructive techniques investigated for application in fresh produce are discussed below (Section 2.2.3.2).

2.2.3.2 Fringe projection

Fringe projection is a non-destructive technique that captures the surface information of an object (Gorthi & Rastogi, 2010) and has been used in many areas, including quality control, reverse engineering, and medical quantification. In the fringe projection process, a sinusoidal fringe pattern is projected onto the surface of an object, and the camera records the distorted pattern. The object's surface structure influences the received pattern, and then the software calculates surface topography mathematically using the Fourier transform method (Gorthi and Rastogi, 2010). Figure 2.9 shows a fringe projection system comprised of a projector, camera and computer (Gorthi & Rastogi, 2010). The fringe projection method has been used to measure skin roughness, evaluate fruit colour changes and capture fruit skin features for apples and kiwifruit (Bloemen et al., 2011; East et al., 2016; López et al., 2017). Lai et al. (2019)

investigated kiwifruit skin properties using fringe projection and attempted to link the results to kiwifruit fruit quality as well as kiwifruit plant growth conditions. Additionally, fringe projection could measure the changes in fruit size and colour during apple ripening (López et al., 2017). Although fringe projection could rapidly and accurately obtain skin information, it cannot provide information directly on internal quality attributes.

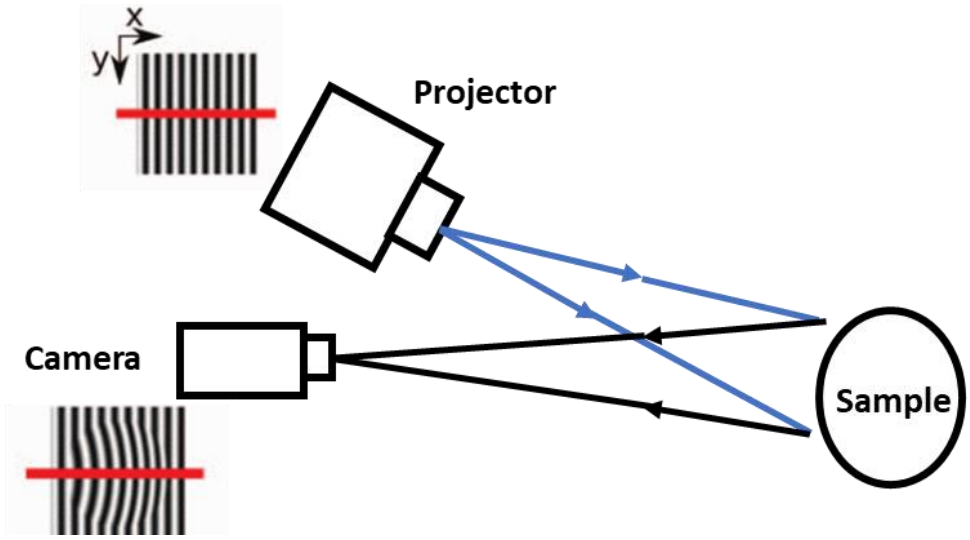

Figure 2.9. Schematic of the fringe projection system (Adapted from Khoiruddin, 2015)

2.2.3.3 Optical coherence tomography

Beyond the skin properties, optical coherence tomography (OCT) could capture two- and three-dimensional images of fruit sub-surface structures (Li et al., 2019). OCT is a fast, contactless optical technique that provides high-resolution images with an axial resolution of 1 to 15 µm and a penetration depth of up to 1.5 mm (Meglinski et al., 2010). Figure 2.10 shows an OCT system schematic

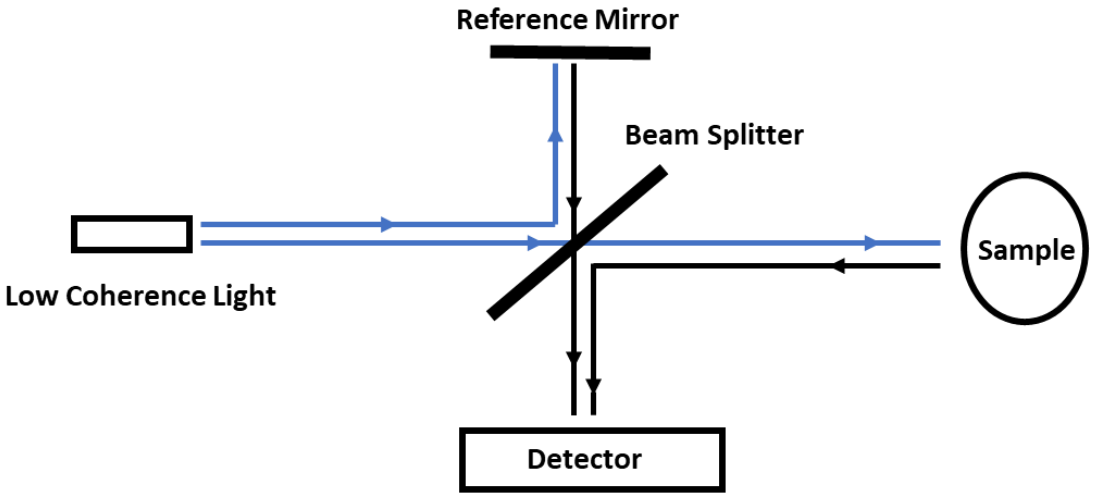

Figure 2.10. Schematic of optical coherence tomography system (Adapted from Thomas & Duguid, 2004)

Studies have been conducted using OCT to monitor near-skin structural properties of horticultural products during postharvest practices. Example images of fruit captured using OCT are presented in Figure 2.11. OCT images could describe fruit skin and internal structure changes during storage. After exposure to pulsed electric fields or with internal disorder, changes are found in appearance from OCT images in apple peel (Verboven et al., 2013), grape (Gocławski et al., 2017) and onion Meglinski et al. (2010). Besides, OCT images may assist in making storage decisions. Li et al. (2021) reported blueberry cell layer thickness was affected by storage humidity using OCT. However, when investigating kiwifruit, Li et al. (2015) noted that several artefacts could be seen in OCT images, likely caused by the various skin structures such as lenticels and trichomes. In conclusion, OCT has the advantages of being non-destructive and can provide real-time measurement with multi-layer subsurface information. However, OCT has limitations between resolution and penetration depth, which must be improved before industrial application.

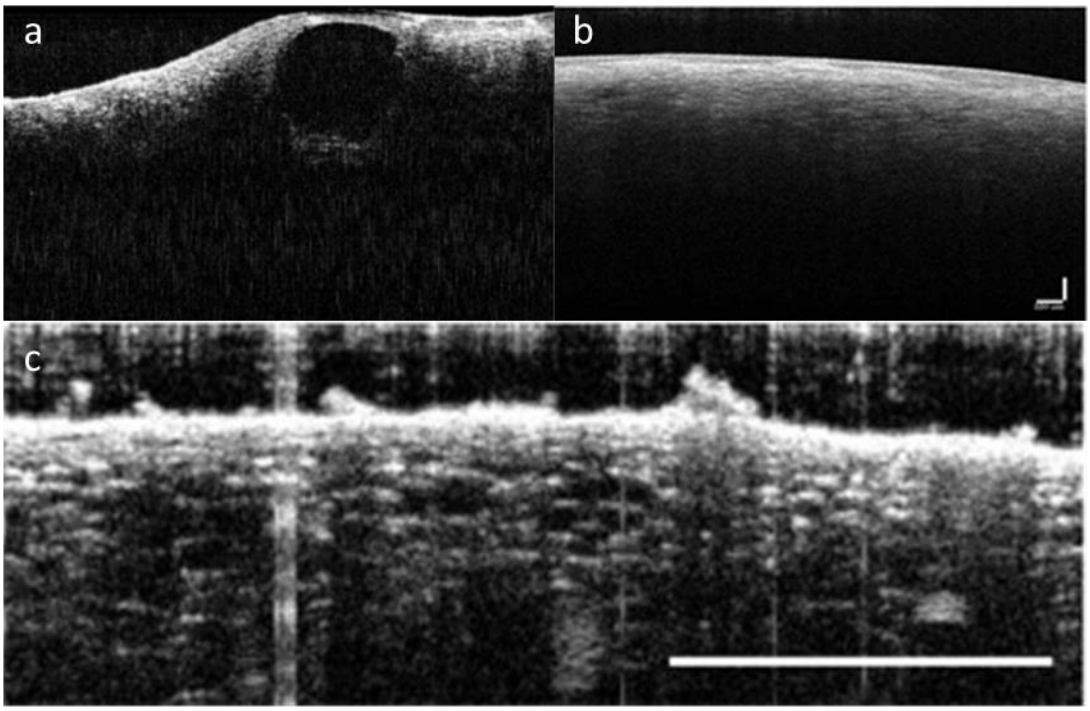

Figure 2.11. Optical coherence tomography images of (a) mandarin with 2 mm wide × 1.1 mm deep, (b) loquat at 250 µm scale bar, (c) kiwifruit at 1 mm scale bar. Retrieved from Magwaza et al. (2013), Zhou et al. (2018) and Li et al. (2015) with permission.

2.2.3.4 X-ray micro-computed tomography

Similar to OCT, which provides three-dimensional information on fruit structure at a micro-scale, other optical techniques, such as X-ray micro-computed tomography (CT) or micro–X-ray CT, provide visualisations of intercellular spaces and pores in the fruit. Compared with OCT, micro–X-ray CT is good at measuring tissue density and porosity, whilst OCT looks at tissue boundaries. A micro X-ray CT system contains an X-ray source tube and a plane detector to convert signals into radiographs (Schoeman et al., 2016), in which received signals are related to the microstructure composition of the sample after exposure to X-ray (Figure 2.12). The micro CT technique has been used for fruit quality attributes and internal disorder assessment. Lammertyn et al. (2003) studied core breakdown disorder development of 'Conference' pears using X-ray CT and reported that the cellular microstructure differed between sound and brown tissues. In addition, microstructure information obtained from X-ray CT was used for studying

fruit ripening processes and linked with scattering properties in mango (Cantre et al., 2014) and apple (Wang et al., 2020). Besides, soft X-ray imaging was applied to classify bruises (Shahin et al., 2002) and water core in apple tissue (Kim & Schatzki, 2000). X-ray CT has the advantage of non-destructively providing useful information on fruit structure. However, X-ray and micro–X-ray CT analyses are relatively expensive, time-consuming, and require heavy computing work. Therefore, this technique is more suitable for supporting other non-destructive methods at a research scale, and micro–X-ray CT is more useful as a disorder detection tool than a quality estimation tool.

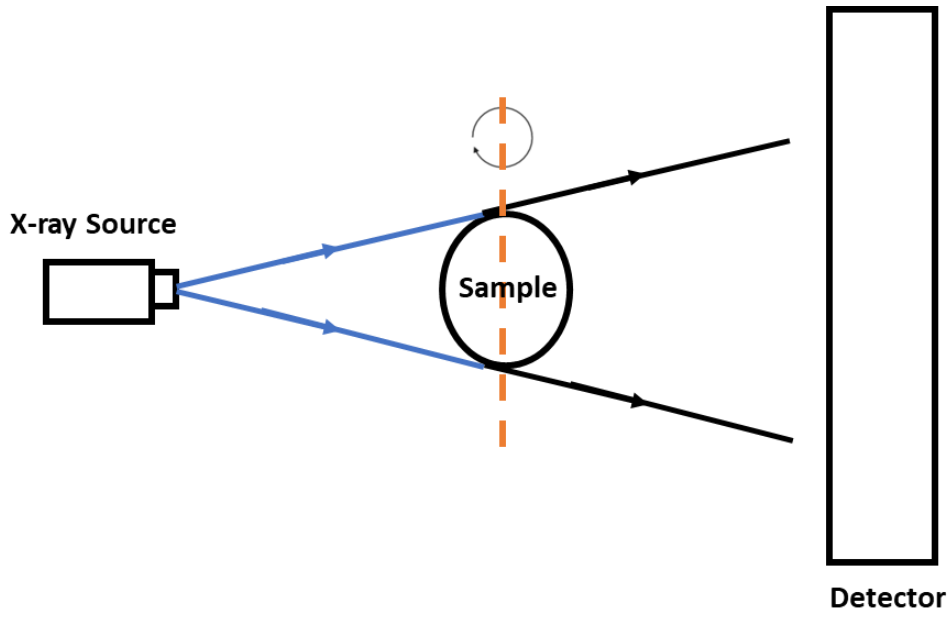

Figure 2.12. Schematic of the micro-X-ray computed tomography (CT) system (Adapted from Schoeman et al., 2016)

2.2.3.5 Visible-near infrared spectroscopy

Unlike the previous techniques providing scattering information, visible-near infrared (Vis-NIR) spectroscopy evaluates fruit and vegetable quality attributes according to the light absorption properties at visible (400-700nm) and near-infrared (780-2500nm) wavelengths (Figure 2.13). When fruit or vegetables are irradiated with Vis-NIR radiation, the emitted light is either diffusionally reflected by the surface or absorbed by the particles inside the fruit tissue (Walsh

et al., 2020). Fruit quality attributes, such as SSC and pigments, contain chemical bonds such as C-H, N-H, OH, and CO. These chemical bonds can absorb energy in specific NIR regions; hence, the related compositional attributes can be observed with their spectral character.

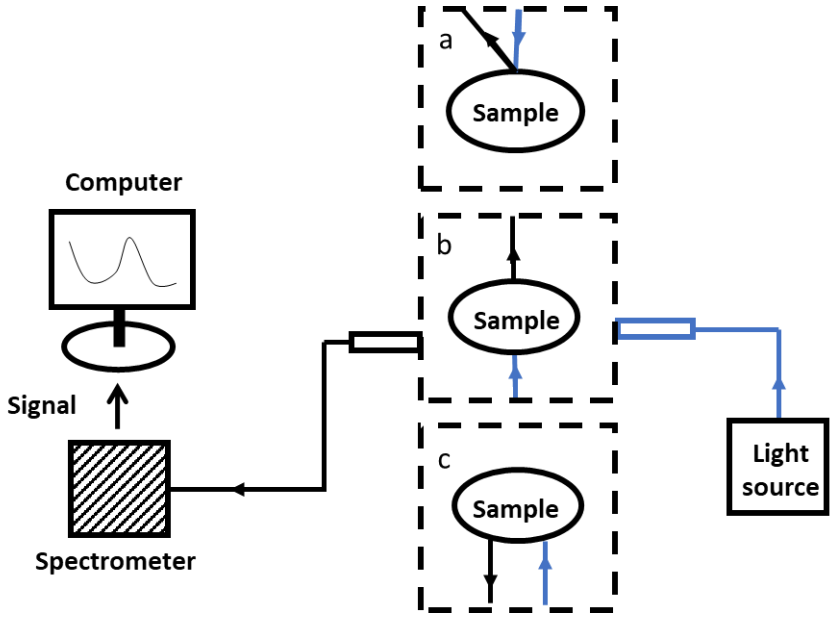

Figure 2.13. Schematic of the visible-near infrared (Vis-NIR) spectroscopy system and the set-up for acquiring (a) reflectance, (b) transmittance and (c) interactance. (Adated from Mendoza et al., 2012; Nicolaï et al., 2014)

Vis-NIR technology has been studied extensively to predict quality attributes in kiwifruit. NIR captures data related to kiwifruit's chemical properties,primarily containing the signal of absorption related to kiwifruit's chemical properties; thus, NIR spectroscopy has been utilized for fruit SSC and DMC measurement. Schaare & Fraser (2000) used the Interactance mode, which combined reflectance and transmission information, of Vis-NIR spectroscopy to predict kiwifruit quality attributes and reported a high SSC prediction performance of R^2=0.93. Clark et al. (2004) used a classification model built with quantitative Vis-NIR reflectance variables and predicted half of the CI incidence observed after 24 weeks of storage. Li et al. (2017) predicted 'Hayward' kiwifruit SSC after storage using Vis-NIR spectroscopy with a decent prediction accuracy of R^2 of 0.58-0.83. Chen (2012) reported a linear relationship between kiwifruit SSC and NIR absorbance (R^2=0.93) within the spectral range of 11991.6 to 5446.2 [cm^{-1}]. However,

the measurement model of SSC and DMC using NIR spectroscopy could be influenced by environmental factors. Chen (2012) pointed out that fruit characteristics and pre-harvest conditions need to be considered when building a prediction model. Peirs et al. (2002) stated that large data sets, including multiple environmental condition factors, are required for prediction model calibration.

Contrastingly, Vis-NIR spectroscopy provides poor prediction performance for FF since FF estimation is indirect, and the accuracy of FF measurement is affected when both textural structures and SSC change during postharvest ripening. However, Berardinelli et al. (2019) determined kiwifruit FF by an NIR device and created an exponential correlation (R^2=0.77). Walsh et al. (2020) stated that NIR cannot measure FF accurately, as the associated changes (pectin levels, cell wall adherence and cell shapes) were not consistent. Thus, using Vis-NIR spectroscopy, FF is usually predicted based on a secondary correlation of pigments or starch-sugar composition with spectrum characters.

Currently, several NIR devices are used in the kiwifruit industry. The FELIX kiwifruit quality meter (F-751-kiwi, FELIX, USA) is a handheld NIR device for measuring the SSC and DMC of kiwifruit (Figure 2.14a). Another similar portable NIR device is the Fruit Quality Meter (H-100C, SUNFOREST, Korea). These portable devices allow for in-orchard fruit monitoring. However, the measurements need to be conducted on individual fruit and hence are more suitable for sub-sample checking. Some packhouse grading equipment suppliers have developed sorting instruments using NIR technology, such as MAF RODA (France) and TOMRA (Norway). These instruments fit into the sorting line (Figure 2.14b) but do not provide perfect grading solutions, especially for FF.

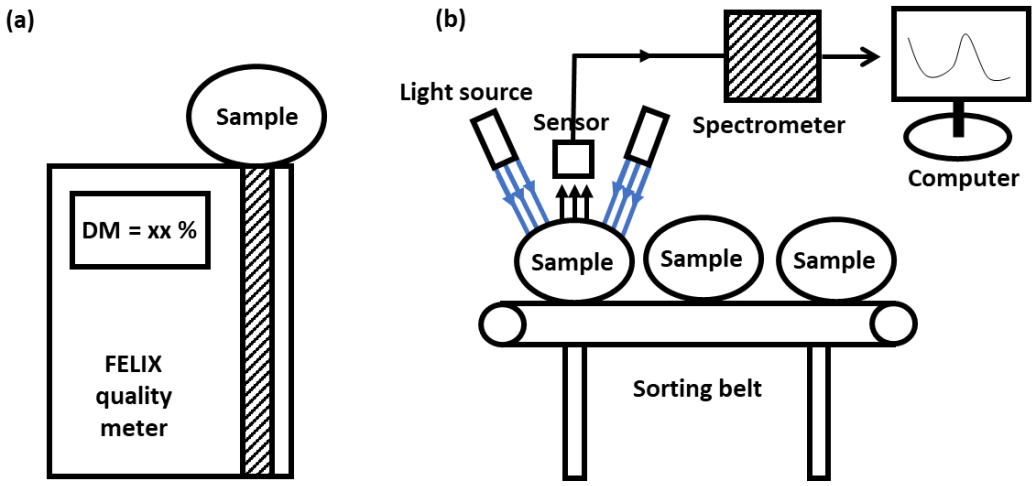

Figure 2.14. Schematic of (a) The FELIX kiwifruit quality meter (b)The visible-near infrared (Vis-NIR) spectroscopy system for a sorting line (Adapted from Ma et al., 2021)

2.2.3.6 Hyperspectral imaging technology

Hyperspectral imaging (HSI) captures a wide spectrum of light across many narrow wavelength bands and provides both spectral and spatial data of the sample simultaneously (Sun, 2010; Lu et al., 2020). An example HSI system contains laser modules as the light beam resource and a CCD (charge-coupled device) camera to acquire diffuse reflectance signals (Figure 2.15). In this system, resulted HSI images can be obtained via 1 of 4 modes, including reflectance, transmittance, interactance and reflectance & fluorescence (Lu et al., 2020). In the HSI system, a small continuous-wave light beam irradiated on the sample surface and emitted light has been linked to the optical properties of biological tissues (Reynolds et al., 1976; Langerholc, 1982; Marquet et al., 1995). Applications of HSI signals are usually for the determination of surface colour or detection of surface disorders (reflectance, fluorescence) or internal disorders (transmittance) for many horticultural products (Lu et al., 2020). Lu & Peng (2006) designed a hyperspectral laser backscattering system to predict the FF of 'Red Haven' and 'Coral Start' peach via a multi-linear regression model. In the FF prediction model, the intensity and displacement of extracted HSI images at 500-1000 nm describe the peach's diffusion profile. In addition, Lu (2007) used the same system and wavelength at 500-1000 nm to predict

'Golden Delicious' and 'Red Delicious' apple quality attributes and found reasonable prediction R^2 between HSI images and quality traits (0.76 for FF and 0.79 for SSC in 'Golden Delicious'; 0.55 for FF and 0.64 for SSC in 'Red Delicious'). Whereas HSI data at wavelengths between 400-1000 nm was investigated for estimating 'Hayward' kiwifruit quality attributes during ripening, the classification accuracy achieved 97 % and 93 % for SSC and FF (Benelli et al. 2022).

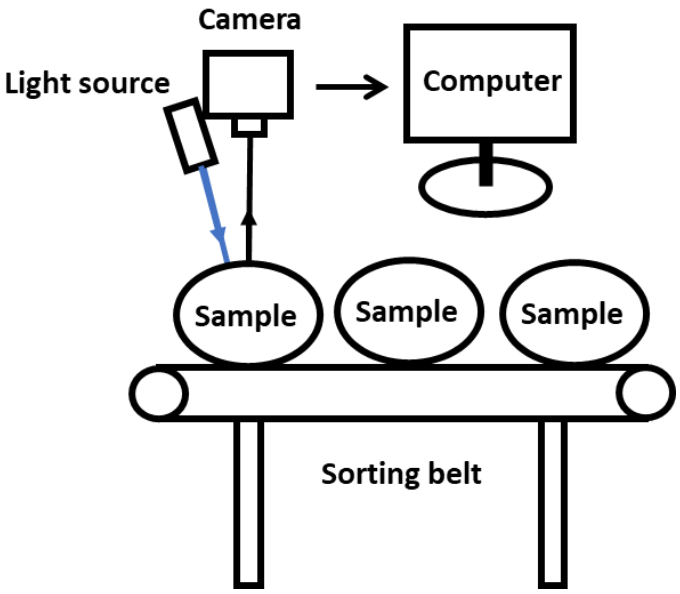

Figure 2.15. Schematic of the hyperspectral imaging system (Adapted from Mendoza et al., 2012)

With its spatially resolved setup, the HSI system has the potential to be adopted in the packhouse sorting line. As a product mapping technology, HSI technologies are useful for capturing irregularities in biological samples by determining discontinuities or changes across a product surface and thus could be advantageous for quality assessments. However, FF is commonly measured indirectly in HSI systems through underlying correlations with colour and chemical bond vibration, as resulting images contain information on mechanical properties and chemical composition (Walsh et al., 2020; Wieme et al., 2022).

2.2.3.7 Multispectral spatially resolved imaging system

Like the hyperspectral approach's spatial set-up, a multispectral spatially resolved imaging system (SRIS) is designed to measure optical properties at key wavelengths. Baranyai & Zude (2008, 2009) designed a multispectral imaging system (Figure 2.16) and used the Monte Carlo simulation method to estimate bruising in 'Golden Delicious' apple and FF of 'Hayward' kiwifruit.

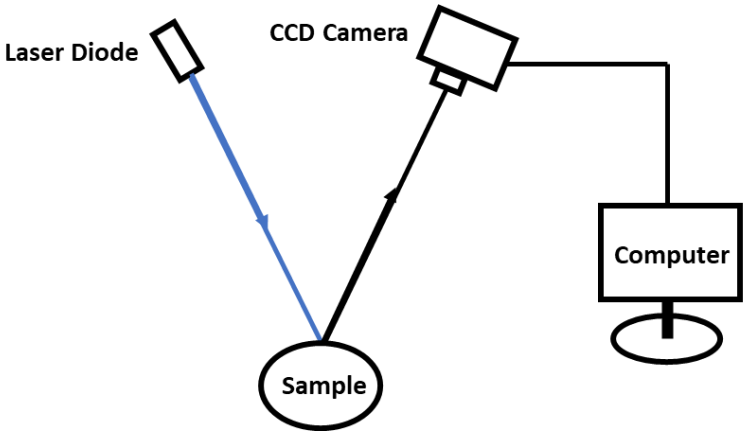

Figure 2.16. Schematic of the spatially resolved imaging system (Adapted from Baranyai & Zude, 2008)

Research was conducted through different analysis methods to obtain the optical properties using SRIS system, such as convert 2-D images to 1-D attenuation profiles and then fitting into curve-fitting. However, challenges could arise in image analysis as results may be affected by signals from the surrounding area, thus creating noise during the fitting process. In addition, the estimation uncertainty in separating optical properties has also been addressed through curve fitting. To improve accuracy of the optical measurements through SRIS system, several processes have been investigated, such as utilising a convolving point-spread function (Pilz et al., 2008) and metamodels (Aernouts et al., 2013) (Section 2.2.2.3). As a non-destructive technique, the spatially resolved imaging technique is more suitable for estimating optical

properties (Section 2.2.1) of fruits and vegetables at an industrial scale, and it has the potential to be implemented in the packhouse sorting line.

2.2.3.8 Time-resolved imaging system

A time-resolved imaging system (TRIS) can minimise surrounding effects mentioned in the previous section. The TRIS system measures the delayed and broadened pulse light travel path through a scattering media. A typical TRIS contains two fixed-distance optical fibres that are in contact with the sample surface (Figure 2.17). Despite the complicated photon movements, optical properties could be extracted from the distribution of the emitted light after a short monochromatic pulse as a result of the strong effect of light scattering in a turbid medium. Cubeddu et al. (2002) found that temporal resolution and sensitivity are the two critical factors in a TRIS, where temporal resolution is primarily affected by the light pulse width, and sensitivity is related to response detection ability. However, the emitting power of the light pulse should be carefully set to avoid possible damage to the sample whilst being strong enough for detection.

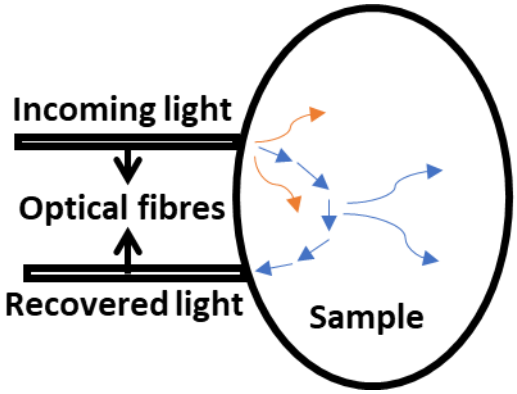

Figure 2.17. Schematic of the time-resolved system (Adapted from Valero et al., 2005).

Studies conducted on the estimation of fruit optical properties using TRIS. Cubeddu et al. (2001) developed a time-resolved spectroscopic measurement system to measure the optical properties of peaches, kiwifruit and apples. Nicolaï et al. (2008) used the same system to

predict pear SSC and FF. Pifferi et al. (2007) measured the optical properties of phantoms and found that the maximum error was obtained with data collected at a wavelength of 730 nm. The TRIS technique was considered more accurate than other non-destructive techniques and was useful in assessing defects in fruit with thicker skin (Cubeddu et al., 2001). However, TRIS is expensive and complex, making the system's implementation unsuitable for the industry sorting line.

2.2.3.9 Spatial-frequency domain imaging system

A spatial-frequency domain imaging system (SFDIS) is another nondestructive technology that measures the interaction of illuminated periodic patterns with a turbid medium using an imaging system. The SFDIS system consists of a digital micromirror device that illuminates different spatial patterns and a CCD camera capturing emitted light (Figure 2.18). In an SFDIS system, light injection and measurement are through the sinusoidal module. Anderson et al. (2007) developed an SFDIS to measure apple optical properties and found that μ_a at 680nm is sensitive to fruit FF. Lakowicz et al. (1989) developed an SFDIS system to measure fluorescence intensity decay from the flexible molecules in proteins. Spichtig et al. (2009) used the frequency-domain method to measure silicone-based model samples at 690 nm and 830 nm. The frequency-domain technique has the advantage of being a real-time measurement that can characterise the entire spectrum from a measurement at a single frequency. However, the current system requires information at multiple spatial frequencies, requiring a long acquisition time. Additionally, several calibration procedures need to be applied to estimate optical properties (Section 2.2.2).

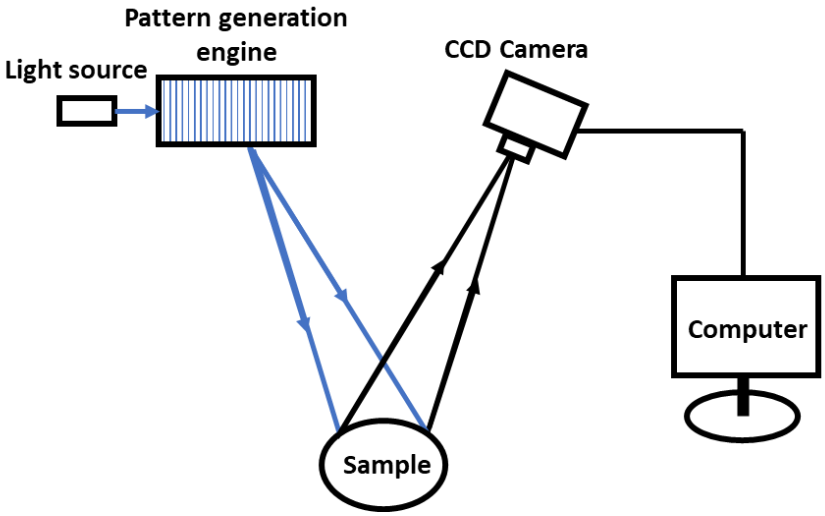

Figure 2.18. Schematic of the spatial frequency domain imaging system (Adapted from Anderson et al., 2007).

2.2.3.10 Other non-destructive technologies

Apart from the above optical non-destructive methods, non-destructive magnetic resonance imaging (MRI) has been utilized to provide information on water distribution inside an object (Figure 2.19). MRI is commonly used for medical examination but could be used to assess the water-content-related quality of fruits and vegetables. Most fruits and vegetables have an abundance of water. Thus, the spin of the protons within fruit water can interact with a strong magnetic field (Chen et al., 1989). MRI can measure the interaction of electromagnetic radiation and create a spatially resolved proton density distribution map, which may provide the internal structure information of fruits and vegetables (Nicolaï et al., 2014). Studies have used MRI to obtain information on bruising and localised drying since MRI can monitor the compositional changes that occur during defect development and food drying or freeze-drying processes. For example, MRI techniques were applied to detect moth infestation rapidly (Haishi et al., 2011), bruising (McCarthy et al., 1995), and mealiness of apples (Barreiro et al., 2002) by transferring the electronic signal of water status into images. Furthermore, Hall et al. (1998) studied the texture of a range of foods using MRI and characterized the structural changes that

result from different maturities and defects. However, due to high cost and low speed, MRI has only been applied in a few lab-scale fruit quality studies and is not suitable for horticulture industry applications. Taglienti et al. (2009) assessed the quality of kiwifruit that were stored at 0°C and 20°C using MRI and found that two different types of water vibrational modes existed in cellular tissues. For kiwifruit studies, Burdon et al. (2015) investigated water mobility among four kiwifruit cultivars and their relationship with shrivel development

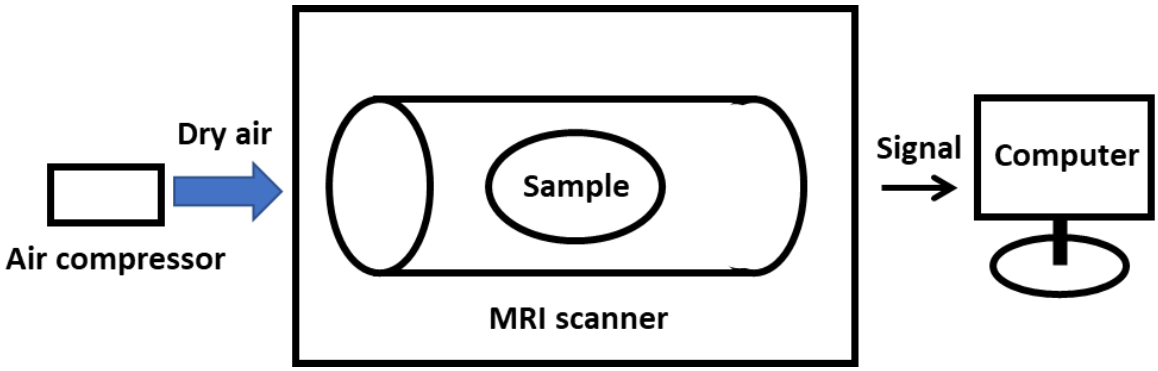

Figure 2.19. Schematic of the Magnetic resonance imaging (MRI) system (Adapted from Zang et al., 2017).

Several non-destructive firmness sensors have been studied for kiwifruit FF measurement. Compression deformation has been applied to describe kiwifruit softness. A softness meter using compression deformation was utilized by Davie et al. (1996) and the softness coefficient variability obtained was similar to that of destructive measurements (Davie et al., 1996). Although compression provides an indicator for monitoring the kiwifruit characteristics during storage, it caused mechanical damage. During kiwifruit ripening, compression accuracy compared with FF varies at different firmness ranges (Li et al., 2016). The correlation between compression and FF varied with different cultivars, with R^2 values of 0.9 and 0.6 reported for 'Hayward' and 'Gold 3', respectively (Li et al., 2016). The laser air-puff method was another non-destructive technique. McGlone & Jordan (2000) reported an R^2 of 0.8 between the non-destructive stiffness value obtained using a laser air-puff method and a penetrometer

measurement in the firmness range of 0 – 30 N. It suggested that such a method could be applied as a screening method for separating fruit into two classes in the softer firmness range. AWETA acoustic firmness was another non-destructive technique that analyses kiwifruit's vibration pattern after a tap. AWETA acoustic firmness was compared to penetrometer FF by Feng et al. (2016), and an R^2 of 0.82 and 0.71 for Gold3 and 'Hayward' was reported. Feng et al. (2016) also discovered that soft kiwifruit's acoustic firmness was more sensitive.

2.2.4 Application of optical properties

The maturation and ripening of fruits and vegetables result in changes in chemical composition, which in turn affect quality attributes (Table 2.2). Many studies have reported that SSC, flesh colour, and the starch index are related to μ_a. Van Beers et al. (2017) reported different absorption peaks relating to the skin colour of the apple, resulting from the spectral absorption peak of the pigments at visible wavelengths (carotenoids at 500nm, anthocyanins at 550-600 nm and chlorophyll at 678nm). In the NIR region, light absorption is mainly due to water, carbohydrates and fat, which contains OH bonds (Hale & Querry, 1973). For example, μ_a at the carotenoid absorption band could be useful for predicting Hayward storage stage due to the degreening process. Particularly, the carotenoid content of kiwifruit is known to decrease with storage duration, and late-harvested kiwifruit possess fewer carotenoids (Tavarini et al., 2008). On the other hand, the fruit storability could also be predicted according to relationships between μ_s' and microstructure. For example, μ_s' obtained from the hyperspectral system is strongly related to apple fruit porosity (Wang et al., 2020). In general, among different fruit, μ_s' was reported to decrease exponentially with increasing wavelength, whilst the peak of μ_a changes during fruit development (Spinelli et al., 2012). Therefore, combining μ_a and μ_s' improved the estimation accuracy during the calibration of optical properties and fruit quality attributes (Cen et al., 2013).

Unlike fruit quality attributes, which may be estimated or predicted using non-destructive techniques, internal disorder measurement is usually an 'after the fact' method (Clark et al., 2004). The use of fruit optical properties for internal disorder detection has been investigated in many research studies (Table 2.2). In general, μ_a is related to disorder symptoms such as tissue discolouration or water soaking, which are detectable with spectral data (ElMasry et al., 2009). For onions with dry skin, different μ_a was reported compared with healthy flesh due to pathogen appearance and reduced moisture content (Wang et al., 2014). Whilst μ_s' is related to disorder symptoms involving tissue texture changes. Wang et al. (2014) stated that the μ_s' of the flesh could be used as an indicator of flesh decomposition from internal disorder. For 'Hayward' kiwifruit, bruised fruit had higher μ_a and lower μ_s' during storage ripening due to the change of tissue colour, FF and microstructure (Gao et al., 2021). The data analysis is usually conducted via discriminant analysis or Naïve Bayes Classifier analysis for disorder detection using non-destructive methods.

Table 2.2. Application of using optical properties for fruit quality assessment and disorder detection.

Fruit	Quality attributes / internal disorder	μ_a	μ_s'	Imaging system	Data analysis	Examples
Apple 'Elstar', 'Pinova'	Pre-harvest maturity	Increased due to anthocyanins	Decreased due to cell elongation	Multispectral SRIS LBI	Curve correction PLS calibration model	(Qing et al., 2007)
Apple 'Golden Delicious' and 'Granny Smith'	Acoustic FF through shelf-life ripening	Decreased at 685 nm and 520 nm	Decreased	Hyperspectral scattering images	Linear regression	(Cen et al., 2013)
Apple 'Elstar', Plum 'Tophit plus'	Maturity or ripeness	peak at 670nm	Decreased at 670 nm	Time-resolved reflectance spectroscopy	Pearson correlation, ANOVA and Tukey post hoc test	(Seifert et al., 2015)
Pear 'Conference'	FF and SSC through fruit development	Relative stable at 515 and 940 nm, Decreased at 690 nm	Decreased, at 515 nm was the most	PDW and LBI	PLS model	(Adebayo et al., 2017; Zude-Sasse et al., 2019)
Pear 'Conference'	SSC and FF	Spectra correlated with SSC	No correlation with FF	Time-resolved continuous wave NIR	PLS model	(Nicolaï et al., 2008)
Banana 'Musa'	Elasticity, SSC and chlorophyll at different ripening stages	High correlation with elasticity at 532 nm, with SSC at 660 nm and with chlorophyll at 532, 785 nm, with the ripening stage at 532 nm	High correlation with elasticity at 532 nm, with SSC at 830 and 660, and with chlorophyll at 532, with the ripening stage at 532 nm	LBI	ANN model	(Adebayo et al., 2016)
Mango 'Palmer ;	Pigments through reining	Decreased through ripening at spectral peak of 670 nm	Decreased	Time-resolved reflectance spectroscopy		(Spinelli et al., 2012)
Kiwifruit 'Hayward'	Apparent photons decreased (through repining)	Increasing	Decreasing	SRIS LBI	Monte Carlo simulation	(Baranyai & Zude, 2009)
Kiwifruit 'Hort16A'	DM, SSC and flesh colour	Spectra DM & SSC (800–1000 nm). Flesh colour 500-750		Vis-NIR spectroscopy (300–1140 nm	Canonical discriminant analysis (CDA) for classification	(Clark et al., 2004)

Fruit	Quality attributes / internal disorder	μ_a	μ_s'	Imaging system	Data analysis	Examples
Apple 'Golden Delicious'	Bruising	Higher for non-bruised fruit at 660 – 680 nm	Higher for non-bruised fruit 650 – 890 nm	Spatial-frequency-domain imaging	Classification with spectral data and frequency	(Anderson et al., 2007)
Apple 'Golden Delicious', 'Idared'	Bruising	Different sizes of the backscattering area at 670 nm		Spatial- resolve LBI	Monte Carlo simulation multi-factor ANOVA	(Baranyai & Zude, 2008)
Apple 'Red delicious'	Chilling injury	Optimal wavelengths (717, 751,875, 960 and 980 nm). Injured fruit had lower relative reflectance for both surface and internal flesh.		Hyperspectral imaging (400-1000 nm)	ANN	(ElMasry et al., 2009)
Apple 'Braeburn',	Mealiness	Low at 912 nm for mealy fruit	High at 790 and 912 nm for mealy fruit	Time-resolved reflectance spectroscopy	ANOVA and T-test	(Vanoli et al., 2009)
Apple 'Granny Smith'	Internal browning	Increased at 750 nm	Decreased at 750 nm			
Apple 'Fuji'	Watercore	High at 790nm for fruit with defects	Low at 790nm for fruit with defects			
Blueberry	Bruising	Lower reflectance for healthy fruit		Hyperspectral imaging (1150-1280 nm)	PLSR	(Jiang et al., 2016)
Nectarines 'Marsiani 90'	Chilling injury	Decrease (at 670 nm) or no change (at 780 nm) without cool store and increase after cool tore (at 670 and 780 nm)	Higher correlation with harvest at 780 nm	Time-resolved reflectance spectroscopy	PCA	(Lurie et al., 2011)
Plum 'Jubileum'	Internal jellying browning	Increased with severity at 670 and 780 nm, Increased after storage	Lower at 670 and 780 nm for disordered fruit, no change after storage	Time-resolved reflectance spectroscopy	ANOVA	(Vangdal et al., 2011)
Onion 'Pungent Spanish'	Rot	Higher of sour skin at 550-750 nm (skin) Higher of neck rot at 550-1100 (tissue)	Lower with sour skin and neck rot at 550-1650 nm (skin & tissue)	Inverse adding doubling	T-test	(Wang et al., 2014)

Fruit	Quality attributes / internal disorder	μ_a	μ_s'	Imaging system	Data analysis	Examples
Kiwifruit 'Zesy002'	Chilling injuries	Higher spectral data between 700 -1000 nm		Vis-NIR spectroscopy	PCA based segregation	(Wang et al., 2020)
Kiwifruit 'Hayward'	Bruising	Higher on day 8 0.03- 0.06 /mm (980 nm) 0.09-0.15 /mm (1175 nm) 0.4-0.9 /mm (1420 nm)	0.7-1.1 /mm healthy (1175 nm) 0.4- 0.8 /mm bruised	Inverse adding doubling (900-1700 nm)	ANOVA	(Gao et al., 2021)
Kiwifruit 'Hort16A'	Chilling injury			Vis-NIR spectroscopy (300–1140 nm)	Canonical discriminant analysis (CDA) for classification	(Clark et al., 2004)
Cucumber 'Excursion'	Chilling injuries	Higher relative intensity after cool store at 700-850 nm		Hyperspectral imaging system (400–675 nm) (675–1000 nm)	Supervised classification	(Cen et al., 2016)
Banana 'Musa'	Chilling injuries	LBI profiles change at different ripeness		Spatial- resolve LBI	ANOVA and classification	(Hashim et al., 2013)

2.2.5 Research gaps and opportunities

In the past 30 years, many novel approaches have been developed for measuring kiwifruit firmness nondestructively or measuring the optical properties of horticulture products to correlate with intrinsic fruit properties to enable the subsequent prediction of fruit qualities (Table 2.3).

Among the non-destructive techniques mentioned in previous sections, NIR spectroscopy is the most frequently applied method in the industry. Using frequency-resolved analysis, NIR spectroscopy has been employed by the kiwifruit industry to estimate fruit SSC and DMC, and those correlations were assumed to be related to the absorption properties of specific molecules (Li et al., 2017). NIR technologies primarily capture the absorption signal related to the fruit's chemical properties, hence, the prediction of FF is indirect and results in estimation uncertainty of FF. Li et al. (2017) investigated using NIR techniques to predict kiwifruit storability and reported poor prediction performance of kiwifruit FF compared to that of SSC.

With the advantages of easy operation, short acquisition time and potential to be adapted at the packhouse sorting line (Qin & Lu, 2008), the spatially-resolved technique, could provide information on fruit physical properties. When fruit are illuminated by light in a spatially resolved system, multiple absorption and scattering events occur due to various cellular structures and molecular components. Light absorption is related to the chemical composition of different compounds underneath the skin (Walsh et al., 2020). On the other hand, light scattering is affected by tissue microstructure within and among cells, such as cell size, cell turgor pressure and cell density (Liu et al., 2019; Wang et al., 2020). During kiwifruit ripening, physiological processes occur, including cell wall degradation, cell wall swelling and loss of middle lamella (Harker & Hallett, 1994), resulting in a reduction of FF. Therefore, capturing the structural changes of the fruit using scattering information may provide a method of assessing

fruit FF related to these changes. Studies have been conducted to obtain physical property changes in fruit using spatially resolved imaging techniques. Lu & Peng (2005) used a multi-spectral scattering profile with Lorentzian distribution to predict peach FF. Authors reported that Lorentzian parameters were linearly related to fruit FF, and a broader scattering in soft fruit was found compared to firm fruit. Although spatially resolved technologies were capable of estimating qualities associated with chemical compositions, they lacked performance with textural properties. Despite a 90 % classification accuracy, ElMasry et al. (2009) obtained a high root mean square error (8.26 and 9.40 N for training and validation, respectively) in 'Red Delicious' apple FF estimation using HSI technology. Van Beers et al. (2015) applied relative reflection profile data to predict apple maturity and observed good performance for at-harvest maturity and starch content, but poor performance for SSC and FF estimation was reported. Thus, there is no non-destructive optical technique that has been accepted by the industry for FF estimation and prediction.

A considerable amount of non-destructive optical techniques has been trialled to link optical properties with fruit quality changes and symptoms of internal disorders during the ripening process. These approaches estimated the absorption and scattering properties of fruit and vegetables to predict changes in their quality attributes or storage performance. Several factors influence FF estimation using spatially resolved technology. Firstly, FF estimation from NIR/HSI data is unreliable when both textural structures and SSC change during postharvest ripening. The spectral-optical information represents the sum signal of absorption and scattering, which is related to multiple quality attributes. Throughout fruit ripening, structural and chemical compositional changes occur and influence the resulting signal simultaneously. Walsh et al. (2020) also confirmed that errors could occur when using spectral reflectance data to predict fruit quality because the sum signal of absorption and scattering changes with chemical composition and physical properties. FF is a physical/textural property and lacks

correlative power with easily measured attributes such as colour and sugar (Lu & Peng, 2006; Li et al., 2022). The estimations of fruit FF are usually based on a secondary correlation with chemical compositions such as SSC. Due to the complex process of FF progression during fruit softening and the difficulties in disentangling FF-related information from other quality influencers, spatially-resolved imaging techniques usually require advanced and appropriate image analysis processes and validation before the industrial application.

In addition, estimating fruit FF from the spatially resolved spectroscopy is related to the varying physical structure of the sample, which affects the spectral intensities measured. Although the fruit subsurface region is regarded as isotropic, fruit and vegetables are complicated inhomogeneous biological tissues containing multiple cellular layers and structures. FF estimation uncertainty may occur due to fruit skin and subsurface structures influencing scattering differently. Besides, there is no standard validation method for these techniques. Thus, the results are not comparable among different techniques, as different instruments provide different optical properties for the same sample (Pifferi et al., 2005). Hence, spatially-resolved techniques are still under investigation to improve measurement accuracy and simplify the complexity of model development.

Moreover, 'point' NIR spectroscopy and HSI incur high hardware and complex data analysis costs. In general, wavelength selection and binning techniques are required to reduce the sensor hardware's data processing time and cost. Therefore, the selection of relevant wavelengths enables a multi-spectral sensor setup with less expensive hardware.

Among many spatially resolved non-destructive measurement approaches, LBI is a low-cost technique that can be rapidly operable under practical packhouse conditions. LBI records backscattering signals after interacting with the fruit tissue at selected visible and NIR

wavelengths. With appropriate data analysis, resulting optical properties from LBI may provide information on internal quality factors, particularly scattering information relating to the fruit's structural properties, including FF and internal disorder symptoms with granular tissue.

In conclusion, while significant progress has been made in developing non-destructive optical techniques to assess fruit quality, challenges remain, particularly in accurately predicting textural properties like FF. The complex nature of fruit tissue and the interplay between structural and chemical changes make it difficult for existing methods to provide consistent and reliable results. LBI presents a promising solution, offering the industry a more practical and cost-effective approach. There is no research on kiwifruit FF and internal disorders detection using LBI. Therefore, research on using LBI for kiwifruit quality assessment is crucial to overcoming current limitations and achieving more accurate and efficient quality assessments for the industry.

Table 2.3. Comparison of different non-destructive quality measurement methods for horticultural products.

Method	Fruit	Application	Advantage	Disadvantage	Industrial sorting line applicability	Examples
Laser air puff	Kiwifruit, apricots	Firmness	Use as screening for class separation	Minor compression	yes	(McGlone & Jordan, 2000)
Acoustic	Kiwifruit	Firmness	Real-time and no compression	Not sensitive at lower firmness range, large variability	no	(Feng et al., 2016)
Compression	Kiwifruit, apple	Firmness	Real-time measurement, high precision	Cause minor damage	no	(Tian et al., 2022)
OCT	Apple, grape, kiwifruit, onion	Subsurface tissue structure measurement	Real-time measurement Multi-layer microstructure	Low penetration depth image quality can be affected by the sample and measurement environment	no	(Li et al., 2015)
Fringe projection	Kiwifruit, apple	Skin features, roughness, colour, structure	Rapid	Require data extraction	no	(Lai et al., 2019)
X-ray CT	Apple, kiwifruit, pear	Internal disorder, microstructure	High precision	Expensive, time-consuming	no	(Wang, Van Beers, et al., 2020)
MRI	Apple	External and internal disorders	Inter-fruit tissue detection.	High cost and low speed	no	(Melado-Herreros et al., 2013)
NIR spectroscopy	Apple, kiwifruit, onion	SSC, DM, internal disorder	Fast and non-destructive	Low accuracy for firmness	yes	(Clark et al., 2004; Li et al., 2017; McGlone & Kawano, 1998; Wang, Künnemeyer, et al., 2020; Zude et al., 2006)
Hyperspectral spectroscopy	Apple, peach, cucumber	Surface colour and disorder, internal disorders.	Both spectral and spatial information	No direct correlation with firmness	yes	(Cen et al., 2013; Lu & Peng, 2006; Qin & Lu, 2008)
SRIS[1]	Apple, kiwifruit, banana	Firmness and internal disorder	Fast and has a direct correlation with FF	Coupling optical properties	yes	(Baranyai & Zude, 2008; Hashim et al., 2014; Zude-Sasse et al., 2019)
TRIS[2]	Peach, kiwifruit, apple	Firmness, peach	More accurate and can measure fruit with thicker skin	expensive and complex	no	(Cubeddu et al., 2001, 2002; Pifferi et al., 2005)
SFDIS[3]	Apple	FF and internal disorders	Multi-spatial information	Longer process time and requires calibration	no	(Hu et al., 2016)

[1]*Muti-spectral spatially resolved system.*
[2]*Muti-spectral time resolved system.*
[3]*Spatial-frequency domain imaging system*

Chapter 3 Laser backscattering imaging system and attenuation analysis using pre-classification models built by optical phantoms

3.1 Introduction

In recent years, there has been increasing interest in developing advanced non-destructive methods for assessing fruit quality to improve the supply chain efficiency and reduce waste in the agricultural sector. Non-destructive optical techniques, such as near-infrared (NIR) spectroscopy, have been investigated for kiwifruit quality estimation. These techniques allow measuring quality changes of each fruit and in summation batches of fruit. For example, soluble solids content (SSC) and dry matter content were determined non-destructively using the intensity of diffuse reflectance by McGlone & Kawano (1998). However, the estimation of FF has not been achieved with adequate accuracy so far. The challenge of using NIR spectroscopy to measure FF is due to the fact that the absorption analysis dominates NIR spectral data because the signal is primarily related to SSC (Li et al., 2022).

LBI technology was developed based on NIR technology to provide information on the photon attenuation profile while travelling through the fruit tissue. The attenuation profile could be analysed based on Farrell's theory (Farrell et al., 1992) and optical properties, μ_a and μ_s', are usually estimated via a curve-fitting process in the diffusion model (Section 2.2.2.1). However, decoupling of μ_a and μ_s' remains a major challenge for LBI when applied to fruit quality estimation. Zude-Sasse et al. (2019) validated the optical properties estimation of pear using the destructive PDW method and found that estimation uncertainty could be introduced due to coupling μ_a and μ_s'. This uncertainty occurs during the curve fitting process without limiting the range of either μ_a or μ_s' according to known values of one variable.

Additionally, there are limited references in existing research for analysing fruit LBI images (particularly kiwifruit), resulting in challenges when calculating kiwifruit μ_a or μ_s'. Baranyai &

Zude (2008) investigated the scattering coefficient for apples from LBI attenuation via Monte Carlo simulation and reported that LBI profiles changed with induced bruising symptoms. However, it was also reported that simulations of 'high scattering – low absorbing' and 'low scattering – high absorbing' samples were hardly distinguishable (Zude-Sasse et al., 2019).

Metamodeling was introduced as a technique to bridge the gap between mathematical models and real-world fruit by obtaining the optical signal of liquid phantoms and providing a reference matrix for estimating optical properties of fruit samples (Lu et al., 2020). In a Metamodel, a set of liquid phantoms are custom-made with turbid media, including absorbers and lipids serving as scatterers (Aernouts et al., 2015; Watté et al., 2015). The μ_a and μ_s' of the resulting liquid phantoms are usually measured by IS-IAD method. However, there is no standard validation method for the measured μ_a and μ_s', thus, whether the output data using IS-IAD is reliable cannot be confirmed.

The objectives of this study are to

(i) introduce LBI system, LBI attenuation analysis and pre-classification approach and

(ii) validate the pre-classification model using optical phantoms with the proposed range of μ_a and μ_s'.

3.2 Laser backscattering imaging technology

3.2.1 Laser backscattering imaging system

The LBI system was assembled and located at ATB, Germany (Figure 3.1). The system includes a charge-coupled device (CCD) camera (CVA50IR, JAI Ltd, Japan) providing an image resolution of 720 × 576 pixels, equipped with an F2.5 aperture zoom lens and 18–108 mm focal length (12VG1040 ASIR-SQ, Tamron Co. Ltd, Japan). A desktop computer controls the laser diodes and camera. An electric moving table was used to adjust the

sample position to maintain a consistent distance of 25 cm between the topmost point of the sample and the lens of the camera. One pixel represented 0.1205 x 0.1205 (mm^2) in the geometric calibration. Laser diodes emitting at 532 nm, 660 nm and 785 nm with a collimated beam were applied as a light source (Baranyai & Zude, 2009). The laser diodes are positioned at a < 10° angle, and the camera is directly above the sample.

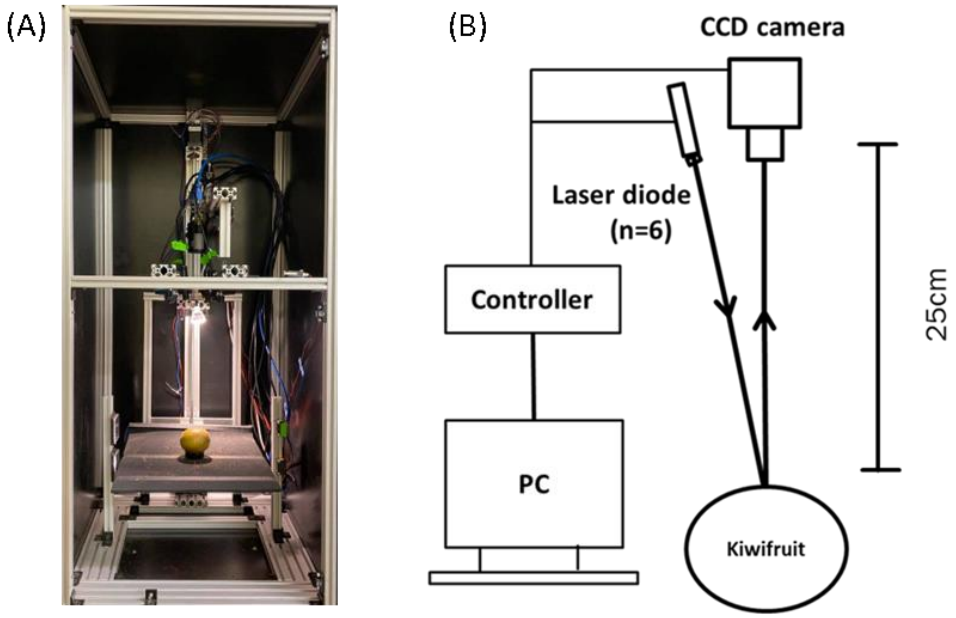

Figure 3.1. Laser backscattering imaging system.

3.2.2 Improved Laser backscattering imaging (LBI) system

The previous version LBI system had fixed power outputs of laser diodes. This created challenges when light was emitted from small fruit (such as blueberry) before attenuation finished or when not enough light penetration occurred in fruit with thick skin (such as watermelon). Therefore, an improved LBI imaging system (Figure 3.1a) with power-adjustable laser diodes was designed at ATB, Germany and assembled at Massey University, New Zealand. Two of the same systems are located at ATB and Massey University, which allow data collection and comparision in Europe and New Zealand.

The system included the light source with a laser diode (FP-D-DIG-520-17-C-F250-USB, Laser Components, Germany) emitting at 520, 660, 685, 785 and 830 nm with 6.8, 28, 12, 12, 28 mW of power output, respectively. In addition to the power-adjustable laser diodes providing flexibility for measuring fruit type, a camera with a higher resolution was selected (Table 3.1). A CCD camera (MER-131-210U3M NIR, China Daheng Group, China) providing a resolution of 1280 × 1024 pixels, equipped with F1.4 aperture zoom lens and 10-40 mm focal length (12VG1040 ASIR-SQ, Tamron Co. Ltd, Japan) was chosen. A desktop computer was used to control the light source and camera. In the geometric calibration, one pixel represented 0.1016 * 0.1016 (mm^2). An electrical moving table was used to adjust the sample position to maintain a 25 cm distance between the highest point of the fruit surface and the camera.

Table 3.1. Comparison of previous laser backscattering imaging system and improved system.

Attributes	Previous version	Improved version
Camera resolution (pixels)	720 × 576	1280 × 1024
Laser wavelength (nm)	532, 660, 785	520, 660, 685, 785, 830
Maximum power output (mW)	10, 60, 45	17, 70, 30, 30, 70
Laser type	Non-focused	focused
Pixel area (mm^2)	0.1205^2	0.1016^2
Laser output	fixed	Adjustable
Image sensitivity	fixed	Adjustable

3.2.3 Image acquisition and attenuation analysis

Images were acquired by manually placing each sample on the system platform below the camera, followed by an automatic location adjustment. The reference point-laser emitted at the measurement point. A custom-written Labview software (National Instruments, USA) was used to control the system. LBI images were acquired using selected laser wavelengths with power outputs (Table 3.1). Acquisition of the images was done in a dark room for the old system. In contrast, in the new system, all measuring parts were secured inside a black cage (Figure 3.1a) to prevent interfering stray light and avoid human exposure to the laser light. Each resulting LBI image (Figure 3.2a) was the average of 10 images acquired at 0.5 s per image.

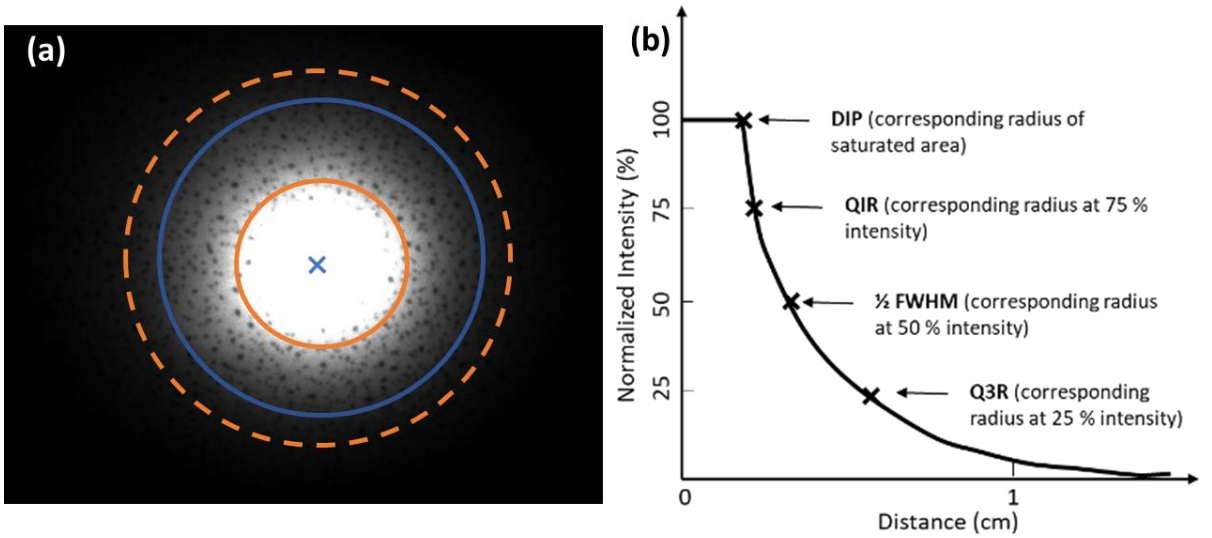

*Figure 3.2. Laser backscattering image (LBI) and attenuation profile (a) Raw image obtained from a kiwifruit sample at 785 nm with an image size of 65.02 * 52.02 (mm^2). The blue cross represents the incident point, the orange circle is the saturated area, the blue circle is around at 1 cm radius and light diffusion stops at the orange dash circle. (b) Transformed diffusion profile (attenuation profile) from LBI. LBI parameters were the radius of the saturated area (DIP), the radius at 75 % of maximum intensity (Q1R), double the radius at 50 % of maximum intensity (FWHM), the radius at 25 % of maximum intensity (Q3R), and the slope of the linear regression model (SLP) built with log-transformed profile data between Q1R and Q3R.*LBI image was analysed by R (version 3.6.0, R Foundation for Statistical Computing, Vienna) running in RStudio (version 1.0.153, RStudio Inc.). The raw image was loaded and normalized into a grey-scale matrix using the 'readbitmap' package (version 0.1.5). After the normalization process, light intensity at each pixel has a value between 0 and 1. The resulting grey-scale matrix contains normalized intensity and coordinates. The saturated area has a light intensity of 1, and the light intensity reduces to 0 at the end of light diffusion (Figure 3.2a). The coordinates of the weighted centre of the saturated area are calculated as incident point coordinates. Thus, the distance between each pixel coordinates and incident point coordinates can be obtained. Pixels at the same distance to the incident point can be calculated in 1-pixel concentric rings around the incident point. The average backscattering intensity of the ring at each radius was computed into LBI light attenuation profiles (Figure 3.2b). Extracted parameters (Figure 3.2) of the profile were full width at half

maximum (FWHM, Eq. 3.1), radial distance of 75% (Q1R, Eq. 3.2) and 25% intensity values (Q3R, Eq. 3.3), the area between Q3R and Q1R (Area, Eq. 3.4) and the slope of the linear regression model (SLP) built with log-transformed profile data between Q1R and Q3R.

$$FWHM = 2 \cdot (r_{I_{m50}} - r_{I_{max}}) \quad \text{Eq. 3.1}$$

$$Q1R = r_{I_{m75}} - r_{I_{max}} \quad \text{Eq. 3.2}$$

$$Q3R = r_{I_{m25}} - r_{I_{max}} \quad \text{Eq. 3.3}$$

$$Area = \pi \, (Q3R^{\,2} - Q1R^{\,2}) \quad \text{Eq. 3.4}$$

With r = radial distance measured from the incident point, I_{max} = maximum intensity value, I_{m75} = 75 % of maximum intensity value (Eq. 3.5), I_{m50} = 50 % of maximum intensity value (Eq. 3.6), I_{m25} = 25% of maximum intensity value I_{min} = minimum intensity value (Eq. 3.7).

$$I_{m75} = I_{max} - 0.25 \, (I_{max} - I_{min}) \quad \text{Eq. 3.5}$$

$$I_{m50} = I_{max} - 0.5 \, (I_{max} - I_{min}) \quad \text{Eq. 3.6}$$

$$I_{m25} = I_{min} + 0.25 \, (I_{max} - I_{min}) \quad \text{Eq. 3.7}$$

3.3 Solid phantoms and pre-classification model

3.3.1 Solid phantom introduction

A set of commercial solid phantoms (PDW Analytics GmbH, Potsdam, Germany) were used to build a pre-classification model (Figure 3.3). The optical properties (μ_a and μ_s') range of solid phantoms were expected to cover most fruits.

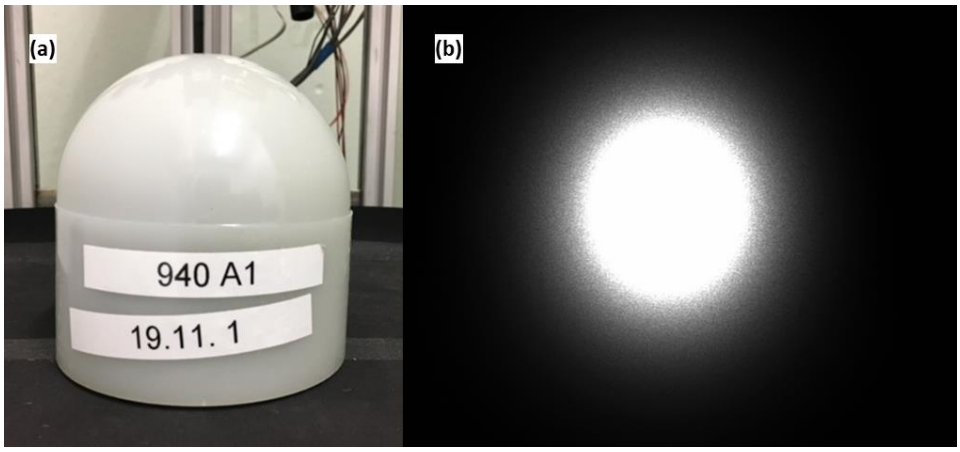

*Figure 3.3. Commercial solid phantom (a) Commercial solid phantom with μ_a =0.1 cm^{-1} and μ_s' = 2.0 cm^{-1}. (b) Laser backscattering image of (a) at 785 nm with an image size of 86.76 * 69.41 (mm^2).*

Ranges for optical properties were obtained from solid phantoms with known μ_a* and μ_s'* described earlier by Zude-Sasse et al. (2019). μ_a class A_1 (Eq. 3.8) was calculated from phantoms A.1, B.1 and C.1, μ_s' class S_1 (Eq. 3.9) range was calculated from phantoms A.1, A.2 and A.3. Full ranges are presented in Table 3.2.

$$\mu_{a_{A1}} \in [(\mu_{a_{A1}}{}^* + \mu_{a_{B1}}{}^* + \mu_{a_{C1}}{}^*)/3 \pm 2SD] \quad \text{Eq. 3.8}$$

$$\mu_{s_{S1}}{}' \in [(\mu_{s_{A1}}{}'^* + \mu_{s_{A2}}{}'^* + \mu_{s_{A3}}{}'^*)/3 \pm 2SD] \quad \text{Eq. 3.9}$$

Table 3.2. Ranges of classes for pre-classification model according to μ_a (Class A) and μ_s' (Class S).*

Class	μ_a range (cm^{-1})	Reference phantoms
A1	0.101-0.111	A.1, B.1, C.1
A2	0.393-0.587	A.2, B.2, C.2
A3	1.163-1.292	A.3, B.3, C.3
Class	μ_s' range (cm^{-1})	Reference phantoms
S1	1.979-2.166	A.1, A.2, A.3
S2	11.516-12.093	B.1, B.2, B.3
S3	20.187-22.807	C.1, C.2, C.3

**Pre-classification ranges were calculated from solid phantoms with predetermined values of μ_a and μ_s' (Zude-Sasse et al., 2019). The lower and upper limits of the range represent the mean with two times the standard deviation.*

3.3.2 Data analysis

These nine solid phantoms with predetermined optical properties were employed to build a pre-classification model with their LBI parameters (Q1R, FWHM, Q3R and SLP, Figure 3.2b) extracted from LBI images (Figure 3.2a). Class A (1 – 3) and Class S (1 – 3) were classified with a flexible discriminant analysis (FDA) algorithm in the 'mda' package (version 0.4-10). Validation was conducted by 'leave one out' cross-validation in the same R package.

The diffusion theory model was used to fit the attenuation profile of solid phantoms (Figure 3.3a) as performed by Farrell et al. (1992) to estimate μ_a and μ_s'. The 'minpack.lm' package (version 1.2-1) was used to perform non-linear curve fitting with the Levenberg-Marquardt nonlinear least-squares algorithm.

The initial class (A or S) of the phantom was determined by a pre-classification result utilizing phantom LBI parameters, whilst the mean of the predicted class was estimated as initial μ_a or μ_s'. The estimated μ_a [cm^{-1}] and μ_s' [cm^{-1}] were calculated according to Farrell's equation with one of the initial optical properties. The class ranges (Table 3.2) were used to limit the Levenberg-Marquardt fitting process for phantoms. Therefore, the resulting pre-classification model allows μ_a and μ_s' estimation using LBI parameters, with possible μ_a and μ_s' class as limited to the ranges provided in Table 3.2. This particular pre-classification model was utilized to estimate kiwifruit μ_a and μ_s' in Chapter 4 (Section 4.3.3).

3.3.3 Estimation of solid phantom optical properties

Estimated μ_a and μ_s' with the established class range (Table 3.2) and with open range were presented in Figure 3.4. For estimated μ_a and μ_s' with the established class, all phantom μ_a were estimated around 1 cm^{-1} with the open range (Figure 3.4). In addition, low μ_a phantoms

(A-C.1) had a low estimated μ_s' regardless of the predetermined μ_s' values, while high μ_a phantoms (A-C.3) had a high predicted μ_s'.

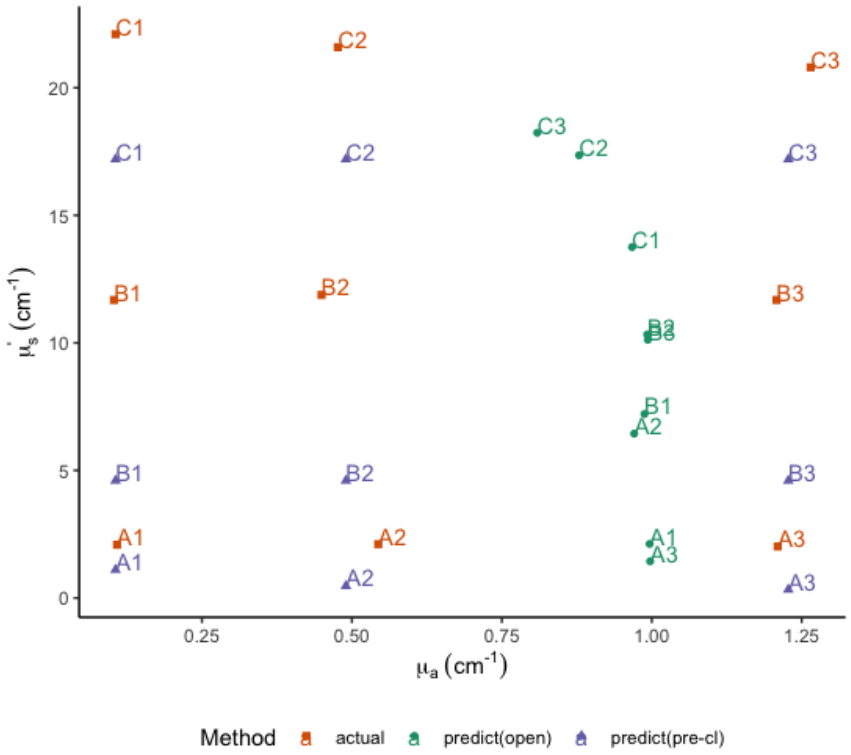

Figure 3.4. Scatter plot of solid phantoms' optical properties. Actual μ_a and μ_s' (orange), estimated μ_a and μ_s' with open range (green) and estimated μ_a and μ_s' after pre-classification (purple). Labels are phantom numbers.

With the pre-classification method (Figure 3.4), estimated μ_a and μ_s' of solid phantom were closer to the actual value. While estimated μ_a and μ_s' with the open range were far from the actual value (Figure 3.4). Therefore, the pre-classification model is useful in estimating solid phantom μ_a and μ_s'. However, with the current pre-classification process, kiwifruit μ_a and μ_s' fall into only part of the classification matrix and in the lower two classes of μ_a and μ_s' (Figure 4.6, Figure 4.7). Consequently, an improved pre-classification model with a finer resolution of μ_a and μ_s' was constructed with liquid phantoms and studies in Section 3.4.

3.4 Liquid phantoms and improved pre-classification model

3.4.1 Liquid phantom introduction

Solid phantoms are manufactured with predetermined μ_a and μ_s' and used preliminarily to investigate the range of estimated kiwifruit μ_a and μ_s'. However, kiwifruit's optical properties are challenging to estimate due to being biologically complex. With the application of the initial pre-classification model (Section3.3), kiwifruit μ_a and μ_s' were mainly classified into four classes with a range of μ_a (cm^{-1}) ∈ [0, 1.2] and μ_s' (cm^{-1}) ∈ [0, 10]. As a result, BMSB damaged kiwifruit were not adequately segregated with estimated kiwifruit μ_a and μ_s' in Section 4.3.3. In addition, estimated μ_a and μ_s' had similar values inside each class and close to the class threshold. This may be due to the limited number of reference classes for estimating μ_a and μ_s'. Therefore, a specific range of μ_a and μ_s' with finer classification ranges could potentially enhance estimated μ_a and μ_s' accuracy. However, manufactured solid phantoms are costly and require a long time to make. As an alternative, a liquid phantom set was designed to provide a greater resolution of classification. It was hoped that this improved pre-classification model could potentially enhance the accuracy of kiwifruit μ_a and μ_s' estimation.

3.4.2 Liquid phantom optical properties

A total of 56 liquid phantoms were prepared for the improved pre-classification model calibration (Figure 3.5). Liquid phantoms were made with Intralipid® 20% (batch 80NC095, Fresenius Kabi, Germany) and Naphthol Blue Black (NBB) (Sigma-Aldrich, Missouri, USA) 5 mM stock solution. The absorbers of liquid phantoms are ink particles, and the scatterers are lipid particles. The designed phantom set had four scattering levels at 3.12 %, 5.2 %, 7.28 % and 9.36 % of Intralipid®, and 14 levels of absorption between 0 – 0.65 % of NBB at 0.05 % intervals. This setup provides a range of expected μ_a (cm^{-1}) ∈ [0, 1.1] and expected μ_s' (cm^{-1}) ∈ [0, 5.6].

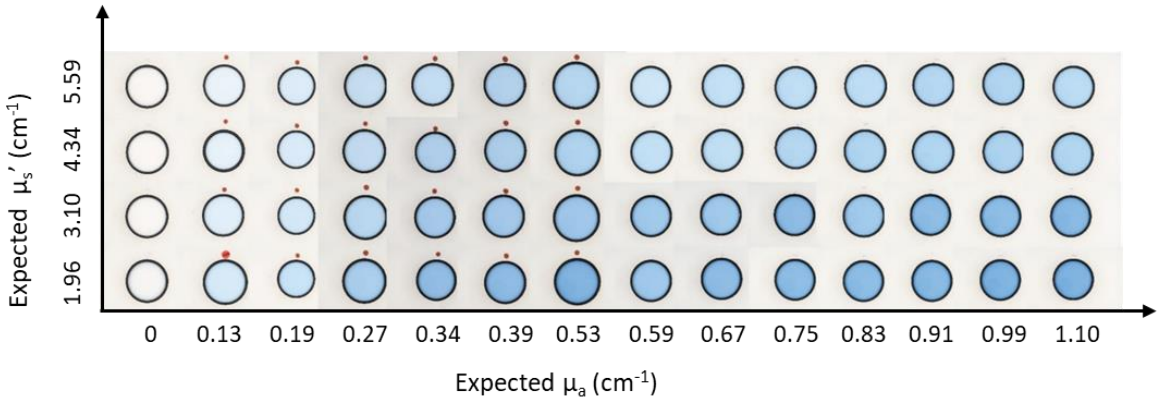

Figure 3.5. Liquid phantom set for building pre-classification model with four levels of scattering and 14 levels of absorption. Absorption increases from left to right with estimated μ_a are 0 – 1.1 cm^{-1}; Scattering increases from bottom to top with estimated μ_s' are 1.86 – 5.59 cm^{-1}.

The absorption coefficient of the liquid phantom μ_a* was expected the same as solutions with different NBB concentrations. NBB solution absorbance (A) was measured using a UV-visible recording spectrophotometer (UV–16 A, SHIMADZU, Japan). Measured μ_a was linearly correlated (R^2 = 0.998) with measured A (Eq. 3.10).

$$\mu_a{}^* = \mu_a = 2.303 \times \frac{A}{t} \mathrm{t} \qquad \text{Eq. 3.10}$$

in which, expected μ_a* of the phantom referred to the calculated μ_a of NBB solution according to A. t is the thickness of the film. This equation was built according to the measured data.

A minimum expected μ_a* was set as 1.e^{-10} with μ_a* ≠ 0 as a condition in the curve fitting process (Farrell et al., 1992). The expected μ_a range was then calculated as

$$\mu_{an}{}^* \in [\mu_{an} - \frac{\mu_{an} - \mu_{a(n-0.05)}}{2}, \mu_{an} + \frac{\mu_{a(n+0.05)} - \mu_{an}}{2}] \qquad \text{Eq. 3.11}$$

in which, μ_{an}* is μ_a* with n % of NBB.

The expected reduced scattering coefficient of the liquid phantom μ_s'* was obtained according to Watté et al. (2015) at different concentrations of Intralipid® 20%. A linear regression (R^2 =

0.99) was found between Intralipid® 20% concentration and expected $\mu_s'^*$. The relationship can be described by

$$\mu_s'^* = -0.003272 + 2.985451 \cdot C \cdot \frac{20}{100} \qquad \text{Eq. 3.12}$$

in which $\mu_s'^*$ represented the expected reduced scattering coefficient of liquid phantoms and C was Intralipid® concentration. The resulting $\mu_s'^*$ levels and ranges are given in Table 3.3

Table 3.3. Liquid phantoms reduced scattering coefficient (μ_s', cm^{-1}) with four expected $\mu_s'^*$ and expected ranges. μ_s' are predicted (a) at expected $\mu_a^* = 0$; (b) directly from non-destructive LBI without pre-classification (both open range); (c) after pre-classification based on LBI parameters

$\mu_s'^*$	$\mu_s'^*$ Range	μ_s' ($\mu_a^* = 0$)	μ_s' (open range)	μ_s' (with pre-classification)
1.86	0.1-2.5	1.41	3.39	1.11
3.10	2.6-3.6	1.56	3.93	2.61
4.34	3.7-4.8	1.73	4.26	3.57
5.59	4.9-6.5	1.90	4.31	4.36

3.4.3 Data analysis

Liquid phantom preparation was conducted in 2 days with phantoms μ_a^* (cm^{-1}) ∈ [0, 0.59] on day 1 and μ_a^* (cm^{-1}) ∈ [0.67, 1.1] on day 2. Phantom solutions were made using 250 mL volume flasks in the morning on each measurement day. Solutions were then transferred into 280 mL round black plastic containers (41 x 118 mm) before being well mixed in the flask, and each solution resulted in one phantom sample for LBI acquisition. Liquid phantom LBI images were obtained immediately after the transfer of solution by placing the container in the centre of the moving table of the LBI system. Liquid phantom LBI images were pre-processed to remove the reflection spot within the diffusion area. LBI diffusion profiles were extracted from the pre-processed picture. Specifically, the LBI parameters DIP, Q1R, FWHM, Q3R, and SLP (Figure 3.2a) were extracted.

The same method for building pre-classification with solid phantoms (Section 3.3.2) was utilized for the improved pre-classification model constructed with liquid phantoms. Liquid phantom extracted LBI parameters, expected μ_a* and expected μ_s'* were used as input parameters to build the pre-classification model using FDA. In the curve fitting process, the ranges of μ_s'* (Table 3.3) were the prediction thresholds for each predicted class. The model was validated with leave-one-out cross-validation for the same liquid phantom set with predicted μ_a and μ_s', and results are presented in Section 3.4.5.

This resulting pre-classification mode was used for segregating kiwifruit with CI in Chapter 5. Kiwifruit LBI parameters DIP, Q1R, FWHM, Q3R, and SLP (Figure 3.2a) were extracted from their attenuation profiles, and then kiwifruit were pre-classified according to the reference classes derived from the liquid phantoms. In the end, estimated μ_a [cm^{-1}] and μ_s' [cm^{-1}] were calculated with Farrell's equation considering the ranges from the validation of the pre-classification models.

3.4.4 Classification model

The results of the classification model are presented using a confusion matrix and evaluated with overall accuracy (Eq. 3.13), precision (Eq. 3.14), sensitivity (Eq. 3.15) and kappa value (Eq. 3.16).

$$Accuracy = \frac{TP + TN}{TP + FP + FN + TN} \quad \text{Eq. 3.13}$$

$$Precision = \frac{TP}{TP + FP} \quad \text{Eq. 3.14}$$

$$Sensitivity = \frac{TP}{TP + FN} \quad \text{Eq. 3.15}$$

$$\kappa = \frac{2 * (TP * TN - FN * FP)}{(TP + FP) * (TN + FP) + (TP + FN) * (FN + TN)} \quad \text{Eq. 3.16}$$

Where True Positive (TP) represents accurately predicted classes, False Negative (FN) represents incorrectly predicted classes, True Negative (TN) represents other accurately predicted classes, and False Positive (FP) represents other incorrectly predicted classes. Model accuracy is the proportion of accurately classified classes for all classes. Sensitivity is the proportion of the accurate target class compared to all phantoms in the target class. Precision is the proportion of the actual target class in all phantoms predicted into that target class.

3.4.5 Estimation of liquid phantom optical properties

3.4.5.1 Laser backscattering imaging parameters of liquid phantoms

LBI attenuation profiles of liquid phantoms were extracted considering varying levels of absorption and scattering. Parameters of the LBI profile (Figure 3.6) showed that DIP, Q1R, FWHM, Q3R and SLP values decreased when the expected μ_a* and expected μ_s'* increased.

The difference in parameters among the scattering levels was somewhat stable at all expected μ_a* levels and were not overlapping at most μ_a* levels. The parameters decreased quickly when μ_a* changed from 0 to 0.19 cm^{-1}. An uncontinuous data point of LBI parameters at μ_a* = 0.59 cm^{-1} was observed, this fluctuation could be due to the absorbance change through time. Liquid phantoms were made in the morning, and LBI acquisition was conducted throughout the day. The LBI of the phantom with μ_a* = 0.53 cm^{-1} was obtained last on day 1, and the LBI of the phantom with μ_a* = 0.59 cm^{-1} was obtained first on day 2. When time increased, the absorbance decreased (Dai et al., 2018), and a lighter colour of phantoms was also shown in Figure 3.5. Thus, replication of phantom measurements is required in the future. Moreover,

the impact of how the time between the creation of solutions and image acquisition is correlated with phantoms' optical properties needs to be investigated further.

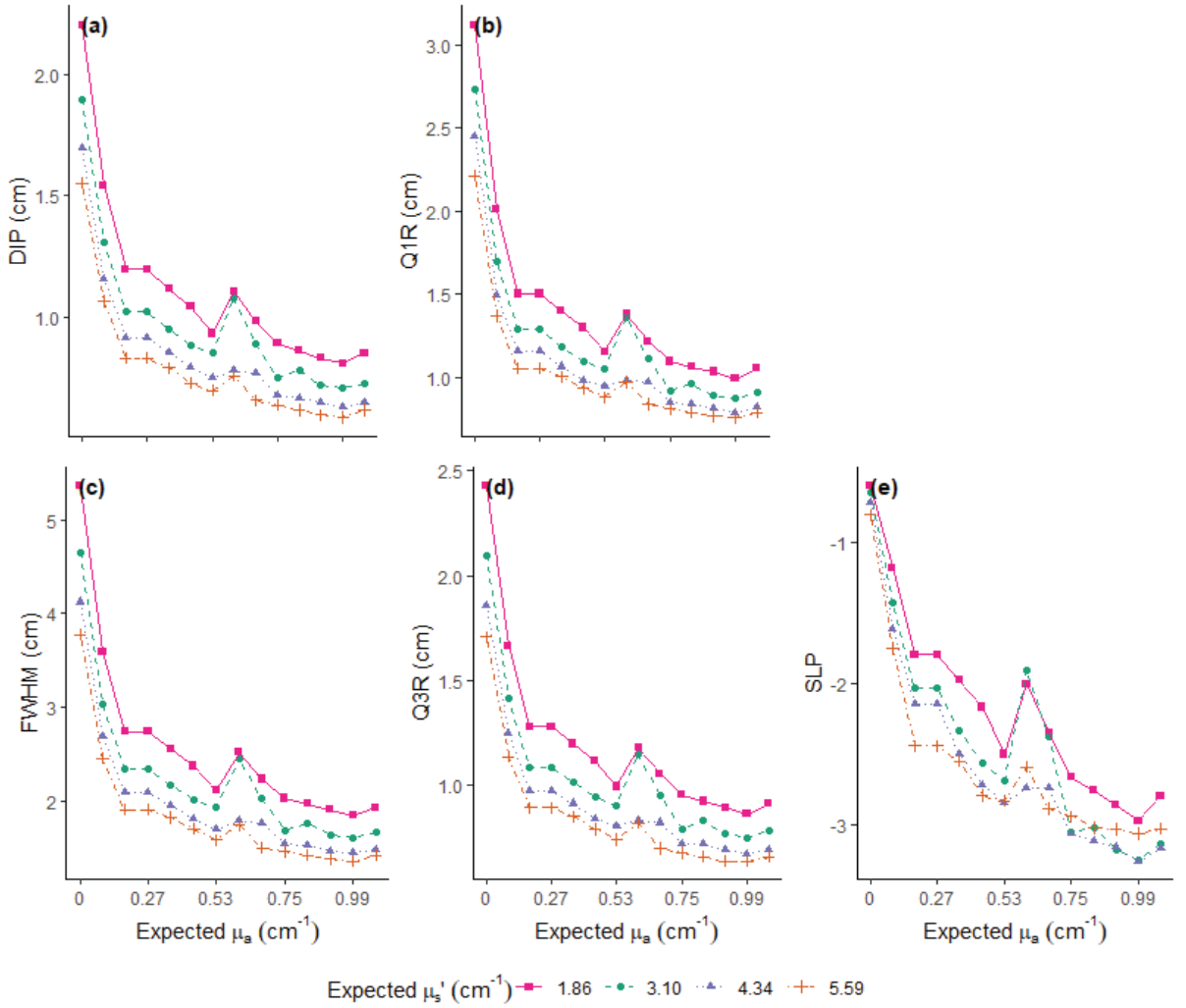

Figure 3.6. Parameters extracted from LBI profiles at 520 nm after image processing considering four expected μs'. Each data point represents a single phantom value. LBI parameters were the radius of the saturated area (DIP), the radius at 75 % of maximum intensity (Q1R), double the radius at 50 % of maximum intensity (FWHM), the radius at 25 % of maximum intensity (Q3R), and the slope of the linear regression model (SLP) built with log-transformed profile data between Q1R and Q3R.*

3.4.5.2 Optical properties of liquid phantoms

Normalized light intensity profile of phantoms with expected μ_a* and expected μ_s'* showed that the profile diffusion distance was shortened when μ_s'* increased (Figure 3.7a,d,g,j). Within the selected phantom optical property ranges, diffusion profiles were separated at the lowest

and highest μ_a*, suggesting that classification according to the chosen range was possible (Figure 3.7a, j). However, the difference among phantoms with varying μ_s'* became less obvious with increasing absorption levels (Figure 3.7a,d,g,j). The LBI profiles separation and the μ_a and μ_s' of 'Conference' pear showed the same trend of decreasing μ_s' with increasing μ_a (Adebayo et al., 2017).

In addition, simulated diffusion profiles based on expected μ_a* and estimated μ_s' were constructed (Figure 3.7b,e,h,k,c,f,i,l). When expected μ_a* is provided, constructed profiles with estimated μ_s' using the Farrell equation directly (Figure 3.7b,e,h,k) were similar to the measured profiles (Figure 3.7 a, d, g, j). This result agrees with the validated result using PDW that the estimation of optical properties is possible when one of them is known (Zude-Sasse et al., 2019). Within expected μ_a* ranges, estimation of μ_s' was possible for μ_a* < 0.7 cm^{-1} when one known variable in the Farrell equation is provided. However, an under-estimation of μ_s' occurred when known μ_a* was above 0.7 cm^{-1} (Figure 3.8a). With enhanced μ_a*, the separation of μ_s' showed greater uncertainty without pre-classification range limits (Figure 3.8a).

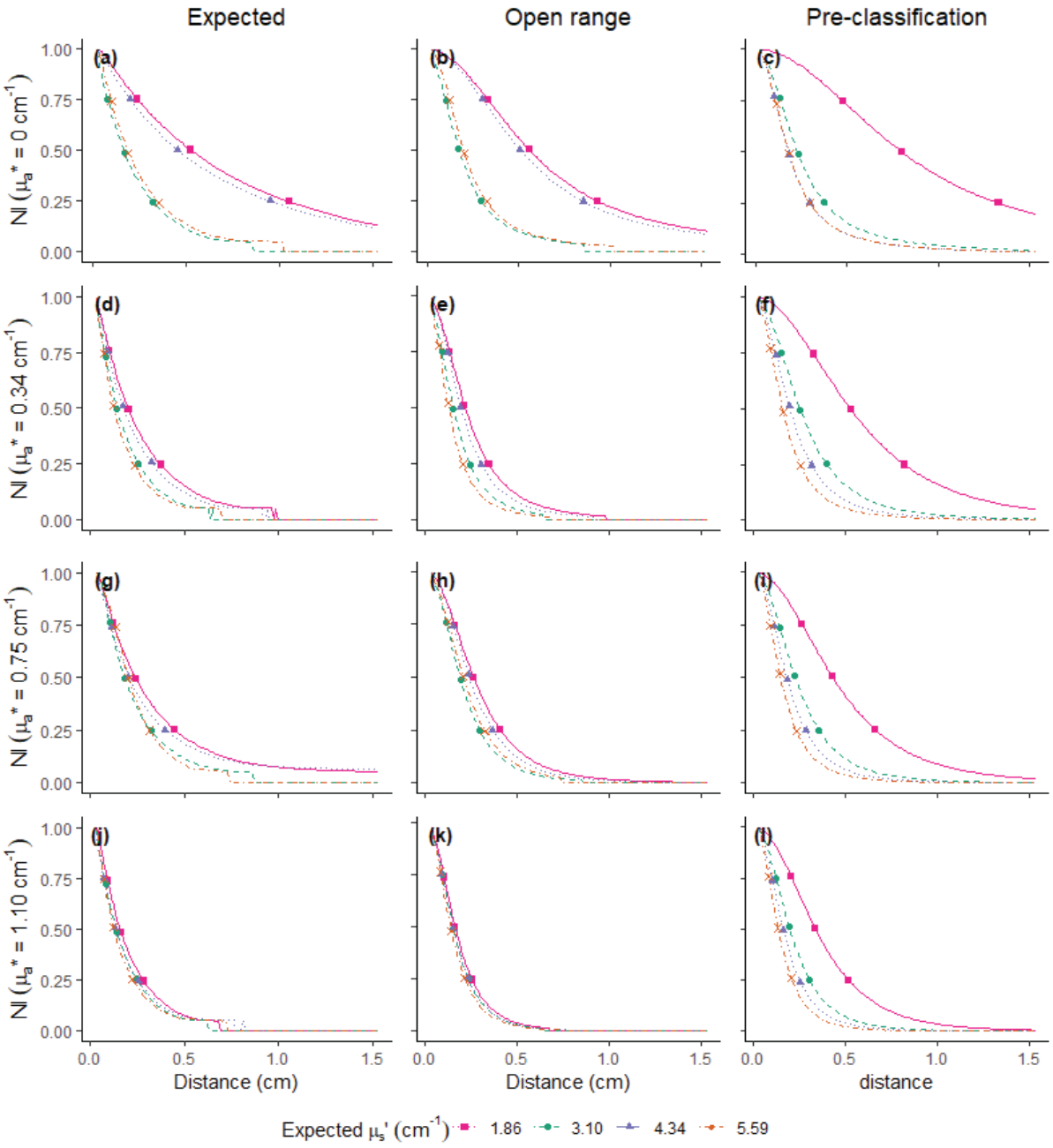

Figure 3.7. Normalized intensity (NI) profiles of liquid phantoms obtained by LBI measurement at 520 nm. (a, d, g, j). Simulated profiles with expected μ_a and expected μ_s'; (b, e, h, k). simulated profiles using Farrell equation with expected μ_a* and estimated μ_s' of phantoms without pre-classification; (c, f, i, l). simulation using Farrell equation with expected μ_a* and estimated μ_s' of phantoms after pre-classification. Dots were marked at a selected intensity (at 75 %, 50 % and 25 % of the maximum intensity).*

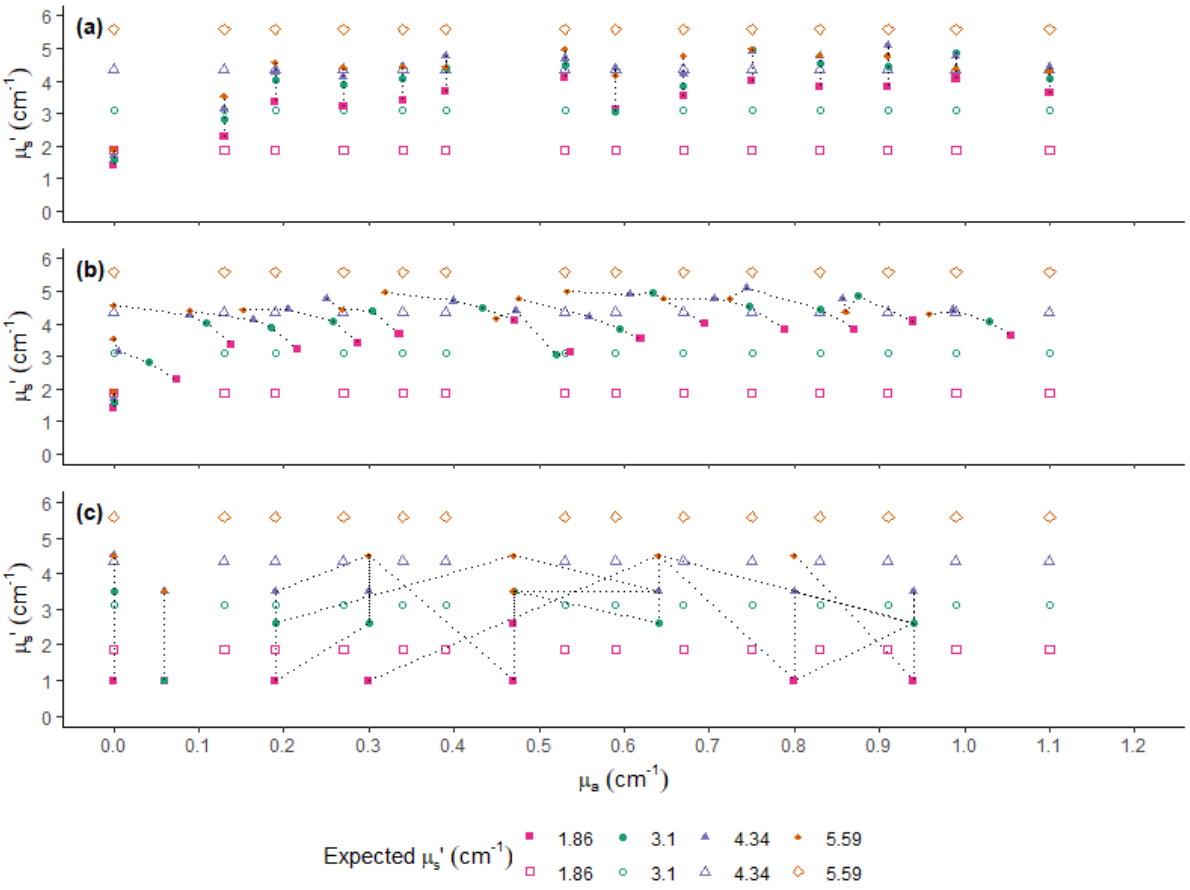

Figure 3.8. Optical properties estimated of liquid phantoms. Empty points are expected μ_a and μ_s'* of liquid phantoms; solid points are estimated μ_a and μ_s'. (a). expected μ_a* and estimated μ_s' directly (μ_s' = open range) according to Farrell equation; (b). estimated μ_a and μ_s' (both open range); (c). estimated μ_a and μ_s' (both after pre-classification). The dotted lines represent phantoms with the same absorption level.*

With the estimated μ_s' after pre-classification, although simulated profiles of phantoms with different μ_s'* were separated, simulated profiles (Figure 3.7c,f,i,l) were quite different from the measured ones (Figure 3.7 a, d, g, j). Thus, the pre-classification method may introduce further simulation uncertainty resulting from μ_s' estimation uncertainty. Estimated μ_a and μ_s' (open-range) are presented in Figure 3.8b, showing an under-estimation of μ_a with increasing μ_s', resulting in diagonal parallel lines shifting towards the top left for the different μ_s' levels at the same theoretical μ_a* level (Figure 3.8b). A similar observation of the underrepresentation of μ_a and over-representation of μ_s' was presented in section 3.3.3. that was using solid phantoms

to build the pre-classification model with μ_a* and μ_s'* ranging between [0.1, 1.3] cm^{-1} and [2.0, 22.8] cm^{-1}, respectively (Figure 3.4).

Following the completion of the pre-classification based on LBI parameters, μ_a and μ_s' were separated (Figure 3.8c). Although estimation bias was found, a potential to use LBI parameters to build a pre-classification model for estimating optical properties (Figure 3.8c) was confirmed in the present study. The bias may be due to the fact that estimated μ_a and μ_s' values tend to be closer to the threshold of each class (Figure 3.4) with the pre-classification method. At lower absorption levels (μ_a* ≤ 0.59 cm^{-1}), segregation among scattering levels could be observed regardless of the shifting of μ_s' with increasing μ_a* (Figure 3.8c). However, the segregation of μ_s' level is less accurate when μ_a* > 0.59 cm^{-1}, which might be expected due to the similarity of LBI profiles at higher μ_a* (Figure 3.7.). Ultimately, greater accuracy was obtained when estimating μ_a at lower μ_s' (Figure 3.8c).

Although the estimated optical properties were not separated well, pre-classification showed improved estimation accuracy for μ_s' (close to the known value, μ_s'*) compared to results without pre-classification (Table 3.3). In the estimation, averaging over the four absorption levels, estimating μ_s' at μ_a* = 0 or estimating μ_s' with an open range without pre-classification, the values differed from actual μ_s'* (Table 3.3). However, when using the pre-classification, μ_s' was predicted in the correct range.

3.4.5.3 Pre-classification model performance

The pre-classification model was cross-validated with the same set of liquid phantoms, LBI profiles and the associated μ_a* and μ_s'*. The overall accuracy after pre-classification was 65.6 % and 91.5 % for μ_a and μ_s', respectively (Table 3.4). The greater classification accuracy of μ_s' (Table 3.4) compared to μ_a may be related to the small absorption class intervals used in the

classification model as indicated by LBI parameters in Figure 3.7. The classification accuracy of predicted μ_s' without pre-classification was worse than that using LBI parameters because without limiting the range, predicted μ_s' tend to be over-estimated at lower μ_s' levels (Table 3.3). This indicated that a μ_s' range is required to be known when using Farrell's equation to get more accurate estimates of μ_s' values.

Table 3.4. Classification accuracy (%) for optical properties (μ_a and μ_s') of liquid phantoms using LBI profile parameter, Farrell-estimated values without pre-classification (Open-range) and Farrell-estimated values after pre-classification (Pre-classification). Values presented are the average classification accuracy for the 4 μ_s' and 14 μ_a ranges.

	LBI	Open-range	Pre-classification
μ_s' (cm^{-1})	87.5	39.3	91.5
μ_a (cm^{-1})	65.6	75.0	65.6

3.4.6 Overall discussion

The estimation error of estimated μ_s' observed in Figure 3.8c is high, which may be due to the narrow μ_s' range in the current study ($\mu_s' \in [0, 5.6]$ cm^{-1}). Compared to previous metamodel approaches using a hyperspectral imaging system, the pre-designed μ_s' levels captured a high range between [3.8, 20] cm^{-1} (Aernouts et al., 2015). Aernouts et al. (2015) found a large variation of μ_a estimation was observed when μ_a ranging between [0, 0.5] cm^{-1}, whereas μ_s' estimation reached an accuracy of $R^2 = 0.997$ and RMSE = 0.226 cm^{-1} at a similar wavelength range (550 – 700 nm and 900 – 950 nm). Moreover, when using liquid phantom sets with a wide range of μ_a and μ_s' between [0, 14] and [0, 275] $cm^{-1,}$ a clear level separation of μ_a and μ_s' was observed (Aernouts et al., 2013). Similar results regarding pre-classification ranges were reported when applying time-resolved methods for low μ_s' and high μ_a. Specifically, when $\mu_s' >$ 20 cm^{-1} and $\mu_a < 0.2$ cm^{-1}, the model performance was good, and the error was less than 20 % when $\mu_s' > 5$ cm^{-1} (Cubeddu et al., 1994). As described by Farrell et al. (1992), curve fitting with the Farrell equation is reliable when $\mu_a << \mu_s'$, while in the current liquid phantom set, μ_s' was studied within a more narrow range between [1.86, 5.59] cm^{-1} with an enhanced resolution

compared to earlier research (Cubeddu et al., 1994; Aernouts et al., 2013). However, the range covered in this study was also observed with kiwifruit samples (Figure 3.4). Consequently, limited estimation capacity of optical properties may be expected in the narrow range. The ranges of optical properties of kiwifruit have been described with μ_a between 0 – 0.4 cm^{-1} and $\mu_s' < 8$ cm^{-1} within the visible-NIR region (Qin & Lu, 2008). Thus, the set of phantoms covers the relevant range for kiwifruit optical property estimation.

Using LBI parameters may have some potential in practice as it is better than open range μ_a and μ_s', yet it does not require prior knowledge of the μ_s' range. However, the calculation error of μ_a and μ_s' still exists with the improved model when applying the model for segregation of kiwifruit with CI (Section 5.3.4 and 5.3.5), thus contributing to segregation error in kiwifruit. Therefore, in Chapters 6 and 7, only LBI parameters without estimated μ_a and μ_s' were utilized when investigating correlations between FF and LBI parameters.

3.5 Conclusion

In this chapter, the methodology of the LBI technique is explained. In addition, pre-classification models were calibrated and validated using optical phantoms. Pre-classification models were confirmed as a feasible approach to decoupling μ_a and μ_s' estimation of optical phantoms. However, the current pre-classification model has estimation uncertainties when $\mu_a < 0.7$ cm^{-1}, which may be difficult to overcome to estimate kiwifruit's optical properties. Alternatively, directly using LBI parameters could describe kiwifruit quality changes during ripening and achieve fruit segregation objectives.

Chapter 4 The application of the pre-classification method for kiwifruit absorption and reduced scattering coefficients estimation: a case study of BMSB damaged kiwifruit

4.1 Introduction

For kiwifruit, BMSB damage is difficult to observe externally. Lara et al. (2018) found that BMSB feeding damage has symptoms of white corky spots and water soaking in the outer pericarp region, which is not acceptable in the market (Figure 4.1).

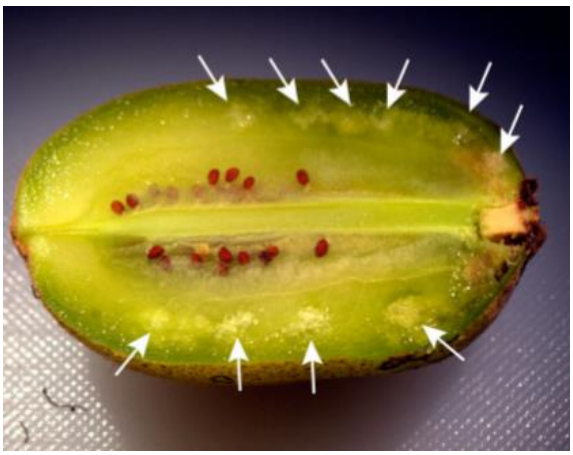

Figure 4.1. Brown Marmorated Stink Bug (BMSB) feeding damage on 'Zesy002' kiwifruit. Retrieved from Lara et al. (2018) with permission.

Li et al. (2018) worked on using non-destructive methods of OCT and fringe projection to detect BMSB damage detection and found that infected kiwifruit had symptoms of water soaking near the proximal end. Chen et al. (2020) investigated BMSB damage on three cultivars of kiwifruit in exclusion cage experiments and reported that kiwifruit could be damaged at any growth stage. Symptoms of BMSB damage can develop as dark green spots (Figure 4.2a) or white corky spots (Figure 4.2b) immediately under the skin. Failure to identify BMSB-caused damage could result in an indirect loss of fruit quality. Damaged fruit may have stimulated wound ethylene biosynthesis and thus release ethylene into the storage environment (Nieuwenhuizen et al., 2021), which may exacerbate the ripening of neighbouring fruit.

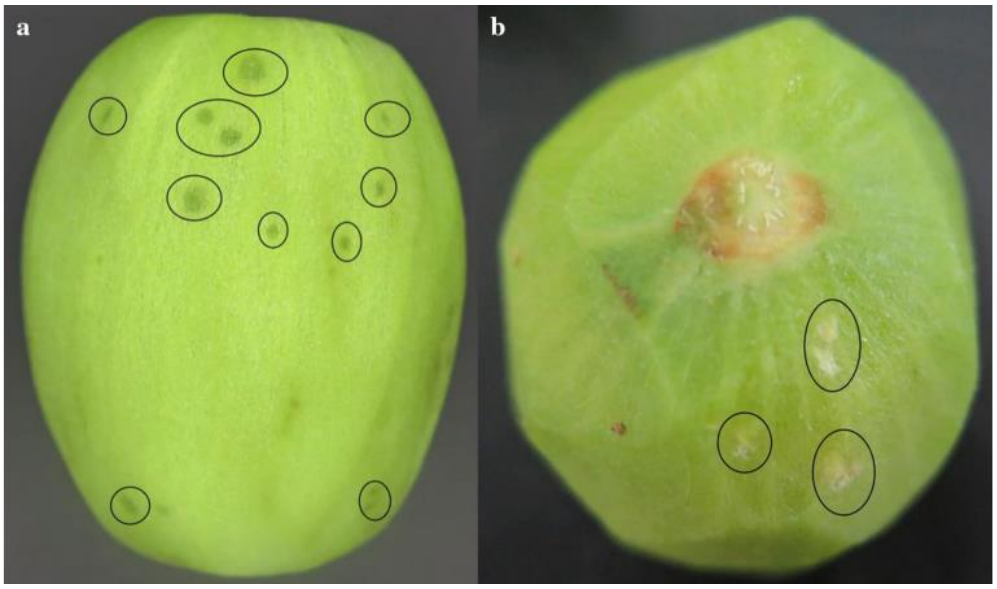

Figure 4.2. Two types of BMSB damage. (a) green spot on 'Hayward'(A.deliciosa); (b) White spot on 'Nongdajinmi' (A.chinensis). Retrieved from Chen et al. (2020) with permission.

Research has been conducted to minimise BMSB damage in the orchard (Rice et al., 2014; Suckling et al., 2019; Ludwick et al., 2020). However, there is no established non-destructive method to identify damaged fruit at an early stage. Non-destructive optical techniques have the potential for BMSB damage detection. As light interacts with tissue, the propagated light is absorbed, specularly reflected, and scattered (diffusively reflected) near the incident point (Holz & Chen, 1978). Light absorption is related to the chemical properties of the sample, whereas light scattering depends on the structural properties and cellular composition. Optical properties, μ_a and μ_s', could potentially be used to detect the damage symptoms of tissue colouration and water soaking (Ekramirad et al., 2016; Adedeji et al., 2020).

In this chapter, kiwifruit with BMSB damage were assessed using a spatially-resolved LBI system with a pre-classification of optical properties (section 3.3). The objectives of this chapter are to:

(i) estimate kiwifruit optical properties of μ_a [cm^{-1}] and μ_s' [cm^{-1}] and

(ii) determine whether kiwifruit with BMSB damage could be segregated using estimated fruit μ_a [cm^{-1}] and μ_s' [cm^{-1}] based on LBI attenuations.

4.2 Materials and Methods

4.2.1 Kiwifruit source

In this study, yellow-fleshed 'Zesy002' (n = 200) and green-fleshed 'Hayward' (n = 200) kiwifruit were sourced in 4 batches (Table 4.1). Each batch contained 50 BMSB-exposed fruit ($Fruit_{exp}$) and 50 control fruit ($Fruit_{ctr}$). Kiwifruit harvest was defined as Earlier or Later depending on the time prior to the main harvest date in the northern hemisphere (Table 4.1). The main harvest for 'Zesy002' and 'Hayward' were on 23rd Sep. and 29th Oct. 2019, respectively. Both batches of 'Zesy002' and the 2nd batch of 'Hayward' were harvested at the later maturity on 20th Sep. and 25th Oct. 2019, respectively, whilst the 1st batch of 'Hayward' was harvested at earlier maturity (18th Oct. 2019).

Table 4.1. Kiwifruit resource information . $Fruit_{exp}$ were kiwifruit exposed to BMSB, $Fruit_{ctr}$ were control kiwifruit covered from BMSB, $Fruit_{BMSB}$ were kiwifruit with visual BMSB feeding damage, $Fruit_{sound}$ were sound kiwifruit without visual BMSB damage, storage time was in days at 4 °C.

	Batch	$Fruit_{exp}$	$Fruit_{ctr}$	Harvest	BMSB	Storage	$Fruit_{BMSB}$	$Fruit_{sound}$
Zesy002	1	50	50	Later	Orchard	14	39	60
	2	50	50	Later	Lab	10	20	79
Hayward	1	50	50	Earlier	Orchard	7	49	51
	2	50	50	Later	Orchard	0	44	54

In addition to harvest time, kiwifruit were stored for a different time at 4 °C after harvest prior to fruit delivery due to the logistics and allowing exposure time with BMSB (Table 4.1). 'Zesy002' were delivered on 10th Oct. 2019, and 'Hayward' were delivered on 28th Oct.2019. The delivery via courier post took 3 days for 'Zesy002' and 4 days for 'Hayward' from Faenza (Italy) to Potsdam (Germany). For the 1st batch of 'Zesy002' kiwifruit and both 'Hayward' batches, $Fruit_{exp}$ and $Fruit_{ctr}$ were harvested after BMSB exposure treatment in the orchard. In the orchard, $Fruit_{exp}$ were exposed individually for 3 days to one adult BMSB, and $Fruit_{ctr}$ were

covered individually with a bag after the fruit set to avoid BMSB damage. For the 2nd batch of 'Zesy002' kiwifruit, $Fruit_{exp}$ were selected from the $Fruit_{ctr}$ population and artificially infested for three days in the laboratory. $Fruit_{exp}$ (n=50) with laboratory infestation were exposed to 50 adult BMSBs to mimic the same infection rate as orchard infestation.

In all cases, the $Fruit_{ctr}$ may also have been infested by wild BMSB due to the orchard being in an area with high natural BMSB infestation. On the other hand, the BMSB fruit damage was not exclusively observed on the BMSB-exposure treatments exposure to BMSB did not always result in damage. As a result, $Fruit_{ctr}$ could have BMSB damage, but not all $Fruit_{exp}$ had BMSB damage. Therefore, independent of fruit source, kiwifruit were additionally segregated as sound fruit ($Fruit_{sound}$) without damage and BMSB damaged fruit ($Fruit_{BMSB}$) after the destructive assessment (Table 4.1) to evaluate LBI with pre-classification method.

4.2.2 Kiwifruit physiology, LBI and quality measurements

Kiwifruit were stored at 1 °C after arrival, with the quality measurements starting on the day after delivery. The total measurements took 4 days for each cultivar. Kiwifruit were warmed to room temperature overnight before quality measurements. Kiwifruit respiration rate (RR), LBI data, and apparent modulus of elasticity (ME, a form of texture measurement) were obtained in order and non-destructively. 'Hayward' FF and SSC were also destructively measured after the non-destructive measurements. Both non-destructive and destructive measurements (damaged observations excluded) were conducted for 50 kiwifruit from each batch per day (n_{exp}=25, n_{ctr}=25), culminating in 4 days of measurements per cultivar in Table 4.1. Injury observations were conducted after all quality measurements on the 5th day.

Kiwifruit RR was measured using a closed system developed by ATB, Germany, which consisted of 9 acrylic glass cylinders (8.2L) with each cylinder fitted with a non-dispersive infrared CO_2

sensor (GMP222, Vaisala GmbH, Bonn, Germany). At each measurement, individual kiwifruit was placed in a cylinder, and the rate of CO_2 production was recorded. The RR was determined as the average CO_2 concentration accumulated per unit kiwifruit weight over a unit period. For each delivered batch of kiwifruit, a total of 36 kiwifruit (18 from $Fruit_{exp}$ and 18 from $Fruit_{ctr}$) were measured for RR in 4 batches.

Kiwifruit LBI images (at wavelengths of 532, 660 and 785 nm) were acquired by manually placing each kiwifruit sample on the fruit platform of the system below the camera (Section 3.2.1 and 3.2.3). The images were acquired in a dark room to prevent interference from stray light. For each kiwifruit, LBI data were acquired at the equator region (Figure 4.3).

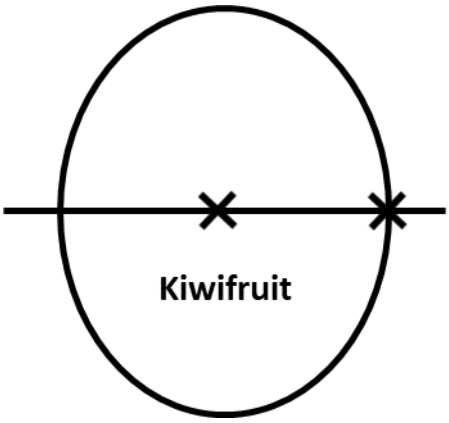

Figure 4.3. Kiwifruit LBI image acquisition positions correspond to cross-marks.

Kiwifruit ME was determined from compression tests at the same position with LBI caption (Figure 4.3) by a texture analyser (TA·XT Plus Texture Analyser, Stable Micro Systems, Godalming, UK) with a spherical steel body (diameter d = 6.35 mm). Elasticity was calculated from the deformation (D) at a set force (F) of 1 N and a speed of 8 mm s^{-1} according to Mohsenin (1986) as Eq. 4.1. Kiwifruit dimensions (minor diameter, major diameter, and length) were measured individually using a digital calliper.

$$E = (0.531 \cdot F(1 - \mu^2))/(D^{3/2}) \left[\frac{2}{R} + \frac{4}{d}\right]^{1/2} \quad \text{Eq. 4.1}$$

Where *D* is the deformation (mm), *F* is the set force of 1 (N), μ is the Poisson's ratio being μ = 0.4 for kiwifruit (McGlone & Jordan, 2000), *d* = 6.35 mm, *R* is the mean radius of individual kiwifruit from minor diameter, major diameter and length.

Kiwifruit FF was determined from penetration tests by a texture analyser (TA·XT Plus Texture Analyser, Stable Micro Systems, Godalming, UK) with a standard 7.9 mm diameter Effegi probe and at a speed of 8 mm s^{-1} to 8 mm depth. Before the measurement, 1 mm of skin slice was removed at two equatorial positions. Kiwifruit FF was recorded as the average of the two readings. The SSC of kiwifruit was measured by a refractometer (DR 301-95, A. Kruss Optronic, Germany) at room temperature. Kiwifruit samples were cut into half at the equator and juice extracted from the distal half by hand.

After all quality measurements for 4 days ('Zesy002' without FF and SSC measurement), kiwifruit samples were cut into 2 mm cross-sectional slices for manual counting of the white corky spots inside the tissue (Figure 4.4). The number of white corky spots of each slice was recorded and the total number in spots represented the severity of BMSB damage. After visual observation of BMSB damage, kiwifruit were classified into sound fruit ($Fruit_{sound}$: white corky spots number = 0) and BMSB damaged fruit ($Fruit_{BMSB}$: white corky spots number > 0).

Figure 4.4. BMSB damage observation of 'Zesy002' kiwifruit cut into 2 mm slices. White corking regions are circled and counted for severity grading. Kiwifruit slices are placed according to the fruit parts: STE is the proximal region, Mid is the equatorial region, and BLE is the distal region.

4.2.3 Data analysis

Kiwifruit LBI images were analysed into LBI attenuation profile according to Section 3.2.3. The diffusion theory model was fit to attenuation profile as performed by Farrell et al. (1992) to estimate kiwifruit μ_a and μ_s' (Section 3.2.3). The applied pre-classification range and model are referred to Section 3.3 and Table 3.2.

The quantitative comparison of kiwifruit quality attributes, μ_a and μ_s' for $Fruit_{sound}$ and $Fruit_{BMSB}$ were subjected to analysis of variance (ANOVA). Post hoc tests conducted after ANOVA identified significant differences in quality attributes or optical properties between sound and damaged fruit. Log transformation was applied to FF for data normalization.

The goal is to segregate kiwifruit with BMSB damage from sound ones. Segregation input parameters were optical properties (μ_a and μ_s') at wavelengths of 532, 660 and 785 nm. The

segregation model was validated with 'leave-one-out' cross-validation. The results of the segregation model were presented using the confusion matrix (Section 3.4.4) and evaluated with Overall accuracy (Eq. 3.13), Precision (Eq. 3.14), Sensitivity (Eq. 3.15) and kappa value (Eq. 3.16). Where True Positive (TP) represents correctly segregated BMSB damaged fruit, False Positive (FP) represents incorrectly segregated sound fruit, True Negative (TN) represents accurately segregated sound fruit, and False Negative (FN) represents incorrectly segregated BMSB damaged fruit. Model accuracy is the proportion of accurately classified both BMSB damaged and sound kiwifruit. Sensitivity is the proportion accurately segregated BMSB damaged kiwifruit in comparison to all BMSB damaged fruit. Precision is the proportion the actual BMSB damaged kiwifruit in all fruit segregated as damaged.

4.3 Results and discussion

4.3.1 Kiwifruit BMSB injury observation

The number of $Fruit_{sound}$ and $Fruit_{BMSB}$ was not balanced (Table 4.1). Less BMSB damaged kiwifruit occurred in the lab exposure condition, resulting in the 2nd batch of 'Zesy002' had less $Fruit_{BMSB}$ than the 1st batch. It is possible that the orchard environment is more feasible for BMSB to feed on kiwifruit or attentively there were more BMSB per fruit in the orchard environment.

White corky spots were observed for both cultivars, but no green spots (Figure 4.2a) were found for 'Hayward'. It's possibly due to the fact that BMSB damage varies in expression during kiwifruit growth (Chen et al., 2020b), and Chen et al. (2020) reported green spots were only found during fruit development on the vine. White corky spots were expressed in more mature kiwifruit, since kiwifruit in this study were mature and close to harvest (Table 4.1), therefore only corky spots were observed.

Additionally, brown corky spots and brown tissue regions were also observed in 'Zesy002' (Figure 4.5). Most brown tissue region was linked to corky spots on the proximal end. However, brown tissue was also observed in the core region without the occurrence of white corky spots. The browning tissue could be due to oxidative damage in the membrane (Wang, 1989; Burdon & Lallu, 2011a; Burdon, Pidakala, et al., 2014). The browning tissue could also be caused by fungal infection through the BMSB wound. Chen et al. (2020) found that kiwifruit with BMSB feeding damage were more sensitive to fungal infection and more likely to develop rot in the postharvest stage compared with sound kiwifruit. Thus, additional research is required to confirm whether the central brown tissue is a direct result of the BMSB damage or decay damage as a secondary consequence of the BMSB damage.

Figure 4.5. Brown tissue of 'Zesy002'in BMSB damage observation.

4.3.2 Kiwifruit physiology and quality assessment

For 'Zesy002', kiwifruit quality attributes were different as a result of BMSB damage (i.e. $Fruit_{sound}$ vs. $Fruit_{BMSB}$) or combined between batches and damage observation (Table 4.2).

Kiwifruit RR were different ($p < 0.05$) between $Fruit_{sound}$ and $Fruit_{BMSB}$, and different ($p < 0.05$) kiwifruit elasticity (ME) was found between damage and batches interactions. For 'Zesy002', RR of $Fruit_{BMSB}$ (368 nmol $kg^{-1}s^{-1}$) was higher than $Fruit_{sound}$ (318 nmol $kg^{-1}s^{-1}$) (Table 4.2). RR represents the metabolic activity of the kiwifruit. During kiwifruit ripening, an increase of RR is expected, and a higher RR represents an advanced ripeness. In addition, stress to the fruit induced by BMSB damage may result in higher fruit RR. The 2nd batch of $Fruit_{BMSB}$ has the lowest ME of 0.79 N/mm^2. Elasticity measures kiwifruit texture alterations resulting from the solubilization of pectin in the cell wall (Redgwell & Percy, 1992), which are correlated with ripening. Thus, low ME and high RR could indicate that BMSB damaged fruit had advanced ripening. However, the measurements were conducted 14 days after harvest. Hence, the ripeness of both $Fruit_{sound}$ and $Fruit_{BMSB}$ may have progressed during storage, meaning BMSB damage was not the only factor influencing kiwifruit quality attributes.

Table 4.2. The difference of average quality attributes between batches and between sound ($Fruit_{sound}$) and BMSB damaged ($Fruit_{BMSB}$) kiwifruit for 'Zesy002'. RR (nmol $kg^{-1}s^{-1}$) is the respiration rate, ME (N/mm^2) is the module of elasticity. Letters in sets of data represent significant differences ($p < 0.05$).

Batch	BMSB	RR No.	RR	Fruit No.	ME
1		36	323	99	1.32
2		36	340	99	0.99
	$Fruit_{sound}$	52	318^b	139	1.23
	$Fruit_{BMSB}$	20	368^a	59	0.98
1	$Fruit_{sound}$	20	301	60	1.49^b
1	$Fruit_{BMSB}$	16	350	39	1.07^b
2	$Fruit_{sound}$	32	328	79	1.04^b
2	$Fruit_{BMSB}$	4	438	20	0.79^a

'Hayward' kiwifruit SSC, FF and RR were different ($p < 0.05$) between $Fruit_{sound}$ and $Fruit_{BMSB}$ (Table 4.3). 'Hayward' kiwifruit RR and ME were different ($p < 0.05$) between batches. However, no difference was observed between interactions. Kiwifruit softening is physically related to the changes in cell wall properties, and SSC quantifies the starch-to-sugar conversion during

ripening. Therefore, RR, ME, FF and SSC indicated that kiwifruit's ripening stage was different batch-wise or for BMSB damage.

Table 4.3. The difference of average quality attributes between batches and between sound ($Fruit_{sound}$) and BMSB damaged ($Fruit_{BMSB}$) kiwifruit for 'Hayward'. RR (nmol kg-1s-1) is the respiration rate, ME (N/mm2) is the module of elasticity, FF (N) is flesh firmness and SSC (%) is total soluble solid contents. Letters in sets of data represent significant differences ($p < 0.05$).

Batch	BMSB	RR No.	RR	Fruit No.	ME	FF	SSC
1		27	338^{a}	100	2.21^{b}	42.20	12.4
2		36	230^{b}	98	2.84^{a}	54.17	10.9
	$Fruit_{sound}$	35	256^{b}	105	2.67	51.23^{a}	11.5^{b}
	$Fruit_{BMSB}$	28	301^{a}	93	2.05	38.48^{b}	12.2^{a}
1	$Fruit_{sound}$	13	303	51	2.24	43.32	12.3
1	$Fruit_{BMSB}$	14	370	49	2.16	40.47	12.5
2	$Fruit_{sound}$	22	229	54	3.07	58.70	10.7
2	$Fruit_{BMSB}$	14	231	44	1.93	36.26	11.9

The 2nd batch of 'Hayward' kiwifruit had lower RR (230, nmol $kg^{-1}s^{-1}$) and higher ME (2.84, N/mm^2) compared with the 1st batch (338 and 2.21, respectively) suggesting a less advanced stage of ripeness (Table 4.3). $Fruit_{BMSB}$ had a higher RR (301, nmol $kg^{-1}s^{-1}$), lower FF (38.5, N) and higher SSC (12.2, %) than $Fruit_{sound}$ (256 nmol $kg^{-1}s^{-1}$, 51.1 N and 11.5 %, respectively). All the quality attributes of RR, FF and SSC indicated that $Fruit_{BMSB}$ had advanced ripeness. Therefore, BMSB damage impacts kiwifruit quality attributes and leads to advanced ripening for kiwifruit.

The 1st batch of 'Hayward' fruit were harvested 7 days earlier and stored at 4 °C for 7 days, hence, the quality attributes may have changed during storage through ripening. During postharvest storage, how the quality changes due to BMSB damage compared to that of the kiwifruit ripening process needs to be further investigated.

4.3.3 Kiwifruit optical property estimation

For 'Zesy002', μ_s' was different at 532 nm ($p < 0.0001$) and 785 nm ($p < 0.05$) between $Fruit_{sound}$ and $Fruit_{BMSB}$. No difference was found of μ_a between $Fruit_{sound}$ and $Fruit_{BMSB}$, however, μ_a was different ($p < 0.1$) between batches at 785 nm.

Boxplot of estimated μ_a for 'Zesy002' (Figure 4.6A,B) shows a wider μ_a distribution in $Fruit_{sound}$ at 532 nm, and there was no difference of μ_a between $Fruit_{sound}$ and $Fruit_{BMSB}$. However, μ_a of $Fruit_{BMSB}$ is expected to be higher due to the absorbance of the browning tissue at 532 nm. It's possible that due to the yellow flesh colour of 'Zesy002', thus the differences in μ_a due to flesh browning may not be detectable in BMSB damaged 'Zesy002' kiwifruit. On the other hand, μ_a at 660 nm was very low compared with the other 2 wavelengths. Since there is minimal chlorophyll absorption in 'Zesy002', low μ_a values at 660 nm were expected. Alternatively, 785 nm is a short-wave NIR wavelength where no pigment absorption takes place. Wider spread μ_a at 785 nm was observed for BMSB damaged kiwifruit in both batches, this might be due to the water absorption as a result of the water-soaking symptoms.

Estimated μ_s' at 520 nm was higher ($p < 0.0001$) for $Fruit_{sound}$ than $Fruit_{BMSB}$ (Figure 4.6C,D). BMSB damaged kiwifruit were usually at an advanced ripening stage with lower FF (Table 4.2), thus μ_s' may be lower for this reason rather than due to cellular structural changes as a result of the corky spots. However, BMSB damaged kiwifruit had higher μ_s' at 785 nm. This higher μ_s' of damaged fruit could be due to the large diffusion area on raw LBI image with high absorption due to water soaking, thus estimated μ_s' may not be accurate since it has not met Farrell model's assumption of $\mu_a \leq \mu_s$'.

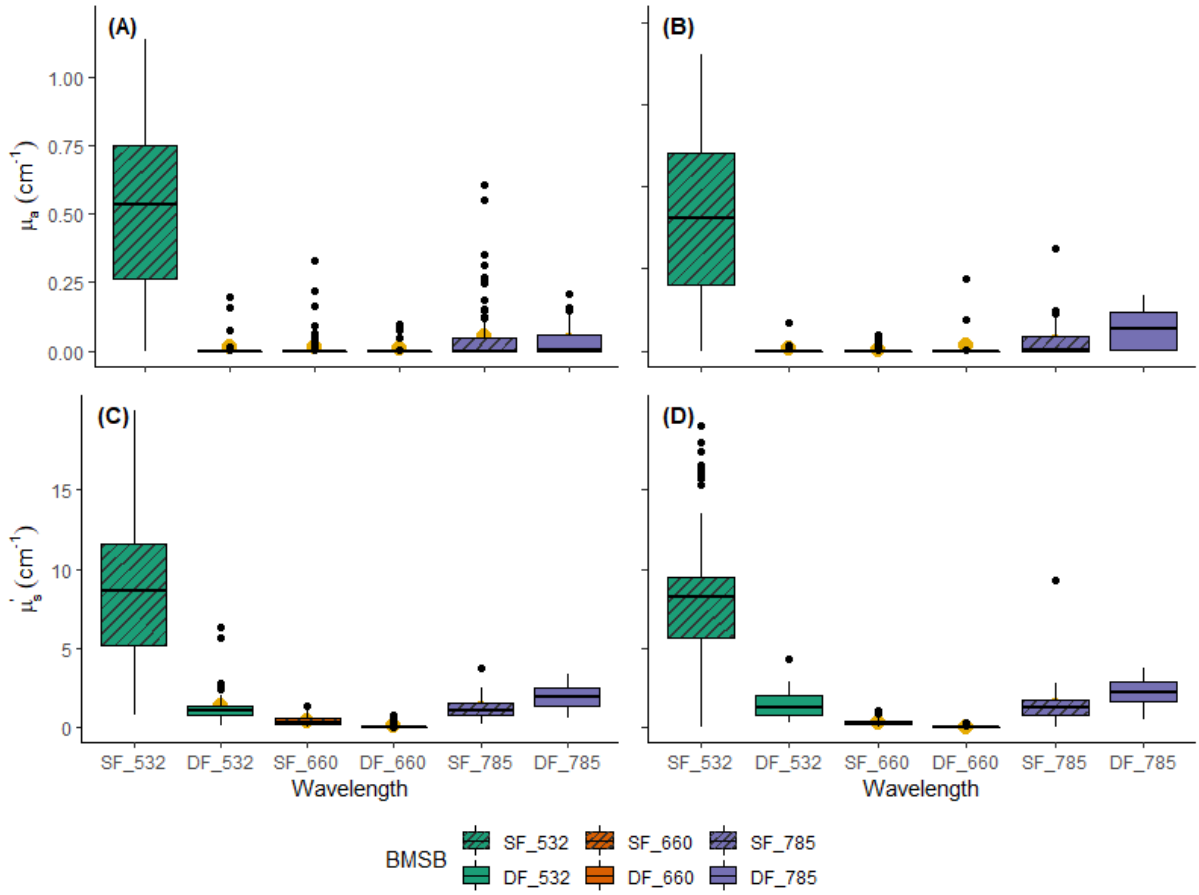

Figure 4.6. Estimated μ_a (A, B) and μ_s' (C, D) of 'Zesy002' kiwifruit from batch 1 (A, C) and batch 2 (B, D). Sound kiwifruit (SF) and BMSB damaged fruit (DF) optical properties at 532, 660 and 785 nm were plotted.

'Hayward' kiwifruit μ_a was different ($p < 0.01$) at 532 nm between batches, and μ_s' was different at both visible region (532 and 660 nm, $p < 0.0001$) and NIR region (785 nm, $p < 0.1$) between batches. In addition, μ_s' was different ($p < 0.1$) between $Fruit_{sound}$ and $Fruit_{BMSB}$ at 660 nm. For 'Hayward' kiwifruit (Figure 4.7), both μ_a and μ_s' were low at 660 nm likely due to chlorophyll absorption or low laser power output. At 532 and 785 nm, similar μ_a was observed for both $Fruit_{sound}$ and $Fruit_{BMSB}$. No difference of μ_a was found between $Fruit_{sound}$ and $Fruit_{BMSB}$ may be due to the lack of browning tissue or water soaking observed in BMSB damaged 'Hayward' kiwifruit. Lower μ_s' were observed for BMSB damaged 'Hayward' fruit, which may be due to that those fruit had lower FF. The quality attributes were significantly different (Table 4.3) between HF and IF in 'Hayward', but no difference was found in μ_s' at 785 nm. It is possible

that corky tissue in damaged fruit enhanced μ_s' and therefore counteracted μ_s' reduction from FF loss of those fruit, resulting in a similar μ_s' value compared to sound fruit.

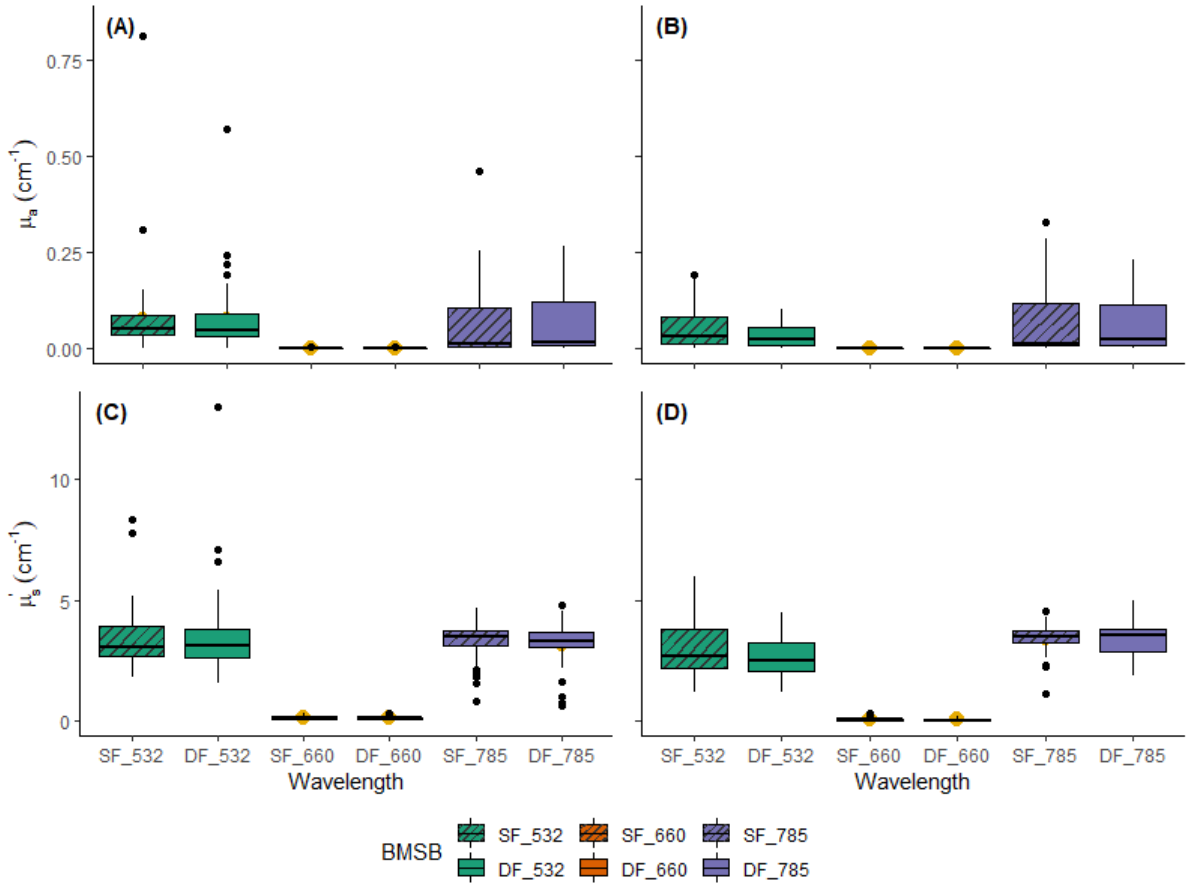

Figure 4.7. Estimated μ_a (A, B) and μ_s' (C, D) of 'Hayward' kiwifruit from batch 1 (A, C) and batch 2 (B, D). Sound fruit (SF) and BMSB damaged fruit (BF) optical properties at 532, 660 and 785 nm were plotted.

4.3.4 Segregation of BMSB damaged kiwifruit

The segregation model had an overall accuracy of 62 % for 'Hayward' and 84 % for 'Zesy002' (Table 4.4). However, the high accuracy for 'Zesy002' may be attributed by the large portion of sound kiwifruit. The unbalanced data tends to give higher overall accuracy statistically but tends to misclassify the minor group, which is often the group of interest. The kappa value can be used to assess the segregation performance for the minority group, for example, BMSB damaged kiwifruit. McHugh (2012) explained that 'Moderate' meant 35 – 63 % of the

segregation is agreeable. The kappa value for 'Zesy002' is 0.64 which is interpreted as 'Moderate' segregation performance.

Table 4.4. Kiwifruit BMSB segregation model performance using fruit sourced from different delivery batches.

Batches	TP	TN	Accuracy	Sensitivity	Precision	Kappa value
Zesy002						
1	82 %	77 %	0.79	0.82	0.70	0.57
2	94 %	87 %	0.89	0.95	0.66	0.70
Combined	86 %	83 %	0.84	0.86	0.68	0.64
Hayward						
1	57 %	61 %	0.66	0.57	0.57	0.16
2	52 %	78 %	0.84	0.52	0.66	0.31
Combined	55 %	68 %	0.62	0.55	0.61	0.24

A confusion matrix was created to display the segregation result using the pooled data from both batches (Table 4.5). In the 'Zesy002' segregation model, 14 % of $Fruit_{BMSB}$ were not identified (false negative, Table 4.5) which could potentially lead to advanced ripening of other sound fruit if stored in the same tray for extended periods of time. Whilst for 'Hayward', the kappa value is only 0.24 with 45 % $Fruit_{BMSB}$ being misclassified as $Fruit_{sound}$. Hence, the segregation model had a poor performance in identifying BMSB damaged fruit for 'Hayward'.

Table 4.5. Kiwifruit BMSB damage detection confusion matrix. $Fruit_{sound}$ and $Fruit_{BMSB}$ were defined as kiwifruit without or with white corking from merged-batch observation.

Zesy002	Actual $Fruit_{BMSB}$	Actual $Fruit_{sound}$
Predicted $Fruit_{BMSB}$	51 (86 %)	24 (17 %)
Predicted $Fruit_{sound}$	8 (14 %)	115 (83 %)
Hayward	Actual $Fruit_{BMSB}$	Actual $Fruit_{sound}$
Predicted $Fruit_{BMSB}$	51 (55 %)	33 (32 %)
Predicted $Fruit_{sound}$	42 (45 %)	72 (68 %)

Moderate segregation performance for 'Zesy002' was observed for both batches, with the 2nd batch of 'Zesy002' having the best performance of 0.89 overall accuracy (Table 4.4). In the 2nd batch, a high Sensitivity of 0.89 but a low Precision of 0.66 were obtained, which may be due to less $Fruit_{BMSB}$ amount compared with $Fruit_{sound}$. The 'Hayward' segregation performance was relatively poor for both batches. Both batches of 'Hayward' presented a low Sensitivity with

0.57 and 0.52, and in those batches 43 % and 48 % of damaged kiwifruit were segregated as sound fruit. Those incorrectly segregated BMSB damaged kiwifruit could potentially lead to advanced ripening for sound kiwifruit. Additionally, a low Precision was also observed of 0.57 and 0.66, resulting in 61 % and 78 % of sound fruit were correctly segregated, the rest of the sound kiwifruit were incorrectly segregated.

4.3.5 Overall discussion

In this study, kiwifruit LBI data was influenced by both BMSB damage and fruit ripening. The changes in quality attributes in this trial, such as ME, FF and SSC, indicate that kiwifruit physical properties and chemical compositions changed during ripening or damage development. Since kiwifruit optical properties extracted from LBI attenuation profiles are theoretically related to fruit physical properties and chemical compositions, thus these changes may also influence the LBI data.

Since the obvious difference in the pigment contents wouldn't be measurable at 785 nm (Figure 2.5), this wavelength may provide mainly information on the scattering properties of the fruit. However, the difference between μ_s' of 'Zesy002' and 'Hayward' in the present study is complicated by the different ripening stages (Table 4.1, Table 4.2 and Table 4.3). Several reasons may influence μ_s' in different ways. Lower FF resulted from advanced ripening and BMSB damage may reduce μ_s', whereas symptoms of corky tissue may influence μ_s' differently.

For both cultivars, μ_a ('Zesy002': 0.01 – 0.3 cm^{-1}; 'Hayward': 0.06 – 1.4 cm^{-1}) was found to be similar or slightly lower than values obtained in previous research using hyperspectral backscattering methods [Qin & Lu, 2008, (0.6 cm^{-1}, 500-1000 nm); Liu et al., 2019, (0.22 cm^{-1}, 950-1650 nm)], time resolved methods [Cubeddu et al., 2001, (0.29 cm^{-1}, 650-1000 nm)], or

single integrating sphere systems [Fang et al., 2016, (below 0.05 cm^{-1}, 632 nm)]. The observed difference could be due to different ripening stages or fruit surface and subsurface structures between crops and/or cultivars.

The μ_s' found in the current study ('Zesy002': 0.02 – 4.9 cm^{-1}; 'Hayward': 0.09 – 3.3 cm^{-1}) was lower than the ranges between 1 – 40 cm^{-1} reported in most publications (Cubeddu et al., 2001; Qin & Lu, 2008; Liu et al., 2019). One possible reason for the difference in kiwifruit μ_s' may be using different optical systems, and there is no standard validation method to compare results obtained from those different systems.

Although the BMSB damaged kiwifruit segregation model for 'Zesy002' had a moderate overall accuracy, it is not clear whether the segregation of $Fruit_{sound}$ and $Fruit_{BMSB}$ was influenced by the difference in kiwifruit quality between these fruit or it was because of textural changes (water soaking) resulting from BMSB damage. Therefore, further research is required to study 'Zesy002' kiwifruit with uniform quality to validate the usefulness of LBI technique for BMSB damage detection.

The poor performance of BMSB damaged fruit segregation for 'Hayward' may be due to two factors. Firstly, 'Hayward' kiwifruit surfaces are hairier, leading to increased diffuse reflection and affecting the LBI data quality. Secondly, 'Hayward' kiwifruit were at lower ripeness with less severe damage, which indicated that early-stage BMSB damage was difficult to identify with the current image process protocol.

Validation of estimated kiwifruit μ_a and μ_s' is required as estimation error is potentially involved. Although kiwifruit μ_a and μ_s' range could be classified into 9 provided classes by solid phantoms, it mainly falls into 4 classes with a range of μ_a (cm^{-1}) $\in$ [0, 1.2] and μ_s' (cm^{-1}) $\in$ [0, 10]. In addition, estimated μ_a and μ_s' were close inside each class thus a specific range of μ_a

and μ_s' with finer class could potentially enhance the accuracy of estimated μ_a and μ_s'. Moreover, LBI can only assess a limited area of tissue, leading to a bias to estimate the whole fruit condition. In the current trial, LBI data was taken from the equatorial region of the fruit, thus, LBI could only capture the damage when severe enough to affect the equator of the kiwifruit.

Based on visual assessment, the white corky spots caused by BMSB feeding mostly occur near the proximal end, possibly due to the natural feeding habit of BMSB. In this work, the segregation model included all the fruit, even though symptoms may not be present in the equatorial region for some of those fruit. Thus, the optical properties of the tissue in the proximal end may provide better information relating to BMSB damage. However, the curvature at the stem end currently limits LBI acquisition.

4.4 Conclusion

In this Chapter, kiwifruit optical properties of μ_a and μ_s' were extracted using LBI technology with the pre-classification approach. Estimated μ_a and μ_s' were utilized for the segregation of BMSB damaged kiwifruit and sound kiwifruit. The results showed BMSB damaged kiwifruit had lower μ_s'. On the other hand, BMSB damaged kiwifruit had higher RR and lower FF, which may also influence μ_s'. Therefore, the current results cannot confirm whether BMSB damage is detectable by the LBI technology because of the significant differences in fruit quality between sound and BMSB damaged fruit. The non-destructive LBI technique with the Metamodel approach can separate μ_a and μ_s' using pre-classification derived from solid phantoms with parameters extracted from LBI attenuation. In the next chapter, a specific range of μ_a and μ_s' built through liquid phantoms (Section 3.4) was utilized for kiwifruit CI detection.

Chapter 5 Improved pre-classification method for kiwifruit absorption and reduced scattering coefficients estimation: a case study of kiwifruit with chilling injury

5.1 Introduction

Optical techniques have been demonstrated to identify fruit with CI non-destructively and have potential for applications in the industry. In particular, NIR spectroscopy and HSI have been applied previously to detect CI in fruits and vegetables (Walsh et al., 2020) and widely investigated for evaluating quality attributes of horticultural products (Lu et al., 2020). Wang et al. (2020) used NIR spectral information to segregate sound kiwifruit and kiwifruit with CI and reported a stronger separation when spectral data were collected at the stylar end (proximal region) than in the equatorial region. Kemsley et al. (2008) investigated NIR diffuse optical tomography at 689 nm, and Garhwal et al. (2020) investigated hyperspectral imaging in the 550 nm–1700 nm range, and reported its possibility for internal defect detection in potatoes. Hyperspectral imaging at selected wavelengths was used for CI detection in apples, obtaining 98.4 % overall classification accuracy (ElMasry et al., 2009). Cen et al. (2016) utilized an HSI system with selected wavelengths and image features to detect CI symptoms of brown spots in cucumber and achieved 100 % classification accuracy for a two-class classification.

Previous Chapters discussed that estimated μ_a and μ_s' are related to fruit chemical composition and physical structure, thus fruit μ_a and μ_s' can be useful to detect changes in the scattering resulting from tissue granulation and in the absorption resulting from pigment changes. The change of μ_a in kiwifruit with CI may be due to kiwifruit discolouration, which is the oxidisation of polyphenolics causing enzymatic browning of tissue. Therefore, estimated μ_a at the wavelength of the carotenoid's absorption peak is likely to pick up the changes. With the NIR technology, Wang et al. (2020) utilized kiwifruit μ_a to segregate severe CI cases when the

external discolouration of skin had already occurred. However, the technology set-up is not suitable for the packhouse sorting line, and early detection of CI in kiwifruit was not achieved. On the other hand, the early stages of CI appear as granular tissue, which may affect μ_s' of the fruit. In this case, using LBI technology may be beneficial as it is potentially more sensitive at detecting changes in photon scattering resulting from tissue granulation. In the past, the LBI profiles have previously been applied to identify CI symptoms in bananas, and the reported LBI parameters were correlated with fruit quality parameters that could potentially indicate pigment changes due to CI (Hashim et al., 2013).

The changeling of using LBI technology for kiwifruit μ_a and μ_s' estimation is the estimation uncertainty of μ_a and μ_s' decoupling process. With the pre-classification approach, estimated kiwifruit optical properties mainly fall into 4 classes with a range of μ_a (cm^{-1}) ∈ [0, 1.2] and μ_s' (cm^{-1}) ∈ [0, 10] (Figure 4.6 and Figure 4.7). However, only 2 classes were provided in those ranges by solid phantoms (Table 3.2), therefore, a finer pre-classification model with more classes was proposed to enhance μ_a and μ_s' estimation accuracy. An improved pre-classification model (Table 3.3 and Figure 3.5) was applied to estimate kiwifruit μ_a and μ_s' and for a CI kiwifruit segregation case study. In addition, in BMSB damaged kiwifruit case study, LBI technology could not detect symptoms outside of the image area (Section 4.3.4). Thus LBI images captured from the stylar end were also analysed as CI symptoms usually develop from the stylar end tissue (Wang et al., 2020) before being visually observable on the skin. The information could be potentially useful for early-stage CI detection since the appearance of CI in the equatorial region only shows severe CI. The objectives of this chapter are to

(i) to estimate kiwifruit μ_a and μ_s' and

(ii) investigate whether optical properties estimated with the improved pre-classification could be used to distinguish sound kiwifruit and kiwifruit with CI symptoms.

5.2 Materials and Methods

5.2.1 Kiwifruit source

Cool stored 'Zesy002' kiwifruit (n = 396) were delivered to Massey University on August 14th, 2020, from 3 orchards after 20 weeks of storage in the packhouse at 1 °C (Table 5.1). Upon arrival, 'Zesy002' kiwifruit samples were stored at 1°C in a cool store room for 30 days and were subsequently measured after warming to 20°C overnight.

'Hayward' kiwifruit (n = 400) were harvested at 8 maturity stages from one commercial orchard from April 6th to June 1st 2020 at weekly intervals. Kiwifruit were stored at – 0.5 °C for 22 weeks to induce CI symptoms and delivered to Massey University weekly after storage. LBI data and CI symptoms were measured after fruit arrival at Massey University.

Table 5.1. Kiwifruit resource information.

	Sourcing orchards	Fruit number	Maturity stages	Storage temperature (°C)	Storage (Week)	Grade
Zesy002	3	396	1	1	20	Graded
Hayward	1	400	8	– 0.5	22	Ungraded

5.2.2 Kiwifruit image acquisition and quality measurement

Non-destructive LBI measurements were conducted at 520 nm, which is the absorption peak of carotenoids and can be useful for tissue discolouration detection. Each kiwifruit was placed longitudinally on the moving table. Kiwifruit LBI images were taken at 4 positions with 2 each (at 90° apart) on the equatorial and the stylar end region (1.5 cm from the end) (Figure 5.1). The 4 positions corresponded to the focus points of the laser pointer when imaging the samples.

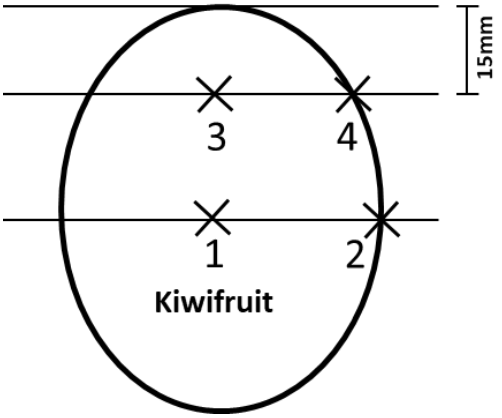

Figure 5.1. Kiwifruit assessment. Cross-marks of the laser pointer focus (3, 4 in the stylar end region; 1, 2 in the equatorial region), cut line to assess kiwifruit chilling injury.

LBI parameters were extracted from attenuations obtained at the stylar end (se; positions 3 and 4; Figure 5.1) and equatorial region (eq; positions 1 and 2; Figure 5.1), respectively, as well as from all images of the whole fruit (whole; mean of positions 1 – 4; Figure 5.1).

Kiwifruit fresh weight was measured using an electronic balance (TW423L, Shimadzu, Japan). The kiwifruit longitudinal profile (Eq. 5.1) describing shape was calculated using kiwifruit length, minor diameter and major diameter measured by a digital calliper (Olatunji et al., 2019).

$$LP = \left(\left[\frac{D_1 - \left(\frac{D_1}{exp(S) - 1} \times \left(exp\left(\frac{S \times L}{D_1}\right) - 1\right)\right)}{2 \cdot D_1}\right] + \left[\frac{\sqrt{{D_1}^2 - L^2}}{2 \cdot D_1}\right]\right) \times D_2 \qquad \text{Eq. 5.1}$$

Where LP is the kiwifruit longitudinal profile, L is half of the kiwifruit length, D_2 is half minor diameter, D_1 is half major diameter, and the shoulder coefficient S=7.

Kiwifruit FF was determined from penetration tests using a penetrometer (Willowbank Electronics Ltd., Napier, New Zealand) with a standard 7.9 mm diameter convex Effegi probe at a speed of 8 mm s^{-1} to 8 mm depth. Before the measurement, 1 mm of skin was removed at two equatorial positions (90° apart). Kiwifruit FF was recorded as the average of the two

readings. The SSC (%) of kiwifruit was measured by a refractometer (PR-32α, Atago, Japan) at 20 °C. Kiwifruit samples were cut in half at the equator, and juice extracted by hand from the stylar end half.

Kiwifruit samples were cut along the marked position at the stylar end (Figure 5.1) for manual observation of the CI severity. The CI assessment was carried out at the four locations matching the LBI measurement area. The severity score was obtained using a scale provided by Wang et al. (2020) and was recorded as CI_{se} and CI_{eq} for the stylar end and equatorial section of kiwifruit, respectively.

5.2.3 Data analysis

Kiwifruit LBI attenuations were analysed referring to Section 3.2.3. Optical properties of kiwifruit μ_a and μ_s' were estimated using LBI parameters with the improved pre-classification method (Section 3.4). The quantitative comparison of LBI parameters (DIP, Q1R, FWHM, Q3R, SLP) and kiwifruit optical properties (μ_a and μ_s') for samples with varying severity of CI symptoms was conducted using analysis of variance (ANOVA). Tukey's HSD test was applied to test the significance of the CI severity effect.

The kiwifruit CI severity segregation was initially conducted using a three-class segregation (Table 5.2). LBI image capturing area (Figure 5.1) and kiwifruit were segregated into Sound (free from CI symptoms), Moderate (CI symptoms of granulation but without water soaking) and Severe (CI symptoms of both granulation and water soaking) groups. Those groups correspond to Scale 1, Scale 2-3 and Scale 4-5 described by Wang et al. (2020). The segregation results of kiwifruit in each group used LBI parameters and estimated optical properties (μ_a and μ_s') at wavelengths of 532 nm as input parameters. In this segregation model, the model performance in segregating kiwifruit with early-stage CI symptoms may be represented by the Moderate CI

group, and then confirm whether LBI technology is feasible for segregating kiwifruit with early-stage CI symptoms.

Since the number of samples in each kiwifruit category is unbalanced, which may lead to further segregation uncertainties (Section 4.3.4), an analysis using subsampling of all the data sets was conducted. The segregation model was performed with the average result of 10 subsample sets to deal with the unbalanced population of Sound, Moderated CI and Severe CI samples (Table 5.2). Samples from each CI severity were chosen by selecting random seeds, resulting in the same number of each kiwifruit CI severity ($n_{Zesy002}$=36, $n_{Hayward}$=252). The segregation model performance of Sound, Moderate CI and Severe CI kiwifruit were validated with 'leave-one-out' cross-validation.

Table 5.2. Kiwifruit average flesh firmness (FF, N), total soluble solid content (SSC, %) longitudinal profile (LP, mm) and weight (g) at different CI severity. Sound means kiwifruit are free from chilling injury (CI) symptoms; Moderate means kiwifruit with CI symptoms of granulation but no water soaking; Severe means kiwifruit with both CI symptoms of granulation and water soaking.

CI severity	n	FF mean	FF sd	SSC mean	SSC sd	LP mean	LP sd	weight mean	weight sd
	Zesy002								
Sound	320	7.27[a]	1.28	15.79[a]	0.96	315.8	15.5	103.0[a]	6.78
Moderate	64	7.40[a]	1.00	14.22[b]	0.93	318.3	15.4	102.0[a]	6.76
Severe	12	8.53[b]	2.39	12.23[c]	1.35	316.8	18.7	97.8[b]	5.48
	Hayward								
Sound	137	11.90[a]	4.77	15.20[a]	0.99	285.4[a]	35.3	97.9[a]	17.1
Moderate	179	9.54[b]	4.86	15.00[a]	1.25	299.8[b]	40.8	104.0[b]	20.9
Severe	84	5.54[c]	1.69	14.60[b]	1.23	313.0[c]	45.3	111.1[c]	24.3

[1]*Different letter for each cultivar and response variable represents a significant difference by Tukey HSD ($p<0.05$).*

The results of the segregation model were presented via a confusion matrix and evaluated by overall Accuracy (Eq. 3.13), Precision (Eq. 3.14), Sensitivity (Eq. 3.15) and kappa value (Eq. 3.16). Additionally, F_1 was selected as a reliable indicator for unbalanced data sets. F_1 was calculated with performance metrics: Precision (P, Eq. 3.14) and Sensitivity (S, Eq. 3.15) as in Eq. 5.2.

$$F_1 = 2 \cdot \frac{P \cdot S}{P + S} \qquad \text{Eq. 5.2}$$

In the 3-class segregation model performance of Moderate CI fruit, TP were kiwifruit correctly segregated with Moderate CI, FP were kiwifruit mistakenly segregated Sound or Severe fruit, TN were kiwifruit correctly segregated as Sound and Severe, FN were kiwifruit mistakenly segregated Moderate CI fruit.

Besides, the 2-class segregation model was also investigated from an industrial applicability point of view. In the industry, Moderate kiwifruit can be acceptable in some conditions and as such, Sound and Moderate CI were grouped as Marketable fruit. Because of the large number of fruit in the Marketable group, data balancing was carried out by assigning the same number of Unmarketable to Marketable kiwifruit through sub-sampling whilst keeping the same ratio of Sound and Moderate fruit ('Zesy002' = 5:1, 'Hayward' = 4:5) in the Marketable group. 'Zesy002' was sourced from packhouse, and the ratio of Marketable and Unmarketable fruit was 384:12. Whilst 'Hayward' kept the ratio of the dataset with 316:84 for Marketable and Unmarketable fruit. In the 2-class segregation model of Unmarketable kiwifruit, TP were kiwifruit correctly segregated Unmarketable fruit, FP were kiwifruit mistakenly segregated Marketable fruit, TN were kiwifruit correctly segregated as Marketable fruit and FN were kiwifruit mistakenly segregated Unmarketable fruit.

5.3 Results and discussion

5.3.1 Kiwifruit quality in the 3-class segregation model

Kiwifruit with CI severities had different FF and SSC (Table 5.2). Sound and Moderate CI 'Zesy002" kiwifruit had lower FF (around 7.40 N) than Severe CI fruit (8.53 N), whilst FF was reduced for 'Hayward' kiwifruit with CI severity from 11.90 N (Sound) to 5.54 N (Severe). The

FF change of 'Hayward' is expected and can be explained by advanced ripening due to enhanced ethylene production caused by CI (Park et al., 2006) or the disintegration of cell structures and associated tissue damage as a result of CI (Bauchot et al., 1999). For 'Zesy002', kiwifruit with CI usually had a thick layer (around 5 mm) of corky tissue (Figure 5.2), which may increase fruit FF.

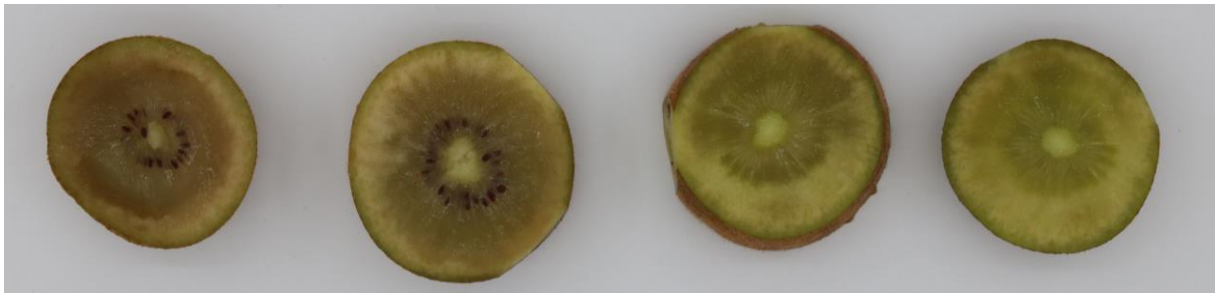

Figure 5.2. The symptoms of think layer tissue for 'Zesy002' kiwifruit with severe chilling injury

SSC of both cultivars decreased with increasing CI severity, and this may be due to Severe CI kiwifruit having a lower DMC and/or lower initial SSC. Kiwifruit with lower SSC at harvest tend to be more susceptible to CI (Burdon, et al., 2014), thus the at-harvest SSC and DMC need to be studied in the future study.

Moreover, shape and size differences may influence LBI parameter extraction. A longitudinal profile (LP) describing the shape difference and weight describing size were observed for different CI categories for kiwifruit (Table 5.2). 'Hayward' kiwifruit was ungraded and could have various CI susceptibilities due to size differences. Kiwifruit with a higher longitudinal profile and larger weight may have a higher susceptibility to CI. In general, the least advanced kiwifruit at harvest tend to be smaller fruit and are more susceptible to CI (Burdon et al., 2014), which agrees with 'Zesy002' weight but does not 'Hayward' LP and weight results in Table 5.2. This finding may be due to the CI of 'Hayward' being incurred at – 0.5 °C while 'Zesy002' being at 1 °C, and freeze injury may occur at – 0.5 °C. Larger fruit may be more sensitive to freeze injury at lower temperature, however, further studies are needed to confirm this assumption.

5.3.2 Kiwifruit LBI parameters in the 3-class segregation model

When comparing LBI parameters, Q1R (Figure 5.3B), FWHM (Figure 5.3C) and Q3R (Figure 5.3D) were lower in 'Zesy002' kiwifruit with severe CI. This was found regardless of the acquisition position of the LBI on the fruit. Even though CI symptoms developed from at the stylar end, the position of LBI measurement hardly showed any effect on the differences of LBI parameters except DIP (Figure 5.3A). 'Zesy002' SLP (Figure 5.3E) was different among all 3 CI severity classes, suggesting that SLP could be useful for segregating kiwifruit according to the CI severity. This assumption is supported by the differences in LBI profiles and corresponding LBI parameters (Figure 3.7) due to changes in optical properties.

For 'Hayward' kiwifruit, similar results were observed with differences found in DIP (Figure 5.4A), FWHM (Figure 5.4C) and Q3R (Figure 5.4D) and Severe CI 'Hayward' kiwifruit had a lower DIP, FWHM and Q3R regardless position, which may be applied to segregate kiwifruit based on CI categories. It's possible that DIP, FWHM and Q3R were correlated with FF, as CI kiwifruit had a lower FF. Unlike 'Zesy002', SLP was similar among different CI severities for 'Hayward' kiwifruit stylar end region (Figure 5.4A), while Severe CI kiwifruit had higher SLP at the equatorial region and for whole fruit. The SLP result for Hayward (Figure 5.4D) was the opposite for 'Zesy002 '(Figure 5.3D), that Severe CI 'Hayward' had a higher SLP while 'Zesy002' had a lower value. It's possible that SLP was correlated with maturity or FF (Table 5.2), as 'Hayward' had 8 maturity stages and kiwifruit with severe CI had lower FF, while 'Zesy002' only had one maturity and Severe CI fruit had the highest FF due to corky tissue.

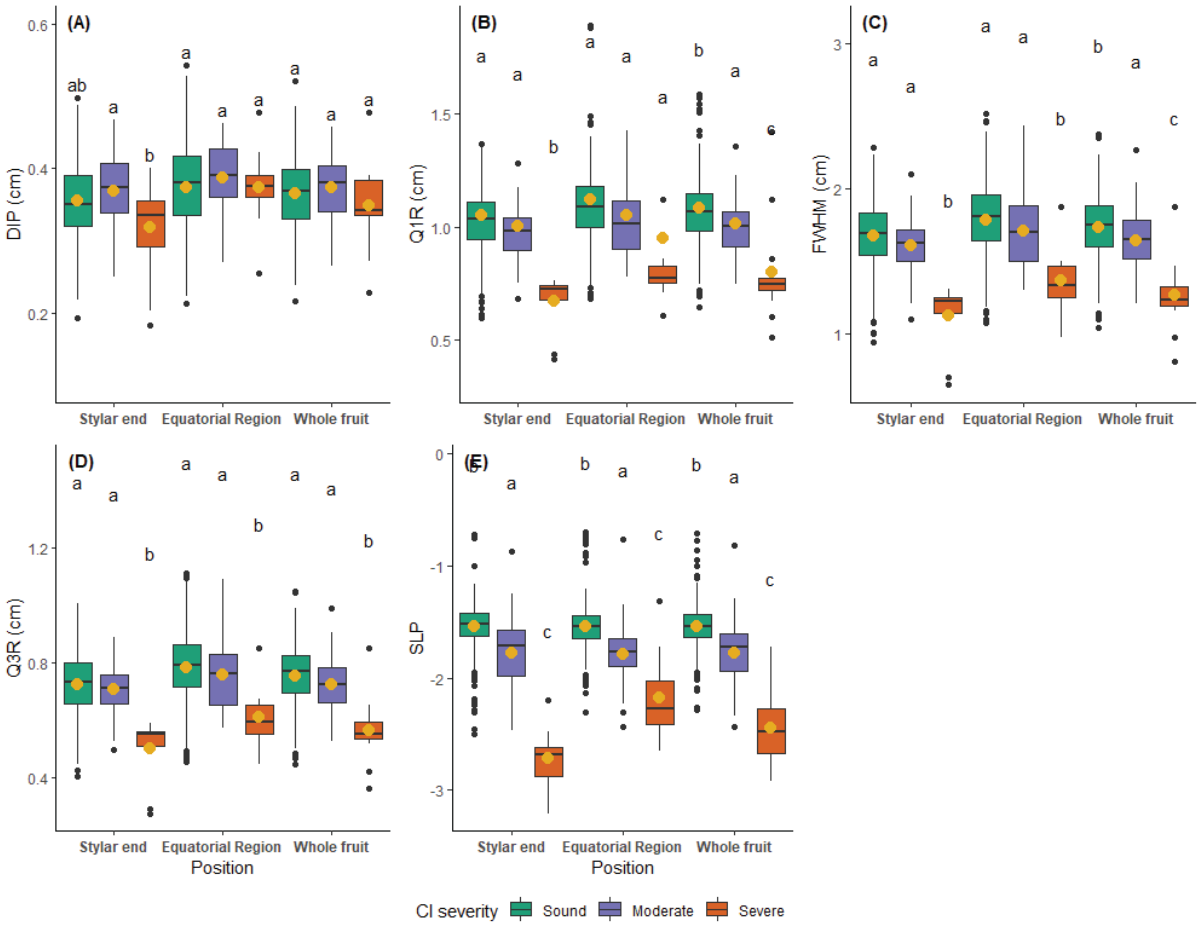

Figure 5.3. 'Zesy002' kiwifruit LBI profile parameters for chilling injury (CI) segregation in stored kiwifruit. Green, purple and orange boxes represent CI severities of sound (free from CI symptoms), moderate (CI symptoms of granulation but no water soaking) and severe (both CI symptoms of granulation and water soaking) kiwifruit. Letters represent a significant difference between three CI severities by Tukey HSD (p-value < 0.05) using LBI taken from two locations or whole fruit. Yellow points represent mean values. LBI parameters were the radius of the saturated area (DIP), the radius at 75 % of maximum intensity (Q1R), double the radius at 50 % of maximum intensity (FWHM), the radius at 25 % of maximum intensity (Q3R), and the slope of the linear regression model (SLP) built with log-transformed profile data between Q1R and Q3R.

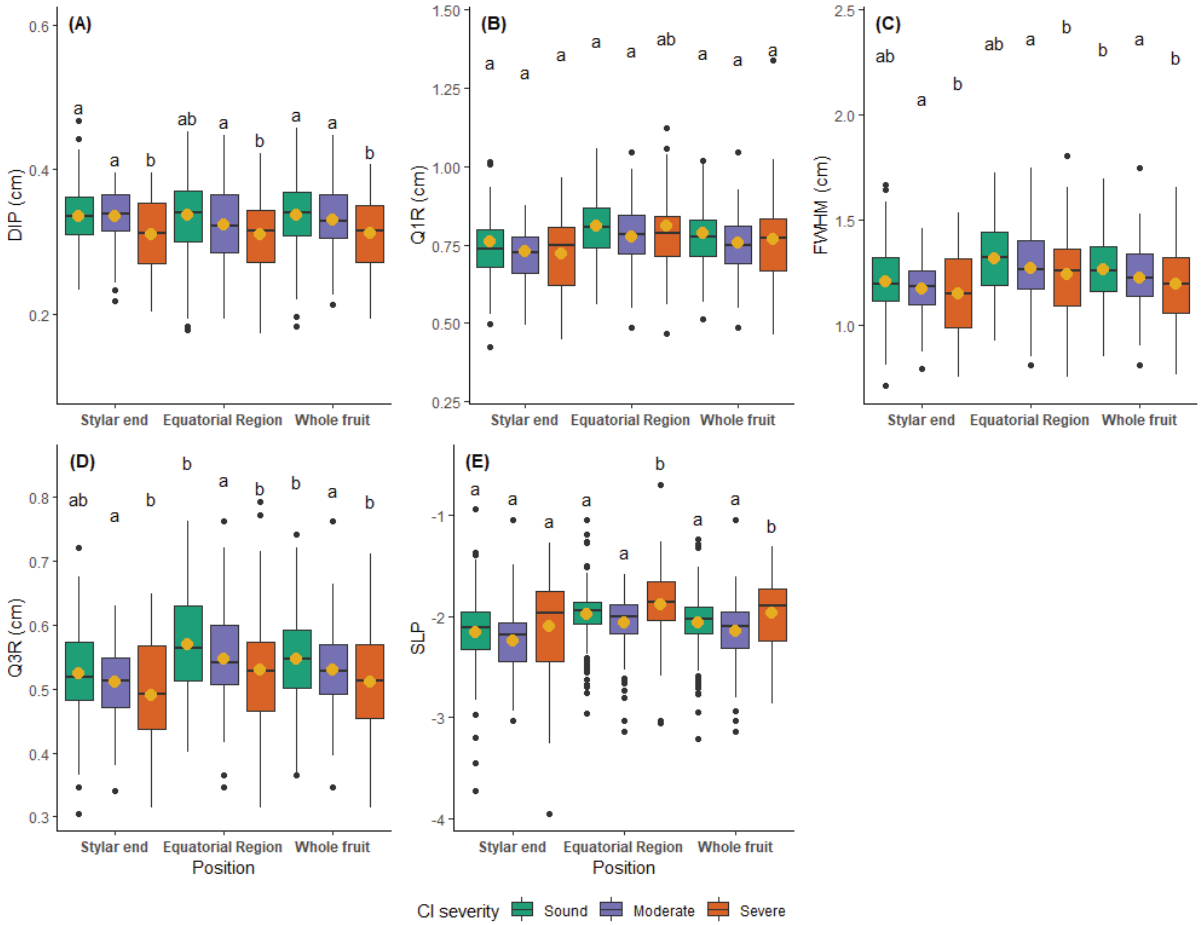

Figure 5.4. 'Hayward' *kiwifruit LBI profile parameters for chilling injury (CI) segregation in stored kiwifruit. Green, purple and orange boxes represent CI severities of sound (free from CI symptoms), moderate (CI symptoms of granulation but no water soaking) and severe (both CI symptoms of granulation and water soaking) kiwifruit. Letters represent a significant difference between three CI severities by Tukey HSD (p-value < 0.05) using LBI taken from two locations or whole fruit. Yellow points represent mean values. LBI parameters were the radius of the saturated area (DIP), the radius at 75 % of maximum intensity (Q1R), double the radius at 50 % of maximum intensity (FWHM), the radius at 25 % of maximum intensity (Q3R), and the slope of the linear regression model (SLP) built with log-transformed profile data between Q1R and Q3R.*

'Zesy002' DIP (Figure 5.3A) of kiwifruit with Severe CI was lower at the stylar end region, this may be due to CI symptoms developed from the stylar end, thus DIP was more sensitive in this region. While at the equatorial region, DIP remained constant for all CI severities and resulted in similar DIP of whole fruit regardless of CI severity. This assumption didn't include shape effects because DIP has the least influence by shape as DIP describes the saturated area of the LBI image, and other parameters describe the attenuation area. The light attenuation may be

stopped by limited path travel length, while the saturated area radius is within 1.5 cm thus (Figure 5.5).

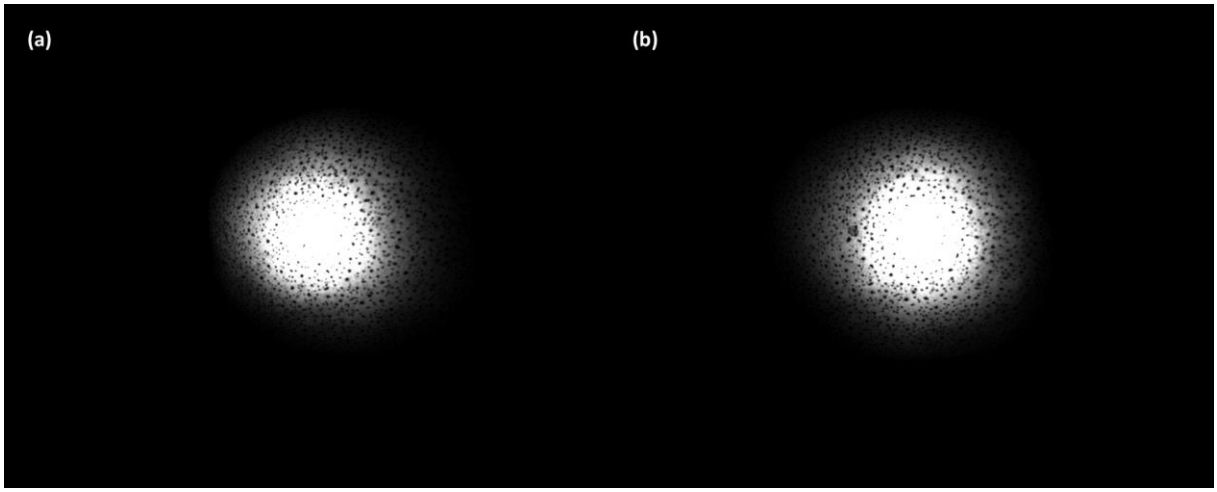

*Figure 5.5. 'Zesy002' kiwifruit LBI image (a). at the stylar end region, (b). at the equatorial region. The image size is 130.04 * 104.04 (mm^2)*

5.3.3 Kiwifruit optical properties estimation in the 3-class segregation model

The estimated μ_a of kiwifruit was between 0.01 – 1 cm$^{-1,}$ and μ_s' was between 0.01 – 3.5 cm^{-1}, which was within the ranges provided by phantoms (Figure 3.5 and Table 3.3). However, a large standard deviation was observed for estimated μ_a and low μ_s' was observed for both cultivars, the comparison with values in other literature will be discussed in Table 5.5

Higher average μ_a was observed for Severe CI 'Zesy002' kiwifruit regardless of position (Figure 5.6A). The higher μ_a for kiwifruit with severe CI is possibly due to CI symptoms of discolouration. Flesh discolouration in the outer pericarp region near the stylar end can be observed when CI symptoms are severe (Wang et al., 2020). Different μ_s' were observed for Sound and Severe CI fruit with Moderate CI for 'Zesy002' at the stylar end or considering the whole fruit (Figure 5.6B). The difference between Sound and Moderate CI kiwifruit might be due to enhanced μ_s' caused by the granulated tissue (Wang et al., 2021). For 'Zesy002' kiwifruit, enhanced estimated μ_s' of Severe CI may result from the high μ_a, which might increase μ_s' during estimation uncertainty.

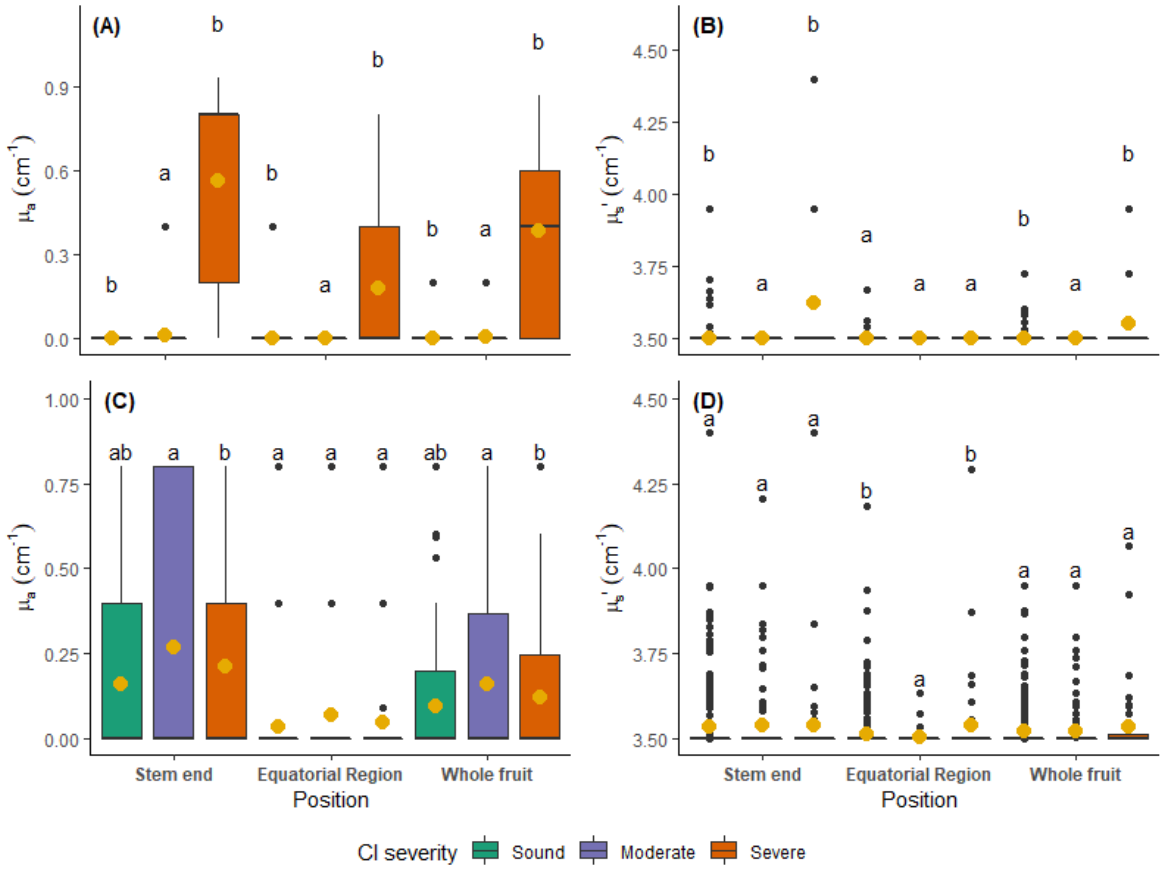

Figure 5.6. 'Zesy002' kiwifruit LBI μ_a (A) and μ_s'(B) and 'Hayward' kiwifruit LBI μ_a (C) and μ_s'(D) for chilling injuries segregation in stored kiwifruit. Green, purple and orange boxes represent CI severities of sound (free from CI symptoms), moderate (CI symptoms of granulation but no water soaking) and severe (both CI symptoms of granulation and water soaking) kiwifruit. Letters represent a significant difference between three CI severities by Tukey HSD (p-value < 0.05) using LBI taken from two locations or whole fruit. Yellow points represent mean values.

On the other hand, higher μ_a was observed for Moderate CI 'Hayward' kiwifruit (Figure 5.6C). Estimated μ_a was different when measuring the stylar end or considering the whole fruit with estimated μ_a measured at the equatorial region for 'Hayward' (Figure 5.6C), this may be due to CI symptoms developed from the stylar end. However, for 'Hayward' kiwifruit, observed CI symptoms in this study don't involve pigment changes in the skin, which influence absorption results at the selected wavelength of 520 nm. The difference of $\mu_s'$was observed for 'Hayward' at the equatorial region (Figure 5.6D). For 'Hayward' kiwifruit, enhanced estimated μ_s' of kiwifruit with Severe CI was observed at the equatorial region (Figure 5.6d). However, it cannot be confirmed whether the segregation of predicted μ_s' was due to corky tissue and water

soaking development around the equator or a difference in FF, which was also measured around the equator. Alternatively, the difference in μ_a could result from estimation uncertainty and be influenced by quality differences (Table 5.2), resulting in variously estimated μ_s'. Although kiwifruit FF was lowest for Severe CI kiwifruit, those kiwifruit had water soaking symptoms, which may also influence μ_s' except FF. For kiwifruit without water soaking, quality differences due to lower FF may result in higher μ_a of Moderate CI kiwifruit in comparison with Sound kiwifruit (Figure 5.6C).

5.3.4 Segregation of kiwifruit with chilling injury in the 3-class segregation model

'Zesy002' kiwifruit had a moderate segregation accuracy for subsampled Sound fruit (82 %) and Moderate CI fruit (71 %), and a high segregation accuracy for Severe CI fruit (94 %) using LBI parameters using stylar end data (Table 5.3). For fruit with CI, a higher segregation accuracy was obtained using LBI taken at the stylar end region compared to images acquired at the equatorial region (Moderate: 71 to 53 %; Severe: 94 to 82 %). However, segregation accuracy was around 82 % regardless of LBI acquired position. This is possible because the kiwifruit stylar end is the location of initial CI development (Wang et al., 2020), and some Moderate CI kiwifruit had no symptoms in the equatorial region. It's also supported by higher overall accuracy (82 %) of Severe CI using equatorial data since CI symptoms were likely spread into the equatorial region of a Severe CI fruit. The segregation accuracy of Sound and Moderate CI kiwifruit was slightly improved by using whole fruit LBI parameter information acquired from both locations (from 82 to 83 %, from 71 to 75 %, respectively). In contrast, the overall accuracy of Sever CI kiwifruit slightly decreased when whole fruit LBI was used. It's possible that LBI data at the stylar end was most useful for CI detection.

Table 5.3. Segregation accuracy (%) of kiwifruit chilling injury severity using LBI parameters and optical properties after subsampling to avoid an unbalanced data set with the same number of kiwifruit in each CI category.

	LBI parameter			μ_a and μ_s'		
	Sound	Moderate	Severe	Sound	Moderate	Severe
Zesy002	n=12	n=12	n=12	n=12	n=12	n=12
Stylar end	82	71	94	100	0	76
Equatorial region	82	53	82	100	0	18
Whole fruit	83	75	92	100	0	75
Hayward	n=84	n=84	n=84	n=84	n=84	n=84
Stylar end	49	47	61	76	43	1
Equatorial region	46	42	57	95	8	12
Whole fruit	52	36	58	70	21	35

Using μ_a and μ_s' as input parameters, the segregation model overall accuracy was improved (100 %) for Sound 'Zesy002' fruit regardless of LBI position, although this was largely attributed to the complete misclassification of Moderate CI fruit (accuracy = 0%). In the current segregation method for 'Zesy002', discolouration symptom is not included in Moderate kiwifruit, thus μ_a obtained at 520 nm may not be able to separate Sound and Moderate kiwifruit, resulting in the model incorrectly segregating all Moderate CI fruit as Sound fruit. On the other hand, the accuracy decreased to around 75 % for Severe CI using whole fruit images. The low accuracy of Severe CI 'Zesy002' kiwifruit segregation using equatorial region obtained optical properties may be because granular tissue was not detectable when water soaking symptoms exit, thus, Sound and Severe CI fruit had similar optical properties and resulting segregation error.

Poorer segregation accuracy was observed for 'Hayward' kiwifruit compared with 'Zesy002' (Table 5.3). Using LBI parameters, the overall accuracy of Sound and Moderate CI fruit were below 50 % and around 60 % for Severe CI fruit regardless of image positions (Table 5.3). This could be due to 'Hayward' kiwifruit being ungraded and thus possessing a large variance in size and shape which influenced the LBI profile. In addition, kiwifruit senescence was observed for

'Hayward', which may also have the water soaking symptom. Thus, segregation of Severe CI fruit may be influence by kiwifruit with senescence. Furthermore, 'Hayward' kiwifruit trichomes could potentially affect the analysis of the diffusion profile.

The segregation model's overall accuracy was improved using estimated μ_a and μ_s' at both the stylar end (76 %) and equatorial region (95 %) for Sound kiwifruit (Table 5.3). However, the improved overall accuracy was contributed by incorrectly segregating Severe CI fruit into the Sound ones since no difference in optical properties was observed for those two severities (Figure 5.6C,D). The accuracy was similar for Moderate CI fruit using μ_a and μ_s' as input parameters using the stylar end data only. However, the model had a bias of segregating CI fruit (Moderate and Severe) as Sound using equatorial or whole fruit data. In CI severity detection, μ_s' was expected to be correlated with the presence of granular tissue, which is the main symptom differentiating Moderate CI and Sound kiwifruit. However, the water soaking symptoms may influence μ_s' differently, as a result, Severe CI fruit were incorrectly segregated as Sound.

5.3.5 Segregation of kiwifruit with chilling injury in the 2-class segregation model

'Zesy002' had a 92 % and 75 % (Table 5.4) TP rate using LBI parameter and optical properties, respectively, using the whole sample population in this study, which has Marketable and Unmarketable fruit ratio at 32:1 (n = 396). The good model performance for 'Zesy002' can be explained by the symptoms of skin discolouration and water soaking of severe CI. These changes in kiwifruit tissue influenced μ_a (Figure 5.3; Figure 5.6A).

Table 5.4. Segregation of true positive accuracy (%) of kiwifruit chilling injury severity using all fruit LBI data without subsampling. F_1 score is the prediction performance indication for severe CI kiwifruit of the unbalanced dataset.

	Marketable	Unmarketable	F_1 score
Zesy002	n = 384	n = 12	
LBI parameters	98	92	0.73
μ_a and μ_s'	99	75	0.72
Hayward	n = 316	n = 84	
LBI parameters	97	39	0.53
μ_a and μ_s'	100	5	0.09

For 'Hayward', using the original population (ratio of Marketable and Unmarketable fruit = 3.65:1; n=400), only a 39 % TP rate was obtained using LBI parameters and 5 % using μ_a and μ_s' (Table 5.4) to segregate Unmarketable kiwifruit. The poor model performance for 'Hayward' was expected as LBI data were insensitive to CI severity with water soaking symptoms and optical property estimation uncertainty (Figure 5.4; Figure 5.6CD).

5.3.6 Overall discussion of kiwifruit optical property estimation

The observed variation in Figure 5.6 might be due to the small predefined μ_a and μ_s' range intervals of the liquid phantoms used for pre-classification, because many of the kiwifruit were predicted at the highest class after pre-classification despite many classes were provided. This result indicates a larger range of μ_a included in the pre-classification model doesn't improve the estimation accuracy. In addition, the low μ_s' in kiwifruit doesn't meet the assumption $\mu_a << \mu_s$' (Farrell et al., 1992), thus estimation of kiwifruit μ_a and μ_s' may be more challenging than other fruit with a higher μ_s', such as apple.

An under-sampling error could occur due to CI symptoms not always appearing in the LBI imaging area, which was also observed in BMSB damaged kiwifruit segregation (Section 4.3.5). The under-sampling error was hoped to be reduced by taking an average of images acquired at multiple locations around the fruit. In this case, LBI image was captured at the stylar end region. However, the kiwifruit shoulder's curvature also influences μ_a and μ_s' estimation (Figure 5.5).

Therefore, both CI symptoms and curvature could affect the difference in LBI image. Enhanced estimated μ_s' was observed for kiwifruit with CI at the equatorial region, but no difference was observed at the stylar end region (Figure 5.6c). It's possible that shape affected LBI results; thus, no difference in predicted μ_s' was observed. In the diffusion model described by Farrell et al. (1992), the influence of sample curvature is not considered. Peng and Lu (2006) calculated a sample size correction factor *sin*θ using spatially resolved diffuse reflectance images and found the corrected μ_s' would be less comparable with the estimated value because *sin*θ < 1. Therefore, the actual μ_s' should be lower than the estimated μ_s' at the stylar end. Since 'Zesy002' kiwifruit were graded and have greater consistency in shape and quality parameters (Table 5.2), the difference in estimated μ_s' was assumed to be more related to the corky tissue or water-soaked tissue as these CI symptoms usually develop from the stylar end region (Wang et al., 2020).

In this study, higher μ_a at 520 nm was observed for Severe CI 'Zesy002' (Figure 5.6) due to the absorption peak of carotenoids in the fruit at 520 nm from enzymatic browning tissue (Ou-Yang et al., 2004). Other useful wavelengths reported for kiwifruit flesh tissue are at 970 nm, 1190 nm and 1390 nm, and the correlation between estimated μ_a at those wavelengths and SSC reached 0.8 R^2 (Liu et al., 2019a). Unlike μ_a, which had absorption peaks for different chemical compositions, kiwifruit μ_s' steadily decreased (Cubeddu et al., 2001; Qin & Lu, 2008). Hence, the fruit quality estimation is more reliable using μ_s' when using selected wavelengths in an LBI system. In Table 5.5, estimated kiwifruit μ_a and μ_s' have been presented. The estimated μ_a was in a similar range compared to other studies, while μ_s' was in a much lower range. Lower values of μ_s' may be due to kiwifruit in this study having a lower FF after 20 – 22 weeks of storage. The lower μ_s' resulted in lower μ_a due to the estimation uncertainty. Estimated kiwifruit μ_a and μ_s' can be affected by multiple factors.

Table 5.5. Optical properties of kiwifruit measured at various wavelength ranges.

Cultivar	Hayward	Unknown	Huayou	Hayward/Zesy002
Method	Time-resolved reflectance	Spatially resolved hyperspectral	Inverse adding doubling	Laser backscattering imaging
Wavelength (nm)	650 - 1000	500 - 1000	900-1700	520 nm
Sample	Intact	Intact	Flesh without skin (4 mm)	Intact
μ_a (cm^{-1})	0.55 – 0.44	0.2 – 1.1	0 – 3	0.01 – 1
μ_s'(cm^{-1})	13 – 16	7 – 8	6 – 16	0.01 –3.5
Reference	(Cubeddu et al., 2001)	(Qin & Lu, 2008)	(Liu et al., 2019a)	Section 5.3.3

Firstly, estimated kiwifruit μ_a and μ_s' can be influenced by internal disorders. A lower transmitted signal intensity of 'Zesy002' was observed for fruit with CI when using a dual-laser system (Wang et al., 2020). Besides, a larger variation of μ_a and μ_s' was reported in kiwifruit skin compared with kiwifruit flesh (Fang et al., 2016; Liu et al., 2019a) due to multiple layers of the structure. Higher μ_s' and lower μ_a at 632.8 nm were observed for kiwifruit flesh (3.8 and 1.17 cm^{-1}) compared to kiwifruit locules (1.2 and 3.08 cm^{-1}) due to different pigment contents and microstructure (Fang et al., 2016). In addition, quality changes affect optical properties. Decreased μ_s' was observed during fruit storage; during this time, FF also decreased (Ma et al., 2020), which may be due to changes in fruit flesh structure. Moreover, pigment absorption due to flesh colour also affects optical properties. The peak of green fleshed kiwifruit μ_a was reported at 675 nm, which was the peak absorption of chlorophyll, and kiwifruit μ_s' had lower accuracy within 650 – 750 nm due to high μ_a (Cubeddu et al., 2001; Qin & Lu, 2008).

In the previous chapter, the water soaking symptom of kiwifruit with BMSB injury could be detected by short-wave NIR wavelengths (785 nm). An additional set of fruit with severe soaking symptoms were studied with LBI at 830 nm. In Figure 5.7, an increased diffusion area and a reduction in saturation were observed in water-soaked fruit compared to sound-soft

fruit. In this study, 520 nm was found to provide information on tissue discolouration due to CI symptoms. Therefore, a combination of 520 and 830 nm could be useful for segregating Moderate CI fruit from Severe CI fruit.

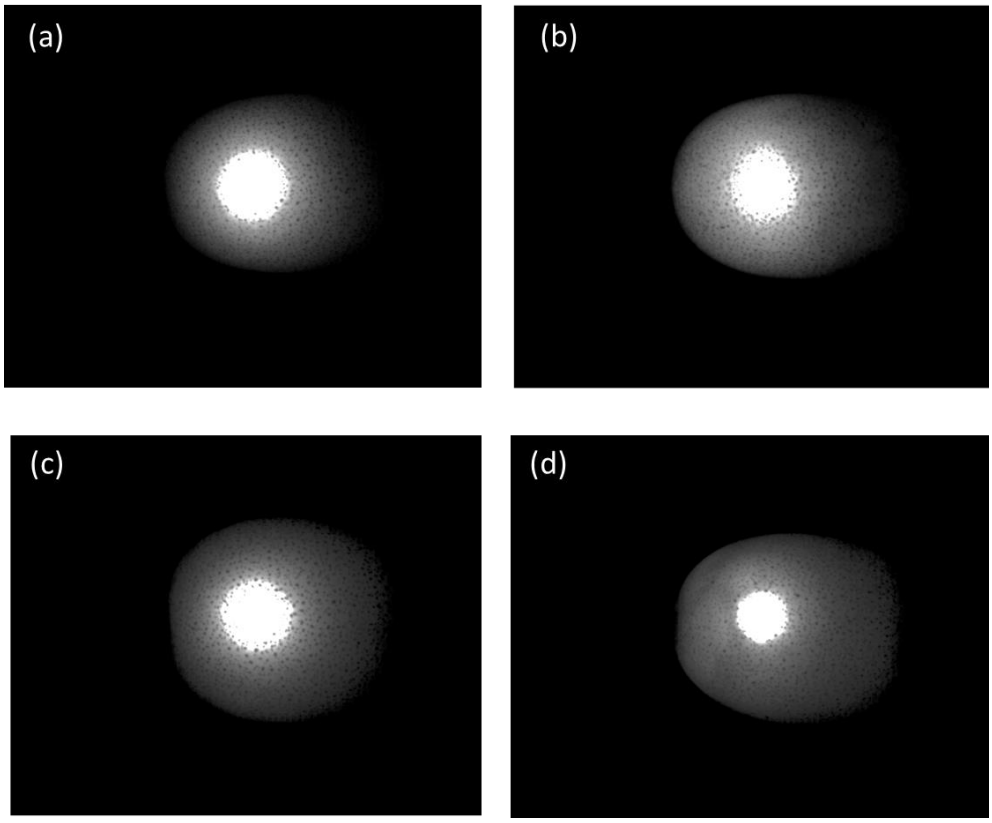

*Figure 5.7. Raw LBI (830 nm) of 'Zesy002' kiwifruit with different water soaking related symptoms as (a) soft (b) freezing injury (c) water patch and (d) water soaking from chilling injury. The image size is 130.04 * 104.04 (mm^2).*

5.4 Conclusion

This study demonstrates that LBI techniques provide a potential non-destructive method for the detection of CI symptoms in kiwifruit. The severity of CI could be segregated using optical properties of the fruit (μ_a and μ_s') for 'Zesy002'. However, whether optical properties could separate CI 'Hayward' required additional study with the same maturity stages. The improved classification method still has limitations, and the developed liquid phantoms could not represent kiwifruit as a simple turbid media, where kiwifruit processes more complicated optical profiles. Since better model performance was observed using LBI parameters (DIP,

FWHM, Q1R, Q3R and SLP) rather than μ_a and μ_s', LBI parameters are potentially useful to describe kiwifruit quality changes. The next chapter will present the study of kiwifruit LBI parameters through ripening.

Chapter 6 Understanding changes in laser backscattering imaging parameters through the kiwifruit softening process using time series analysis

6.1 Introduction

A three-phase softening curve (Figure 2.1) has been reported for kiwifruit ripening, including a relatively stable initial lag phase, then a rapid exponential decline to 20-30 N, followed by a slow FF loss to eating ripeness (Hewett et al., 1999). The softening rate in the 2nd phase and length of the 1st phase may be influenced by multiple factors, including temperature, storage time, environment ethylene concentration and maturity (Ritenour et al., 1999; Jabbar & East, 2016; Burdon et al., 2017). Several mechanistic models have been reported to quantify the kiwifruit FF softening trend. Hertog et al. (2016) developed a softening model that considers enzyme processes related to the kiwifruit physiology of cell wall breakdown and ripening. The model had good performance and explained 97 % of the data variation in FF. However, this model has a limitation to be applied to industrial practice because the at-harvest FF of each kiwifruit had to be acquired non-destructively using compression firmness.

In previous chapters, large variations were observed from estimated μ_a and μ_s' of kiwifruit (Figure 4.6, Figure 4.7, Figure 5.6), given that kiwifruit is a complex biological matrix compared with homogenous optical phantoms. These estimation errors of μ_a and μ_s' further introduce segregation uncertainties in identifying kiwifruit with BMSB damage (Section 4.3.4) or with CI (Section 5.3.4) from sound ones. As a result, estimation uncertainty of optical properties would be a potential issue for using μ_s' to predict FF. Alternatively, LBI parameters derived directly from the attenuation profile are feasible in identifying kiwifruit with CI without estimated μ_a and μ_s' (Table 5.3). In particular, DIP and SLP in Figure 5.4 showed differences in 'Hayward' Sound and Severe CI fruit, where quality was the main influence of LBI parameters. Therefore,

LBI parameters could potentially be utilized for FF estimation. To minimise the influence on LBI parameters due to pigment absorption in kiwifruit flesh colour (Figure 4.6, Figure 4.7), the wavelength of 830 nm is considered appropriate to extract LBI parameters that are associated with FF.

Statistical analyses of LBI parameters could be useful to understand changes in optical properties. Time series analysis is a statistical method that builds a model to provide a plausible description of the observed data and facilitates trend forecasts on the sample development (Shumway & Stoffer, 2017). Time series analysis has been used in many fields (sales price, fights, customer numbers), but little work has been published in using the approach to predict fruit quality change. Weng et al. (2019) applied an AutoRegressive Integrated Moving Average (ARIMA) model to predict agricultural product sales price, and found it suitable to predict short periodical data rather than daily price estimation. Verroens et al. (2006) compared 4 time-series models to predict bell pepper cyclic production and found that utilizing fruit size and hardness at harvest reached a better yield prediction than using colour. González-Teruel et al. (2022) used a time series model to predict cherry tree water stress based on soil moisture and provided an on-day alert for farmers. Times series analysis has the potential to investigate the correlation of the data and decompose influencing factors into different parts, thus better interpreting the meaning of a data set.

This chapter aims at monitoring the changes in LBI parameters that are assumed to be associated with the softening of kiwifruit during shelf life ripening and attempts to use time series analysis methods for data interpretation. The specific objectives are to:

(i) describe changes in kiwifruit LBI parameters during shelf life ripening.

(ii) determine whether LBI parameters are useful for describing kiwifruit softening and

(iii) discuss possible kiwifruit quality changes associated with LBI parameters during ripening.

6.2 Materials and Methods

6.2.1 Fruit source

'Zesy002' and 'Hayward' kiwifruit were harvested from the Bay of Plenty region, New Zealand, in April and May 2021, respectively. Kiwifruit were graded and delivered to Massey University from commercial packhouses on 2nd and 27th May. The time-series study started on 31st May. Hence, 'Zesy002' were stored at 1 °C for 26 days before being taken out of cool storage on 30th May and warmed to room temperature (20 °C) overnight prior to the start of a shelf-life study. 'Hayward' were stored at 0 °C for 2 days with ripening starting simultaneously with 'Zesy002' after warming overnight. Fruit of uniform shape, and with no scar or sunburn observed on the surface were used.

6.2.2 Kiwifruit image and quality measurement

The LBI setup was consistent with that described in Chapter 3 (Section 3.2.2) using the laser emitting at 830 nm. Kiwifruit LBI were taken in the equatorial region at 2 positions, 90° apart (Figure 4.3).

The kiwifruit sample was segregated into 2 lots. Lot 1 kiwifruit were measured for the purpose of time series model development. Kiwifruit (n=30) were selected as 3 fruits from 10 grower lines (GL) for each cultivar. The LBI parameters of each individual fruit were monitored for 13.5 days at 12 h intervals, resulting in 27 LBI observations at 20 °C. The initial acoustic firmness (AF) of each kiwifruit was measured using AWETA AFS (AWETA International Ltd., Nootdrop, Holland) at fruit shoulders around both stem and blossom ends, and the average reading of AFs from two locations was recorded as kiwifruit AF.

Lot 2 kiwifruit (n=40) was used as a reference for monitoring FF changes. For Lot 2 fruit, 1 kiwifruit was selected per GL (n=10) for each cultivar on 4 measurement occasions, resulting in a total of 10 fruit on each measurement occasion. FF was then measured destructively after LBI acquisition using a penetrometer (Willowbank Electronics Ltd., New Zealand) with a standard 7.9 mm diameter convex Effegi probe at a speed of 8 mm s^{-1} to 8 mm depth. Kiwifruit FF was measured at 3-day intervals on days 1, 4, 7 and 10, representing the 1st, 7th, 13th and 19th LBI observation for Lot fruit.

Kiwifruit samples collected from lot 2 kiwifruit on day 1 and 10 were further subjected to microscopy following same methodology as described previously (Li et al. 2021). Kiwifruit tissue samples were collected in the light diffusion area and stored in standard FFA fixative (100 ml fresh fixative contained 53 ml 95% ethanol, 10 ml 37% formaldehyde and 5 ml glacial acetic acid) at a 5 °C chiller. A total of 20 kiwifruit samples per cultivar were fixed and processed. Kiwifruit samples were re-cut to fit and transferred to a wax embedding cassette The cassettes with kiwifruit sections were dehydrated with a Leica TP1020 Semi-enclosed Benchtop Tissue Processor (Leica Microscopy Systems Ltd., Heerbrugg, Switzerland) with the process of dehydration in ethanol holding solutions at 50 % (15 min), 70 % (3 h), 95 % (3 h), 100 % (3 h), 100 % (pure, 3 h) and 100 % (pure, 3 h). For the wax infiltration, sections were processed with pure ethanol and xylene (1:1, 3 h), xylene (3 h) and xylene (3 h). The section was processed automatically over 2.5 days. Kiwifruit sections were then transferred from the processing basket to the wax hold bath. The embedding process used 3.0 cm x 2.4 cm mould with a kiwifruit sample sitting in the middle using a Leica EG1160 paraffin dispensing system (Leica Biosystems, Heerbrugg, Switzerland). Kiwifruit sections were orientated with the outer pericarp side facing the short sides of the

embedding cassettes. Once the samples stable, they were stored at room temperature. Embedded samples were sectioned using a Leitz 1512 rotary microtome (Leitz, Germany) and a 0.25 mm disposable microtome steel blade. The wax sample were trimmed into a triangular shape first. The 15 µm sample were sectioned, placed in a 42 °C water bath (Leica HI1210, Leica Biosystems, Heerbrugg, Switzerland) then collected onto a slide and dried at 40 °C overnight. Dry sections on slides were stained in the Coplin staining jar with a 0.05% aqueous solution of toluidine blue for 5 minutes. Sections then were rinsed in water and left to dry for 30 minutes at 40 °C then be deparaffinized. Sections were taken through xylene 1 to 4 for 15 minutes each in Coplin staining jars, then air-dried and permanently mounted with a 24 x 50 mm glass coverslip using TBS SHUR/Mount™ liquid mounting medium (Triangle Biomedical Science, North Carolina, United States). Mounted slides were left in a fume hood overnight at room temperature before microscopic evaluation. The samples were analyzed using an Olympus light microscope (Vanox AHT3, Olympus Optical Co. Ltd., Tokyo, Japan) and the image were captured and visualized by a colour camera (DP74, Olympus Optical Co. Ltd., Tokyo, Japan) and cellSens standard digital imaging software version 1.7 (Olympus Optical Co. Ltd., Tokyo, Japan).

6.2.3 Time series analysis input parameters

LBI images were analysed as described in Section 3.2.3. Kiwifruit LBI parameters of SLP, DIP, FWHM, and Q3R at 830 nm were extracted for time series analysis using the extraction method described in Section 3.2.3. A new parameter of half width of quarter maximum (HWQM) was calculated using FWHM and Q3R to describe the radius between 25 % - 50 % of the maximum intensity (Eq. 6.1).

$$HWQM = Q3R - (\frac{FWHM}{2}) \quad \text{Eq. 6.1}$$

The average LBI parameters from two positions of each kiwifruit were used for time series analysis model development and forecasting. The time series model of each LBI parameter was developed using a simple linear regression model, Holt-Winters smoothing (HWS) and ARIMA. Details are provided in the following sections.

The time series analysis models of LBI parameters were developed based on the first 20 observations, and the assessment was conducted with the last 7 values forecasted using the developed models and compared with the actual observations. Fitted values using a regression model were calculated with Eq. 6.2. The forecasting via HWS and ARIMA was conducted using the 'Forecast' package (version 8.15). Data smoothing methods were applied to the averaged LBI data in HWS and ARIMA to compare the performance of forecasting.

6.2.4 Time series analysis with linear regression model

The regression model was built by

$$\widehat{y_t} = at^2 + bt + c \quad \text{Eq. 6.2}$$

Where $\widehat{y_t}$ is the fitted value at t^{th} observation, *a* and *b* polynomial coefficients, *c* is a constant. The model is fitted with the average LBI parameters of 30 fruit.

In the regression model evaluation, the mean of residuals e_t (Eq. 6.3) is zero. Better-fitted models have the lowest minimum sum of squared errors (SSE, Eq. 6.4) and maximum adjusted R^2 ($\bar{R}^2$, Eq. 6.5).

$$e_t = y_t - \widehat{y_t} \quad \text{Eq. 6.3}$$

$$SSE = \sum_{t=1}^{T} {e_t}^2 \quad \text{Eq. 6.4}$$

$$\bar{R}^2 = 1 - (1 - R^2)\frac{T-1}{T-k-1} \quad \text{Eq. 6.5}$$

Where y_t is the observed value and $\widehat{y_t}$ is the fitted value at t^{th} observation. e_t is the residual at t^{th} observation. *T* is the total number of observations and *k* is the number of predictors (*k* = 3 in this study).

6.2.5 Time series analysis with Holt-Winters smoothing

Holt-Winters smoothing (HWS) forecasting is described below in Eq. 6.6 - Eq. 6.9 (Holt, 2004):

$$S_t = \alpha \cdot y_t \,/\, (I_t - L) + (1 - \alpha)(S_{t-1} + b_{t-1}) \quad \text{Eq. 6.6}$$

$$b_t = \beta \cdot (S_t - S_{t-1}) + (1 - \beta) \cdot b_{t-1} \quad \text{Eq. 6.7}$$

$$I_t = \gamma \cdot y_t \,/\, S_t + (1 - \gamma)\, I_{t-\mathrm{L}} \quad \text{Eq. 6.8}$$

$$F_{t+m} = (S_t + mb_{t-1}) \cdot I_{t-L+m} \quad \text{Eq. 6.9}$$

Where α is the level smoothing factor, β is the trend smoothing factor, γ is the seasonality smoothing factor, y_t is the actual value at t^{th} observation, S_t is the smoothed value at t^{th} observation, b_t is the best linear trend regardless of seasonal changes and I_t is the seasonal factor. *b* is the trend factor, F_{t+m} is the forecast value at m steps ahead from t^{th} observation, *L* is cycle length (Holt, 2004).

Unlike regression with simple smoothing, which allocates the same weight to both the previous and the newly observed values, the HWS exponentially varies weights and values towards recent data (Gelper et al., 2010). In HWS, the three parameters α, β and γ represent the weight

of the recent data, the trend and the seasonality, respectively. The range of α, β and γ are between 0 and 1. In this study, only double exponential smoothing (α, β) was used as no seasonality or cyclic pattern is expected. In kiwifruit postharvest softening, a single decreasing trend is expected (Figure 2.1). Holt (2004) explained that a smaller α and β (closer to 0) indicate a greater smoothing effect, which means that forecasting is based on a longer period of the previous level (*L*) and a long-term trend (*T*), respectively. Alternatively, a larger α and β (closer to 1) indicates fewer smoothing effects, with the forecasting giving greater weight to the recent *L* and *T* in the data. When α and β equal 1, the forecast output is the same as the last actual observation.

6.2.6 Time series analysis with ARIMA

ARIMA (*q*, *d*, *p*) is usually employed for investigating the irregular component of a time series (Box et al., 2015). The general forecasting process introduced by Box et al. (2015) using ARIMA includes first finding the differencing coefficient (d, Eq. 6.10 - Eq. 6.11) to make the data set stationary. Once the distribution of observation (y_t) is not affected by the time points, the data is stationary (Kwiatkowski et al., 1992).

Secondly a residual test is conducted to determine the order for autoregressive (AR, *p*, Eq. 6.12) and moving average (MA, *q*, Eq. 6.13) by Autocorrelation Function (ACF) and partial autocorrelation Function (PACF) tests. Autocorrelation measures the correlation between observations of a time series data separated by a specific time lag to identify residuals. The ACF is used to identify the significance of these correlations at various lags (Box et al., 2015). For example, a significant correlation can be observed at lag 1 in a MA (1) process. Patial autocorrelation measures the correlation between observations at all shorter lags and helps understand the direct impact of past values on the current one. The PACF is used to identify

the direct relation between the observation and the lagged value (Box et al., 2015). For example, significant values can be only observed at lag 1 and 2 in an AR (2) process. ACF and PACF plots helps to determine appropriate parameters for the ARIMA model.

Thirdly, the models are compared using Akaike information criterion (AIC, Eq. 6.24) and Bayesian information criterion (BIC, Eq. 6.25) to identify the best model with the minimum AIC and BIC. The AIC helps to select the best model with fewest parameters to avoid overfitting. The BIC imposes a larger penalty for models with more parameters in a large data set. The Lower AIC and / or BIC indicate a better model, where AIC focus on forecasting accuracy while BIC focus on the model simplicity (Schwarz, 1978).

The *d* or integration (*I*) in the ARIMA model computes the differences between observations to make non-stationary time series stationary and exclude the underlying correlation with time. The first-order differenced time series (*d* = 1) can be written as Eq. 6.10

$$y'_t = y_t - y_{t-1} \qquad \text{Eq. 6.10}$$

Where y_t is the observation at t^{th} observation point with $d = 1$ and $t \geq 2$. y'_t is the observation at t^{th} after the differentiation.

The second-order differenced time series (*d* = 2) can be written as Eq. 6.11

$$y''_t = y_t - 2y_{t-1} - y_{t-2} \qquad \text{Eq. 6.11}$$

Where y_t is the observation at t^{th} observation point with $d = 2$ and $t \geq 3$. y''_t is the observation at t^{th} after the differentiation.

The order of *d* refers to the successive first differences, and y'_t represents the mean of time series by removing the change of level; thus, the trend or seasonality influence can be limited

(Kwiatkowski et al., 1992). In general, when there is constant *c* (Eq. 6.12 - Eq. 6.14), the forecasted values could be the mean of data (when *d* = 0), follow a straight line (when *d* = 1) or in a quadratic trend (when *d* = 2). In this study, kiwifruit FF is expected to have *d* = 2 as an exponentially decreasing FF trend was expected in Figure 2.1.

The AR (*p*) in the ARIMA model utilizes a linear combination of the past values to forecast future values as described in Eq. 6.12. The MA (*q*) in ARIMA model uses past forecast errors to make forecasts (Eq. 6.13). In this study of kiwifruit ripening, non-seasonal ARIMA is expected and can be written as Eq. 6.14

$$y_t = c + \emptyset_1 y_{t-1} + \emptyset_2 y_{t-2} + \cdots + \emptyset_p y_{t-p} + \varepsilon_t \quad \text{Eq. 6.12}$$

$$y_t = c + \varepsilon_t + \theta_1 \varepsilon_{t-1} + \theta_2 \varepsilon_{t-1} + \cdots + \theta_q \varepsilon_{t-q} \quad \text{Eq. 6.13}$$

$$y'_t = c + \emptyset_1 y'_{t-1} + \emptyset_2 y'_{t-2} + \cdots + \emptyset_p y'_{t-p} + \theta_1 \varepsilon_{t-1} + \theta_2 \varepsilon_{t-1} + \cdots + \theta_q \varepsilon_{t-q} + \varepsilon_t \quad \text{Eq. 6.14}$$

Where ε_t is the white noise, $\emptyset_1$,..., $\emptyset_p$ are parameters of the lagged values of y_t. These parameters determine the pattern of the time series data. The restrictions of the value of $\emptyset$ for AR (*p* = 1) are Eq. 6.15 and for AR (*p* = 2) are Eq. 6.16-Eq. 6.18. Similarly, the restrictions of the value of θ for MA (*q* = 1) are Eq. 6.19 and for MA (*q* = 2) are Eq. 6.20-Eq. 6.22 (Box et al., 2015).

$$-1 < \emptyset_1 < 1 \quad \text{Eq. 6.15}$$

$$-1 < \emptyset_2 < 1 \quad \text{Eq. 6.16}$$

$$\emptyset_1 + \emptyset_2 < 1 \quad \text{Eq. 6.17}$$

$$\emptyset_2 - \emptyset_1 < 1 \quad \text{Eq. 6.18}$$

$$-1 < \theta_1 < 1 \quad \text{Eq. 6.19}$$

$$-1 < \theta_2 < 1 \quad \text{Eq. 6.20}$$

$$\theta_1 + \theta_2 < 1 \quad \text{Eq. 6.21}$$

$$\theta_2 - \theta_{1_1} < 1 \quad \text{Eq. 6.22}$$

The value of AR order (*p*) and the MA order (*q*) could be considered using ACF and PACF plots comparing the pattern (either gradually decreasing or significant cut at certain lags). The maximum likelihood estimation (MLE), AIC and BIC are used for model evaluation. The best model will be selected with the maximum MLE and minimum AIC and BIC (Eq. 6.23 - Eq. 6.25).

$$MLE = \sum_{t=1}^{T} {\varepsilon_t}^2 \quad \text{Eq. 6.23}$$

$$AIC = Tlog\left(\frac{SSE}{T}\right) + 2(k+2) \quad \text{Eq. 6.24}$$

$$BIC = Tlog\left(\frac{SSE}{T}\right) + (k+2)log\ (T) \quad \text{Eq. 6.25}$$

where *T* is the total number of observations used for estimation and k is the number of predictors in the model.

6.3 Results and discussion

6.3.1 LBI parameter analysis

6.3.1.1 LBI parameter trends

The DIP represents the saturated area around the incident point of the laser beam in light diffusion inside kiwifruit. A higher DIP indicates that the photon detectable signal started to reduce at a larger radius from the incident point (Figure 3.2). The SLP represents the rate of attenuation of backscattering intensity between 75 % and 25 % of maximum intensity in the diffusion region. Hence higher SLP indicates a longer travel path of photons. The ½ FWHM and HWQM represent the diffusion area within 75 % to 50 % and 50 % to 25 %, respectively. Higher FWHM and HWQM also indicate less photon energy reduction in the first and second half of the photon travel region, respectively.

'Zesy002' kiwifruit DIP, SLP and HWQM showed a quadratic increasing trend over the 27 observations captured (Figure 6.1). The increased LBI parameters of DIP (Figure 6.1a), SLP (Figure 6.1c) and HWQM (Figure 6.1d) indicate that the photon's travel path becomes longer during storage at 20 °C resulted from less scattering. The average LBI parameter of Lot 2 kiwifruit (Figure 6.1 red dashed lines) showed similar trends as Lot 1 kiwifruit (Figure 6.1 black solid lines), and FF decreased during storage (Figure 6.1 purple dashed lines). Therefore, FF reduction may increase LBI parameter values resulting from physical property changes. However, a large variation of LBI parameters was observed due to different fruit samples on each measurement day in Lot 2 and FF variation was observed on day 1 and day 4. Kiwifruit used for time series analysis in Lot 1 had less variation of LBI parameters compared with Lot 2 fruit samples, as the same kiwifruit samples were measured on each measurement occasion. The increase of FWHM in the later storage may indicate that FWHM may be sensitive at the

lower FF range and could determine the stage of the softening process when FF reduction plateaus.

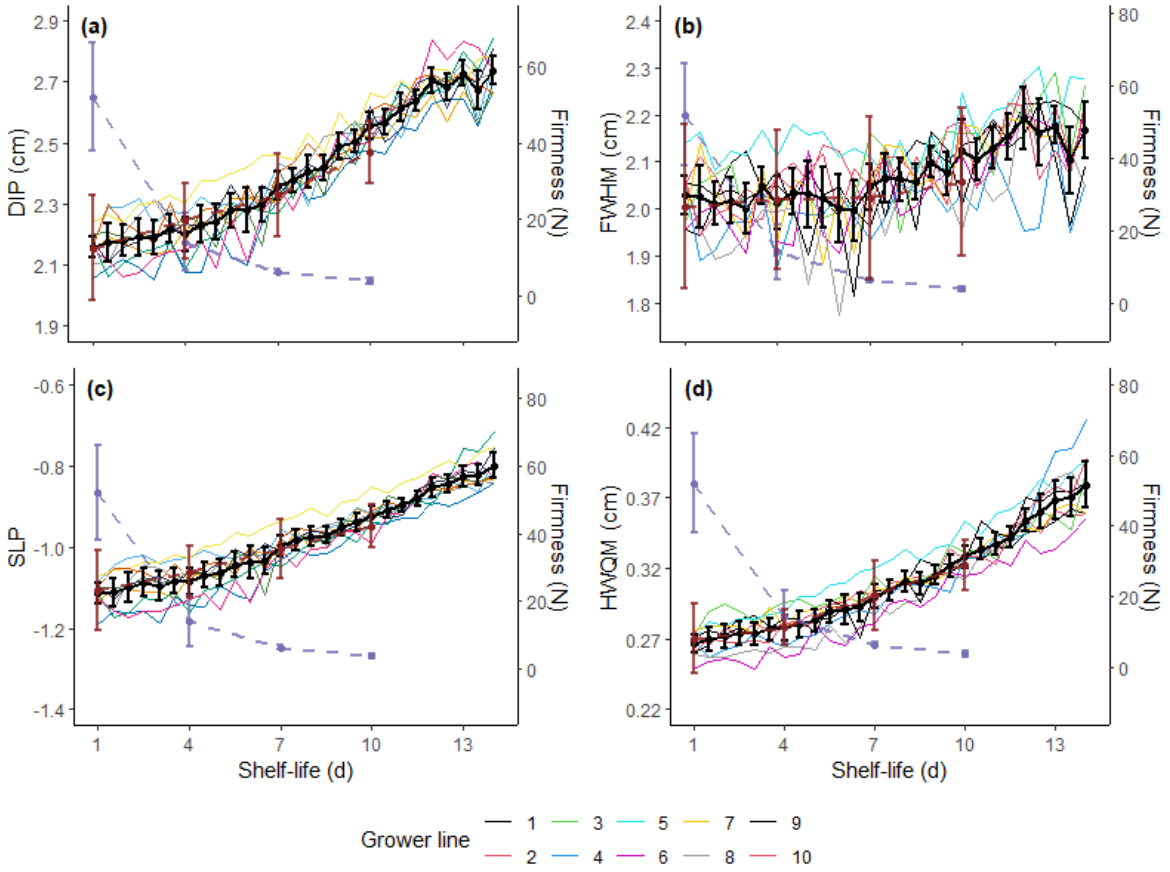

Figure 6.1. Changes in laser backscattering imaging (LBI) profile parameters during 14 days at 20 °C for 'Zesy002' kiwifruit at 830 nm. LBI parameters are DIP (a, the radius of the saturated area), FWHM (b, double the radius at 50 % of maximum intensity), SLP (c, the slope of the linear regression model built with log-transformed profile data between 25% - 75 % of maximum intensity) and HWQM (d, the radius between 25 % - 50 % of maximum intensity). Coloured solid lines are the average LBI parameter for each grower line (n=3), the black solid line is the average LBI parameter for all grower lines (n=30). The purple dashed line is the average firmness, and the red dashed line is the average LBI parameter for kiwifruit (n=10) sourced from the same batch. Errorbar is stand deviation.

A similar result was observed for 'Hayward' kiwifruit (Figure 6.2), all LBI parameters showed an increasing trend through ripening. In addition, a stable lag phase of 'Hayward' was observed from day 1 to day 6 for DIP, SLP and HWQM (Figure 6.2a,c,d), whilst a longer lag phase was observed for FWHM (Figure 6.2b). No lag phase after the increasing period was observed for

all LBI parameters. The negative correlation of LBI parameters and FF was also observed for 'Hayward', where FF variation was reduced on day 10.

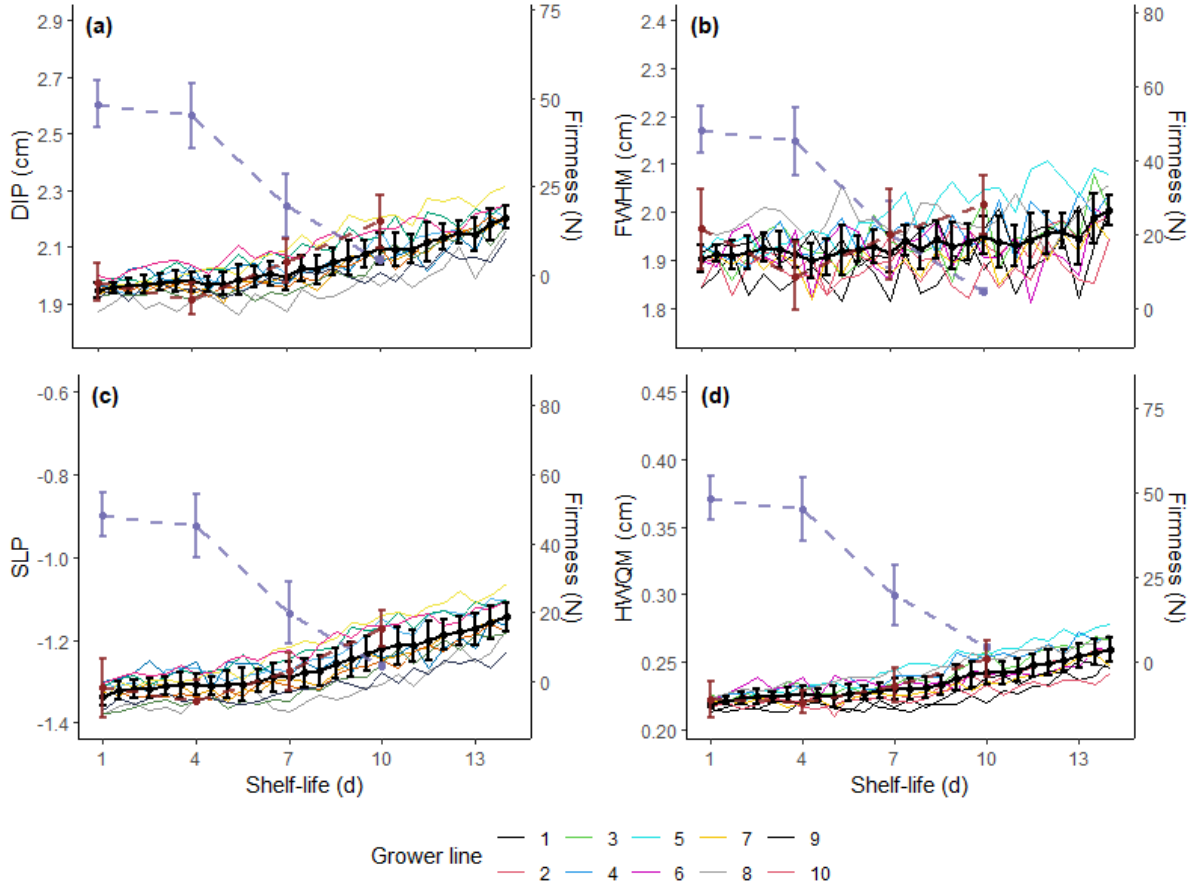

Figure 6.2. Changes in laser backscattering imaging (LBI) profile parameters during 14 days at 20 °C for 'Hayward' kiwifruit at 830 nm. LBI parameters are DIP (a, the radius of the saturated area), FWHM (b, double the radius at 50 % of maximum intensity), SLP (c, the slope of the linear regression model built with log-transformed profile data between 25% - 75 % of maximum intensity) and HWQM (d, the radius between 25 % - 50 % of maximum intensity). Coloured solid lines are average LBI parameter for each grower line (n=3), the black solid line is average LBI parameter for all grower lines (n=30). The purple dashed line is average firmness, and red dashed line is average LBI parameter for kiwifruit (n=10) sourced from the same batch. Errorbar is stand deviation.

6.3.1.2 Simple regression model

For the first 20 observations of 'Zesy002' kiwifruit, the regression model fitted well for DIP, SLP and HWQM with a high R^2 over 0.99 (Table 6.1). The model has a positive coefficient *a*, reflecting a positive relationship between LBI parameters and storage time. A lower R^2 was

obtained for FWHM, where no clear trend was observed (Figure 6.1b). An interpretation of *c* is the average initial value of LBI parameters when $t = 0$. For 'Hayward' kiwifruit, the R^2 of the simple regression model was lower than for 'Zesy002', with the R^2 being over 0.9 in DIP, SLP and HWQM, (Table 6.1). A low R^2 was also observed for 'Hayward' FWHM, where no clear trend was observed (Figure 6.2b). The coefficients of the simple regression model only describe the general trends based on previous observation data without identifying the phase switching point during the kiwifruit softening/ripening process. Putting the same weight on each observation may not well represent well future changes during ripening.

Table 6.1. Kiwifruit laser backscattering imaging (LBI) parameter analysis with simple linear regression

LBI	*a*	*b*	*c*	R^2	sse
Zesy002					
DIP	$1.05e^{-03}$	$-8.27e^{-05}$	2.17	0.99	$2.76e^{-03}$
FWHM	$5.33e^{-04}$	$-6.53e^{-03}$	2.03	0.77	$5.79e^{-03}$
SLP	$3.35e^{-04}$	$4.08e^{-03}$	-1.12	0.99	$8.87e^{-04}$
HWQM	$1.24e^{-04}$	$8.11e^{-04}$	2.67	0.99	$5.10e^{-05}$
Hayward					
DIP	$4.29e^{-04}$	$-1.75e^{-03}$	1.96	0.97	$1.44e^{-03}$
FWHM	$8.98e^{-05}$	$-7.46e^{-05}$	1.91E	0.64	$1.31e^{-03}$
SLP	$3.52e^{-04}$	$-1.79e^{-03}$	-1.32	0.97	$6.90e^{-04}$
HWQM	$5.65e^{-05}$	$-1.05e^{-04}$	2.22	0.95	$4.69e^{-05}$

6.3.1.3 Holt-Winters smoothing model

In the HWS model (Table 6.2), DIP and FWHM for 'Zesy002' had a lower α (0.33 and 0.12) but higher β (1.00), which indicates that the forecasted *L* based on long-term observation, while the forecasted *T* is built on the most recent data. HWQM was the opposite (α =0.73, β=0.30), indicating that the forecasted *L* was based on recent data while the *T* was on a long-term basis. For SLP, both α and β were around 0.5, thus the *L* and *T* forecasts were equivalently influenced by the past data regardless of the observation period. 'Zesy002' SLP did steadily increase with no lag phase observed (Figure 6.1c), thus the forecasts didn't put particular weight on historical

data or more recent data. On the other hand, a lag phase in DIP (Figure 6.1a) and FWHM (Figure 6.1b) was observed followed by a period of increase, where a stable forecast is expected (α = 0.33 and 0.12). For 'Zesy002' HWQM (Figure 6.1d), no lag phase was observed after a steady increase. Therefore, the forecasted value will follow the recent *T*, or increasing rate, and continue to increase (α = 0.73).

Table 6.2. Kiwifruit laser backscattering imaging (LBI) parameter analysis with Holt-Winters Smoothing

LBI	*a*	*b*	α	β	sse
Zesy002					
DIP	2.58	0.03	0.33	1.00	0.01
FWHM	2.11	0.02	0.12	1.00	0.01
SLP	-0.91	0.01	0.51	0.42	0.00
HWQM	0.33	0.01	0.73	0.30	0.00
Hayward					
DIP	2.09	0.01	0.83	0.00	0.00
FWHM	1.94	0.00	0.61	0.29	0.00
SLP	-1.21	0.01	0.82	0.78	0.00
HWQM	0.24	0.00	1.00	0.28	0.00

In 'Hayward' HWS model (Table 6.2), DIP and FWHM had a short-term *L* forecast (α = 0.83 and 0.61) and a long-term *T* forecast (β = 0 and 0.29). This finding for 'Hayward' DIP and FWHM was opposite with 'Zesy002'. As shown in Figure 6.2, DIP (Figure 6.2a) and FWHM (Figure 6.2b) had a lag phase prior to an increasing phase. HWQM (Table 6.2) showed the same short-term *L* forecast and long-term *T* forecast (α = 1, β = 0.28). SLP (Table 6.2) has both high α (0.82) and β (0.78), indicating that both *L* and *T* will follow the recent data and are expected to continue increasing.

6.3.1.4 ARIMA model

The selected ARIMA models of 'Zesy002' LBI parameter are presented in Table 6.3. DIP, SLP and HWQM had a *d* = 2, which indicated a quadratic trend. Whilst FWHM had a *d* = 1, indicating a

straight line. The *d* values of each parameter agree with the observation in Figure 6.1. HWQM had the highest log-likelihood and lowest AIC, hence better performance of forecasting is expected. DIP and FWHM had a lower log-likelihood and higher AIC, thus the ARIMA model might not be suitable for analysing 'Zesy002' ripening data.

Table 6.3. Kiwifruit laser backscattering imaging (LBI) parameter analysis with Auto Regressive Integrated Moving Average (ARIMA) model.

LBI	*p*	*d*	*q*	AIC	loglik
Zesy002					
DIP	1.00	2.00	2.00	-87.87	47.93
FWHM	1.00	1.00	0.00	-84.29	44.15
SLP	0.00	2.00	1.00	-110.65	57.33
HWQM	0.00	2.00	1.00	-156.36	80.18
Hayward					
DIP	0.00	1.00	0.00	-108.31	55.15
FWHM	1.00	1.00	0.00	-115.48	59.74
SLP	1.00	2.00	0.00	-131.67	67.83
HWQM	0.00	2.00	0.00	-175.80	88.90

The selected ARIMA model of LBI parameters had a higher log-likelihood and lower AIC for 'Hayward' HWQM and SLP (Table 6.3). Alternatively, less variation was observed in SLP and HWQM than DIP and FWHM (Figure 6.2). Looking at *d* values, SLP and HWQM were described the same as 'Zesy002' with a quadric trend. The straight trend of DIP (*d* = 1) could be due to missing the second lag phase in Figure 6.2a.

6.3.2 LBI parameter forecasting using time series analysis

For both kiwifruit cultivars, the forecast of the final 7 observations showed that regression was the best model to forecast HWQM, while HWS and ARIMA provided the lowest deviation for DIP and FWHM (Figure 6.4). Although neither HWS nor ARIMA achieved good fitted results (first 20 observations) and forecasted results (last 7 observations) for FWHM, HWS still obtained some fluctuation during the ripening process. The ARIMA model is not ideal for kiwifruit shelf-life ripening data analysis due to the data size, as the data set is reduced after

differencing and smoothing (MA process). On the other hand, ARIMA is more powerful in cyclic or periodical data analysis. For example, agricultural product monthly sales price (Weng et al. 2019) and bell pepper yearly production (Verroens et al. 2006).

The residual analysis for time series models is presented in Figure 6.3. For all LBI parameters, residuals of fitted values were within the 95 % confidence interval, while residuals of the later stage forecasted values were outside of the threshold of 95 % confidence interval. Forecasted DIP were overestimated for 'Zesy002' and underestimated for 'Hayward' (Figure 6.3a, Figure 6.4a,b). 'Zesy002' forecasted FWHM using the ARIMA model were underestimated, while overestimated using regression or HWS (Figure 6.3b, Figure 6.4c). 'Hayward' forecasted FWHM were underestimated using all time series models (Figure 6.3b, Figure 6.4d). All forecasted SLP residuals were within the 95 % confidence interval for both cultivars except regression for 'Hayward' (Figure 6.3c), while most 'Zesy002' SLP were underestimated while 'Hayward' SLP were overestimated (Figure 6.4e,f). Forecasted 'Hayward' HWQM residuals were out of 95 % confidence interval using ARIMA (Figure 6.3d), and forecasted HWQM were underestimated for both cultivars (Figure 6.4g,h).

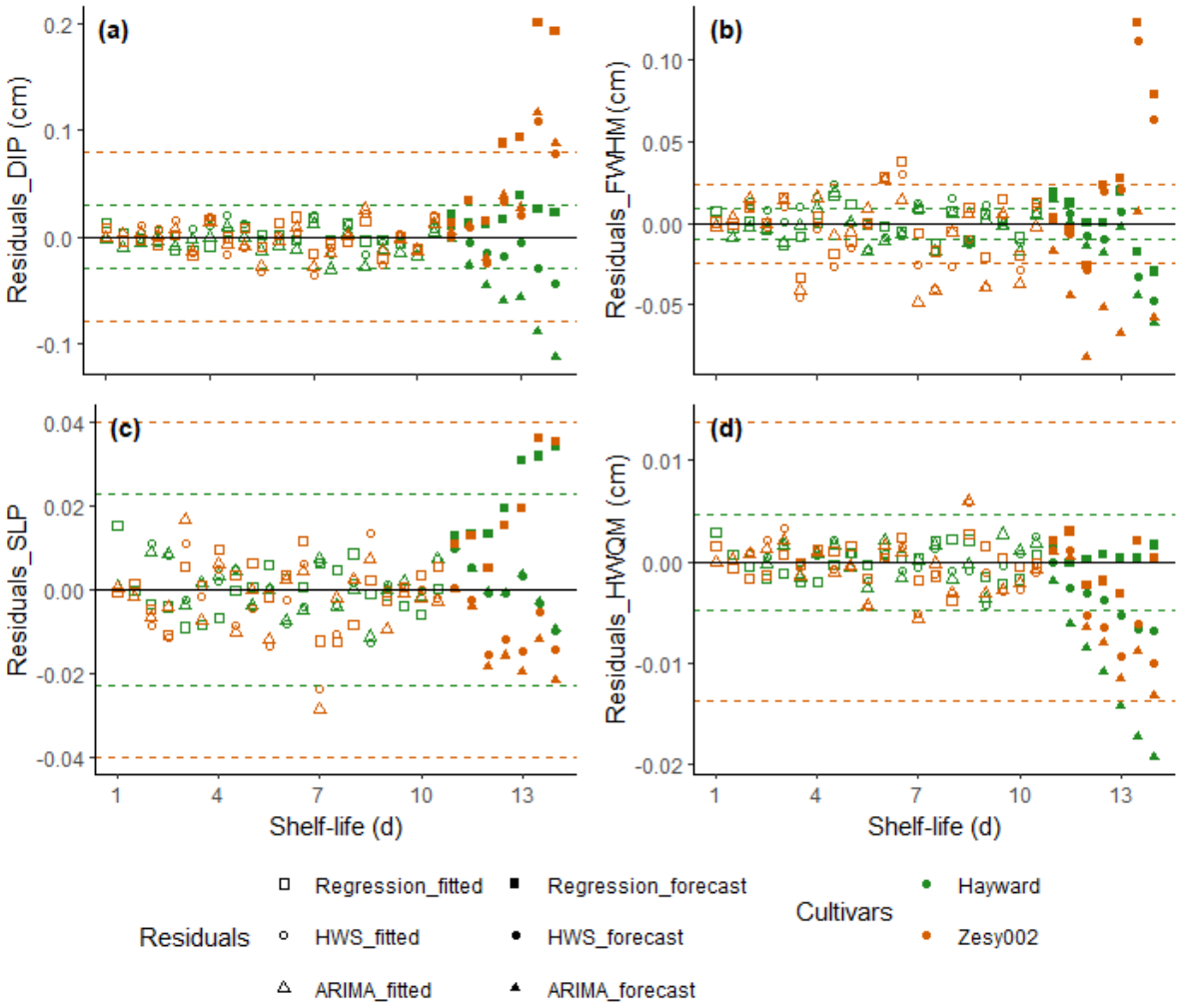

Figure 6.3. Residuals analysis of times series analysis models. Residuals of fitted (empty) and forecasted (solid) values using Simple regression, Holt-Winters Winters smoothing (HWS) and Auto Regressive Integrated Moving Average (ARIMA) model were compared with measured data. LBI parameters of DIP (a, the radius of the saturated area), FWHM (b, double the radius at 50 % of maximum intensity), SLP (c, the slope of the linear regression model built with log-transformed profile data between 25% - 75 % of maximum intensity) and HWQM (d, the radius between 25 % - 50 % of maximum intensity) are presented. Dash lines are the upper and lower residual thresholds for a 95 % confidence interval.

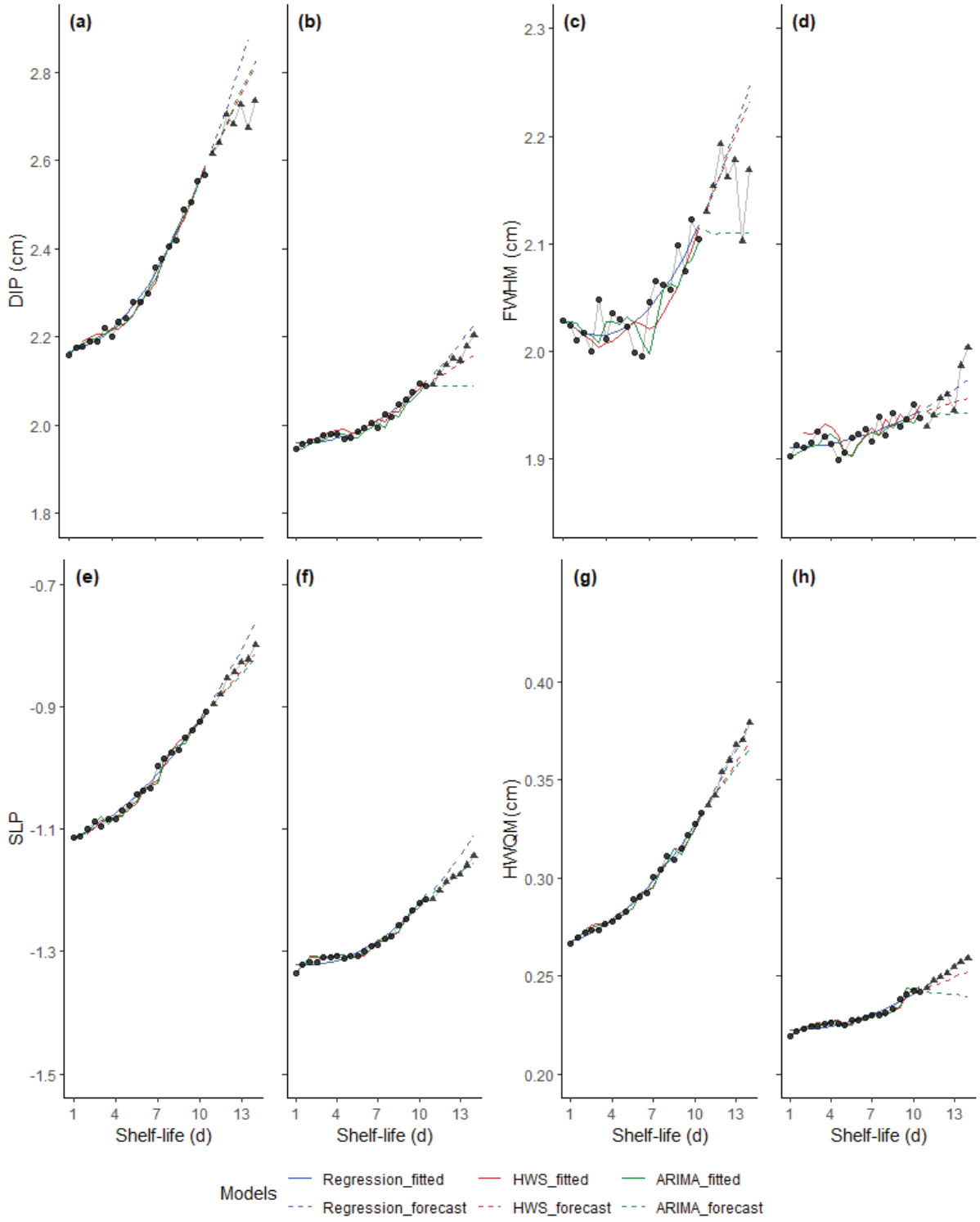

Figure 6.4. Fitted and forecasted kiwifruit laser backscattering imaging (LBI) profile parameters. DIP (a,b, the radius of the saturated area), FWHM (c,d, double the radius at 50 % of maximum intensity), SLP (e,f, the slope of the linear regression model built with log-transformed profile data between 25% - 75 % of maximum intensity) and HWQM (g,h, the radius between 25 % - 50 % of maximum intensity) for "Zesy002' (a,c,e,g) and 'Hayward' kiwifruit (b,d,f,h) for 14 days at 20 °C measured at 830 nm. Simple regression, Holt-Winters smoothing (HWS) and Auto Regressive Integrated Moving Average (ARIMA) model were compared with measured data.

6.3.3 Discussion of LBI parameter changes associated with kiwifruit ripening

6.3.3.1 LBI parameter and firmness

Pearson correlation coefficients of LBI parameters and FF of 'Zesy002' were -0.51, -0.08, -0.55 and -0.57 for DIP, FWHM, SLP and FWQM, respectively (Table 6.4). Pearson correlation coefficients for 'Hayward' were -0.74, -0.36, -0.73 and -0.66 (Table 6.4). For both cultivars, parameter FWHM had the poorest correlation. In general, LBI parameters had a higher correlation with FF for 'Hayward' than 'Zesy002', possibly due to 'Hayward' having a wider FF range. During the experimental period, FF reached 3.7 N (from 57 N) and 2.3 N (from 32 N) for 'Hayward' and 'Zesy002', respectively.

Table 6.4. LBI parameter and kiwifruit flesh firmness correlation for 'Zesy002' and 'Hayward'. Numerical values are Pearson correlation coefficients. LBI parameters at 830 nm include the radius of the saturated area (DIP), double the radius at 50 % of maximum intensity (FWHM), and the slope of the linear regression model (SLP) built with log-transformed profile data between the radius at 75 % of maximum intensity and the radius at 25 % of maximum intensity, the radius between 50 % and 25% of maximum intensity (HWQM).

	DIP	FWHM	SLP	FWQM
Zesy002	-0.51	-0.08	-0.55	-0.57
Hayward	-0.74	-0.36	-0.73	-0.66

For both cultivars, higher LBI parameters were observed with lower FF of Lot 2 kiwifruit in the early storage stages (Figure 6.5). A large variation of LBI parameters was observed when FF over 15 N, however, a separation tendency of firm fruit (> 9.8 N) with lower LBI parameters and soft fruit (< 9.8 N) with higher LBI parameters was observed (Figure 6.5). The individual correlation of LBI parameter and FF will be further investigated with a larger data set in Section 7.3.2.

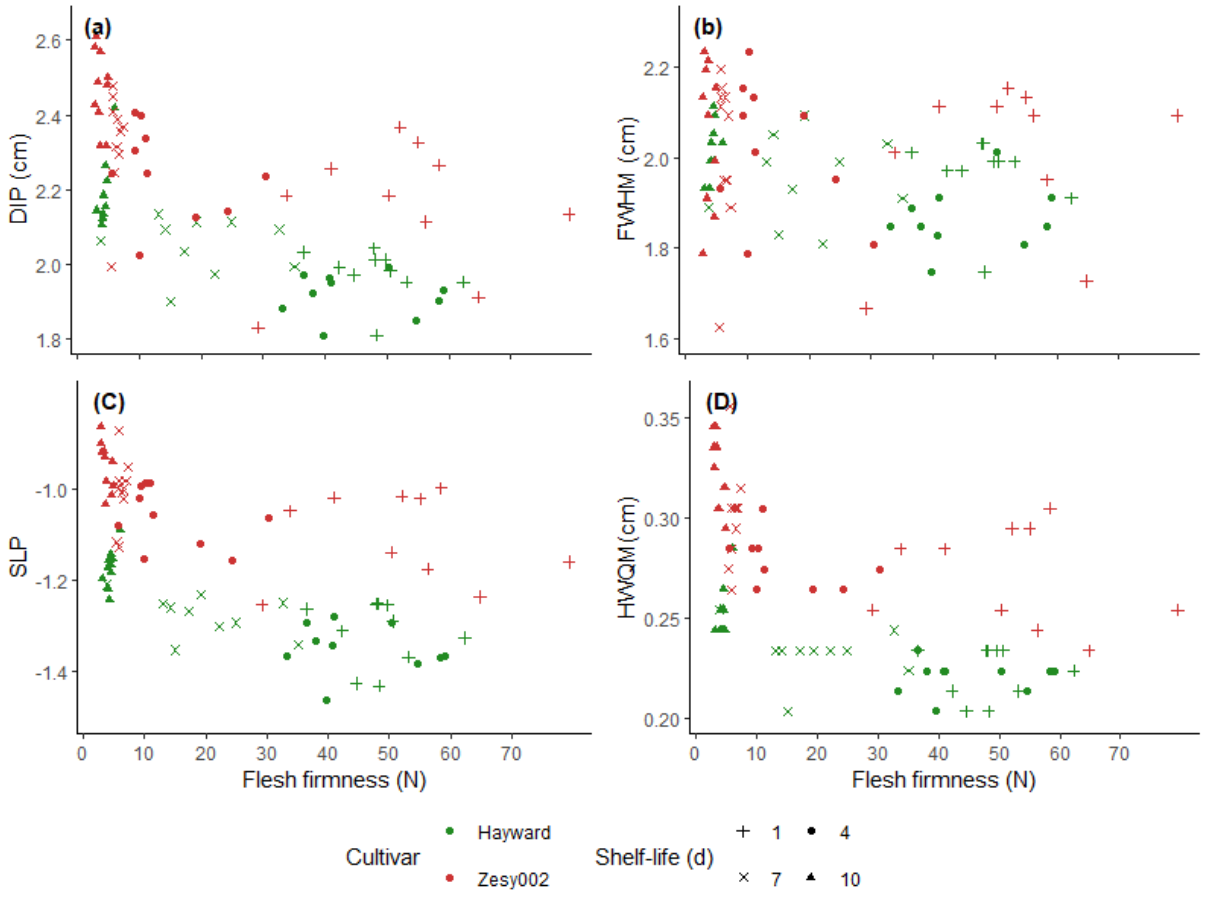

Figure 6.5. Laser backscattering imaging (LBI) profile parameters and kiwifruit firmness correlation over 10 days at 20 °C for 'Zesy002' kiwifruit (red) and 'Hayward' kiwifruit (green) at 830 nm. LBI parameters are DIP (a, the radius of the saturated area), FWHM (b, double the radius at 50 % of maximum intensity), SLP (c, the slope of the linear regression model built with log-transformed profile data between 25% - 75 % of maximum intensity) and HWQM (d, the radius between 25 % - 50 % of maximum intensity)

6.3.3.2 LBI parameter and microstructure

The increase in LBI parameters with the decrease in FF (Figure 6.1, Figure 6.2 and Figure 6.5) could be explained by how microstructure influences optical properties. During kiwifruit softening, kiwifruit microstructure changes include cell wall swelling and pectin disintegration during the softening process (Hallett et al., 1992). Kiwifruit samples collected from Lot 2 kiwifruit on days 1, 4, 7 and 10 were further conducted microcopy images capture (Figure 6.6 and Figure 6.7). Cell swelling and cell degradation could be observed from light dye colour and shriveled cells, which could result in scattering reduction. For 'Hayward' kiwifruit, bruised fruit

had higher μ_a and lower μ_s' during storage ripening due to the change of tissue colour, FF and microstructure (Gao et al. 2021). Besides, microstructure information obtained from X-ray CT was used for studying fruit ripening processes and linked with scattering properties in mango (Cantre et al., 2014) and apple (Wang et al., 2020)

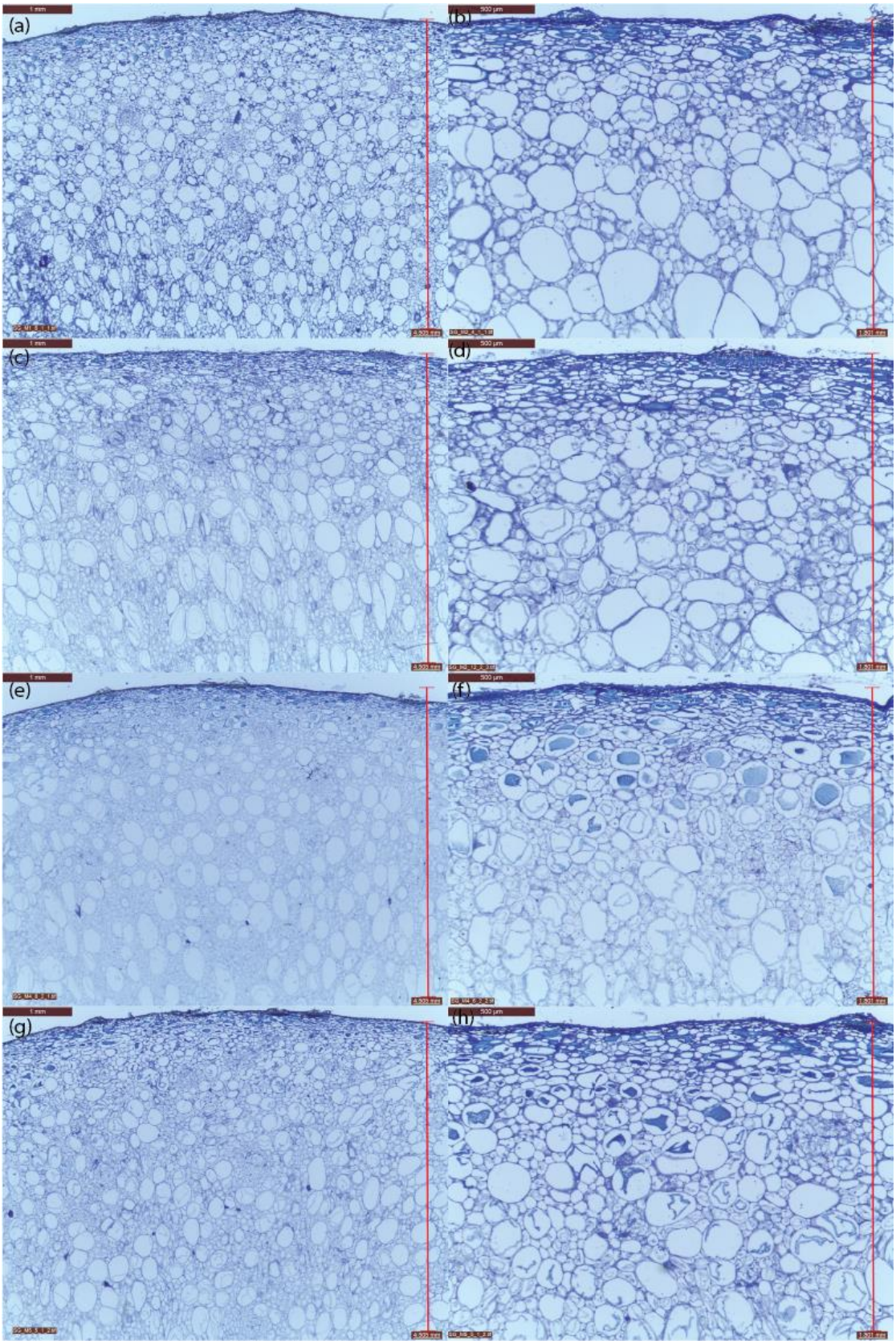

Figure 6.6. Kiwifruit microstructure image over 10 days at 20 °C for 'Zesy002' kiwifruit. (a,c,e,g) kiwifruit microstructure in the outer pericarp region and bar = 1 mm, (b,d,f,h) kiwifruit microstructure in the subsurface region and bar = 500 µm. Microscopy samples were collected on day 1 (a,b), day 4 (c,d), day 7 (e,f) and day 10 (g,h).

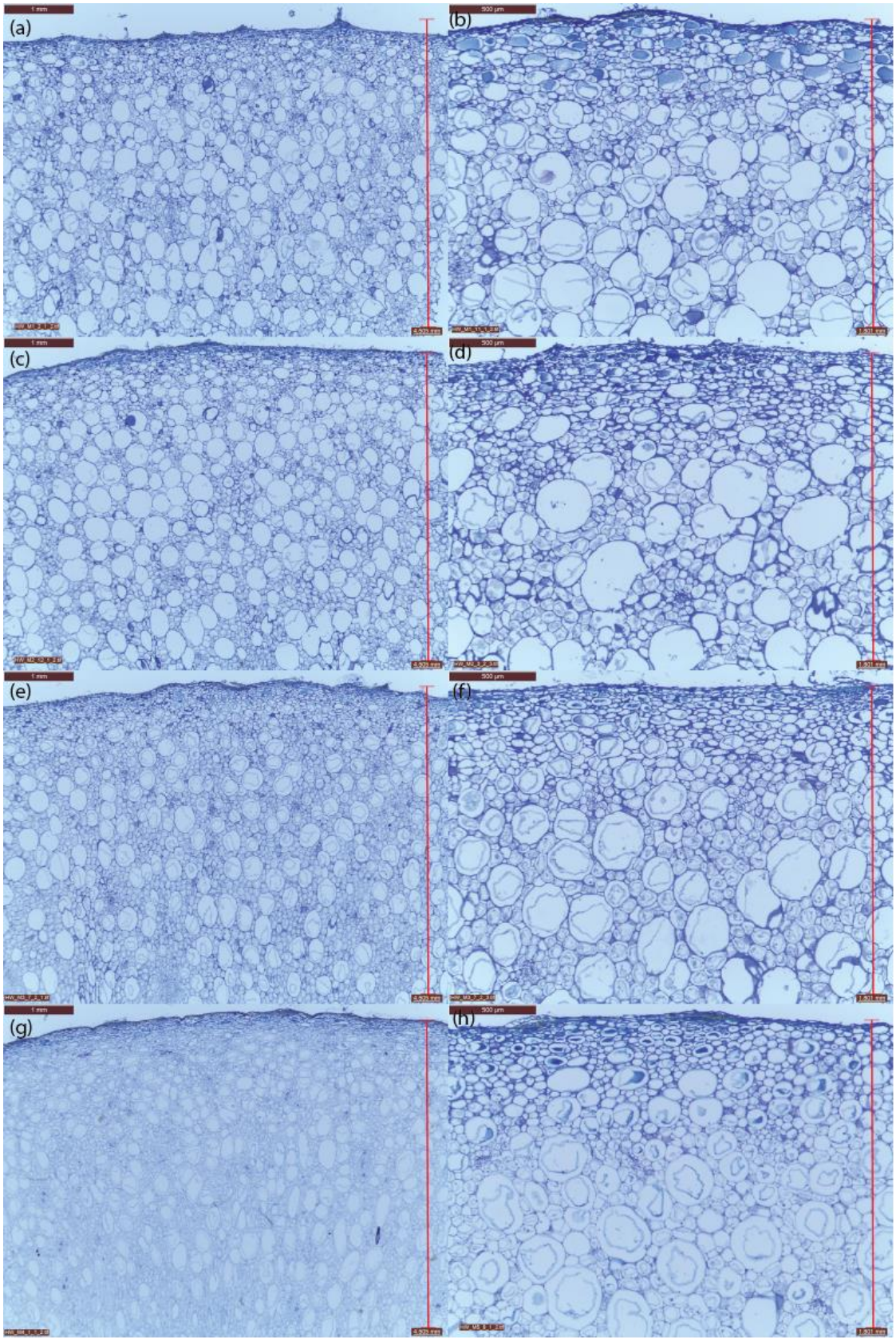

Figure 6.7. Kiwifruit microstructure image over 10 days at 20 °C for 'Hayward' kiwifruit. (a,c,e,g) kiwifruit microstructure in the outer pericarp region and bar = 1 mm, (b,d,f,h) kiwifruit microstructure in the subsurface region and bar = 500 µm. Microscopy samples were collected on day 1 (a,b), day 4 (c,d), day 7 (e,f) and day 10 (g,h).

Any correlation between LBI parameters and FF may vary through the ripening stages. Firstly, different microstructure changes occur at different ripening stages. The changes that were observed for SLP and HWQM (Figure 6.1c,d and Figure 6.2c,d) could be a result of cell wall degradation involved in the 2nd rapid softening phase, whilst the increase of FWHM (i.e. less reduction of photon energy) in the later ripening process could result from cell wall swelling or loss of the middle lamella occurs in the 3rd softening phase. As a result, the reduction of energy occurs at a slower rate when fruit are soft, which may slow down SLP and HWQM increase (Figure 6.1c,d and Figure 6.2c,d).

6.3.3.3 LBI parameter and light absorption

Different LBI parameters are associated differently with optical properties. It has been previously reported that absorption and scattering properties carry information along different parts of the LBI attenuation curve using time-resolved analysis (Cubeddu et al., 1996). Alternatively, the different regions of the LBI profile (Figure 3.2), defined as LBI parameters, possibly carry different information on absorption and scattering in spatial-resolved system. Therefore, individual LBI parameter may correlate with μ_a and μ_s' differently, thus resulting in different correlations with FF (Table 6.4). In this work, no trend of FWHM was observed at 830 nm in the first 8 days (Figure 6.1b and Figure 6.2b), which suggested LBI attenuation between 75 % to 50 % of LBI maximum intensity is not influenced by fruit softening during the first 8 days. The decrease in FWHM was previously reported by Hashim et al. (2013) during banana ripening, with an absorption decrease at 660 nm. This may be due to chlorophyll content reduction. In this work, LBI parameters were assumed to carry mainly scattering information at 830 nm, where minimal absorption is expected, and thus the change in FWHM is not clear. To further investigate whether FWHM carries absorption information and can be utilized for

estimating absorption related fruit quality attributes, FWHM obtained at wavelengths of 520 nm and 685 nm could be studied during the 'Zesy002' early ripening stage. These 2 wavelengths correspond to the absorption peaks of carotenoids and chlorophyll, which may be useful in representing the de-greening process in 'Zesy002'.

6.3.4 Discussion of kiwifruit LBI parameter trends using Holt-Winter smoothing analysis

Absolute LBI parameter values of 'Hayward' kiwifruit were lower ($p < 0.01$) compared with 'Zesy002' through the experiment period (Figure 6.4). Besides optical properties that may differ between kiwifruit cultivars, the lower LBI may be due to 'Zesy002' and 'Hayward' being through different ripening stages. 'Zesy002' ripening in this work may begin from an advanced stage. This assumption is consistent with the AF measurement of that 'Zesy002' AF (18 10^6 Hz^2 $g^{2/3}$) being lower at the beginning of the experiment than 'Hayward' AF (27 10^6 Hz^2 $g^{2/3}$), which may be a result of 'Zesy002' being stored 26 days prior to measurement. The initial AF of 'Zesy002' and 'Hayward' is equivalent to approx 32 N and 57 N FF (Figure I.1). Coordinately, the initial LBI parameters of 'Zesy002' (2.18 cm, 1.1 and 0.27 cm for DIP, SLP and HWQM, respectively) were higher than 'Hayward' (2.10 cm, 1.3, and 0.25 cm for DIP, SLP and HWQM, respectively). During the experimental period, 'Hayward' also maintained consistently higher FF (3.7 N at day 20) compared with 'Zesy002' (2.3 N at day 20). Coordinately, 'Hayward' LBI parameters on day 13 (2.20 cm, 1.15 and 0.26 cm for DIP, SLP and HWQM, respectively) were similar to 'Zesy002' on day 1.

The trend of LBI parameters may vary at different ripening stages, which corresponding to β is HWS (Table 6.2). The fruit condition of 'Zesy002' was assumable within the 2nd and 3rd phases of the softening process, which captured a rapid decreasing and slowly decreasing trend, resulting in a lower FF decreasing rate in the 3rd phase. Coordinately, 'Zesy002' SLP and HWQM,

which had a high correlation with FF (Table 6.4), had a lower β in HWS analysis. The lower β indicated that increasing the rate of SLP and HWQM may pass the rapidly increasing period and become increasing slower. This is also supported by residuals of forecasted SLP and HWQM, which were within a 95 % confidence interval (Figure 6.3c,d). The fruit condition of 'Hayward' was assumable within the 1st and 2nd phases of the softening process, which captured a stable lag phase and a rapid decrease phase of FF. Coordinately, a stable lag phase was observed from day 1 to day 6 for 'Hayward (Figure 6.2), whilst no lag phase was observed for 'Zesy002' (Figure 6.1). Since the LBI data for time series analysis may be collected when FF was within 1st and 2nd softening phases and may be about to enter or just entered the slower decreasing FF phase, the forecasted LBI parameters were likely to be over-estimated (Table 6.2). 'Hayward' forecasted SLP residuals supported this assumption (Figure 6.3c). 'Hayward' DIP and HWQM in HWS analysis had a higher α but lower β (Table 6.2)., which indicated LBI parameters were continuously increasing. However, the increasing trend effect was diluted due to the lag phase, thus resulting in an underestimation of forecasted DIP and HWQM (Figure 6.3a,d).

The α and β were similar (with lower β than α) of SLP in HWS analysis for both 'Zesy002' and 'Hayward'. Therefore, the value of α and β of LBI might be a single useful information that represents the ripeness. Lower α and β of 'Zesy002' SLP may be due to advanced ripening than 'Hayward'. For 'Hayward' SLP, higher α and β determined the forecast *L* and *T*. Therefore, instead of forecasting LBI parameters, the α and β of SLP may be useful to analyse which phase the kiwifruit is located in. Apart from α and β in HWS, there might be other potential LBI parameters. For both cultivars, DIP, FWHM and HWQM followed the same trend but showed varied phase lengths (for example. HWQM entered the 2nd lag phase the last), the ratio of LBI parameters might be useful in determining the ripening stage instead of a single LBI parameter.

Although the starting point of the rapidly increasing phase in LBI parameter curve could be influenced by the at-harvest maturity of kiwifruit. In this study, both cultivars were selected from the main harvest. Thus, each cultivar was assumed to have similar at harvest maturity, and the miss of the initial lag phase of 'Zesy002' was assumed due to the extra postharvest storage time.

6.3.5 Discussion of time series model performance

Time series model performance could be influenced by an incomplete data set used for fitting. Both 'Zesy002' and 'Hayward' LBI parameters curves may be incomplete due to kiwifruit softening in this work were not through all 3 phases. Therefore, Figure 6.1 might represent the 'Middle to end' (5 – 60 N of FF) LBI parameter curve, while Figure 6.2 represents the 'Start to middle' (5 – 60 N of FF) LBI parameter curve. As a result, 'Zesy002' data may lack the 1st phase of softening data and hence, the models reflect more on the exponential FF decrease during the rapid 2nd phase of softening. For 'Hayward' kiwifruit, the data collection may lack the 3rd phase of softening to obtain a wider range of the ripening process. Alternatively, together Figure 6.1 and Figure 6.2, a 3-phase curve with a lag phase, an increasing phase and a lag phase is expected and corresponds to the softening curve.

Although, in practice, kiwifruit ripening is likely to correspond to only part of the LBI parameter curve, a complete curve is desired for model calibration. Therefore, to gain a better forecasting result of LBI parameters during ripening, fruit at a firmer range with a longer storage time are required to be studied. For time series analysis, more data points (observations) could enhance the model's performance. More data points could be achieved with a shorter data collection interval using an automation system or through a longer storage time using kiwifruit samples during cool storage.

On the other hand, other quality attributes apart from FF may influence time series analysis of 'Hayward' softening. Despite the overall firmer fruit for 'Hayward' through the study period, the hairy surface of 'Hayward' and the subsurface structure are also likely to contribute to a higher scattering, resulting in lower LBI parameters (Section 5.3.2). In general, 'Hayward' have a less uniform shape than 'Zesy002'. The time series model may be influenced by kiwifruit LBI data obtained from various curvatures (Section 5.3.6) at the equatorial region being averaged. The quantitative analysis of the curvature effect was not taken into consideration in modelling. Moreover, each kiwifruit sample may differ in DMC, SSC and skin colour as they had different pre-harvest conditions (Hewett et al., 1999). Pre-harvest conditions include (micro) climate, irrigation, nutrition, fruit position and orchard management (Hewett et al., 1999). Differences in LBI parameters among GLs were observed when sourced from different GLs despite the fact that kiwifruit were selected with similar FF and stored at the same condition. For 'Zesy002' kiwifruit, the trendlines of GLs 5 and 6 appeared largely separated. Similarly, for 'Hayward', GLs 1 and 10 had lower LBI parameter values compared with GLs 2 and 8. Therefore, the time series analysis model may be influenced when averaging different trends. In the future, multi-time series analysis may be studied.

6.4 Conclusion

Among the 3 time series analysis models tested, the α and β in HWS model are potentially useful for the LBI parameter forecast. However, none of the time series analysis models achieved promising forecasting results. Time-series analysis may indicate changes and trends in LBI parameters (DIP, FWHM, SLP and HWQM) associated with kiwifruit ripening. As a non-destructive method, LBI parameters and subsequent time-series analyses could be utilised to monitor the kiwifruit ripening stage changes resulting in kiwifruit quality changes. In the next chapter, the relationship of LBI parameters and FF with consideration of the ripening process

will be further investigated with kiwifruit samples having firmer initial FF and covering the three softening phases.

Chapter 7 Using laser backscattering imaging parameters for kiwifruit firmness segregation

7.1 Introduction

Kiwifruit are harvested at high FF (70 – 90 N) and kept in cool storage to delay reaching the eating FF of about 5 – 10 N (Hewett et al., 1999). Monitoring the softening process during storage and throughout the logistic chain till fruit consumption would be desirable as the obtained data could be useful for industry inventory decision-making. The traditional destructive measurement of FF captures a small sub-sample from the entire batch of fruit, resulting in a batch estimation for the kiwifruit population.

Non-destructive NIR spectroscopy has been investigated for kiwifruit quality estimation, allowing the monitoring of quality changes of each individual or batch of fruit. NIR spectroscopy captures data containing primarily the signal of absorption that is related to kiwifruit's chemical properties. The challenge of FF measurement using NIR spectroscopy appears in the absorption analysis because the absorbing molecules show no stoichiometrical relationship to FF during the dynamic softening process. When both textural structures and SSC change during kiwifruit ripening, correlations of absorption analysis and FF change. Therefore, the FF estimation is indirect, and the NIR data is not consistently correlated with different FF levels (Walsh et al., 2020).

It has been frequently assumed that μ_s' in the short-wave NIR range is correlated to FF, and μ_s' could be estimated using the LBI attenuation profile (Section 3.2.3). In Chapter 6, an increasing trend of kiwifruit LBI parameters during kiwifruit ripening was observed (Figure 6.1, Figure 6.2) for both kiwifruit cultivars. This data indicates that LBI parameters could be potentially utilized for soft kiwifruit identification and segregation in later storage. For example, at the minimum

exporting threshold (9.8 N) and also around the lower boundary between the 2nd and 3rd kiwifruit softening phase (Figure 2.1).

Given the potential for utilizing LBI parameters to segregate soft kiwifruit, the objectives of this chapter are to:

(i) explore the correlation between kiwifruit FF and LBI parameters;

(ii) develop and validate an FF segregation model to sort soft kiwifruit from firm ones and

(iii) investigate model feasibility with various subsampled populations representing commercially oriented scenarios.

7.2 Materials and Method

7.2.1 Research outline

Kiwifruit data was collected in 2020 and 2022. Kiwifruit were harvested from multiple orchards with multiple maturities and stored in different conditions to obtain a wide range of FF and LBI data. In Table 7.1, experiments conducted to achieve research objectives were listed.

Table 7.1. Research outline.

<table>
<tr><td colspan="2">Objectives</td><td>I. Ripening through 14 days at 20 °C (2020)
$n_{Zesy002}$=627
$n_{Hayward}$=2032</td><td colspan="2">II. Ripening after 7 days at 20 °C (2022)
$n_{Zesy002}$=810
$n_{Hayward}$=810</td><td>III. Ripening after cool storage at 1 °C (2022)
$n_{Zesy002}$=810
$n_{Hayward}$=716</td></tr>
<tr><td colspan="2">i. Correlation</td><td>FF & LBI changes and correlation</td><td colspan="2"></td><td></td></tr>
<tr><td rowspan="2">ii. Model evaluation</td><td>Zesy002</td><td>Test_1</td><td>$Data_{cal}$</td><td>$Data_{val}$</td><td>Test_2</td></tr>
<tr><td>Hayward</td><td>$Data_{cal}$ | $Data_{val}$</td><td colspan="2">Test_1</td><td>Test_2</td></tr>
<tr><td rowspan="2">iii. Model feasibility</td><td rowspan="2">Ripening stages 5 % soft fruit</td><td colspan="2">$Data_{cal}$</td><td colspan="2">$Data_{val}$</td></tr>
<tr><td colspan="2">$Data_{cal}$</td><td>$Data_{val}$</td></tr>
</table>

The correlation between FF and LBI was investigated using kiwifruit data collected through shelf-life ripening. Then the FF segregation model was calibrated, validated and tested with

different data sets. In the end, the FF segregation model feasibility was evaluated with different subsamples. These subsamples may represent kiwifruit populations expected at different ripening stages during storage and at late ripening stages where the population contained 5% soft fruit.

7.2.2 Fruit source

Kiwifruit 'Zesy002' and 'Hayward' were harvested from the Bay of Plenty, New Zealand, in 2020 and 2022. Kiwifruit were commercially graded at the packhouse and delivered to Massey University. In this study, fruit of uniform shape and no scar or sunburn observed on the surface were selected.

In 2020, 'Zesy002' (n=627) were delivered on 6th May from 3 commercial orchards. 'Hayward' (n=2032) were delivered on 21st, 27th May and 5th June 2020 from 9 orchards, fruit were sourced from 3 orchards on each delivery day. 'Zesy002' were stored at 1 °C for 6 days prior to the study, while 'Hayward' analysis started the day after each arrival. After each arrival, kiwifruit were randomised into trays and packed commercially (including a polyliner to reduce water loss). 'Zesy002' (n=30) and 'Hayward' (n=30) were measured on each occasion after being stored for 1, 3, 5, 7, 9, 11 and 13 days at 20 °C. Various harvest times and ripening times resulted in different FF of kiwifruit at each assessment.

In 2022, 'Zesy002' were delivered on 21st April, 5th May and 20th May from 9 orchards with fruit from 3 orchards on each delivery day, and 'Hayward' were delivered on 2nd, 10th May and 21st June 2022 from 9 orchards with fruit from 3 orchards on each delivery day. Kiwifruit of each cultivar were divided into 2 lots according to the storage method. In fruit lot 1, 'Zesy002' (n=810) and 'Hayward' (n=810) were assessed after 7 days of storage at 20 °C. In fruit lot 2, 'Zesy002' (n=810) and 'Hayward' (n=716) were stored at 1 °C for (52-100 days) before

assessment. Kiwifruit stored at the cool store were warmed to room temperature overnight before assessment.

Table 7.2. 'Zesy002' and 'Hayward' fruit source. The correlation of fruit flesh firmness (FF) and Laser backscattering parameters is investigated with $Data_{cor}$ data set. Fruit information is provided for the segregation model with fruit number and flesh firmness (FF) in model calibration ($Data_{cal}$), cross-validation ($Data_{val}$) and test set validation (Test_1&2). Kiwifruit were harvested with Early (E), Middle (M) and Late (L) maturities from different commercial orchards in2 harvested years. Kiwifruit were ripened at different temperatures (Temp, °C) and through different storage times (D). Model feasibility is evaluated with calibration ($Data'_{cal}$), and cross-validation ($Data'_{val}$) data set.

Maturity	Orchards	Year	Fruit number	Temp	Storage	Correlation	Segregation	Feasibility
Zesy002								
E, M & L	9	2022	640	20	7		$Data_{cal}$	$Data'_{cal}$
E, M & L	9	2022	170	20	7		$Data_{val}$	(n=1787)
L	3	2020	627	20	1-13	$Data_{cor}$	Test_1	& $Data'_{val}$
E, M & L	9	2022	810	0	80, 94, 102		Test_2	(n=430)
Hayward								
E, M & L	9	2020	1640	20	1-13	$Data_{cor}$	$Data_{cal}$	$Data'_{cal}$
E, M & L	9	2020	392	20	1-13	$Data_{cor}$	$Data_{val}$	(n=2863)
E, M & L	9	2022	810	20	7		Test_1	& $Data'_{val}$
E, M & L	9	2022	716	0	58, 66, 70		Test_2	(n=725)

Kiwifruit collected from 2020 were ripened at 20 °C ($Data_{cor}$) to study the correlation between FF and LBI (Table 7.2). For FF segregation model calibration (Table 7.2), 80% of the 2022-harvested lot 1 'Zesy002' population ($Data_{cal}$) were randomly selected (n=640), and 20% of fruit (n=170) were used in cross-validation ($Data_{val}$). For 'Hayward', 80% of the 2020-harvested population were randomly selected as $Data_{cal}$ (n=1640) and 20% of fruit (n=392) were used in $Data_{val}$. For test validation, 2020-harvested 'Zesy002' and 2022-harvested lot 1'Hayward' were used for Test _1, whilst 2022-harvested lot 2 kiwifruit were used for Test _2. For segregation model feasibility assessment, 80% of all kiwifruit were randomly selected (n=1787, 2863) as calibration data ($Data'_{cal}$) and 20% (n=430, 725) were validation data ($Data'_{val}$) for 'Zesy002' and 'Hayward', respectively.

7.2.3 Kiwifruit image and quality measurement

Paired kiwifruit FF and LBI data were collected on the same measurement day. Each kiwifruit was placed longitudinally on the moving table. Kiwifruit LBI were taken at 2 positions 90° apart at an equatorial region (Figure 4.3) with the improved LBI imaging system (Section 3.2.2). The 2 positions corresponded to the focus points of the laser pointer when imaging the samples.

Kiwifruit FF and SSC measurement methods were described in Section 5.2.2. DMC was measured at harvest. A 2 mm flesh slice was obtained from the equator of each fruit and placed in a petri dish, then dried using a food dehydrator (ULTRA FD1000, Ezidri, New Zealand) at 65°C for 24 h. The fresh weight (FW) and dry weight (DW) of the flesh slice were determined using an electronic balance (TW423L, Shimadzu, Japan). DMC was calculated using Eq. 7.1. The DMC of kiwifruit after storage was estimated using at-harvest fruit DMC of the same batch.

$$DMC = \frac{DW}{FW} \times 100 \qquad \text{Eq. 7.1}$$

where DW is the weight of the fruit slice after drying (g) and FW is the weight of the fruit slice before dehydrating (g).

Kiwifruit Brix when fully ripe (BWFR, %) is a maturity indicator utilized in the industry for at-harvest quality assessment. The BWFR indicates the starch-sugar conversion status during fruit ripening (Eq. 7.2). Therefore, BWFR was selected to investigate kiwifruit at harvest maturity and ripening stages in this work.

$$BWFR = \frac{SSC}{DMC + \frac{DMC - SSC}{9} - 3.5} \times 100 \qquad \text{Eq. 7.2}$$

where SSC is total soluble solid content (%) and DMC is dry matter content (%).

7.2.4 Data analysis

Kiwifruit LBI image analysis method was described in Section 3.2.3. A total of 20 LBI parameters at 5 wavelengths were extracted for kiwifruit considering all variables at different wavelengths, which are DIP, FWHM, SLP and HWQM (Eq. 6.1) at 520, 660, 685, 785 and 830 nm, respectively. In this study, LBI parameters per kiwifruit were averaged with extracted LBI parameters from two LBI images obtained in the equatorial region (Figure 4.3). LBI parameters were normalized at each wavelength to compare among the wavelengths and the normalized LBI parameter (NLBI) at each wavelength is calculated as Eq. 7.3

$$NLBI_n = \frac{LBI}{LBI_{max} + LBI_{min}} \qquad \text{Eq. 7.3}$$

Where LBI is the LBI parameter value for induvial kiwifruit, LBI_{max} and LBI_{min} are the maximum and minimum LBI parameter values at a selected wavelength *n* within the kiwifruit population, respectively.

Kiwifruit FF and SSC data collection were described in Section 5.2.2. The means of at-harvest fruit quality attributes were compared by ANOVA with Tukey HSD test (p-value < 0.05). Pearson correlations between 20 LBI parameters and kiwifruit FF were analysed using 'stats' package (version 3.6.2). LBI parameters were selected based on the correlation significance, and selected parameters were utilized for FF estimation with partially least square analysis (PLS) via 'pls' package (version 0.13.0) with 2 components. PLS could reduce the noise of complex data and predictor multicollinearity, where selected LBI parameters were correlated in this study. In addition, PLS extracted latent variables for reduce data dimension and capture the important features. Compared with other regression models, PLS usually has a better prediction accuracy by maximizing the covariance between predictors and responses (Wold, 1975). In the PLS

analysis, input LBI parameters and FF were normalized with log transformation to avoid negative FF estimation values. PLS model was developed using $Data_{cal}$, then validated and tested with $Data_{cal}$ and Test_1 & 2 (Table 7.2). Root mean square error (RMSE), residual sum of squares (RSS), total sum of squares (TSS), coefficient of determination (R^2 for $Data_{cal}$ and Q^2 $Data_{val}$) and mean bias error (MBE) were compared for model performance assessment (Eq. 7.4 - Eq. 7.8).

$$RMSE = \sqrt{\frac{\sum_{i=1}^{n}(y_i - \hat{y}_i)^2}{n}} \quad \text{Eq. 7.4}$$

$$RSS = \sum_{i=1}^{n}(y_i - \hat{y}_i)^2 \quad \text{Eq. 7.5}$$

$$TSS = \sum_{i=1}^{n}(y_i - \overline{y})^2 \quad \text{Eq. 7.6}$$

$$R^2/Q^2 = 1 - \frac{RSS}{TSS} \quad \text{Eq. 7.7}$$

$$MBE = \frac{\sum_{i=1}^{n}(y_i - \hat{y}_i)}{n} \quad \text{Eq. 7.8}$$

Where y_i is the destructively measured FF of the *i*th fruit, $\hat{y}_i$ is the estimated FF of the *i*th fruit, *n* is the total fruit number, $\overline{y}$ is the average FF. Good FF estimation model performance can be interpreted with high R^2 or Q^2, low RMSE and low MBE.

As FF value estimation is challenging, the FF segregation model was developed using Gause Naïve Bayes Classifier via 'klaR' package (version 1.7-1). FF segregation model was trained, calibrated, validated and tested with associated data sets (Table 7.3). Kiwifruit segregation model performance was presented using a confusion matrix (Section 3.4.4).

Table 7.3. 'Zesy002' and 'Hayward' flesh firmness (FF) segregation model development.

Segregation	Training	Calibration	Validation	Test	Section
Different FF threshold	$Data_{cal}$	$Data_{cal}$	$Data_{val}$	Test_1&2	7.3.3
Different BWFR threshold	$Data'_{cal\_L,M,E}$	$Data'_{cal\_L,M,E}$	$Data'_{val\_L,M,E}$		7.3.4.2
Late ripening	$Data^*_{cal\_L}$	$Data^*_{cal\_L}$	$Data^*_{val\_L}$		7.3.4.3

The segregation model was first evaluated using the minimal FF export threshold at 9.8 N, then at 2 additional thresholds of 6.9 and 19.6 N, which are the 'Eating firmness' and 'Ripening' thresholds, respectively (Fullerton et al., 2020). The integrating FF threshold was assessed using the soft fruit incidence (SFI) to the soft fruit percentages Eq. 7.9.

$$SFI = \frac{n_{soft}}{n_{soft} + n_{firm}} \quad \text{Eq. 7.9}$$

Where n_{soft} is the soft fruit number, n_{firm} is the firm fruit number. SFI is a parameter describing soft fruit percentage in data sets at different FF thresholds.

The segregation model was then evaluated using BWFR as a threshold to segregate kiwifruit at different ripening stages. In the end, the segregation model performance at the late ripening stage was evaluated. A 5 % SFI was designed and may represent the before-exporting scenario with a low incidence of soft fruit within a large amount of firm fruit. Details of BWFR threshold and subsampling are described in Section 7.3.4.

7.3 Results and discussion

7.3.1 Kiwifruit harvest quality

In 2020, 'Zesy002' kiwifruit at-harvest FF (Figure 7.1A) was similar at 45 N for all 3 orchards. However, for BWFR (Figure 7.1B), orchard 2 had a lower BWFR (85.5 %) compared with the other two orchards (90.8 and 92.4 %). Fruit from all 3 orchards showed advanced maturity, given the high BWFR values. There is a tendency for higher FF corresponding to lower BWFR, but there can be a wide range of FF values at a given BWFR (Figure 7.1C).

In 2022, 'Zesy002' at-harvest FF (Figure 7.2A) was lower (35 N) for late harvest compared with early and middle harvests (55 N). Co-ordinately, orchards 7 - 9 in late harvested kiwifruit had higher BWFR (> 95%) compared to other orchards. Other orchards had around 80 % BWFR except for orchard 2 which had the lowest BWFR at 62.5 % (Figure 7.2B). FF reduced with increasing BWFR (R = -0.77, p-value < 0.05, Figure 7.2C) in 2022, while the correlation was not as clear in 2020 (R = -0.31, p-value < 0.05, Figure 7.1C), which might be due to the fruit variability among orchards. A lag phase of correlation trend for 'Zesy002' was observed in Figure 7.2C, this lag phase contained kiwifruit with FF in the range between 50 – 70 N and BWFR below 80 %. The lag phase could be due to the fact that kiwifruit starch breakdown begins in the 1st phase of softening, while SSC increases coincides with softening during the early stage of rapid 2nd softening (Zhao, 2017).

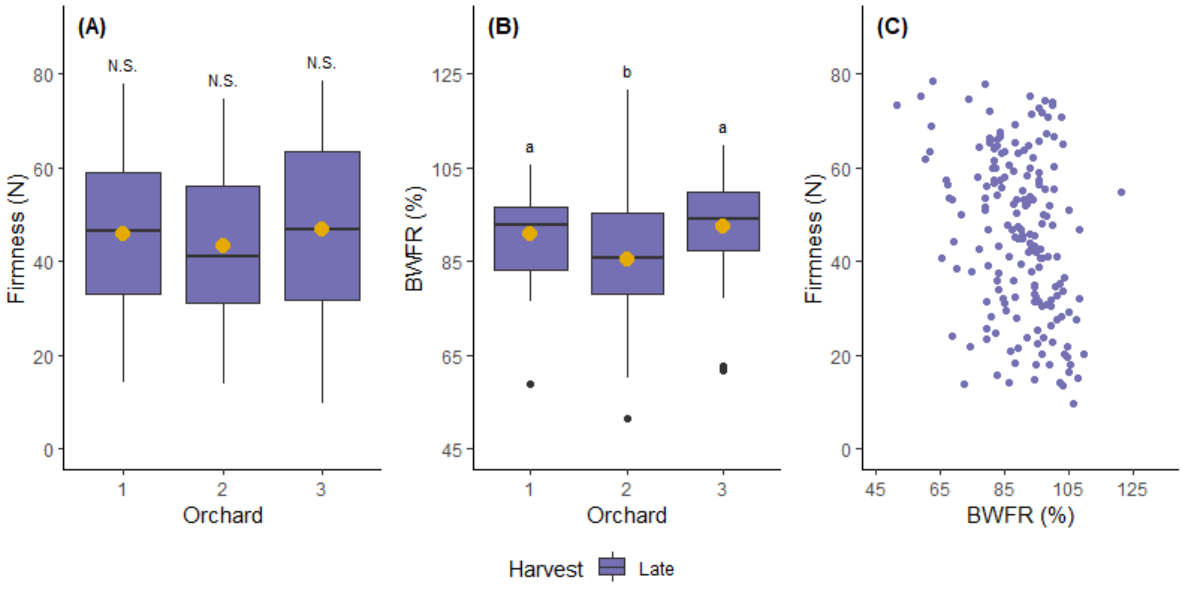

Figure 7.1. Kiwifruit (n=90) at harvest quality assessment in 2020 for 'Zesy002' of (A) flesh firmness, (B) Brix when fully ripe (BWFR) and (C) individual fruit correlation between (A) and (B). Letters represent a significant difference between orchards by Tukey HSD (p-value < 0.05). The yellow point represents the mean in A and B.

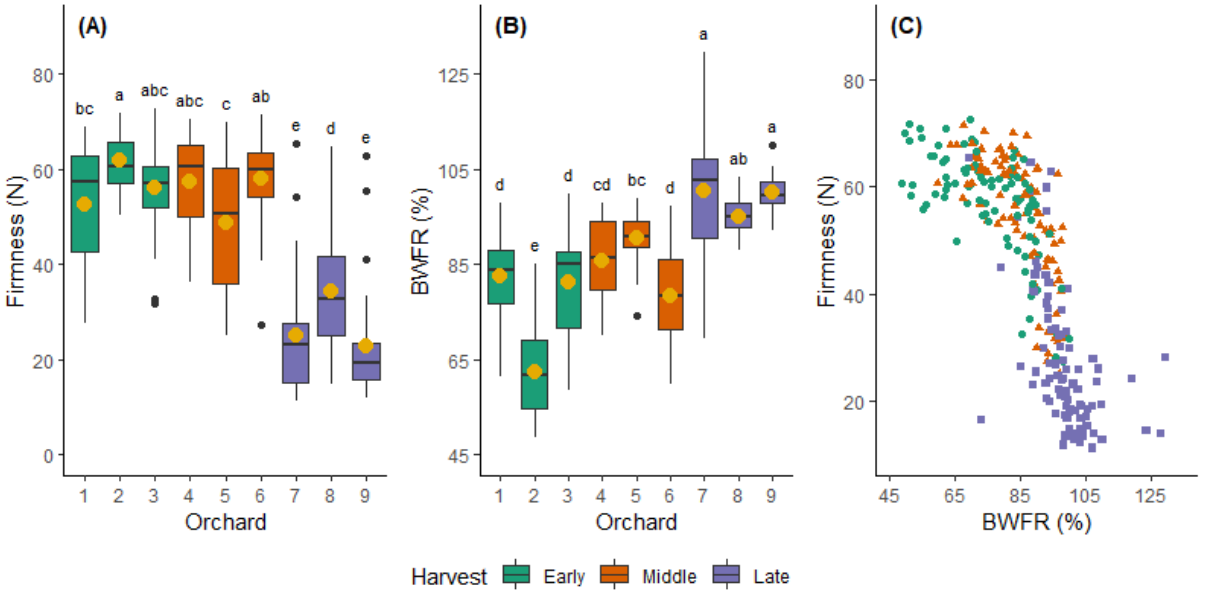

Figure 7.2. Kiwifruit (n=270) at harvest quality assessment in 2022 for 'Zesy002' of (A) flesh firmness, (B) Brix when fully ripe (BWFR) and (C) individual fruit correlation between (A) and (B). Letters represent a significant difference between orchards by Tukey HSD (p-value < 0.05). The yellow point represents the mean in A and B.

For 'Hayward', kiwifruit at-harvest FF (Figure 7.3A) was 40 N for late harvest and 59 N for early and middle harvest in 2020. 'Hayward' orchards 1-2 from early harvest had the lowest BWFR (Figure 7.3B) of 65.5 % compared with orchards 3, 5 & 6 (73.3, 77.5 and 72.8 %) and orchards 4 (82 %). Orchards 7-9 in late harvest had the highest BWFR of around 85 %. However, the lag phase (around FF between 60 – 70 N and BWFR between 50 – 75 %) obtained in Figure 7.2C wasn't observed in Figure 7.3C. This may be due to the difference between cultivars and at harvest maturity, as 'Hayward' had a higher at-harvest FF of around 55 % BWFR.

In 2022, 'Hayward' kiwifruit at-harvest FF (Figure 7.4A) was 34 N for orchards 4 & 7-9, and 56 N for orchards 1-3 & 5-6. Orchards 2-3 at early harvest had the lowest BWFR (Figure 7.4B) of around 70 % compared with orchards 1 & 4-6 (around 83 %) and orchards 7-9 (97 %). The negative relationship between BWFR and FF was observed for 2020 (R = -0.78, p-value < 0.05, and 2022 (R = -0.82, p-value < 0.05, respectively (Figure 7.3C, Figure 7.4C).

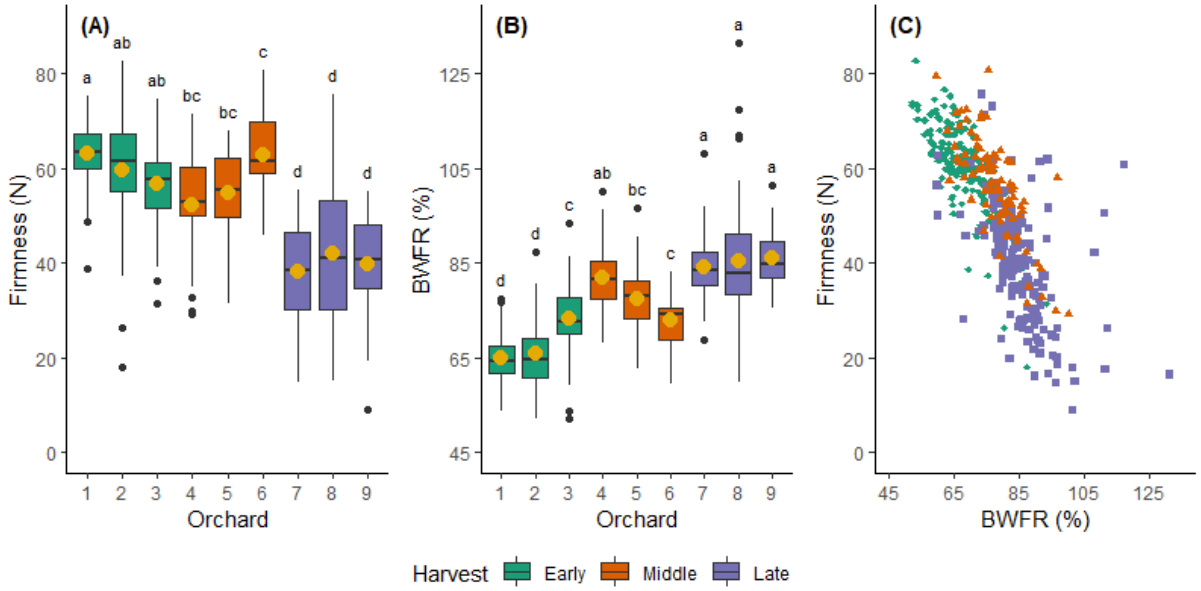

Figure 7.3. Kiwifruit (n=270) at harvest quality assessment in 2020 for 'Hayward' of (A) flesh firmness, (B) Brix when fully ripe (BWFR) and (C) individual fruit correlation between (A) and (B). Letters represent a significant difference between orchards by Tukey HSD (p-value < 0.05). The yellow point represents the mean in A and B.

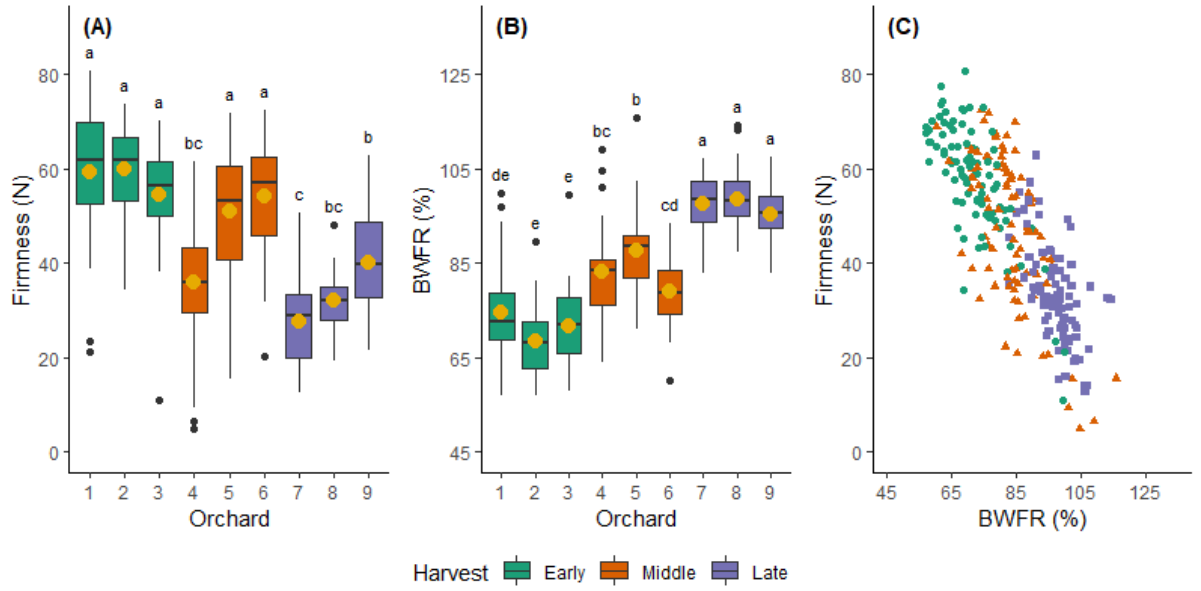

Figure 7.4. Kiwifruit (n=270) at harvest quality assessment in 2022 for 'Hayward' of (A) flesh firmness, (B) Brix when fully ripe (BWFR) and (C) individual fruit correlation between (A) and (B). Letters represent a significant difference between orchards by Tukey HSD (p-value < 0.05). The yellow point represents the mean in A and B.

As expected, later harvested kiwifruit had lower FF and higher BWFR. However, kiwifruit at harvest FF was influenced by harvest timing and other orchard practices, therefore, it's difficult to predict FF based on harvest timing only.

7.3.2 Changes in kiwifruit firmness and LBI parameter

7.3.2.1 Kiwifruit quality changes during shelf-life ripening

A decreasing FF (Figure 7.5A) and increasing BWFR (Figure 7.5B) was observed for 'Zesy002' through postharvest ripening in 2020. During kiwifruit ripening, decreasing FF results from cell wall degradation, and increasing BWFR is due to increasing SSC resulting from sugar-starch conversion (Kim et al., 1999; Schröder & Atkinson, 2006). A large variation was observed for the ripening process, which may be due to the variation of fruit batches from different orchards, resulting in un-uniform shelf-life ripening patterns (Figure 2.1).

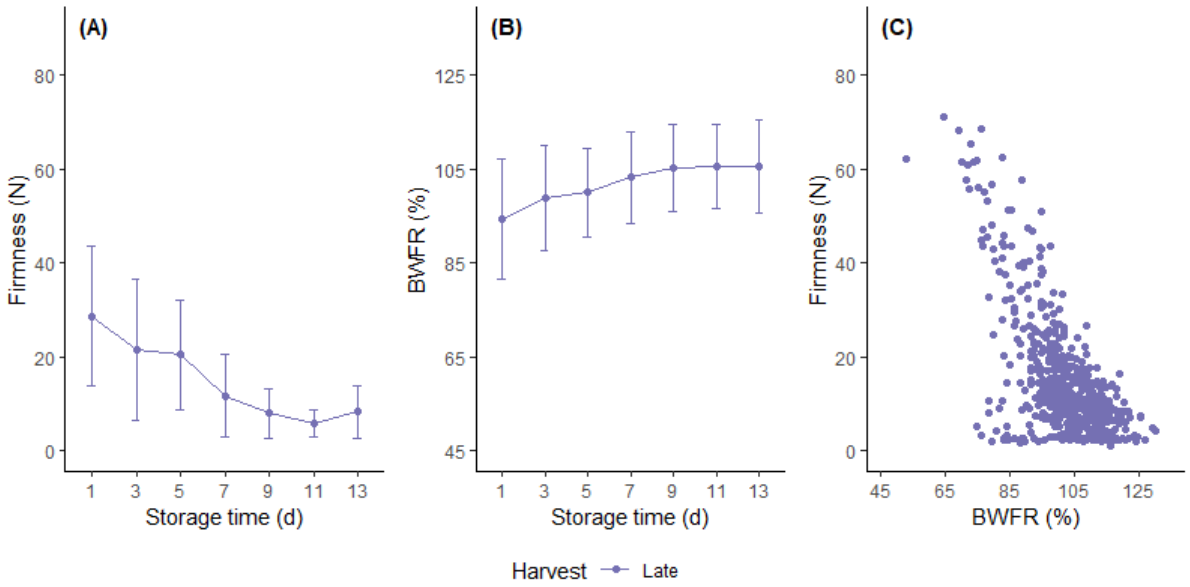

Figure 7.5. Averaged kiwifruit (A) flesh firmness (FF), (B) Brix when fully ripe (BWFR) and (C) individual fruit correlation of FF and BWFR during shelf-life ripening at 20 °C for 'Zesy002' in the FF segregation model calibration dataset. Each data point in A and B represents a destructive measured sub-sample (n = 30). Error bars represent the standard deviation.

For 'Zesy002' kiwifruit (Figure 7.5C), a negative correlation of FF and BWFR was observed, and a larger range of BWFR was observed at lower FF. Those low FF could be resulted from lower initial BWFR (Figure 7.1C) or underestimated BWFR due to an overestimation of kiwifruit DMC after storage using the at harvest data (Eq. 7.2). In the 3rd rapid softening stage, internal ethylene production is triggered and starch-sugar conversion results in increased SSC (Schröder

& Atkinson, 2006), and it's not consistently correlated with FF. Therefore, BWFR cannot be used as a single factor to explain the FF variability in post-storage repining.

When looking at the shelf-life ripening of 'Hayward' kiwifruit (Figure 7.6), similar trends and large variability were observed as for 'Zesy002'. Additionally, differences were observed for different harvests. Early and middle-harvested kiwifruit had higher FF than late-harvest kiwifruit at the beginning but reached a similar FF range at the end of the storage (Figure 7.6 A). For BWFR (Figure 7.6B), the initial BWFR was affected by the harvest time, fruit reached a similar BWFR at the end of storage. In general, late-harvest kiwifruit have a lower initial FF and higher BWFR, this agrees with previous knowledge of kiwifruit softening (Lallu et al., 1989; MacRae et al., 1990; Jabbar et al., 2014). Similar to 'Zesy002', the FF and BWFR of 'Hayward' fluctuated during shelf-life ripening due to the variability among fruit samples sourced from different orchards.

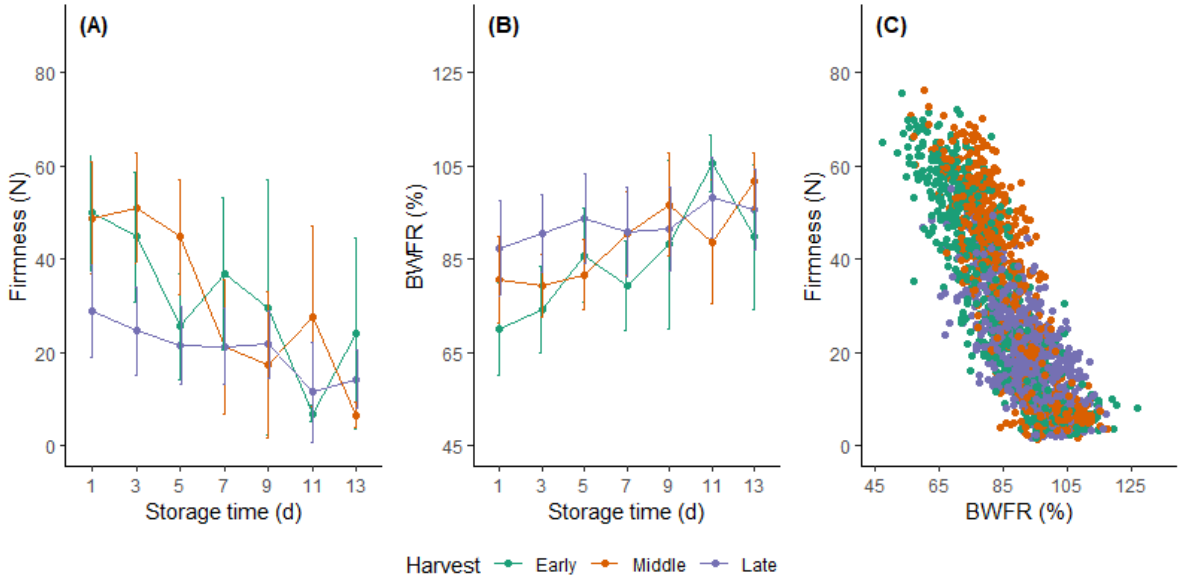

Figure 7.6. Average kiwifruit (A) flesh firmness (FF), (B) Brix when fully ripe (BWFR) and (C) individual fruit correlation of FF and BWFR during shelf-life ripening at 20 °C for 'Hayward' in the FF segregation model calibration dataset. Each data point in A and B represents a destructive measured sub-sample (n = 30). Error bars represent the standard deviation.

7.3.2.2 Kiwifruit LBI parameter changes during shelf-life ripening

LBI parameters were normalized using Eq. 7.3 to compare trends at different wavelengths. Average normalized LBI parameters (NLBI) of the subsample kiwifruit increased through shelf-life ripening (Figure 7.7). This observation agreed with the findings in previous results (Figure 6.1, Figure 6.2). Large variation at each measurement occasion ($n_{Zesy002}$ = 30, $n_{Hayward}$ = 90) was also observed for all wavelengths for both cultivars.

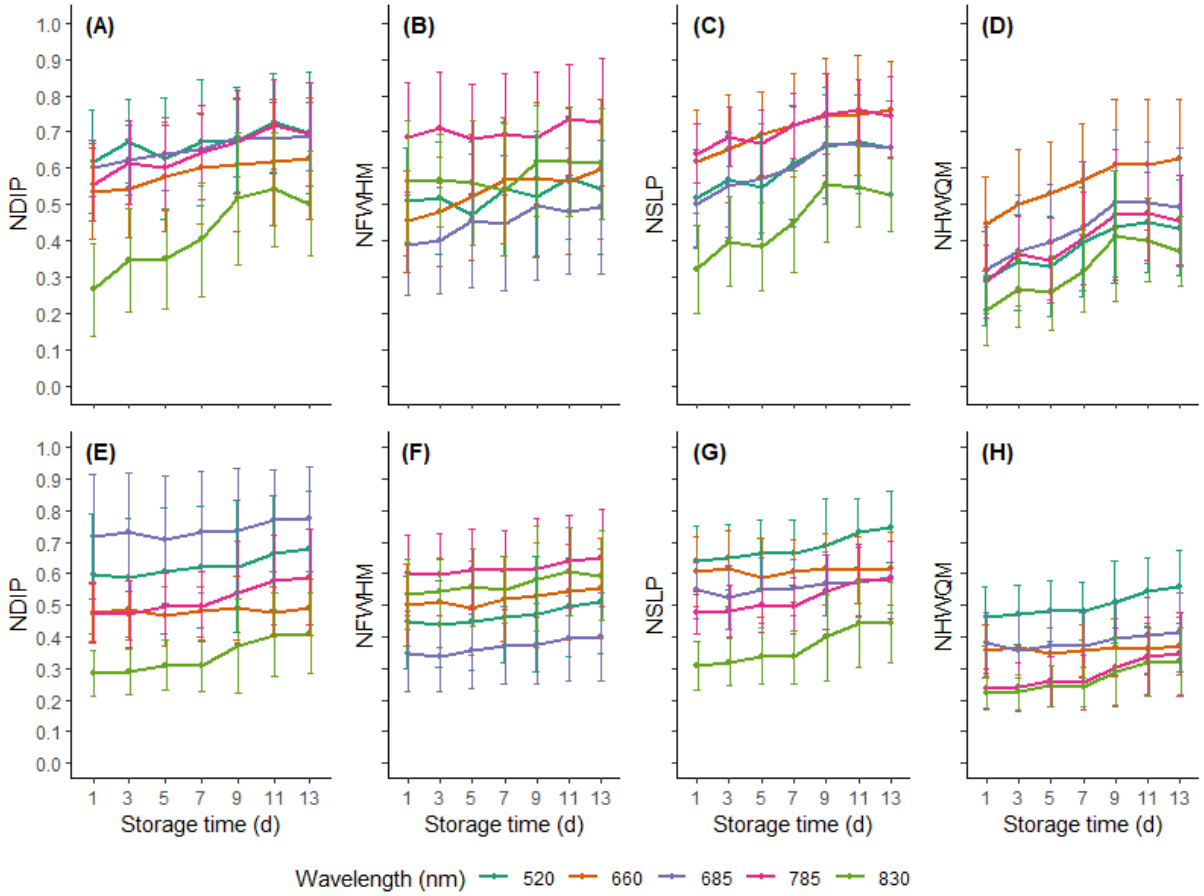

Figure 7.7. Average normalized kiwifruit LBI parameter change during shelf-life ripening at 20 °C for 'Zesy002' (A-D) and 'Hayward' (E-H) in the model calibration dataset. Each data point represents a non-destructive measured sub-sample ($n_{Zesy002}$ = 30, $n_{Hayward}$ = 90). Error bars represent the standard deviation. Different colour represents different wavelengths which LBI parameters are extracted from.

For 'Zesy002', the average NDIP (Figure 7.7A) increased from 0.25 to 0.50 at 830 nm, and from around 0.55 to around 0.70 at other wavelengths. Average NSLP (Figure 7.7C) and average NHWQM (Figure 7.7C) increased steadily (around 0.20-unit increase) through storage at all

wavelengths. Average NFWHM (Figure 7.7B) was relatively stable at all wavelengths compared with other LBI parameters.

For 'Hayward' (Figure 7.7E-H), similar increasing trends were observed for LBI parameters through shelf-life ripening but to a lesser extent. Average NDIP (Figure 7.7E) increased around 0.1 for 3 wavelengths (0.3 – 0.4 at 830 nm, 0.5 – 0.6 at 785 nm and 0.6 – 0.7 at 532 nm), agreeing with previous results (Figure 6.2a). However, steady trends were observed at 660 and 685 nm. This result is possibly due to the chlorophyll absorption of the green flesh, which also influences the LBI result as those 2 wavelengths are at the chlorophyll absorption peak. Similar trends were observed for average NSLP (Figure 7.7G) and average NHWQM (Figure 7.7H) at 520, 785, and 830 nm, with a 0.1-unit increase observed. Less fluctuation was observed in average NFWHM (Figure 7.7F) compared with 'Zesy002' (Figure 7.7B), possibly due to 'Hayward' having a bigger sample size (Table 7.2). For wavelengths 785 and 830, the trend of all LBI parameters was similar and almost in parallel, which the minimal absorbance of pigment may explain at these two wavelengths.

7.3.2.3 Kiwifruit LBI parameter and firmness correlation

During shelf-life ripening, increasing LBI parameters were observed with decreasing FF regardless of the ripening stage (Figure 7.8), agreeing with previous results (Figure 6.5). LBI parameters of 'Zesy002' (Figure 7.8A-D) trends were clear at 785 and 830 nm, potentially resulting from minimal influence from pigments at these two wavelengths. A negative correlation between FF and LBI parameters was also observed for 'Hayward' (Figure 7.8E-H). The lower LBI parameter values with large variability for 'Zesy002' at 520 nm and for 'Hayward' at 660 and 685 nm could be because flesh colour also influences LBI parameters at those wavelengths.

Pearson correlations of kiwifruit FF and LBI parameters are presented in Table 7.4. In general, kiwifruit LBI parameters are negatively correlated with FF, supporting previous research that light scattering decreases with FF reduction resulting from cell wall degradation (Harker & Hallett, 1994; Baranyai & Zude, 2009).

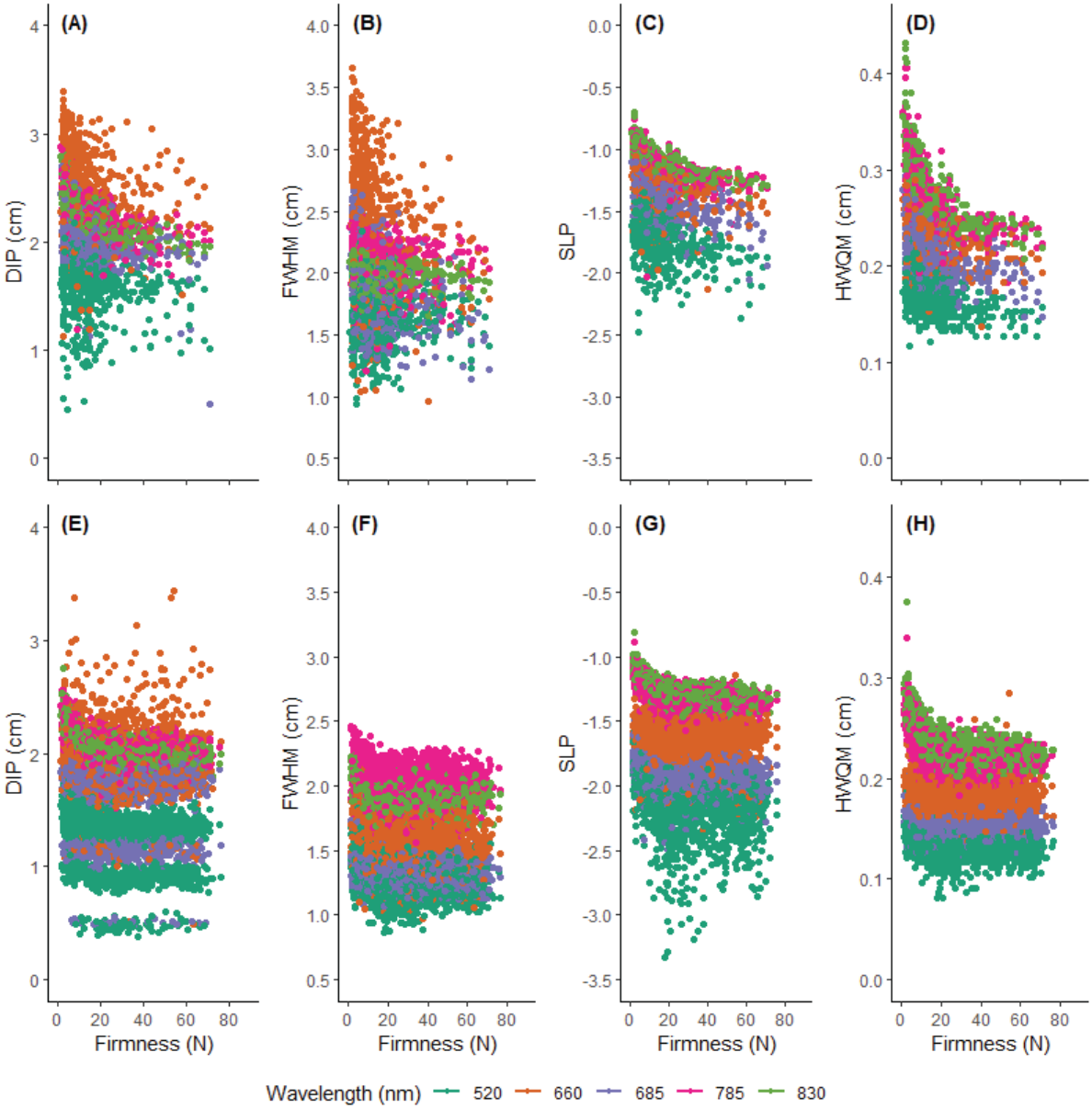

Figure 7.8. LBI parameter correlation to flesh firmness for 'Zesy002' (n=600, A-D) and 'Hayward' (n=1960, E-H) in the model calibration dataset. Different colours represent different wavelengths which LBI parameters are extracted from.

'Zesy002' FF had higher correlations with SLP at 520, 785 and 830 nm (-0.8 to -0.6), with DIP at 785 and 830 nm (-0.8 to -0.5). 'Hayward' FF higher had correlations with SLP and with DIP at

785 and 830 nm with (-0.7 to -0.5). Thus, DIP and SLP could be potentially useful LBI parameters for FF segregation (Table 7.4).

Table 7.4. LBI parameter and kiwifruit flesh firmness correlation for 'Zesy002' and 'Hayward' in model calibration dataset. Numerical values are Pearson correlation coefficient. LBI parameters at 5 wavelengths (520, 660, 685, 785 and 830 nm) include the radius of the saturated area (DIP), double the radius at 50 % of maximum intensity (FWHM), and the slope of the linear regression model (SLP) built with log-transformed profile data between the radius at 75 % of maximum intensity and the radius at 25 % of maximum intensity, the radius between 50 % and 25% of maximum intensity (HWQM).

Wavelength	520	660	685	785	830
Zesy002					
FWHM	-0.33	-0.37	-0.37	-0.13	-0.22
DIP	-0.4	-0.38	-0.41	-0.54	-0.77
SLP	-0.6	-0.47	-0.56	-0.6	-0.8
HWQM	-0.57	-0.52	-0.56	-0.65	-0.76
Hayward					
FWHM	-0.31	-0.26	-0.36	-0.22	-0.31
DIP	-0.29	-0.06	-0.17	-0.53	-0.67
SLP	-0.44	-0.07	-0.3	-0.59	-0.68
HWQM	-0.06	-0.03	-0.04	-0.58	-0.66

Although the HWQM had a high correlation with FF, it was also highly correlated (0.8) with SLP at all wavelengths. This could be due to SLP containing largely attenuation information (75 % to 25 % of maximum intensity) and includes the information that HWQM carries (the second part of the attenuation profile). Thus, HWQM was excluded for the FF segregation model to avoid overfitting of the model.

FWHM was the least correlated parameter at all wavelengths for both cultivars, thus, FWHM does not look to be a suitable parameter for FF estimation. FWHM represents information on the first half of the attenuation profile, which possibly carries information related to absorption rather than scattering. Absorption and scattering properties affect information at different parts of the attenuation curve as determined using time-resolved analysis (Cubeddu et al., 1996). Besides, Hashim et al. (2014) reported that FWHM was related to banana ripening stages

as a result from chlorophyll absorption changes. Therefore, the relationship between SSC and FWHM could be studied in the future.

In conclusion, DIP and SLP in the short-NIR region (785 and 830 nm) were identified as the most suitable LBI parameters for FF segregation. The selected LBI parameters were utilized to estimate FF and investigate the ability to classify soft fruit from firm fruit in the next sections.

7.3.2.4 Kiwifruit firmness estimation using partially least square analysis

For 'Zesy002' PLS analysis, R^2 was 0.58 for $Data_{cal,}$ and Q^2 was 0.61 and 0.47 for $Data_{val}$ and Test_1, respectively. A negative Q^2 was found for Test_2, which indicated the FF estimation model had a poor fit for Test_2. 'Hayward' PLS model had both low R^2 (0.32) and Q^2 (0.32) and showed poor FF estimation performance. For both cultivars, negative MBE indicated that the estimated FF was underestimated in $Data_{cal}$ and $Data_{val}$, whilst the estimated FF was overestimated for Test_1 and Test_2 with MBE above 0.

Table 7.5. Kiwifruit 'Zesy002' and 'Hayward' estimated firmness with partial least square regressing analysis. Mean square error (RMSE, N), coefficient of determination (R^2/Q^2) and mean bias error (MBE, N) for calibration ($Data_{cal}$), cross-validation ($Data_{val}$) and test validation (Test_1, Test_2) are provided.

	n	RMSE	R^2/Q^2	MBE	n	RMSE	R^2/Q^2	MBE
	Zesy002				Hayward			
$Data_{cal}$	640	14.03	0.58	-3.16	1640	15.66	0.32	-2.78
$Data_{val}$	170	11.91	0.61	-3.43	392	14.94	0.32	-2.00
Test_1	627	9.37	0.47	2.91	810	13.67	0.03	5.50
Test_2	810	9.65	-18.17	5.54	716	6.60	-2.46	1.88

A scatter plot of kiwifruit measured FF and estimated FF using PLS regression was presented for 'Zesy002' and 'Hayward' (Figure 7.9). For both cultivars, there were significant displacements of the estimated FF from the 1:1 reference line showing the difference in FF described. This result was similar to other non-destructive FF estimations. Li et al. (2016) reported a log-fitted curve between non-destructive and penetrometer FF, whilst this curve

covered a wider range than this study. McGlone & Jordan (2000) reported that non-destructive air-puff FF measurement had better performance in soft fruit classification than FF estimation. The incorrect estimation of FF between 10 – 90 N could result from multiple factors causing FF reduction, such as cell wall, cell size and porosity (Hallett et al., 1992), whilst all those could influence LBI parameters differently. Therefore, estimating FF quantitatively is challenging, while the segregation of FF may be achievable.

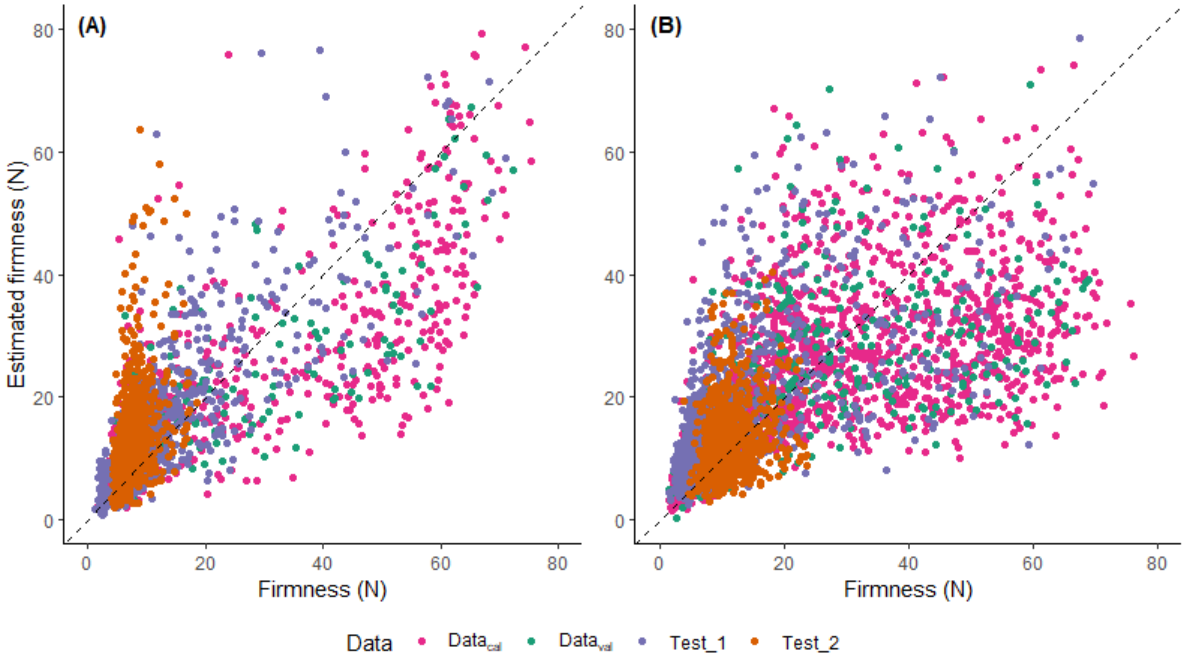

Figure 7.9. Estimated flesh firmness using PLS regression with LBI parameters for 'Zesy002' (A) and 'Hayward' (B). Pink scatter points were fruit data in the calibration (Data$_{cal}$), green scatter points were fruit data in the cross-validation (Data$_{val}$), purple scatter points were fruit data in the test validation 1 (Test_1), orange scatter points were fruit data in the test validation 2 (Test_2).

7.3.3 Kiwifruit firmness segregation

7.3.3.1 Fruit quality in model calibration, validation and tests.

The kiwifruit FF segregation model was built with a calibration data set collected through ripening and then tested with separated kiwifruit datasets from different seasons and with different storage methods. The Data$_{cal}$ is expected to encompass the widest range of FF variability as the calibration dataset to ensure the segregation model is robust. However,

'Zesy002' ripening study data (in 2020) covered a narrower FF range than in 2022 (Figure 7.10), which may affect the performance of segregation model. Therefore, the segregation model utilized the dataset in 2022 with the largest FF range for calibration and internal validation. The smaller FF range dataset in 2020 was utilized as a test set instead (Table 7.2).

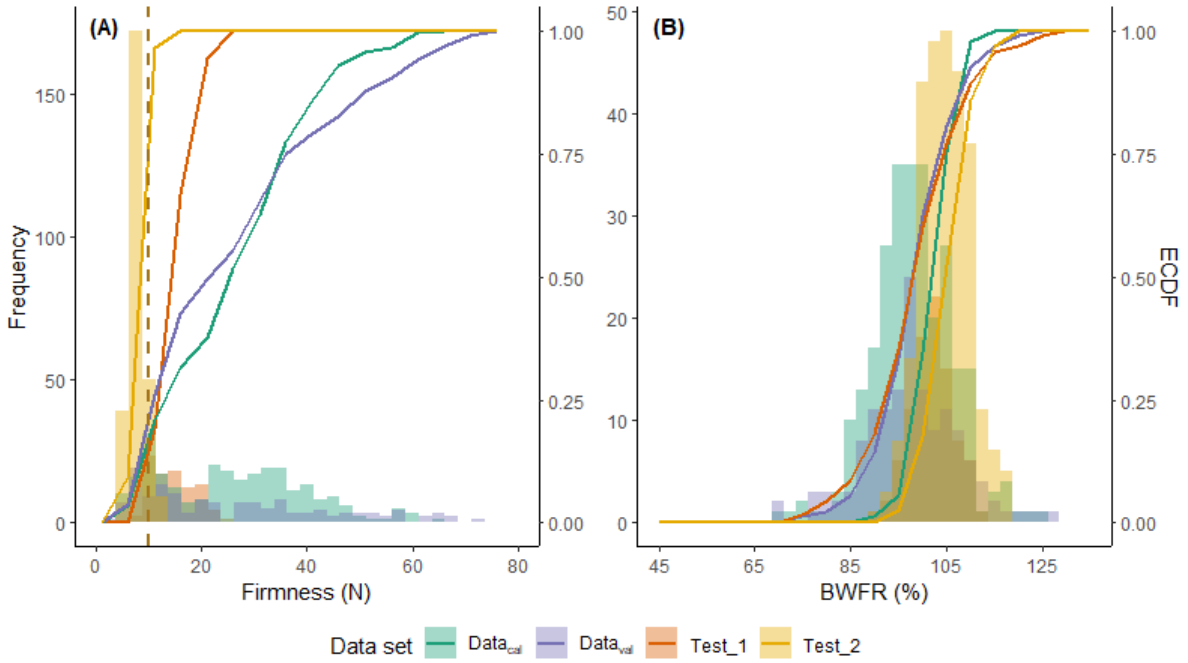

Figure 7.10. Kiwifruit 'Zesy002' population density and empirical cumulative distribution function (ECDF) line among flesh firmness (FF, A) and Brix when fully ripe (BWFR, B) for data sets of model calibration (Data$_{cal}$), cross-validation (Data$_{val}$), and test validation (Test_1, Test_2).

For 'Zesy002', Data$_{cal}$ and Data$_{val}$ populations have a widely distributed FF between 5 – 75 N (Figure 7.10a). Test_ 1 had the most FF ranging between 5 – 20 N, and Test_2 had most low FF fruit below 10 N (Figure 7.10a). Test_1 had the smallest average FF for soft fruit at 5.8 N compared with Data$_{cal}$ (6.9 N), Data$_{val}$ (7.2 N), and Test _2 (7.2 N) (Table 7.6). Both test sets had lower averaged FF (22.2 N and 12.3 N) compared with Data$_{cal}$ (37.6 N) and Data$_{val}$ (32.3 N) for firm kiwifruit (Table 7.6). Co-ordinately, 'Zesy002' Data$_{cal}$ and Data$_{val}$ populations' BWFR were the widest and between 60 – 100 % (Figure 7.10B). Test _2 had more high BWFR (90 – 110 %) fruit than Test _1.

Table 7.6. Kiwifruit 'Zesy002' and 'Hayward' number (n), average firmness (FF_mean, N) and firmness standard deviation (FF_sd, N) of soft (< 9.8 N) and firm kiwifruit

	Soft			Firm		
	n_1	FF_mean	FF_sd	n_2	FF_mean	FF_sd
Zesy002						
$Data_{cal}$	225	6.85	1.72	415	37.59	19.90
$Data_{val}$	44	7.17	1.65	126	32.31	18.19
Test_1	302	5.75	2.54	325	22.12	13.36
Test_2	704	7.22	1.24	106	12.33	2.29
Hayward						
$Data_{cal}$	488	6.05	2.00	1152	33.94	16.75
$Data_{val}$	124	6.17	2.00	268	32.81	16.06
Test_1	447	5.71	2.02	363	25.35	14.65
Test_2	304	8.25	1.11	412	13.34	3.16

'Hayward' kiwifruit FF had a normal distribution for $Data_{cal}$ and $Data_{val}$, while Test_1 and Test_2 had a narrow range of FF around 10 N (Figure 7.11a). $Data_{cal}$ and $Data_{val}$ had higher average FF than Test_1 for both soft and firm kiwifruit at around 6 N and 33 N, respectively (Table 7.6). Test_2 had a higher average FF at 8.3 N for soft fruit, but a lower FF (13.3 N) in firm fruit compared with other data sets. In Test_1 soft kiwifruit average FF (5.7 N) was the lowest and firm fruit FF (25.4 N) was higher than Test_2 but lower than $Data_{cal}$ and $Data_{val}$. 'Hayward' kiwifruit BWFR also had a normal distribution (50 % – 110 %) for $Data_{cal}$ and $Data_{val}$ (Figure 7.11b). BWFR of Tests were around 85 % – 110 %. At the 9.8 N firmness threshold, Test_1 and Test_2 had around 40% soft fruit, while $Data_{cal}$ and $Data_{val}$ contained less than 25% soft fruit. The sample difference could result in different model performances and will be presented in the next section.

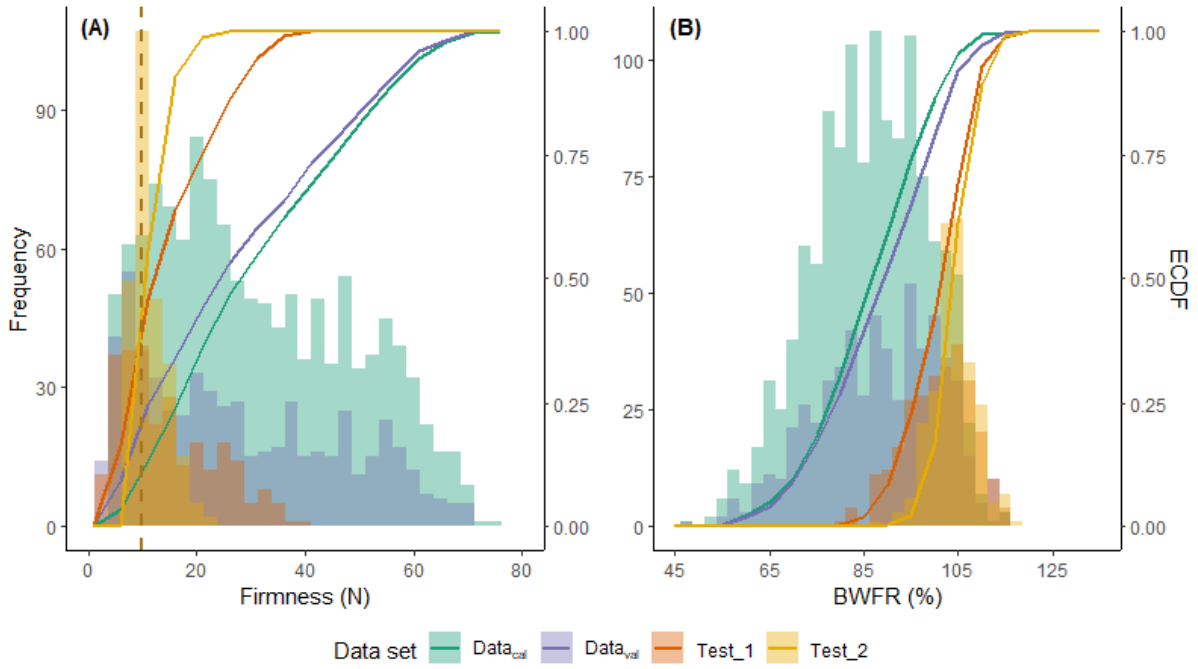

Figure 7.11. Kiwifruit 'Hayward' population density and empirical cumulative distribution function (ECDF) line among flesh firmness (FF, A) and maturity ratio (MR, B) for data sets of model calibration ($Data_{cal}$), cross-validation ($Data_{val}$), and test validation (Test_1, Test_2).

7.3.3.2 Fruit segregation using the threshold of the minimum export threshold

In this study, the minimal FF threshold for exporting at 9.8 N was used to segregate soft and firm kiwifruit (Li et al., 2017). The resulting 'Zesy002' FF distribution at each estimated FF class is presented (Figure 7.12). At the 9.8 N firmness threshold, $Data_{cal}$ and $Data_{val}$ had 35 % and 25 % soft fruit, respectively (Table 7.6). For $Data_{cal}$ and $Data_{val}$, around 80 % of soft kiwifruit were correctly segregated for kiwifruit (Table 7.7). Incorrect FF segregation (20 %, Table 7.7) was observed from underestimating firm kiwifruit into soft class (Figure 7.12AB). The overall Accuracy (0.8) and Sensitivity (0.8) were good, and Precision (0.7 and 0.5) was moderate for $Data_{cal}$ and $Data_{val}$ data sets (Table 7.7). The model performance could be interpreted as 80 % of kiwifruit were correctly segregated regardless of firmness class. In soft kiwifruit, 80 % were correctly segregated. However, only 69 % and 54 % of the segregated-soft fruit were actual soft fruit.

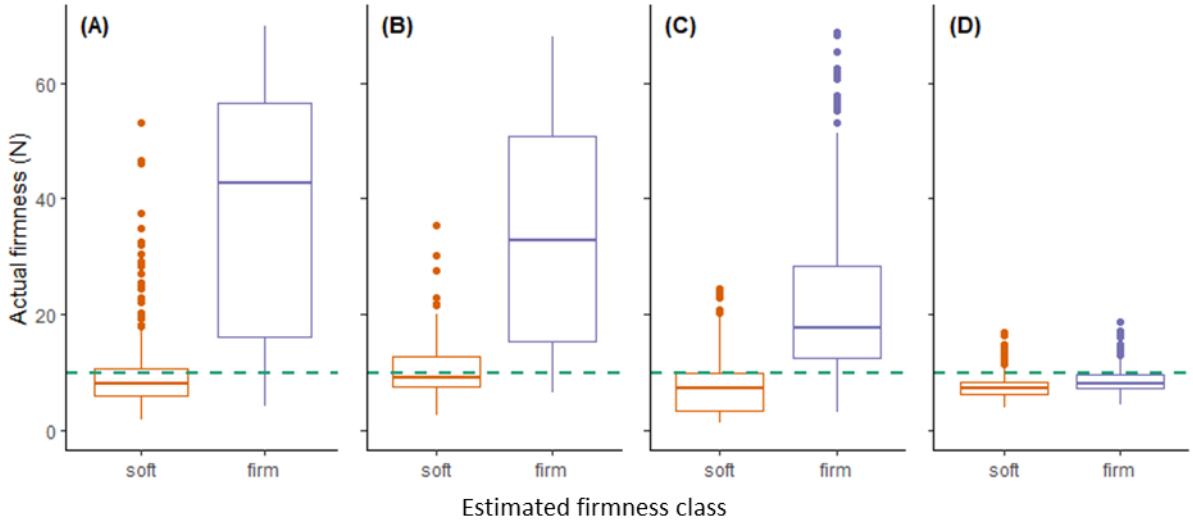

Figure 7.12. 'Zesy002' kiwifruit firmness distribution at estimated soft and firm firmness classes with the threshold of 9.8 N. Data is presented for (A) calibration model, (B) cross validation, (C) test validation 1 and (D) test validation 2. The green horizontal line represents the firmness threshold at 9.8 N.

Table 7.7. Kiwifruit 'Zesy002' and 'Hayward' firmness segregation model performance in confusion matrix with Gaussian naïve Bayes classifier (GNB). The calibrated model built with $Data_{cal}$ was validated via cross-validation dataset ($Data_{val}$) and test validation datasets (Test_1 & 2). TP and TN were correctly predicted soft (< 9.8 N) and firm kiwifruit fractions, respectively. FP and FN were incorrectly predicted firm and soft kiwifruit fractions. Segregation model performance was assessed using overall accuracy (Acc), precision (Pre) and sensitivity (Sen).

	TP	FN	FP	TN	Acc	Sen	Pre
Zesy002							
$Data_{cal}$	0.8	0.2	0.2	0.8	0.8	0.8	0.69
$Data_{val}$	0.77	0.23	0.23	0.77	0.77	0.77	0.54
Test_1	0.87	0.13	0.25	0.75	0.8	0.87	0.74
Test_2	0.71	0.29	0.45	0.55	0.69	0.71	0.92
Hayward							
$Data_{cal}$	0.89	0.11	0.08	0.92	0.91	0.89	0.82
$Data_{val}$	0.82	0.18	0.1	0.9	0.88	0.82	0.79
Test_1	0.66	0.34	0.13	0.87	0.76	0.66	0.86
Test_2	0.7	0.3	0.56	0.44	0.55	0.7	0.48

Test_1 had around 45 % soft fruit, while Test_2 contained about 87 % soft (Table 7.6). In Test_1, 87 % of soft kiwifruit and 75 % of firm kiwifruit were correctly segregated (Table 7.7). For Test_2, although 71 % of soft kiwifruit were correctly segregated, 45 % of firm kiwifruit were also incorrectly segregated into soft class (Table 7.7). The overall Accuracy (0.8) and Sensitivity (0.9) were good for Test_1 (Table 7.7), it also appears that incorrect segregation happen in firm

fruit (Figure 7.12C). Lower overall Accuracy (0.7) and Sensitivity (0.7) were observed for Test_2, however, a separation tendency could still be observed with a different mean for each segregation class (Figure 7.12D). A greater Precision was observed for both Test_1 (0.7) and Test_2 (0.9). The increase in Precision could be due to an increased soft fruit population in both Tests, while the lower overall Accuracy and Sensitivity are possible due to the overlapping of LBI parameters resulting in segregation uncertainty (Section 7.3.3).

'Hayward' $Data_{cal}$ and $Data_{val}$ had about 30 % soft fruit (Table 7.6). Segregation of soft and firm fruit were moderately successful in both $Data_{cal}$ (89 % and 92 %) and $Data_{val}$ (82 % and 90 %) (Table 7.7). Only a few firm kiwifruit (FF > 20 N) were incorrectly segregated to soft class, most incorrectly segregated firm fruit had FF below 20 N in $Data_{cal}$ and $Data_{val}$ (Figure 7.13A,B). High overall Accuracy (0.9), Sensitivity (0.9 and 0.8) and Precision (0.8) were observed for $Data_{cal}$ and $Data_{val}$ (Table 7.7).

Test_ 1 and Test_2 had 55 % and 45 % soft kiwifruit (Table 7.6). Moderate segregation accuracy of soft fruit (0.7) was observed for both Test sets, while good (0.9) and poor (0.4) segregation of firm fruit were observed for Test_ 1 and Test_2, respectively (Table 7.7). A greater overall Accuracy (0.75) was observed for Test_1 than for Test_2 (0.55) (Table 7.7). In Test_1, firm fruit FF ranging from 10 – 50 N were incorrectly segregated into soft class (Figure 7.13C). 'Hayward' had a reduced Sensitivity (0.7) in both Test sets, where 30 % of soft fruit were segregated into the firm class. The segregation model for 'Hayward' had a low Precision (< 0.5) in Test_2, the segregation performance is getting worse at the late storage stages, with 52 % firm fruit found in the soft estimation class. The assumption is that the LBI parameter overlapping of soft and firm kiwifruit could influence model performance (Section 7.3.3).

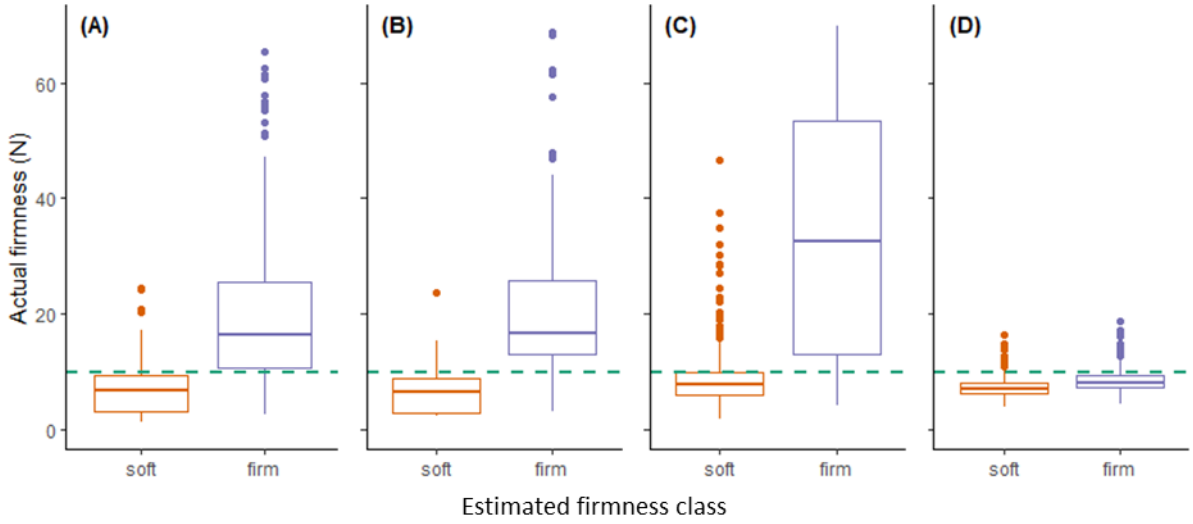

Figure 7.13. 'Hayward' kiwifruit firmness distribution at estimated soft and firm firmness classes with the threshold of 9.8 N. Data is presented for (A) calibration model, (B) cross validation, (C) test validation 1 and (D) test validation 2. The green horizontal line represents the firmness threshold at 9.8 N.

7.3.3.3 LBI parameters distribution influences segregation model performance

The different performance among different data sets could be due to different post-harvest ripening stages between data populations, resulting in LBI differences. 'Zesy002' LBI parameter exhibited Gaussian distribution of intensity frequency for each FF class, and LBI parameters were separated for soft and firm kiwifruit (Figure 7.14). When comparing data sets, the combined population of $Data_{cal}$ and $Data_{val}$ (Figure 7.14A) and Test_1 (Figure 7.14B) had a larger FF mean difference between soft and firm fruit than Test_2 (Figure 7.14C). In Test_2, LBI parameter population for soft and firm fruit had overlaps (Figure 7.14C), resulting in a lower overall accuracy (Table 7.7). The overlapping of LBI parameters led to incorrect segregation when LBI parameters were similar at the late storage stage (Figure 7.12D).

When comparing the density curve shape, SLP at 785 nm is less spreader than other parameters. This could be due to different power output between two wavelengths, as LBI images at 785 nm had a larger diffusion area than 830 nm (Figure 5.7).

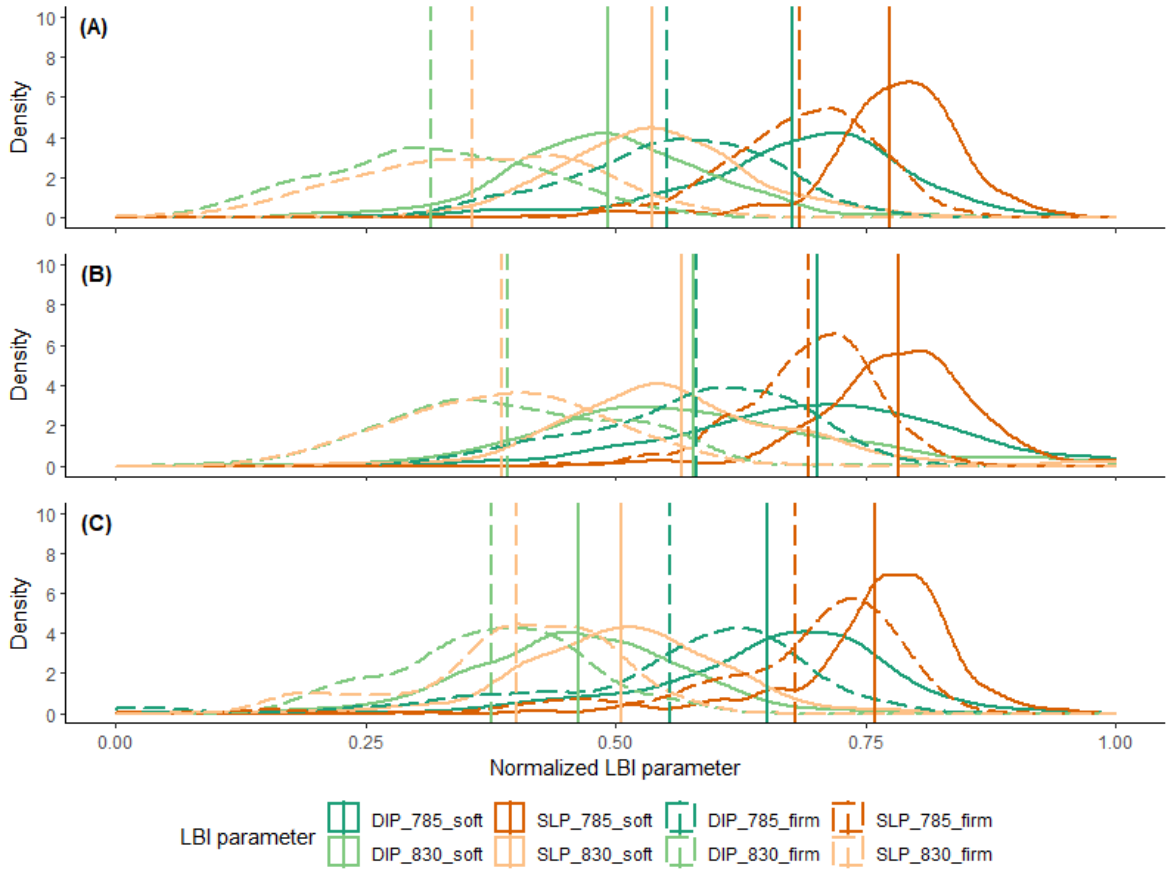

Figure 7.14. Normalized LBI parameter density for soft and firm 'Zesy002' kiwifruit for combined model calibration and cross validation data set (A), test validation data set 1(B) and test validation data set 2 (C). Soft kiwifruit were flesh firmness equal to or below 9.8 N. LBI parameters at 785 nm and 830 nm were the radius of the saturated area (DIP), the slope of the linear regression model (SLP) built with log-transformed profile data between the radius at 75 % of maximum intensity and the radius at 25 % of maximum intensity. Vertical lines represent the population mean of each LBI parameter.

LBI parameter densities of 'Hayward' kiwifruit showed a similar distribution as 'Zesy002' (Figure 7.15) and agreed with 'Zesy002' that LBI parameter distribution could influence model performance. 'Hayward' performance among sample sets and wavelength was similar to 'Zesy002'. The combined population of $Data_{cal}$ and $Data_{val}$ (Figure 7.15A) and Test_1 (Figure 7.15B) had a larger FF mean difference between soft and firm fruit than Test_2 (Figure 7.15C)

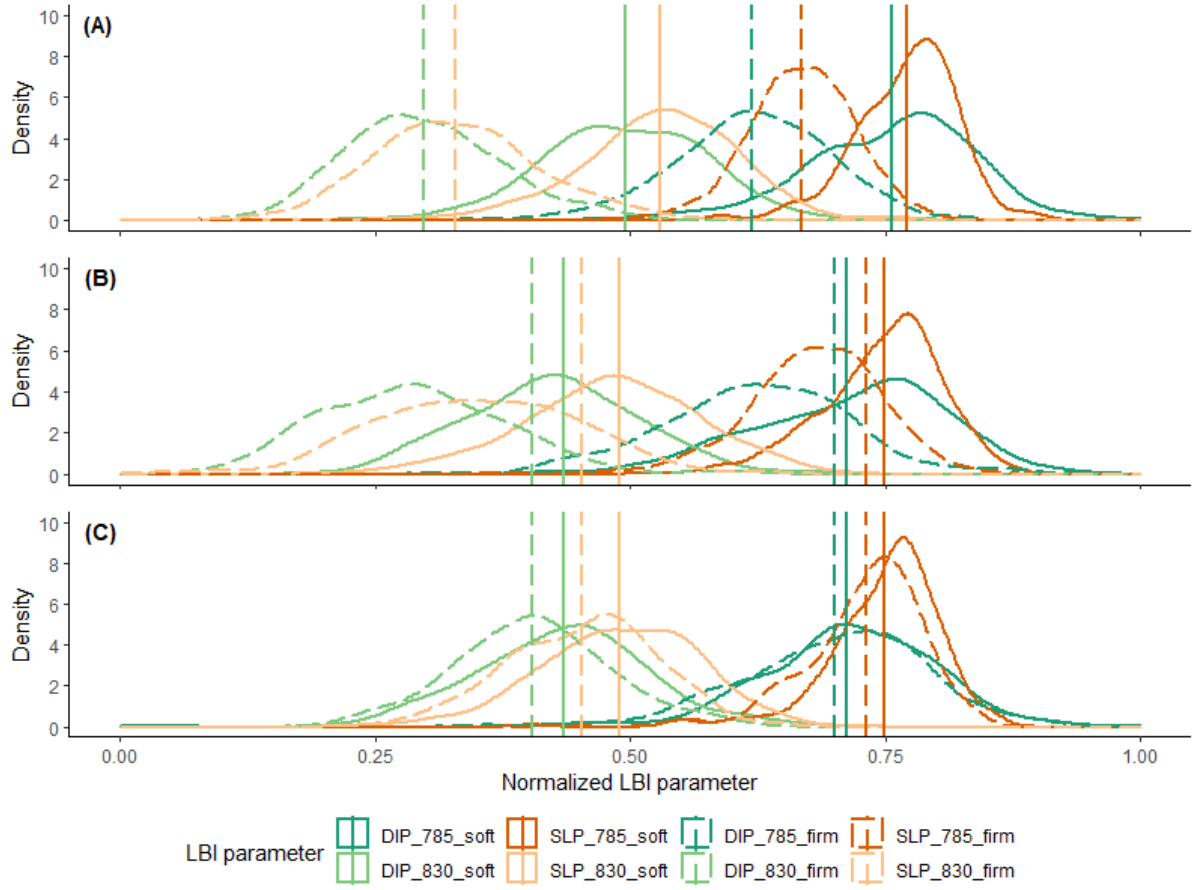

Figure 7.15. Normalized LBI parameter density for soft and firm 'Hayward' kiwifruit for combined model calibration and cross validation data set (A test validation data set 1(B) and test validation data set 2 (C). Soft kiwifruit were flesh firmness equal to or below 9.8 N. LBI parameters at 785 nm and 830 nm were the radius of the saturated area (DIP), the slope of the linear regression model (SLP) built with log-transformed profile data between the radius at 75 % of maximum intensity and the radius at 25 % of maximum intensity. Vertical lines represent the population mean of each LBI parameter.

The overlapping of LBI parameters is potentially because low FF could be a result of multiple factors. FF reduction may include turgor pressure loss, cell wall swelling and other microstructural changes (Hallett et al. 1992), whilst how those properties interact with LBI parameters is not clear.

Besides the LBI parameter distribution, inaccurate segregation of soft 'Hayward' fruit could result from its texture character as soft 'Hayward' had a 'mealy' texture due to loss of cell-to-cell adhesion (Schroeder et al., 2018). Light scattering may decrease when the cell-cell adhesion loss due to pectin solubilization and dissolution of the middle lamella , and then increases LBI

parameters (Figure 3.6). The mealiness could potentially influence LBI parameter extraction and affect the model performance. The influence of texture needs to be further investigated.

Test_2 data set in both cultivars represent the late storage stages when LBI technology is most likely to be required. The poor segregation performance could be due to overlapping LBI parameters in both fruit classes (Figure 7.14, Figure 7.15) or different population density distribution in $Data_{cal}$ and Tests (Figure 7.12, Figure 7.13). For the first assumption, the sensitivity of FF segregation decreases when the LBI parameter mean becomes smaller, resulting from a similar FF for each FF class. Solutions would be exploring other advanced data analysis and segregation methods, such as machine learning and deep learning, that capture more characters from each class. In the meantime, improved LBI image analysis is required. With more information extracted from LBI images, enhanced image sensitivity is expected. The next Section will explore the feasibility of GNB classifier applied in different populations using the current analysis method.

7.3.3.4 Influence of firmness threshold selection on segregation performance

As mentioned in the previous section, FF segregation model performance could be affected when Test sets had different population density distribution of LBI parameters with $Data_{cal}$. A suitable FF threshold may vary in different data sets, where the LBI parameter minimally overlaps with the GNB classifier, resulting in the best segregation performance. This Section applied integrated FF thresholds and investigated potential patterns of model performance changes with a set threshold. If suitable FF thresholds and trends of threshold shifting could be observed, an integration coefficient might be able to be added into the segregation model to describe the population with different density distributions. Since population density changes

in soft and firm kiwifruit could be correlated with the kiwifruit softening process, the integration coefficient might be described by time.

SFI naturally increases when the FF threshold increases (Figure 7.16A). To achieve a SFI at 0.5, an FF threshold of 19.6 N for $Data_{cal}$ and $Data_{val}$, 9.8 N for Test_1 and 4.9 N for Test_2 is required. The overall Accuracy was similar (0.75 – 0.85) and remained stable at all thresholds in all data sets (Figure 7.16B). Sensitivity and Precision were relatively stable above the threshold at 9.8 N and 14.7 N for all data sets (Figure 7.16C, D). Therefore, good model performance for 'Zesy002' was observed at the FF threshold between 9.8 N and 14.7 N, where soft fruit incidence was within 0.4 – 0.6.

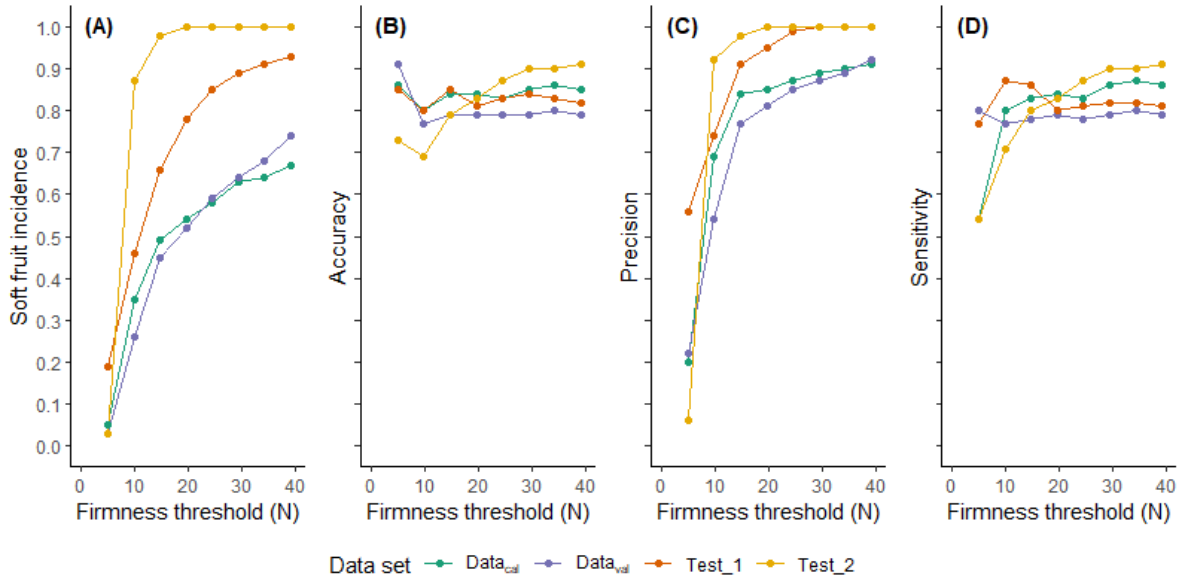

Figure 7.16. 'Zesy002' firmness segregation model performance with a function of firmness thresholds integration for model calibration data set ($Data_{call}$), cross-validation data set ($Data_{va}$) and test validation data sets (Test_1, Test_2). (A). The soft fruit fraction on each data set at the given threshold is the soft fruit incidence. (B). Model accuracy was the accurately estimated classes for both soft and firm kiwifruit. (C). Sensitivity was the correctly estimated soft kiwifruit among all soft fruit. (D). Precision was the actual soft kiwifruit in all estimated soft fruit.

For 'Hayward', to achieve a soft fruit incidence of 0.5, the FF threshold of 24.5 N is required for $Data_{cal}$ and $Data_{val}$, and 9.8 N is required for Test sets (Figure 7.17A). In $Data_{cal}$ and $Data_{val}$, both overall Accuracy (from 0.9 to 0.7) and Sensitivity (from 0.9 to 0.6) decreased from a FF

threshold of 9.8 N onwards, while Precision remained relatively stable (0.7) (Figure 7.17B,C,D). Thus, 9.8 N might be a suitable FF threshold for data sets with a similar SFI to $Data_{cal}$ and $Data_{val}$ at around 0.3. In Test_1, the highest overall Accuracy was at 4.9 N FF threshold, however, Precision and Sensitivity was the lowest at this threshold (Figure 7.17B,C,D). In Test_2, the lowest overall Accuracy and low Precision and Sensitivity were reported at 9.8 N FF threshold (Figure 7.17B,C,D). Although high Precision and Sensitivity were observed with increasing FF thresholds for Test sets, the good Precision and Sensitivity are possibly due to a higher proportion of soft fruit at those thresholds. The suitable FF threshold may be between 4.9 N and 9.8 N for both Test sets.

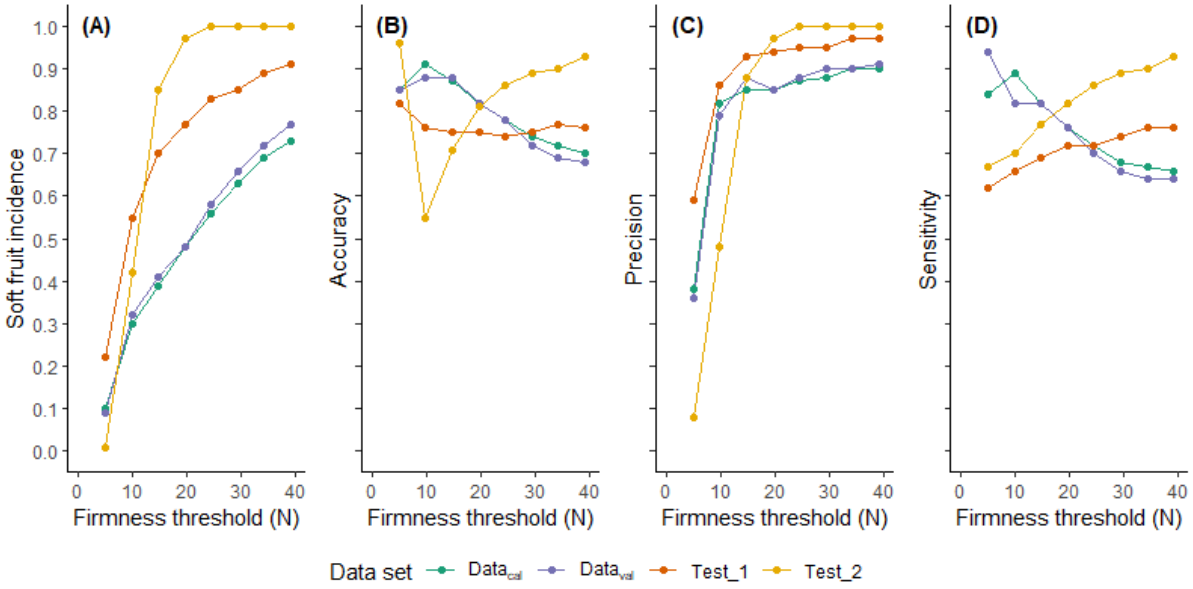

Figure 7.17. 'Hayward' firmness segregation model performance with a function of firmness thresholds integration for model calibration data set ($Data_{call}$), cross-validation data set ($Data_{va}$) and test validation data sets (Test_1, Test_2). (A). The soft fruit fraction on each data set at the given threshold is the soft fruit incidence. (B). Model accuracy was the accurately estimated classes for both soft and firm kiwifruit. (C). Sensitivity was the correctly estimated soft kiwifruit among all soft fruit. (D). Precision was the actual soft kiwifruit in all estimated soft fruit.

Since a good segregation performance for both cultivars at a low FF threshold, a 6.9 N FF threshold is investigated with segregated FF classes for 'Zesy002' (Figure 7.18) and 'Hayward'

(Figure 7.19). 6.9 N FF threshold is considered the threshold for entering the eating window (Fullerton et al., 2020), thus, the segregation result could demonstrate the capability of LBI to assess the eating quality of the fruit.

For 'Zesy002', a large amount of firm ripe kiwifruit were incorrectly segregated into the eating ripe class for both $Data_{cal}$ and $Data_{val}$ (Figure 7.18A,B). Test_1 had a less firm ripe kiwifruit portion being incorrectly segregated into the eating ripe class compared with $Data_{cal}$ and $Data_{val}$. Test_2 showed slightly better separation between firm ripe and eating ripe kiwifruit, although the two groups remained largely overlapping, and a large portion of firm ripe kiwifruit were incorrectly estimated into the eating ripe class

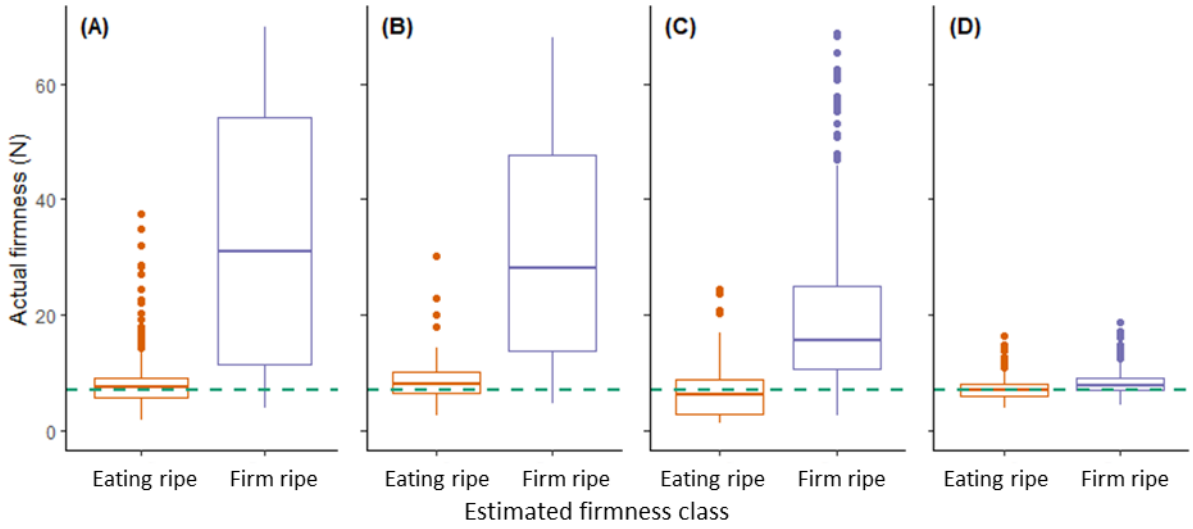

Figure 7.18. 'Zesy002' kiwifruit firmness distribution at estimated firmness class with the threshold of 6.9 N. (A) calibration model, (B) cross validation, (C) test validation 1 and (D) test validation 2. The green horizontal line represents the firmness threshold at 6.9 N.

'Hayward' $Data_{cal}$ and $Data_{val}$ (Figure 7.19A,B) showed better segregation performance for estimating FF classes at 6.9 N compared with 'Zesy002'(Figure 7.18A,B). The better segregation in $Data_{cal}$ and $Data_{val}$ could be due to a wider kiwifruit FF range in the data set. 'Hayward' kiwifruit FF was obtained through shelf-life ripening from 3 maturities, where 'Zesy002' didn't include kiwifruit FF measured through shelf-life ripening. This could be supported by Figure

7.10 and Figure 7.11. Many firm ripe 'Hayward' kiwifruit (> 6.9 N) were incorrectly segregated into the eating ripe class in Test_1 (Figure 7.19C). This finding was similar to 'Zesy002' (Figure 7.18A,B), which indicated that FF segregation had a better performance in the data set with a wider FF range. The current segregation model had a poor performance due to similarity in FF between easting ripe and firm ripe classes (Table 7.6).

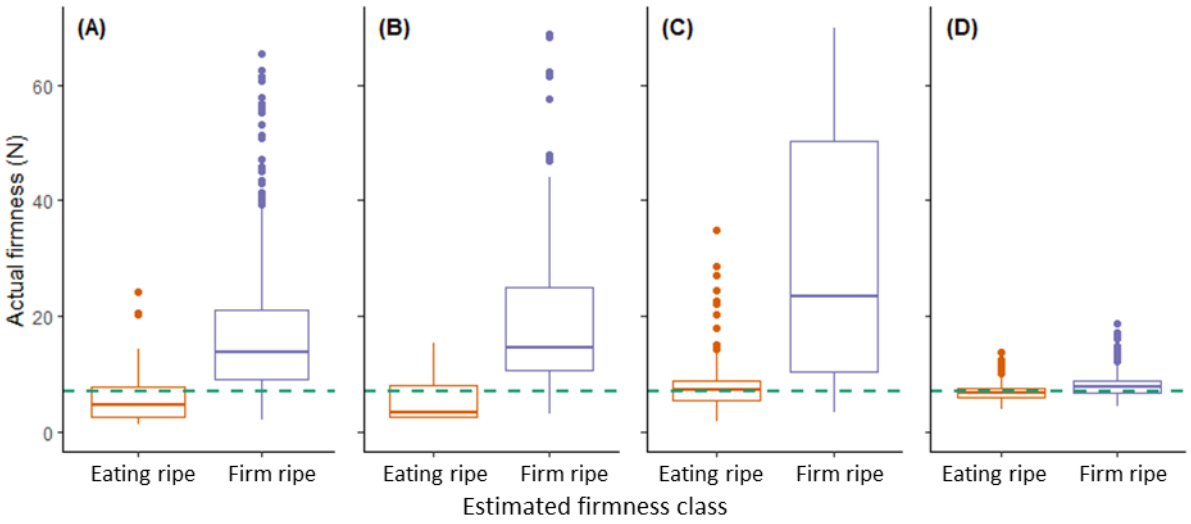

Figure 7.19. 'Hayward' kiwifruit firmness distribution at estimated firmness class with the threshold of 6.9 N. (A) calibration model, (B) cross validation, (C) test validation 1 and (D) test validation 2. The green horizontal line represents the firmness threshold at 6.9 N.

FF threshold at 19.6 N is considered the threshold for entering the third ripening phase (Fullerton et al., 2020), thus, the model performance could demonstrate the segregation capability using LBI in the repacking process. Many unripe kiwifruit (FF > 19.6 N) were incorrectly segregated into the ripe class in 'Zesy002' $Data_{cal}$ and $Data_{val}$ (Figure 7.20A,B), while a greater percentage of ripe kiwifruit (FF < 19.6 N) were incorrectly segregated into the unripe class for Test_1. Test_2 kiwifruit FF were under 19.6 N.

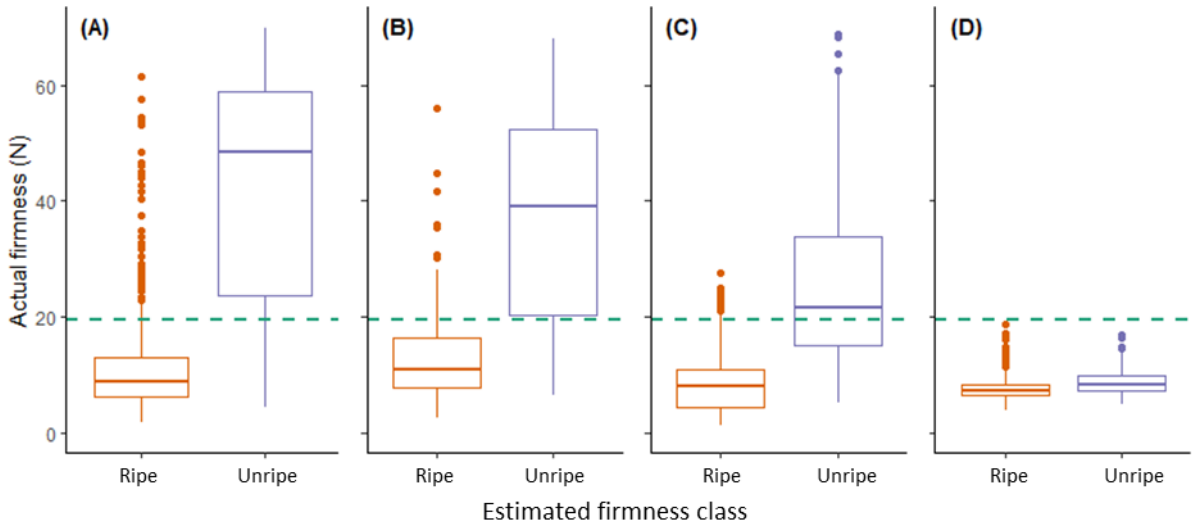

Figure 7.20. 'Zesy002' kiwifruit firmness distribution at estimated firmness class with the threshold of 19.6 N. (A) calibration model, (B) cross validation, (C) test validation 1 and (D) test validation 2. The green horizontal line represents the firmness threshold at 19.6 N.

For 'Hayward', many ripe kiwifruit were incorrectly segregated as unripe fruit in $Data_{cal}$ and $Data_{val}$ (Figure 7.21A, B). While Test_1 was the opposite, many unripe kiwifruit were segregated as ripe ones. This may be due to the fact that the data set had different FF distributions (Figure 7.11A), thus the segregation model is not robust.

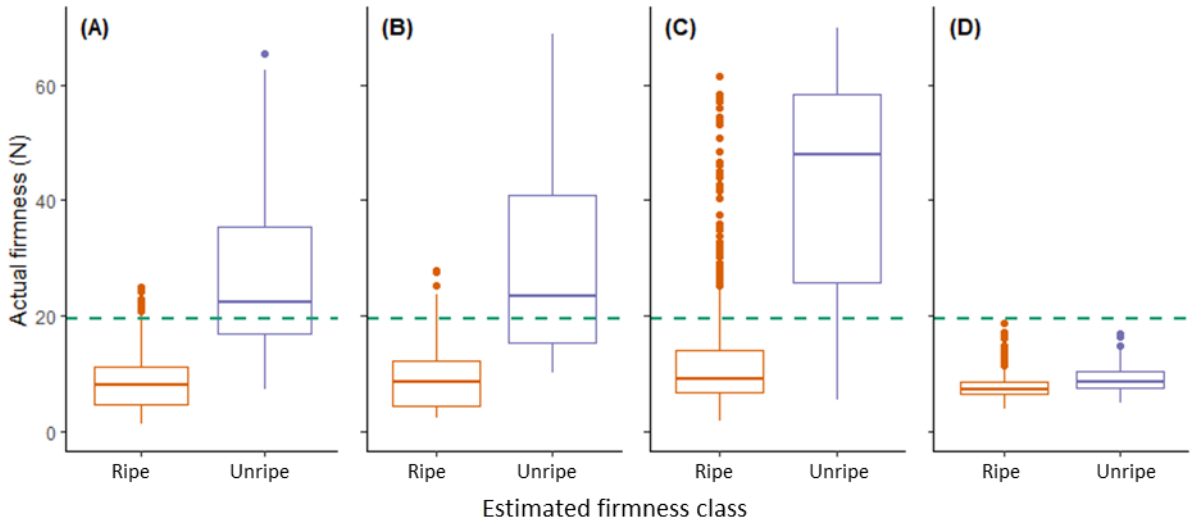

Figure 7.21. 'Hayward' kiwifruit firmness distribution at estimated firmness class with the threshold of 19.6 N. (A) calibration model, (B) cross validation, (C) test validation 1 and (D) test validation 2. The green horizontal line represents the firmness threshold at 19.6 N.

Current results cannot confirm whether an integration coefficient can be used to improve the model performance when data set was imbalanced. The segregation performance could be influenced when data is unbalanced, as reported in Chapter 4. Thus, good segregation performance at low FF threshold (< 9.8 N) or high (> 24.5 N) could result from fruit being segregated into the majority group regardless of the real FF.

It's more valuable to segregate kiwifruit at a lower FF range in practice. Test_2 only contained kiwifruit with lower FF, which is the fruit population distribution in practice after long time storage. The model performance was not as good as that of other data sets with a more spread FF distribution. Therefore, the capability of classifying soft fruit among those in the lower FF range needs to be further investigated.

7.3.4 Segregation model feasibility at different ripening stages

7.3.4.1 Ripening stage threshold determination

As mentioned in the previous section, GNB classifier demonstrated the capability to segregate soft and firm kiwifruit (Figure 7.12 and Figure 7.13). However, the segregation performance was influenced by the overlapping of LBI parameter distribution, and segregation performance got worse when the kiwifruit LBI parameters overlap increased (Figure 7.14 and Figure 7.15). FF segregation performance varied in different populations, resulting from variations in kiwifruit maturity and ripeness, and understandably, the model performance was worse when LBI parameter was not considerably different between soft and firm fruit. Therefore, the GNB classifier segregation performance may vary at different ripeness stages. When fruit have similar LBI parameters in the later ripening stage (Figure 6.1, Figure 6.2), the segregation accuracy may decrease with increasing ripening stages.

The segregation model also needs to be adjusted coordinately to be applied in various commercially oriented scenarios, where difference in maturity and ripeness is expected. Thus, the resulting performance may influence FF segregation capability using LBI at different ripening stages in practice. For instance, the probability of identifying soft fruit at the early ripening stage may be higher than at the later stage because the difference in average FF in each class decreased during ripening. Therefore, in this section, the feasibility of the FF segregation model was studied in samples with different ripening stages.

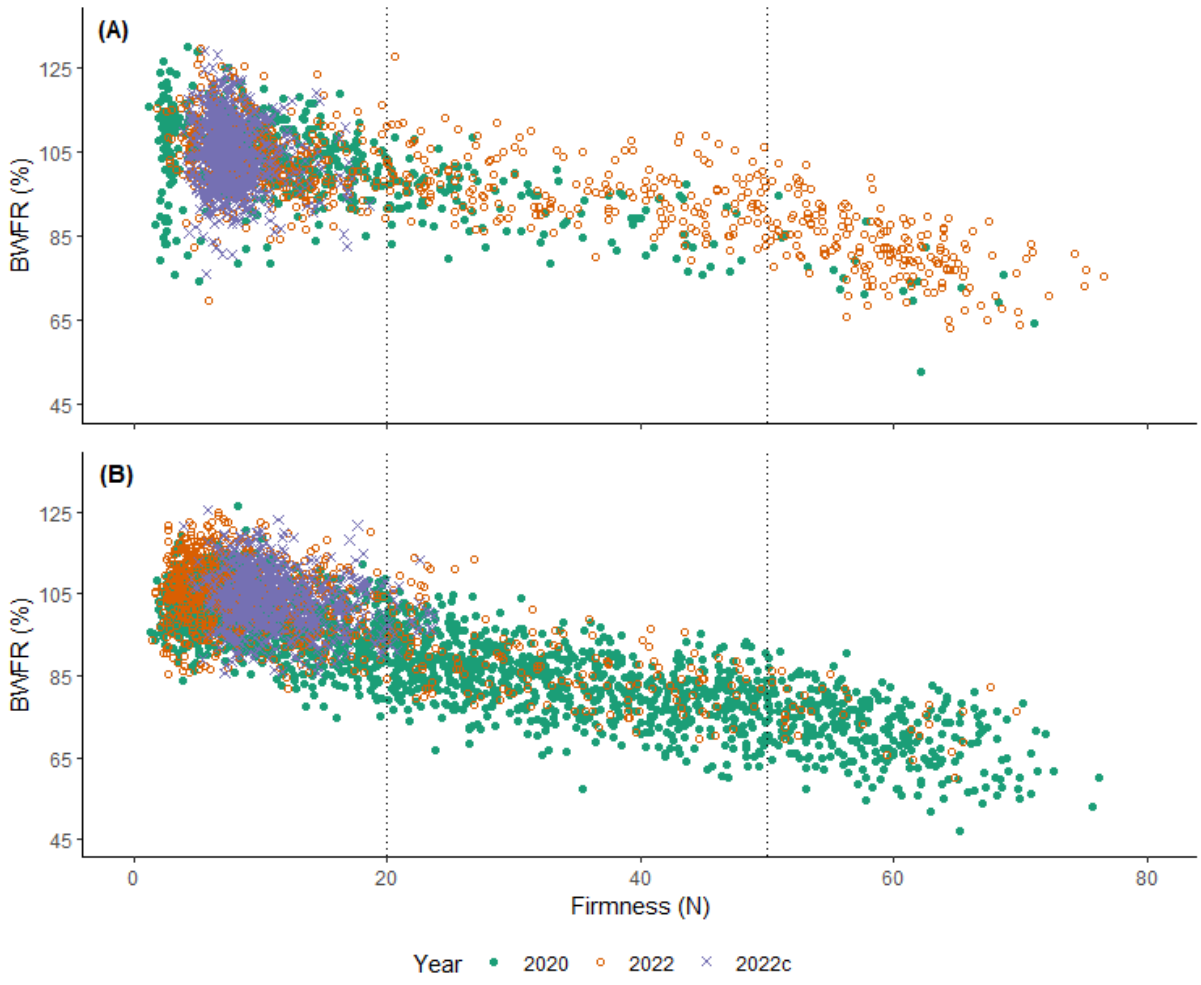

Figure 7.22. Individual correlation of (A) 'Zesy002' and (B) 'Hayward' flesh firmness and Brix when fully ripe (BWFR). Scatter points represent kiwifruit measured through ripening at 20 °C in year 2020 (green solid circle), measured on day 7 after ripening at 20 °C in year 2022 (orange empty circle) and measured after ripening at 1 °C (purple cross) around 100 days in year 2022. Dotted lines at 20 and 50 N indicate thresholds of kiwifruit softening phases.

Kiwifruit BWFR is correlated with the ripening stage (Figure 7.5, Figure 7.6), thus, kiwifruit ripeness may be segregated with the BWFR threshold. Kiwifruit in Table 7.2 (Section 7.3.3) were pooled together and then subsampled with different BWFR. Individual kiwifruit FF and BWFR data are presented in Figure 7.22. In the new data set, kiwifruit FF were between 0 – 80 N and BWFR were between 45 – 135 %; these ranges are expected to cover the entire kiwifruit ripening.

In industry, BWFR is utilized as the at-harvest maturity indicator, and no information is available on the correlation between BWFR and fruit ripening through storage. Alternatively, kiwifruit ripening stage could be interpreted with FF reduction. According to kiwifruit softening curve (Figure 2.1), kiwifruit has thresholds around 50 N and 20 N to enter the 2nd and 3rd phases. In the new pooled data set, kiwifruit were segregated into 3 fruit groups, firm (FF > 50 N), medium (50 N ≥ FF >20 N) and soft (20 N ≥ FF). Those kiwifruit could represent samples at early, middle and late ripening stages (Table 7.8). Within each fruit group, the average BWFR and standard deviation were calculated and then utilized as ripening thresholds (Table 7.8).

Table 7.8.Kiwifruit Brix when fully ripe (BWFR) for kiwifruit at difference firmness (FF). Fruit number (n), average BWFR (mean, %), BWFR standard deviation (sd, %) and BWFR range (%) are presented.

Ripening	Fruit	FF range	n	Mean	sd	range
Zesy002						
early	firm	(50, ∞)	209	82.23	8.61	[73.61, 90.84]
middle	medium	(20, 50]	302	95.17	7.76	[87.41, 102.93]
late	soft	(0, 20]	1736	104.91	8.22	[96.69, 113.13]
Hayward						
early	firm	(50, ∞)	353	72.24	7.99	[64.24, 80.23]
middle	medium	(20, 50]	910	85.38	9.14	[76.24, 94.52]
late	soft	(0, 20]	2295	102.51	7.90	[94.61,110.41]

Kiwifruit BWFR population density was presented at 3 ripening stages (Figure 7.23A,D), with the increasing ripeness stage represented by increasing BWFR. The resulting BWFR thresholds of 'Zesy002' and 'Hayward' are: below 88 % and 77 % for early ripening kiwifruit, and above

103 and 95 % for late ripening kiwifruit, respectively (Table 7.8). These thresholds are also supported by mid and late-ripening stages in kiwifruit shelf life ripening (Figure 7.5B, Figure 7.6B).

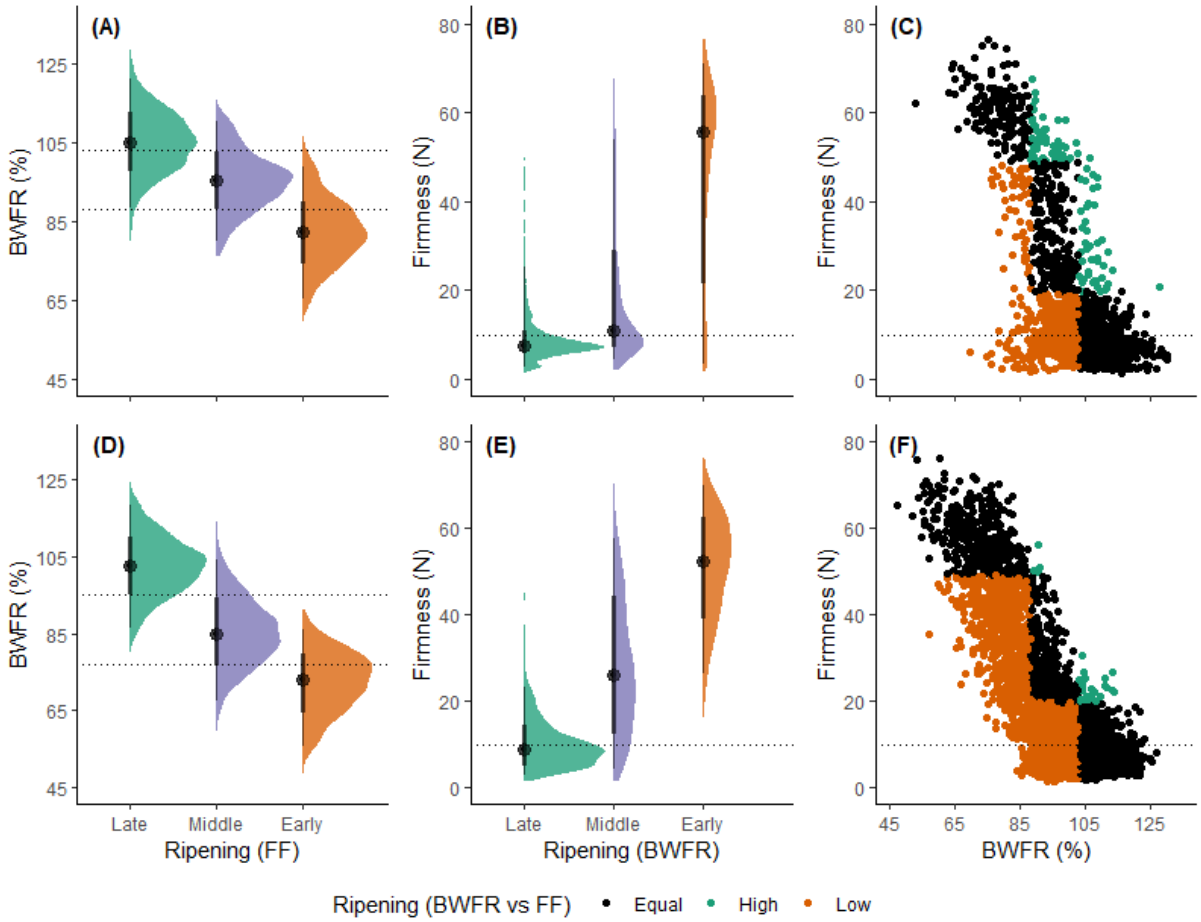

Figure 7.23. Kiwifruit Brix when fully ripe (BWFR) and firmness (FF) of 3 ripening groups and individual kiwifruit correlation for 'Zesy002' (A,B,C) and 'Hayward' (D,E,F). Kiwifruit ripening stage (A, C) was segregated according to FF into late (FF ≤ 20 N), middle (20 < FF ≤ 50 N) and early (FF > 50 N) stages. Dotted line (A, C) are BWFR thresholds for ripening with 88 & 103 % for 'Zesy002' (A) and 77 & 95 % for 'Hayward' (C). Kiwifruit ripening stage (B, E) was segregated according to BWFR into late (BWFR > 103 and 95 %), and early (BWFR ≤ 88 and 77 %) stages for 'Zesy002' (B) and 'Hayward' (E). Dotted lines (B, C, E, F) are FF thresholds at 9.8 N. Orange points are softer kiwifruit at the ripening stage based on BWFR, green points are firm kiwifruit, and black points are kiwifruit at the same ripening stage based on BWFR and FF (C,F).

With selected BWFR thresholds, kiwifruit ripening stages were re-categorized and FF population density was presented (Figure 7.23B,E). Kiwifruit with high FF usually have low BWFR, however, some soft kiwifruit (< 20 N) were also observed in early ripening for 'Zesy002' (Figure 7.23B). Some firm kiwifruit (> 50 N) were also observed at the middle ripening stage,

but FF were mainly spread from 5 – 30 N. At late ripening, FF were below 20 N and the shape of the distribution curve was narrower.

'Hayward' (Figure 7.23E) FF was around 50 N at early ripening stage. The average FF was lower and but the spread range was larger (5 – 60 N) at the middle ripening stage compared with 'Zesy002'. For both cultivars, FF was below 20 N and the FF distribution was similar at the late ripening stage.

Depending on the BWFR, kiwifruit samples could be segregated into different ripening stages (Figure 7.23C,F), which are the thresholds that will be used to investigate FF segregation further. In Section 7.3.4.2, resulting thresholds based on the current dataset will be applied to segregate kiwifruit into different ripening stages. In addition, FF segregation will be investigated in samples with assumed ripening stages according to BWFR.

7.3.4.2 Firmness segregation at different ripening stages

This section developed and assessed kiwifruit FF segregation model using kiwifruit sample at 3 ripening stages ($Data_{all}$, Eq. 7.10, Table 7.8). The model was trained with a training data set ($Data'_{tra}$, Eq. 7.11) by pooling together 80 % subsampled fruit from each ripening stage. The model performance was assessed with samples at each ripening stage (calibration data, $Data'_{cal}$) and validated with the remaining 20 % kiwifruit sample (validation data, $Data'_{val}$). The objective of this section is to investigate if GNB classifier could sort soft kiwifruit (< 9.8 N) at different ripening stages.

$$Data_{all} \in (Data'_{cal_L}, Data'_{cal_M}, Data'_{cal_E}, Data'_{val_L}, Data'_{val_M} \& Data'_{val_E}) \quad \text{Eq. 7.10}$$

$$Data_{tra} \in [Data'_{cal_L}, Data'_{cal_M} \,\&\, Data'_{cal_E}] \qquad \text{Eq. 7.11}$$

Where $Data'_{cal_L}$, $Data'_{cal_M}$ and $Data'_{cal_E}$ were calibration data sets at late, middle and early ripening stages, respectively. $Data'_{val_L}$, $Data'_{val_M}$ and $Data'_{val_E}$ were validation data sets at the late, middle and early ripening stages, respectively. At the early ripening stage, most kiwifruit FF was about 50 N for both cultivars (Table 7.9). Limited soft fruit data was collected for 'Zesy002' and no soft fruit were collected for 'Hayward' for early ripening population. For both cultivars, the average FF for soft kiwifruit was around 7 N regardless of the ripening stage. 'Zesy002' firm kiwifruit was 25 N and 15 N for the middle and late ripening stages, respectively. Meanwhile, the firm 'Hayward' average FF was 30 N and 18 N in the middle and late ripening stages.

Table 7.9. Kiwifruit firmness at three ripening stages in calibration data sets (Data'$_{cal}$) and validation data sets (Data'$_{val}$). The kiwifruit ripening stage was segregated according to Brix when fully ripe (BWFR). Kiwifruit number (n), average firmness (FF_mean) and firmness standard deviation (FF_sd) were presented for soft and firm kiwifruit at the threshold of 9.8 N.

Ripening	BWFR (%)	Data	Soft			Firm		
			n	FF_mean	FF_sd	n	FF_mean	FF_sd
Zesy002								
Late	(103,135]	Data'$_{cal}$	686	6.70	1.80	190	16.61	8.47
		Data'$_{val}$	168	6.71	1.77	58	14.75	6.46
Middle	(88,103]	Data'$_{cal}$	312	7.20	1.69	396	25.00	14.52
		Data'$_{val}$	83	7.44	1.42	104	25.18	14.63
Early	(45,88]	Data'$_{cal}$	21	4.91	2.04	182	51.12	15.70
		Data'$_{val}$	5	5.83	2.43	42	55.43	13.55
Hayward								
Late	(95,135]	Data'$_{cal}$	996	6.86	1.78	663	18.83	10.52
		Data'$_{val}$	233	6.84	1.68	162	18.40	10.98
Middle	(77,95]	Data'$_{cal}$	110	6.47	2.26	761	30.41	13.25
		Data'$_{val}$	24	6.71	2.16	201	31.16	14.13
Early	(45,77]	Data'$_{cal}$				333	51.04	11.68
		Data'$_{val}$				75	50.73	11.80

FF segregation model performance of segregation soft and firm fruit at the threshold of 9.8 N was compared with kiwifruit subsampled from 3 ripening stages. The model achieved similar performance for both Data'$_{cal}$ and Data'$_{val}$ (Table 7.10). For 'Zesy002', moderate model

performance was observed for the middle and late ripening stages. The overall accuracy of firmness segregation was around 0.8 and 0.7 for late and middle repining stages, respectively (Table 7.10). The Sensitivity and Precision were higher at the late ripening stage (0.8, 0.9) than at the middle ripening stage (0.7). The segregation model achieved a good performance for early ripening with over 0.9 Accuracy. However, low Precision (0.6) in $Data_{cal}$ was observed due to the larger proportion of soft fruit being incorrectly segregated as firm. For 'Hayward', the segregation model had good performance in the middle ripening stage and moderate performance at the late ripening stage (Table 7.10). At the middle ripening stage, both data sets of 'Hayward' $Data'_{cal}$ and $Data'_{val}$had a high overall accuracy (0.9) while a lower overall accuracy of 0.7 in late ripening. The Sensitivity was similar and around 0.8 for both middle and late ripening stages, except $Data_{val}$ at middle ripening had a lower Sensitivity (0.7). In 'Hayward' $Data_{val}$ at middle ripening, low sensitivity was also observed.

Table 7.10. Kiwifruit firmness segregation model performance in confusion matrix with Gaussian naïve Bayes classifier at 3 ripening stages. Model was evaluated with calibration data sets ($Data'_{cal}$) and validated with validation data sets ($Data'_{val}$). Soft and firm kiwifruit are segregated at the threshold of 9.8 N. CRT and INC are correctly and incorrectly segregated kiwifruit.

Ripening	Data	soft		firm		Accuracy	Sensitivity	Precision
		CRT	INC	CRT	INC			
Zesy002								
Late	$Data'_{cal}$	559	127	106	84	0.76	0.81	0.87
	$Data'_{val}$	140	28	36	22	0.78	0.83	0.86
Middle	$Data'_{cal}$	235	77	291	105	0.74	0.75	0.69
	$Data'_{val}$	61	22	75	29	0.73	0.73	0.68
Early	$Data'_{cal}$	19	2	168	14	0.92	0.9	0.58
	$Data'_{val}$	4	1	41	1	0.96	0.8	0.8
Hayward								
Late	$Data'_{cal}$	769	227	413	250	0.71	0.77	0.75
	$Data'_{val}$	180	53	91	71	0.69	0.77	0.72
Middle	$Data'_{cal}$	89	21	689	72	0.89	0.81	0.55
	$Data'_{val}$	16	8	179	22	0.87	0.67	0.42
Early	$Data'_{cal}$	0	0	331	2	0.99		
	$Data'_{val}$	0	0	74	1	0.99		

For fruit at the early ripening stage, the segregation model performance was good in Accuracy (over 0.9) but with low Precision. The cause of low Precision at the middle – late ripening stage cannot be confirmed. However, this could possibly be due to model limitations, such as the small amount of soft kiwifruit in the population. Therefore, model performance at the early ripening stage needs to be further investigated with an additional kiwifruit data set.

Segregation model performance was moderate at the early and middle ripening stages for both cultivars. This agrees with the observation that the capability of GNB reduces through ripening where the distribution of the input LBI parameters overlap between soft and firm fruit (Section 7.3.2.3). This could bring segregation uncertainty in this scenario, i.e. kiwifruit at the later post-harvest storage. 'Hayward' had a higher segregation accuracy in the middle ripening stage (0.9) than in the late ripening stage (0.7), while 'Zesy002' had similar accuracy in both middle and late ripening stages (0.7). It may be due to the fact that each cultivar had a different ripening threshold based on BWFR. This observation could be due to a greater difference between the average FF (24 N) in 'Hayward' (Table 7.9), whilst 'Zesy002' had a smaller FF difference (18 N) at the middle ripening stage.

7.3.4.3 Segregation model performance with 5% soft fruit at late ripening

In practice, fruit in the late ripening stage represent the sample within the interest range before exporting checking and repacking. In the current late ripening data set, 78 % and 60 % of the population were soft fruit for 'Zesy002' and 'Hayward', respectively. However, the soft kiwifruit population is assumed to be less than 5 % of the population in realistic supply chain scenarios. Therefore, a subsample ($Data^*_{spl}$) containing 5 % soft kiwifruit and 95 % firm was pooled together using late-ripening kiwifruit (Table 7.9). The training segregation model was the same as Eq. 7.11. For model performance, 80 % of the fruit ($Data_{cal}$') in $Data_{spl}$ (Eq. 7.12)

were assessed and validated with the remaining 20 % of fruit ($Data_{val}$'). The segregation model performance could represent the reality where soft fruit was only a small amount during postharvest practice.

$$Data^*_{spl} \in [Data^*_{cal_L} \& Data^*_{val_L}] \quad \text{Eq. 7.12}$$

The kiwifruit FF segregation model had a moderate accuracy (0.6) for both cultivars in late-ripening kiwifruit containing 5 % soft fruit (Table 7.11). The segregation accuracy was lower than kiwifruit at the same ripening stage but with more soft fruit (Table 7.10). 'Zesy002' $Data_{cal}$' had a high Sensitivity of 0.9, while 'Zesy002' $Data_{val}$' and both 'Hayward' data sets had lower Sensitivity of around 0.7. However, this low Sensitivity might be due to a small amount of soft fruit. In addition, around 40 % of firm kiwifruit was incorrectly estimated as soft fruit, which led to a very low Precision. Therefore, additional classification methods, such as machine learning, are required to reduce segregation uncertainty.

Table 7.11. Kiwifruit firmness (FF) segregation model performance in confusion matrix with Gaussian naïve Bayes classifier at late ripening stage. The model was evaluated with calibration data sets ($Data^*_{cal}$) and validated with validation data sets ($Data^*_{val}$). Soft and firm kiwifruit are segregated at a threshold of 9.8 N. CRT and INC are correctly and incorrectly segregated kiwifruit.

	Soft			Firm			Accuracy	Sensitivity	Precision
	FF (N)	CRT	INC	FF (N)	CRT	INC			
Zesy002									
$Data^*_{cal}$	7.1±1.4	9	1	16.6±8.4	106	84		0.9	0.1
$Data^*_{val}$	6.3±0.8	2	1	14.8±6.5	36	22	0.62	0.67	0.08
Hayward									
$Data^*_{cal}$	6.0±2.16	24	10	18.8±10.5	413	250	0.63	0.71	0.09
$Data^*_{val}$	5.8±2.3	6	2	18.4±11.0	91	71	0.57	0.75	0.08

7.3.5 Overall discussion

7.3.5.1 LBI parameters associated with firmness changes during ripening

The LBI parameter increased during the kiwifruit ripening process, which resulted from the reduction of energy loss during light propagation. The changes in kiwifruit's physical structure

during the fruit softening process could affect scattering properties and thus influence light propagation. Those physiological processes involve cell wall degradation, cell wall swelling and middle lamella adhesion (Harker & Hallett, 1994). Kiwifruit cell wall thickness at harvest can be 3-4 times greater than soft-ripened kiwifruit (Hallett et al., 1992). Additionally, changes in cell orientation may influence scattering properties. Kiwifruit cells are longitudinally orientated and shift vertically during softening (Li et al., 2015). Firm kiwifruit usually have flat and large cells, whereas soft fruit have spherical cells (Harker & Hallett, 1994). The difference in light propagation during ripening results in optical property changes (Baranyai & Zude, 2009) and further influences LBI parameters. The increasing trend of LBI parameter was mainly observed in the later storage stage or lower FF with small FF changes (Figure 7.8). These results could explain that most microstructure changes occurred at the 3rd ripening phase and FF is relatively stable during this phase (MacRae et al., 1990).

LBI parameter trends were slightly different at different wavelengths during kiwifruit ripening, as light absorption due to pigments within fruit could affect LBI parameter trends (Walsh et al., 2020). At 785 and 830 nm, the absorption during pigments was minimal (Walsh et al., 2020), thus LBI parameters were assumed to carry mainly scattering information. In this work, FF is assumed to be related to scattering differentiation at short-NIR wavelengths resulting from microstructure changes. Therefore, the correlation between FF and LBI parameters observed in Table 7.4 could be potentially useful for FF estimation. However, linear regression between FF and LBI parameters cannot be concluded. Firstly, the FF reduction results from multiple microstructure changes, which could affect LBI parameters differently. For example, the cell wall degradation is assumed to result in an LBI parameter increase, as the attenuation of photon energy decreases when photon travel paths are extended. On the other hand, the turgor pressure reduction could increase the photon energy loss by allowing more light

scattering to occur and decrease LBI parameter. Although the affected photons due to turgor pressure are supposed to be minimal compared with the cell wall, FF estimation error could still occur. Moreover, the variability among fruit samples (Costa et al., 2003; East, 2011) also cause variation in LBI parameters of kiwifruit with the same FF.

7.3.5.2 LBI parameters in firmness segregation

Although FF estimation is challenging, LBI technology demonstrated its ability to segregate FF using $Data_{cal}$, $Data_{val}$ and Test sets. Those data sets have kiwifruit harvested from different seasons, experienced different storage practices, or at different ripening stages (with different BWFR). The FF segregation model had an overall accuracy of around 0.8 for 'Zesy002' ($Data_{cal}$, $Data_{val}$ and Test_1), and around 0.8-0.9 for 'Hayward' ($Data_{cal}$, $Data_{val}$ and Test_1). However, the segregation model built with GNB showed poorer performances in Test_2 with an overall accuracy of about 0.7 and 0.6 for 'Zesy002' and 'Hayward', respectively. Test_2 may represent kiwifruit at later storage stages. This explains why the model performance was poorer in a late ripening population than in an early ripening population (Table 7.10), where the average FF has less difference between soft and firm kiwifruit.

The segregation model built in this chapter shows segregation uncertainty for 'Zesy002' kiwifruit with BWFR between 85 – 125 % and FF under 20 N (Figure 7.24A). While for 'Hayward', the segregation uncertainty appears in the same BWFR range but FF under 15 N (Figure 7.24A). Therefore, LBI technology may be applied for cool storage monitoring where the soft kiwifruit (FF < 9.8 N) could be identified from firm kiwifruit (FF > 20 N for 'Zesy002' and FF > 15 N 'Hayward' respectively). The difference between 'Hayward' and 'Zesy002' could be resulted from different texture characters during the softening process (Schroeder et al., 2018).

However, the relationship between texture character and LBI parameters must be further investigated.

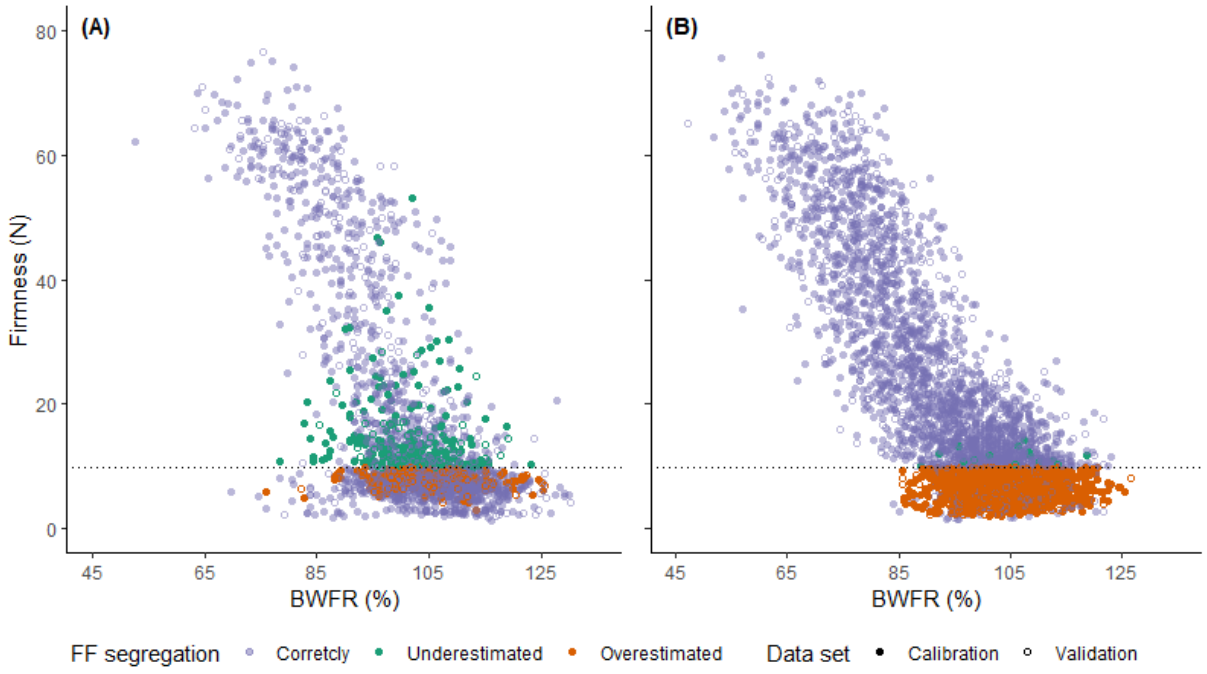

Figure 7.24. Kiwifruit Brix when fully ripe (BWFR) and firmness (FF) individual correlation for 'Zesy002' (A) and 'Hayward' (B). The dotted line (B, C, E, F) is FF threshold at 9.8 N. Orange points are soft kiwifruit but overestimated using LBI, green points are firm kiwifruit but underestimated using LBI, and purple points are kiwifruit are correctly segregated.

In Section 7.3.4, FF segregation model performance was evaluated with sub-samples representing kiwifruit at different ripening stages in the industrial scenarios. For a later storage assessment with lower FF, for instance, before exporting or the re-pack process in the industry, the segregation method needs to be further investigated and improved. For example, advanced algorithms can reduce uncertainty and error. In addition, FF thresholds may be reassigned with additional datasets to enlarge the model training population.

7.3.5.3 LBI technology advantages and future study

Although LBI technology capability was limited with an FF segregation uncertainty in the range of 5 – 20 and 5 – 15 N for 'Zesy002' and 'Hayward', respectively, LBI technology has its advantages. The advantage of LBI technology compared with commonly used NIR

spectrometer is that LBI undertakes information directly related to FF, whilst NIR spectrometer carries out correlated SSC information and indirectly estimates FF change. Therefore, the LBI data is considered to be relatively more objective and has a smaller influence from inherent variation caused by seasonality and growing locations etc.

The estimation error of the GNB-based LBI model is caused differently by NIR spectroscopy and is possible to overcome with improved analysis methods. The limitation of GNB is the performance is highly affectable by the input parameter distribution. It's a weak performance for classifying a similar population where input parameters largely overlap. Other segregation approaches, such as multi-factor segregation using machine learning or multi-factor neural network methods, could potentially overcome this limitation and therefore should be investigated for future studies. Besides, time series analysis and mechanistic analysis could be added to estimate the FF value using other physiological information, such as the enzyme process.

For future studies, kiwifruit FF segregation may be conducted by estimating soft fruit probability in the late ripening stage when soft and firm fruit fall into a narrow FF range. This approach may require high sensitivity/resolution of extracted LBI parameters or additional LBI parameters. The significance and confidence interval may be converted into soft fruit probability. This new probability could be validated against the industry assessment.

7.4 Conclusions

FF segregation using LBI parameters is possible with kiwifruit data sets from different seasons, at different maturity, and with different ripening stages. Using different validation and subsampling methods, the correlation between LBI parameters and kiwifruit FF was consistent. By comparing the result with dataset distribution, the error observed from validation datasets

could be mainly caused due to the difference in population distribution. The overall accuracy of using LBI parameters for FF segregation was over 0.8 for both kiwifruit cultivars with a wider range of FF (5 – 80 N), whilst the overall accuracy was over 0.6 when FF was in a smaller range (5 – 20 N).

Chapter 8 Summary and future works

8.1 Summary of results

Kiwifruit is an important horticultural product in NZ; however, there is a large inherent variability in quality that leads to supply chain losses. Thus, non-destructive technology is desired to ensure that the quality is consistent. FF is the primary quality attribute; however, challenges have been identified in FF measurement using commercialized spatially resolved technologies, such as NIR spectroscopy. FF change is related to fruit physical properties which don't have direct correlations with spectral absorption data obtained from NIR spectroscopy. This PhD work investigated a non-destructive approach based on the LBI technique through signal analysis and kiwifruit quality segregation assessment. The developed LBI methodology was utilized to extract kiwifruit LBI parameters, μ_a and μ_s' and results demonstrated its ability to estimate kiwifruit FF and detect internal disorders.

In Chapter 3, the LBI system, image acquisition and signal analysis methods were introduced. With the signal analysis process, backscattered light could be transformed into LBI parameters. Prior to the calculation of μ_a and μ_s', a pre-classification method was developed to align ranges of μ_a and μ_s', thus reducing the influence of coupling μ_a and μ_s'. Pre-classification models were developed using LBI parameters as input parameters. The resulting optical properties of optical phantoms were then validated using known values. The result demonstrated that using a pre-classification model built on optical phantoms is a feasible approach to decoupling μ_a and μ_s' of phantoms. However, whether pre-classification models could be utilized for estimating kiwifruit μ_a and μ_s' was not confirmed with results in Chapters 4 and 5.

Estimated kiwifruit μ_a and μ_s' obtained through the pre-classification approach were utilized for kiwifruit BMSB damage (Chapter 4) and CI (Chapter 5) detection. In those two Chapters,

differences in μ_a and μ_s' between sound and defect kiwifruit could be correlated with internal disorder symptoms. Symptoms of tissue discolouration and water soaking may influence μ_a, and corky tissue may affect μ_s'. For segregation of BMSB damaged kiwifruit using μ_a and μ_s' at 532, 660 and 785 nm, good and moderate segregation performances were obtained for 'Zesy002' and 'Hayward' with 84 % and 62 % over accuracy, respectively. In CI kiwifruit segregation using μ_a and μ_s' at 520 nm, 75 % and 5 % true positive accuracy were obtained for 'Zesy002' and 'Hayward' despite an over 90 % overall accuracy. High overall accuracy with a low true positive accuracy may result from low defective kiwifruit percentage and wavelength selection. Besides, the current pre-classification model has estimation uncertainties in kiwifruit μ_a and μ_s', which may influence segregation model performance in disordered and sound kiwifruit. Therefore, whether kiwifruit μ_a and μ_s' could be utilized for internal disorder detection is not confirmed. This estimation uncertainty may be difficult to overcome due to the complexity of kiwifruit structures. On the other hand, LBI parameters (DIP, Q1R, FWHM, Q3R, SLP) demonstrated the ability to segregate unmarketable kiwifruit with CI. They resulted in 92 % true positive accuracy in 'Zesy002' and 39 % true positive accuracy in 'Hayward'. Fruit segregation in certain situations may not require high precision from using optical properties but could be conducted using LBI parameters absent of μ_a and μ_s'. Therefore, LBI parameters were utilized for the kiwifruit ripening study in Chapter 6.

In Chapter 6, kiwifruit LBI parameters through ripening were analysed using time series analysis and increases in LBI parameters were observed. The trends of LBI parameters during ripening may be associated with kiwifruit microstructural changes as FF decreases. In addition, coefficients in time series analysis models showed the potential to describe LBI increase rate resulting from different kiwifruit ripeness patterns. However, the forecasting accuracy of LBI parameters may be influenced by the limited number of data points in the current time series

analysis and data collected from an incomplete ripening process due to the lack of initial ripeness stage for 'Zesy002'. Furthermore, correlations between LBI and FF, time series analysis coefficients, and FF decreasing rate require further study with accompanying kiwifruit FF data, which is absent in the current study.

Given the potential that LBI parameters may correlate with kiwifruit FF and be utilized for FF segregation, the FF segregation model was investigated with kiwifruit from multiple maturities and from multiple seasons in Chapter 7. Chapter 7 presented the correlation between LBI parameters and kiwifruit FF and confirmed the correlation is consistent regardless of kiwifruit maturity or ripeness. An FF segregation model for soft kiwifruit was developed using LBI parameters of DIP and SLP at 785 and 830 cm. The FF segregation model demonstrated its ability to segregate soft fruit at different FF and BWEF thresholds. However, segregation performance varies in different data sets, resulting in overlapping LBI parameter ranges in both soft and firm classes due to the less difference in soft fruit FF and firm fruit FF.

8.2 Laser backscattering imaging with the pre-classification approach

LBI system has the advantage of reduced data reading and processing time (Baranyai & Zude, 2009) and the cost of LBI system components (laser diodes and CCD camera) is reasonable compared with other non-destructive systems. With the potential to be added to the packhouse sorting line with its spatially resolved setup, the LBI technique is a promising non-destructive method to estimate kiwifruit quality and identify disordered kiwifruit in the industry. LBI utilized multiple wavelengths and recorded backscattered signals. The LBI signal can be transformed into radial attenuation profiles, in which radial length represents the distance between the light incident point and the measuring point of propagated light. The radial length at propagated light intensity is determined by μ_a and μ_s' (Baranyai & Zude, 2009).

and extracted μ_a and μ_s' from LBI are related to the kiwifruit microstructure and chemical components.

Calculating and decoupling of μ_a and μ_s' nondestructively have proven challenging. To calculate μ_a and μ_s', studies have been reported through diffusion theory directly (Lu & Peng, 2006; Cen et al., 2013; Hashim et al., 2014). However, paired μ_a and μ_s' cannot be separated using diffusion unless one of the optical properties could be calculated or was already known (Zude-Sasse et al., 2019). The known μ_a and μ_s' could be measured destructively using IS-IAD (Wang et al., 2020) or PDW (Zude-Sasse et al., 2019). Alternatively, to estimate kiwifruit μ_a and μ_s' non-destructively, Monte Carlo simulation (Baranyai & Zude, 2008) or finite element analysis (Canteli et al., 2015) demonstrated the feasibility but required a heavy calculation process and complex model development.

In this PhD work, an adapted metamodeling method from Aernouts et al. (2015) with optical phantoms was investigated. Optical phantoms with known μ_a and μ_s' provide reference LBI images for pre-classification model development. With this approach, the initial value for the curve fitting process and estimated range of optical properties were aligned. The pre-classification model in Chapter 3 demonstrated its ability to limit μ_a and μ_s' into the pre-defined ranges (Figure 3.4) with solid phantoms, and the classification performance was consistent with more classes and finer class intervals (Figure 3.8c), resulting in a 91.5 % and 65.6 % classification accuracy for μ_s' and μ_a respectively. Although the pre-classification model developed in Chapter 3 showed promising results in optical phantom, estimation uncertainty was observed in kiwifruit μ_a and μ_s' (Figure 4.6, Figure 4.7 and Figure 5.6). The estimation uncertainty of μ_a and μ_s' could lead to further segregation errors between kiwifruit with internal disorders and sound ones.

The estimation uncertainty of kiwifruit μ_a and μ_s' may be introduced by μ_a and μ_s' estimation using liquid phantoms. In the pre-classification model (Section 3.4), liquid phantom μ_a and μ_s' were measured individually without validation of the mixed solution. In this method, the estimated μ_a could be higher than the actual μ_a as the interaction of absorption and scattering could cause an additional error as added scattering could dilute absorber particle concentration (Sun et al., 2022). In addition, estimation uncertainty may occur using homogenous phantoms as a reference. Although the most accurate μ_a and μ_s' of liquid phantom could be measured using a double sphere IS-IAD limiting scattering escape at the lab scale (Pickering et al., 1993), it's very challenging to use homogenous phantoms to estimate kiwifruit optical properties accurately when kiwifruit has different microstructure between and within structural layers (Fang et al., 2016), and the multi-layer structure of fruit requires more complex mathematical modelling of photon pathways than simple turbid media.

8.3 Kiwifruit segregation model

8.3.1 Segregation with optical properties

Optical property analysis has been widely explored for *in-situ* sensing, sorting, and grading fresh produce. In this PhD work, kiwifruit μ_a and μ_s' can segregate kiwifruit with severe internal disorders (Chapters 4 and 5). For internal disorder detection, μ_a at 785 and 830 nm due to water absorption are sensitive to internal disorders with water-soaking symptoms (Figure 4.6, Figure 4.7 and Figure 5.7). Alternatively, μ_a at 520 and 532 nm, due to the absorption of carotenoids, may be useful for detecting internal disorder with tissue discolouration symptoms (Figure 4.6, Figure 4.7 and Figure 5.6).

In the BMSB damaged kiwifruit case study (Chapter 4), the discolouration symptoms in the pericarp region (Figure 4.5) appeared prior to the watering soaking. Thus, μ_a may be more sensitive at 532 nm than at 785 nm for early-stage symptom detection (Figure 4.6, Figure 4.7).

However, whether μ_a is directly correlated with the discolouration symptom in the outer parenchyma region is not confirmed because the penetration of laser light (around 5 mm) may not reach the depth in Figure 4.5. Besides, μ_a could also be affected by estimation uncertainty, where low μ_s' resulted in low estimated μ_a. In contrast, tissue discolouration in the outer pericarp region (Figure 2.2D,E) developed and appeared later than the water-soaking for CI kiwifruit. In Chapter 5, μ_a and μ_s' at 520 nm were investigated, and results showed that wavelength at 520 nm is useful to identify CI kiwifruit with discolouration symptoms. Wang et al. (2020) also utilized kiwifruit μ_a at 400 – 1100 nm to segregate severe CI kiwifruit with water-soaking symptoms. Therefore, 785 and 830 nm could potentially be useful in identifying water soaking (Figure 5.7) as it develops after a long time of cool storage when kiwifruit is at a similar FF range.

In both case studies, kiwifruit μ_a and μ_s' may be influenced by FF despite internal disorder symptoms, as kiwifruit with internal disorder had different quality attributes (Table 4.3, Table 5.2). Therefore, the segregation of disordered kiwifruit could be due to several factors. Lower μ_s' was observed in BMSB damaged kiwifruit at 785 nm (Figure 4.7), while no difference of μ_a at 785 nm was found between sound and kiwifruit with BMSB damage. Although μ_a at 780 nm could be higher in kiwifruit with BMSB damage that had water-soaking symptoms, the lower FF (Table 4.3) in kiwifruit with BMSB damage may lead to μ_s' decrease and result in a lower μ_a due to the estimation uncertainty.

Kiwifruit μ_s' in this work were lower than results obtained from other research works (Table 8.1); this may be because kiwifruit FF were lower after disorder development and storage. Low FF resulting from cell wall degradation increases LBI parameters (Figure 7.8), while high LBI parameters could result from either low μ_a or low μ_s' or both. Thus, whether the difference in

kiwifruit μ_a at 785 nm results from water-soaking symptoms or different FF remains unanswered. Therefore, a stepwise classification method of 785 nm and 532 nm needs to be investigated. For instance, kiwifruit μ_a and μ_s' at 785 nm may be analysed first then used to segregate soft or kiwifruit with internal disorder. After the first-step segregation, kiwifruit μ_a and μ_s' at 532 nm can be analysed for segregating fruit with discoloured tissues.

Table 8.1. Optical properties of kiwifruit measured with different methods.

Cultivar	Method	Wavelength (nm)	Sample	μ_a (cm^{-1})	μ_s' (cm^{-1})	Reference
Huayou	IS-IAD[1]	900-1700	Flesh slice (4 mm)	0 - 3	6 - 16	(Liu et al., 2019a)
Zesy002	IS-IAD	400-1100	Flesh slice (3.3 mm)	0.1-0.7	1-3	(Z. Wang, Künnemeyer, McGlone, & Burdon, 2020)
Hayward	IS-IAD	900-1700	Flesh slice (3 mm)	1-9	3-10	(Gao et al., 2021)
Hayward	TRS[2]	650 - 1000	Intact	0.4 - 0.6	13 - 16	(Cubeddu et al., 2001)
Unknown	SRS[3]	500 - 1000	Intact	0.2 – 1.1	7 - 8	(Qin & Lu, 2008)
Hayward	LBI[4]	785	Intact	0.7-1.1	32-40	(Baranyai & Zude, 2009)
Zesy002	LBIP[5]	520, 532, 660 and 785	Intact	0.01-0.3,	0.02-4.9	(Section 4.3.3 & 5.3.3)
Hayward	LBIP	520, 532, 660 and 785	Intact	0.06-1.4	0.09-3.5	(Section 4.3.3 & 5.3.3)

[1]*Integrating sphere - inverse adding double method.*
[2]*Muti-spectral time-resolved system.*
[3]*Muti-spectral spatially resolved system.*
[4]*Laser backscattering imaging with Monte Carlo simulation*
[5]*Laser backscattering imaging with pre-classification*

Although μ_a and μ_s' are assumed to be correlated with internal disorder symptoms, the segregation of sound fruit and kiwifruit with the internal disorder could be affected by the estimation uncertainty of μ_a and μ_s'. In addition, there is currently no standard method to validate the estimated kiwifruit μ_a and μ_s' (Walsh et al., 2020), as optical values vary with different optical systems (Table 8.1). Therefore, it's challenging to confirm estimated μ_a and μ_s'. Alternatively, relative (non-validated) μ_a and μ_s' could be an option for estimating kiwifruit

μ_a and μ_s' within the different tissue layers using IS-IAD (Fang et al., 2016). However, the requirement for the measurement system of IS-IAD is high for obtaining accurate values. In addition, relative (non-validated) μ_a and μ_s' are also expected to be frequently calibrated with kiwifruit harvested from different seasons, orchards or maturity stages. In real practice, neither frequent calibration in the research lab nor IS-IAD in the packhouse lab would be suitable for the industry.

8.3.2 Segregation with LBI parameters

Instead of estimating μ_a and μ_s' of kiwifruit, LBI parameters at 520 cm directly extracted from the attenuation profile demonstrated its ability to segregate kiwifruit with CI (Figure 5.3 and Figure 5.4), and kiwifruit with water soaking symptoms have a larger diffusion area (Figure 5.7). During kiwifruit ripening, LBI parameters followed an increasing pattern (Figure 6.1 and Figure 6.2) and are correlated with FF decreases (Figure 7.8). At the wavelength of 830 nm, ripe or soft kiwifruit had lower scattering due to cell wall degradation, which corresponded with an increase in LBI parameters due to reduced attenuation.

Directly extracted LBI parameters showed limitations in estimating FF values with R^2 of 0.5 and 0.03 for 'Zesy002' and 'Hayward' Test_1 using a PLS model (Table 7.5). This may be due to that LBI parameters are influenced by μ_a and μ_s', thus FF estimation is not consistent when SSC changes at the same time. However, LBI parameters can be utilized for qualitative kiwifruit FF segregation, and the segregation model had a moderate performance with over 80 % overall accuracy for 'Zesy002' and 'Hayward'. However, the performance of the segregation model varies in different data sets (Table 7.7), with different FF thresholds (Figure 7.16 and Figure 7.17) and at different maturities (Table 7.10). Results indicate that FF segregation error likely occurs for soft kiwifruit with FF range between 5 – 15 N and late maturing fruit with BWFR between 85 – 125 % with the current methodology (Figure 7.24). The segregation uncertainty

may be due to the small difference in average kiwifruit FF between soft and firm fruit (Table 7.6 and Table 7.9), which results in overlapping LBI parameters (Figure 7.14 and Figure 7.15). Therefore, a possible future research direction is to improve LBI image analysis and apply machining learning or deep learning methods, such as Convolutional Neural Networks, to improve the FF segregation model.

8.4 Laser backscattering imaging technology limitations and future works

8.4.1 Attenuation analysis, LBI parameters and optical properties

Research was conducted to achieve the objectives in Chapter 1 following a research outline in Figure 1.1. With the results summary and discussion above, limitations and future work of the current LBI methodology is presented in Figure 8.1

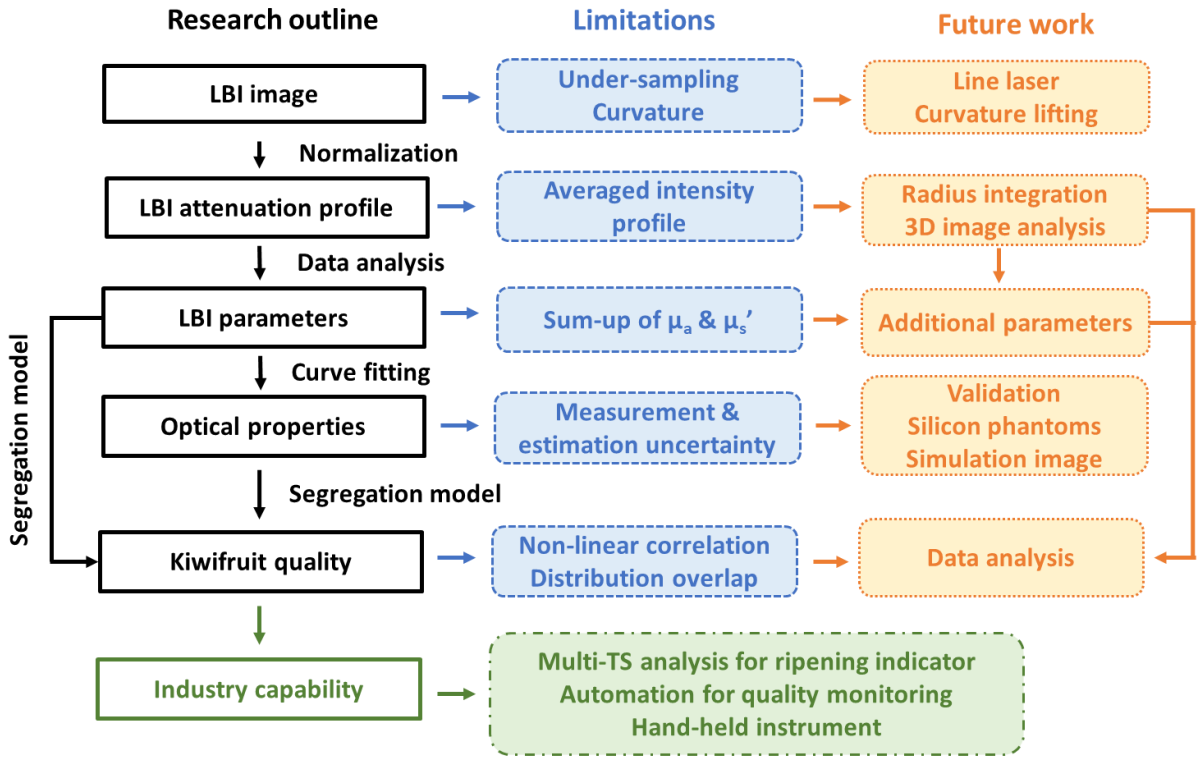

Figure 8.1. Laser backscattering imaging technology limitations and future work direction.

Limitations in the currently developed LBI image analysis could result in uncertainty of optical properties estimation and then, further influence kiwifruit segregation. Firstly, LBI is a 'point measurement' and attempts to describe the overall quality of the kiwifruit with information

extracted from a limited area of tissue, ignoring any tissue information outside of this measured region. For example, in Table 5.3, LBI had a greater segregation accuracy at the Stylar end than in the equatorial region, resulting from kiwifruit CI symptoms developed from the stylar end. In BMSB injured kiwifruit case study, LBI data was taken from the equatorial region of the fruit, thus, LBI could only capture the damage when severe enough to affect the equator of the kiwifruit. Therefore, the ability to detect early-stage disorder symptoms is not available. In addition, the curvature of the fruit surface may further influence image analysis (Qing et al., 2007; Qin & Lu, 2008) with images obtained from kiwifruit shoulders. However, this curvature influence was not considered in the CI kiwifruit study; thus, the difference in LBI between the stylar end and equatorial region may be attributed to both CI symptoms and shape effect.

A line laser that scans the whole fruit surface could be implemented to obtain more information, especially for localised bruising or water-soaking patches, which can potentially lead to more severe damage in the rest of the fruit (Figure 8.2).

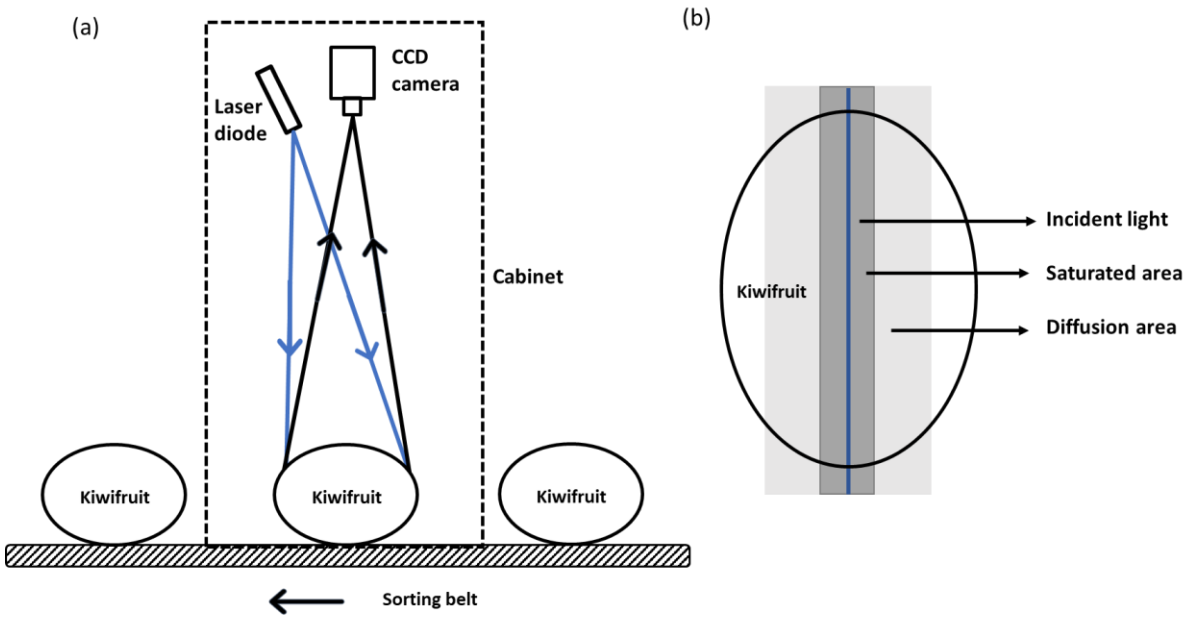

Figure 8.2. Schematic laser backscattering imaging (a) system with line laser as the light source. (b) possible light diffusion after light and tissue interaction.

Secondly, the LBI profile lost information when transformed from averaged weighted intensity. Averaged LBI profile can potentially ignore corky or granular tissues in the early stages of internal disorder development or FF difference of kiwifruit at similar ripeness. Additional LBI parameters extracted from multiple radii of 3D LBI attenuation (Figure 8.3c,d) could be investigated with advanced data analysis, such as machine learning. Figure 8.3 is an example of 3D LBI attenuation. The improved LBI profile extraction could be useful for abnormal tissue areas, such as tissue with granulation or dead cells induced by mechanical injuries or internal disorders.

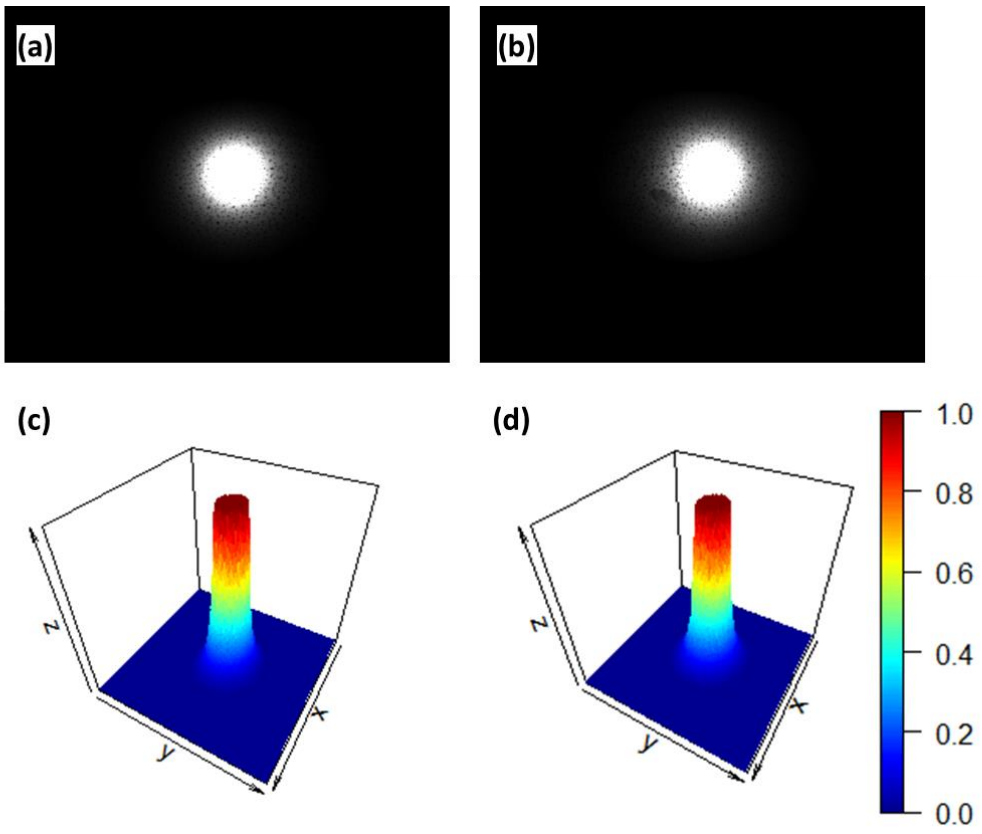

*Figure 8.3. Example of 2D (a,b) and 3D (c,d) image at 780 nm of 'Zesy002' kiwifruit on day 1 (a,c) and day 13 (b,d) stored at 20 °C. x * y represent image (a,b) sizes of 130.04 * 104.04 (mm^2), and z is normalized backscattered light intensity.*

Several reasons may lead to incorrect estimation of optical properties. The error could be due to the complexity of biological tissue. For kiwifruit, the measured optical properties also

capture various surface properties (such as colour, hair, lenticel, and sunburn), which can impact the estimation of quality attributes (such as FF). Without an appropriate method to isolate the effect of skin appearance or fruit quality, estimation errors could arise from bulk optical information of multiple surface features. The pre-classification approach has the potential to provide reference attention profiles; however, μ_a and μ_s' were not validated in this PhD work. Therefore, validation is required for optical phantoms and phantoms made from other materials, such as silicone, may also be considered for repeat measurements. Alternatively, simulation of the attenuation profile may be considered using methods such as Monte Carlo simulation.

Current LBI technology may qualitatively segregate kiwifruit that were either severely damaged or below 9.8 N. However, conducting an additional microstructure study and investigating correlations between LBI and cell distribution within the near-surface tissue zone may be beneficial, such as periderm thickness, small to large cell ratio and cell density (Harker & Hallett, 1994).

8.4.2 Industry capability

8.4.2.1 Kiwifruit segregation

As a low-cost, fast, spatially resolved imaging system, LBI could be adapted into packhouse sorting lines with its spatially resolved set-up. In addition to limitations in attenuation analysis and optical property estimation, the LBI parameter result could be influenced by fruit appearances, such as colour or skin texture. In addition, transferring the segregation model to different populations of kiwifruit without prior validation can result in poor performance. This could be due to LBI parameters containing estimated bulk optical information linked to kiwifruit FF and SSC, but whether and how they are directly or indirectly related is unknown. During

kiwifruit ripening, both kiwifruit FF and SSC changed at the same time, and there is no standard calibration method representing the dynamic scenario.

In both BMSB damaged kiwifruit and CI kiwifruit studies, early-stage disorder detection does not work with the current methodology. The recommended approach would be to improve the pre-classification model and validate using a numeric simulation. Other easier alternatives would be improved image analysis and combined wavelength assessments. A possible approach is to conduct stepwise segregation using multiple wavelengths. Given the factor that absorption is influenced by water and soluble carbohydrates at 830 nm, the wavelengths at 1060 nm may be useful for FF estimation after excluding kiwifruit with water soaking or water patches. Other useful wavelengths could be 660 nm and 685 nm which coincide with the chlorophyll absorption band (Seifert et al., 2015). These wavelengths could be used to describe the change of flesh colour from green to yellow in early harvested 'Zesy002' when FF is relatively stable. Moreover, a decision boundary (Lee & Landgrebe, 1993) according to optical properties could be considered to adjust segregation thresholds. This process could consider additional factors, such as pre-harvest conditions.

8.4.2.2 Monitoring and prediction

LBI technology may be utilized to monitor kiwifruit ripening during postharvest storage. A handheld device could be investigated for quick assessment. Using a turning table, an automated measurement set-up has been adapted to the current LBI system (Figure 8.4). The improved system in Figure 8.4 allows hourly measurement of 16 kiwifruit at 5 wavelengths in rotation. The customized automation system demonstrated that the LBI system can conduct continuous measurements, which may provide reference library data in a packhouse environment.

Figure 8.4. Turning table set up for automotive measurement.

Additionally, follow-up research on time-series analysis would be useful for describing softening phase-shifting points and forecasting FF value based on the LBI trend model. LBI parameter changes may be correlated with physical structure changes during kiwifruit ripening. LBI parameters extracted at 830 nm may be useful for describing the ripening process (Figure 6.1 and Figure 6.2), and time series analysis coefficients could also forecast the trend (Figure 6.4 and Figure 6.5). To approach this, a data set of kiwifruit measured at a greater frequency is required. In addition, more advanced data analysis such as multivariate time series analysis, utilising machine learning, and data mining should be investigated to find potential underlying patterns.

The segregation model for kiwifruit FF and internal disorders may be correlated with industry assessment criteria during inspections at export and repacking. Overall accuracy, Precision and Sensitivity of the segregation model could be expected when data set SFI is provided (Figure 7.16 and Figure 7.17). This approach should be validated with a bigger targeted kiwifruit population before the application.

In addition, fruit quality assessment at the repacking stage is conducted with cold fruit. A supplement trial of the cold kiwifruit FF segregation model was conducted in Nov 2022 to assess the model consistency when the temperature changes. The FF segregation model was

built with LBI parameters (SLP and DIP) at 830 to minimise the influence of temperature. The model had Overall accuracy, Precision and Sensitivity of 0.8, 0.9 and 0.5, respectively, using the penetrometer FF as reference and 0.7,0.6 and 0.6 using Soft Fruit Tester (Willowbank Electronics Ltd., Napier, New Zealand) firmness as reference. In the future, studies may be conducted to investigate the correlation between Soft Fruit Tester firmness and LBI data. The combined non-destructive LBI and Soft Fruit Tester technology may provide more feasibility in kiwifruit segregation.

8.5 Final conclusion

The main objective of this PhD work was to investigate whether LBI technology could segregate kiwifruit with internal disorders [brown marmorated stink bug (BMSB) feeding injury and chilling injury (CI)], as well as soft fruit at FF threshold of 9.8 N. In this work,

(i) An LBI technique methodology was established, including system setup and attenuation analysis protocol.

(ii) LBI parameters and estimated optical properties were correlated with kiwifruit quality attributes during ripening and disorder existence.

(iii) The segregation models were developed to enable quality estimation of kiwifruit FF and internal disorder symptoms based on LBI parameters and optical properties.

(iv) Improvements for the industrial applicability were addressed.

The research was first conducted to develop an LBI attenuation analysis methodology for LBI parameter extraction. A pre-classification approach was then investigated and validated with optical phantoms. According to LBI parameters, classification accuracy achieved 56.6 % and 91.5 % for μ_a and μ_s' class of liquid phantoms, respectively. The pre-classical model was then utilized for kiwifruit μ_a and μ_s' estimation. The segregation accuracy for kiwifruit with BMSB

damage was 84 % and 62 % for 'Zesy002' and 'Hayward' using estimated kiwifruit μ_a and μ_s'. Using extracted parameters, the segregation accuracy for kiwifruit with CI was 92 % and 39 % for 'Zesy002' and 'Hayward'. Therefore, LBI technology has the potential to segregate kiwifruit with internal disorders. Prior to developing kiwifruit firmness segregation model, kiwifruit LBI parameters through the kiwifruit ripening process were studied, and the increasing trend of LBI parameters may be correlated with kiwifruit softening. The firmness segregation model achieved the accuracy for segregating fruit based on the 9.8 N FF threshold was 75 % and 70 % for 'Zesy002' and 'Hayward' in test sets.

In conclusion, LBI is a low-cost, fast, real-time non-destructive measurement that has the potential to be used on industrial sorting lines. This work confirms that LBI technology can potentially sort soft kiwifruit or kiwifruit with early internal disorder symptoms and be adapted to packhouse sorting. However, in this work, FF segregation uncertainty at the 9.8 N threshold was observed when 'Zesy002' FF (N) $\in$ (5,15) and 'Hayward' FF (N) $\in$ (5,20) due to LBI parameter overlapping. Improved image analysis and segregation algorithms need to be investigated to enhance the segregation sensitivity for kiwifruit FF in the lower firmness range. In the future, LBI technology could also be transferred into handheld equipment and extended to monitor fruit development and other cultivars.

References

Adebayo, S. E., Hashim, N., Abdan, K., Hanafi, M., & Mollazade, K. (2016). Prediction of quality attributes and ripeness classification of bananas using optical properties. *Scientia Horticulturae*, *212*, 171–182. https://doi.org/10.1016/j.scienta.2016.09.045

Adebayo, S. E., Hashim, N., Hass, R., Reich, O., Regen, C., Münzberg, M., Abdan, K., Hanafi, M., & Zude-Sasse, M. (2017). Using absorption and reduced scattering coefficients for non-destructive analyses of fruit flesh firmness and soluble solids content in pear (Pyrus communis 'Conference')—An update when using diffusion theory. *Postharvest Biology and Technology*, *130*, 56–63. https://doi.org/10.1016/j.postharvbio.2017.04.004

Adedeji, A. A., Ekramirad, N., Rady, A., Hamidisepehr, A., Donohue, K. D., Villanueva, R. T., Parrish, C. A., & Li, M. (2020). Non-Destructive Technologies for Detecting Insect Infestation in Fruits and Vegetables under Postharvest Conditions: A Critical Review. *Foods*, *9*(7), 927. https://doi.org/10.3390/foods9070927

Aernouts, B., Erkinbaev, C., Watté, R., Van Beers, R., Do Trong, N. N., Nicolai, B., & Saeys, W. (2015). Estimation of bulk optical properties of turbid media from hyperspectral scatter imaging measurements: Metamodeling approach. *Optics Express*, *23*(20), 26049. https://doi.org/10.1364/OE.23.026049

Aernouts, B., Zamora-Rojas, E., Beers, R. V., Watté, R., Wang, L., Tsuta, M., Lammertyn, J., & Saeys, W. (2013). Supercontinuum laser based optical characterization of Intralipid® phantoms in the 500-2250 nm range. *Optics Express*, *21*(26), 32450–32467. https://doi.org/10.1364/OE.21.032450

Aitken, A. G., & Warrington, I. J. (2021). *Fresh Facts: New Zealand horticultural exports 2021 [Fact Sheet]*.

Anderson, E. R., Cuccia, D. J., & Durkin, A. J. (2007). *Detection of bruises on golden delicious apples using spatial- frequency-domain imaging* (T. Vo-Dinh, W. S. Grundfest, D. A. Benaron, G. E. Cohn, & R. Raghavachari, Eds.; p. 64301O). https://doi.org/10.1117/12.717608

Andreadis, S. S., Navrozidis, E. I., Farmakis, A., & Pisalidis, A. (2018). First Evidence of Halyomorpha halys (Hemiptera: Pentatomidae) Infesting Kiwi Fruit (Actinidia chinensis) in Greece1. *Journal of Entomological Science*, *53*(3), 402–405. https://doi.org/10.18474/JES18-19.1

Andrew McGlone, V., Jordan, R. B., & N. Schaare, P. (1997). Anomalous firmness changes in cool-stored kiwifruit. *Postharvest Biology and Technology*, *12*(2), 147–156. https://doi.org/10.1016/S0925-5214(97)00049-5

Baranyai, L. (2020). Laser induced diffuse reflectance imaging – Monte Carlo simulation of backscattering measured on the surface. *MethodsX*, *7*, 100958. https://doi.org/10.1016/j.mex.2020.100958

Baranyai, L., & Zude, M. (2008). Analysis of laser light migration in apple tissue by Monte Carlo simulation. *Progress in Agricultural Engineering Sciences*, *4*(1), 45–59. https://doi.org/10.1556/Progress.4.2008.3

Baranyai, L., & Zude, M. (2009). Analysis of laser light propagation in kiwifruit using backscattering imaging and Monte Carlo simulation. *Computers and Electronics in Agriculture*, *69*(1), 33–39. https://doi.org/10.1016/j.compag.2009.06.011

Barreiro, P., Moya, A., Correa, E., Ruiz-Altisent, M., Fernández-Valle, M., Peirs, A., Wright, K. M., & Hills, B. P. (2002). Prospects for the rapid detection of mealiness in apples by nondestructive NMR relaxometry. *Applied Magnetic Resonance*, *22*(3), 387–400. https://doi.org/10.1007/BF03166119

Bauchot, A. D., Hallett, I. C., Redgwell, R. J., & Lallu, N. (1999). Cell wall properties of kiwifruit affected by low temperature breakdown. *Postharvest Biology and Technology*, *16*(3), 245–255. https://doi.org/10.1016/S0925-5214(99)00016-2

Beever, D. J., & Hopkirk, G. (1990). Fruit development and fruit physiology. In 'Kiwifruit: Science and management'. *Ray Richards, Auckland*, 97–126.

Benelli, A., Cevoli, C., Fabbri, A., & Ragni, L. (2022). Ripeness evaluation of kiwifruit by hyperspectral imaging. *Biosystems Engineering*, *223*, 42–52. https://doi.org/10.1016/j.biosystemseng.2021.08.009

Berardinelli, A., Benelli, A., Tartagni, M., & Ragni, L. (2019). Kiwifruit flesh firmness determination by a NIR sensitive device and image multivariate data analyses. *Sensors and Actuators A: Physical*, *296*, 265–271. https://doi.org/10.1016/j.sna.2019.07.027

Bergh, J. C., Joseph, S. V., Short, B. D., Nita, M., & Leskey, T. C. (2019). *Effect of pre-harvest exposures to adult Halyomorpha halys (Hemiptera: Pentatomidae) on feeding injury to apple cultivars at harvest and during post-harvest cold storage*. https://doi.org/10.1016/j.cropro.2019.104872

Bessemans, N., Verboven, P., Verlinden, B. E., & Nicolaï, B. M. (2016). A novel type of dynamic controlled atmosphere storage based on the respiratory quotient (RQ-DCA). *Postharvest Biology and Technology*, *115*, 91–102. https://doi.org/10.1016/j.postharvbio.2015.12.019

Biswas, P., East, A. R., Hewett, E. W., & Heyes, J. A. (2016). Chilling Injury in Tomato Fruit. In *Horticultural Reviews, Volume 44* (pp. 229–278). John Wiley & Sons, Ltd. https://doi.org/10.1002/9781119281269.ch5

Bloemen, M. C. T., van Gerven, M. S., van der Wal, M. B. A., Verhaegen, P. D. H. M., & Middelkoop, E. (2011). An objective device for measuring surface roughness of skin and scars. *Journal of the American Academy of Dermatology*, *64*(4), 706–715. https://doi.org/10.1016/j.jaad.2010.03.006

Box, G. E. P., Jenkins, G. M., Reinsel, G. C., & Ljung, G. M. (2015). *Time Series Analysis: Forecasting and Control*. Wiley.

Bressel, L., Hass, R., & Reich, O. (2013). Particle sizing in highly turbid dispersions by Photon Density Wave spectroscopy. *Journal of Quantitative Spectroscopy and Radiative Transfer*, *126*, 122–129. https://doi.org/10.1016/j.jqsrt.2012.11.031

Brizzolara, S., Manganaris, G. A., Fotopoulos, V., Watkins, C. B., & Tonutti, P. (2020). Primary Metabolism in Fresh Fruits During Storage. *Frontiers in Plant Science*, *11*. https://www.frontiersin.org/articles/10.3389/fpls.2020.00080

Brown, M. W., & Short, B. D. (2010). Factors Affecting Appearance of Stink Bug (Hemiptera: Pentatomidae) Injury on Apple. *Environmental Entomology*, *39*(1), 134–139. https://doi.org/10.1603/EN09175

Burdon, J., & Lallu, N. (2011). Kiwifruit (Actinidia spp.). In *Postharvest Biology and Technology of Tropical and Subtropical Fruits* (pp. 326–362e). Elsevier. https://doi.org/10.1533/9780857092885.326

Burdon, J., Lallu, N., Pidakala, P., & Barnett, A. (2013). Soluble solids accumulation and postharvest performance of 'Hayward' kiwifruit. *Postharvest Biology and Technology*, *80*, 1–8. https://doi.org/10.1016/j.postharvbio.2013.01.009

Burdon, J., Pidakala, P., Martin, P., & Billing, D. (2017). Softening of 'Hayward' kiwifruit on the vine and in storage: The effects of temperature. *Scientia Horticulturae*, *220*, 176–182. https://doi.org/10.1016/j.scienta.2017.04.004

Burdon, J., Pidakala, P., Martin, P., Billing, D., & Boldingh, H. (2016). Fruit maturation and the soluble solids harvest index for 'Hayward' kiwifruit. *Scientia Horticulturae*, *213*, 193–198. https://doi.org/10.1016/j.scienta.2016.10.027

Burdon, J., Pidakala, P., Martin, P., McAtee, P. A., Boldingh, H. L., Hall, A., & Schaffer, R. J. (2014). Postharvest performance of the yellow-fleshed 'Hort16A' kiwifruit in relation to fruit maturation. *Postharvest Biology and Technology*, *92*, 98–106. https://doi.org/10.1016/j.postharvbio.2014.01.004

Burdon, J., Punter, M., Billing, D., Pidakala, P., & Kerr, K. (2015). SHRIVEL IN KIWIFRUIT. *Acta Horticulturae*, *1096*, 309–315. https://doi.org/10.17660/ActaHortic.2015.1096.34

Burdon, J., Wohlers, M., Pidakala, P., Laurie, T., Punter, M., & Billing, D. (2014). The potential for commonly measured at-harvest fruit characteristics to predict chilling susceptibility of 'Hort16A' kiwifruit. *Postharvest Biology and Technology*, *94*, 41–48. https://doi.org/10.1016/j.postharvbio.2014.03.005

Canteli, D., López, J. M., Lauzurica, S., Lluscà, M., Sánchez-Aniorte, M. I., Bertomeu, J., Morales, M., & Molpeceres, C. (2015). Analysis by Finite Element Calculations of Light Scattering in Laser-textured AZO Films for PV thin-film Solar Cells. *Energy Procedia*, *84*, 78–85. https://doi.org/10.1016/j.egypro.2015.12.298

Cantre, D., East, A., Verboven, P., Trejo Araya, X., Herremans, E., Nicolaï, B. M., Pranamornkith, T., Loh, M., Mowat, A., & Heyes, J. (2014). Microstructural characterisation of commercial kiwifruit cultivars using X-ray micro computed tomography. *Postharvest Biology and Technology*, *92*, 79–86. https://doi.org/10.1016/j.postharvbio.2014.01.012

Cantre, D., Herremans, E., Verboven, P., Ampofo-Asiama, J., & Nicolaï, B. (2014). Characterization of the 3-D microstructure of mango (Mangifera indica L. cv. Carabao) during ripening using X-ray computed microtomography. *Innovative Food Science & Emerging Technologies*, *24*, 28–39. https://doi.org/10.1016/j.ifset.2013.12.008

Cen, H. (2011). *Hyperspectral imaging-based spatially-resolved technique for accurate measurement of the optical properties of horticultural products*. http://adsabs.harvard.edu/abs/2011PhDT.....195C

Cen, H., Lu, R., Mendoza, F., & Beaudry, R. M. (2013). Relationship of the optical absorption and scattering properties with mechanical and structural properties of apple tissue. *Postharvest Biology and Technology*, *85*, 30–38. https://doi.org/10.1016/j.postharvbio.2013.04.014

Cen, H., Lu, R., Zhu, Q., & Mendoza, F. (2016). Nondestructive detection of chilling injury in cucumber fruit using hyperspectral imaging with feature selection and supervised classification. *Postharvest Biology and Technology*, *111*, 352–361. https://doi.org/10.1016/j.postharvbio.2015.09.027

Chen, J.-H., Avila, G. A., Zhang, F., Guo, L. F., Sandanayaka, M., Mi, Q.-Q., Shi, S.-S., & Zhang, J.-P. (2020). Field cage assessment of feeding damage by Halyomorpha halys on kiwifruit orchards in China. *Journal of Pest Science*, *93*(3), 953–963. https://doi.org/10.1007/s10340-020-01216-8

Clark, C. J., McGlone, V. A., De Silva, H. N., Manning, M. A., Burdon, J., & Mowat, A. D. (2004). Prediction of storage disorders of kiwifruit (Actinidia chinensis) based on visible-NIR spectral characteristics at harvest. *Postharvest Biology and Technology*, *32*(2), 147–158. https://doi.org/10.1016/j.postharvbio.2003.11.004

Costa, G., Noferini, M., Montefiori, M., & Brigati, S. (2003). NON-DESTRUCTIVE ASSESSMENT METHODS OF KIWIFRUIT QUALITY. *Acta Horticulturae*, *610*, 179–189. https://doi.org/10.17660/ActaHortic.2003.610.24

Cubeddu, R., D'Andrea, C., Pifferi, A., Taroni, P., Torricelli, A., Valentini, G., Dover, C., Johnson, D., Ruiz-Altisent, M., & Valero, C. (2001). Nondestructive quantification of chemical and physical properties of fruits by time-resolved reflectance spectroscopy in the wavelength range 650–1000 nm. *Applied Optics*, *40*(4), 538–543. https://doi.org/10.1364/AO.40.000538

Cubeddu, R., Musolino, M., Pifferi, A., Taroni, P., & Valentini, G. (1994). Time-resolved reflectance: A systematic study for application to the optical characterization of tissues. *IEEE Journal of Quantum Electronics*, *30*(10), 2421–2430. https://doi.org/10.1109/3.328616

Cubeddu, R., Pifferi, A., Taroni, P., & Torricelli, A. (2002). Measuring fresh fruit and vegetable quality: Advanced optical methods. *Fruit and Vegetable Processing*, 150.

Cubeddu, R., Pifferi, A., Taroni, P., Torricelli, A., & Valentini, G. (1996). Time-resolved imaging on a realistic tissue phantom: Ms′ and μa images versus time-integrated images. *Applied Optics*, *35*(22), 4533–4540. https://doi.org/10.1364/AO.35.004533

Dai, Z., Flatberg, G., Preisig, H., & Deng, L. (2018). Kinetic Studies of Fenton Oxidation Reaction by UV-VIS Spectroscopy. *Journal of Laboratory Chemical Education*, *6*, 141–147. https://doi.org/10.5923/j.jlce.20180605.01

Davie, I. J., Banks, N. H., Jeffery, P. B., Studman, C. J., & Kay, P. (1996). Non-destructive measurement of kiwifruit firmness. *New Zealand Journal of Crop and Horticultural Science*, *24*(2), 151–157. https://doi.org/10.1080/01140671.1996.9513947

Dintwa, E., Jancsók, P., Mebatsion, H. K., Verlinden, B., Verboven, P., Wang, C. X., Thomas, C. R., Tijskens, E., Ramon, H., & Nicolaï, B. (2011). A finite element model for mechanical deformation of single tomato suspension cells. *Journal of Food Engineering*, *103*(3), 265–272. https://doi.org/10.1016/j.jfoodeng.2010.10.023

East, A. R. (2011). Accelerated libraries to inform batch sale scheduling and reduce postharvest losses of seasonal fresh produce. *Biosystems Engineering*, *109*(1), 1–9. https://doi.org/10.1016/j.biosystemseng.2011.01.008

East, A. R., Bloomfield, C., Trejo Araya, X., & Heyes, J. A. (2016). Evaluation of fringe projection as a method to provide information about horticultural product surfaces. *Acta Horticulturae*, *1119*, 189–196. https://doi.org/10.17660/ActaHortic.2016.1119.26

Ekramirad, N., Adedeji, A. A., & Alimardani, R. (2016). *A Review of Non-Destructive Methods for Detection of Insect Infestation in Fruits and Vegetables*.

ElMasry, G., Wang, N., & Vigneault, C. (2009). Detecting chilling injury in Red Delicious apple using hyperspectral imaging and neural networks. *Postharvest Biology and Technology*, *52*, 1–8. https://doi.org/10.1016/j.postharvbio.2008.11.008

Esau, K. (1953). Plant Anatomy. *Soil Science*, *75*(5), 407.

Fang, Z., Fu, X., & He, X. (2016). Investigation of absorption and scattering characteristics of kiwifruit tissue using a single integrating sphere system. *Journal of Zhejiang University SCIENCE B*, *17*, 484–492. https://doi.org/10.1631/jzus.B1500086

Farrell, T. J., Patterson, M. S., & Wilson, B. (1992). A diffusion theory model of spatially resolved, steady-state diffuse reflectance for the noninvasive determination of tissue optical properties in vivo. *Medical Physics*, *19*(4), 879–888. https://doi.org/10.1118/1.596777

Feng, J., MacKay, B. R., & Maguire, K. M. (2001). A procedure for calculating storage life of Hayward kiwifruit. *II International Symposium on Application of Modelling as an Innovative Technology in the Agri-Food Chain; MODEL-IT 566*, 455–460.

Feng, J., Wohlers, M., Olsson, S. R., White, A., McGlone, V. A., Seelye, R. J., Tanner, D., & Bollen, F. (2016). Comparison between an acoustic firmness sensor and a near-infrared spectrometer in segregation of kiwifruit for storage potential. *Acta Horticulturae*, *1119*, 279–288. https://doi.org/10.17660/ActaHortic.2016.1119.39

Ferguson, A. R. (1984). Kiwifruit: A botanical review. *Horticultural Reviews*, *6*, 1–64.

Ferguson, A. R., & Seal, A. G. (2008). Kiwifruit. In J. F. Hancock (Ed.), *Temperate Fruit Crop Breeding* (pp. 235–264). Springer Netherlands. https://doi.org/10.1007/978-1-4020-6907-9_8

Fuke, Y., Sasago, K., & Matsuoka, H. (1985). Determination of Chlorophylls in Kiwi Fruit and Their Changes during Ripening. *Journal of Food Science*, *50*(5), 1220–1223. https://doi.org/10.1111/j.1365-2621.1985.tb10446.x

Fullerton, C. G., Prakash, R., Ninan, A. S., Atkinson, R. G., Schaffer, R. J., Hallett, I. C., & Schröder, R. (2020). Fruit From Two Kiwifruit Genotypes With Contrasting Softening Rates Show Differences in the Xyloglucan and Pectin Domains of the Cell Wall. *Frontiers in Plant Science*, *11*. https://www.frontiersin.org/articles/10.3389/fpls.2020.00964

Gao, M., Guo, W., Huang, X., Du, R., & Zhu, X. (2021). Effect of pressing and impacting bruises on optical properties of kiwifruit flesh. *Postharvest Biology and Technology*, *172*, 111385. https://doi.org/10.1016/j.postharvbio.2020.111385

Garhwal, A. S., Pullanagari, R. R., Li, M., Reis, M. M., & Archer, R. (2020). Hyperspectral imaging for identification of Zebra Chip disease in potatoes. *Biosystems Engineering*, *197*, 306–317. https://doi.org/10.1016/j.biosystemseng.2020.07.005

Gelper, S., Fried, R., & Croux, C. (2010). Robust forecasting with exponential and Holt–Winters smoothing. *Journal of Forecasting*, *29*(3), 285–300. https://doi.org/10.1002/for.1125

Gocławski, J., Sekulska-Nalewajko, J., Korzeniewska, E., & Piekarska, A. (2017). The use of optical coherence tomography for the evaluation of textural changes of grapes exposed to pulsed electric field. *Computers and Electronics in Agriculture*, *142*, 29–40. https://doi.org/10.1016/j.compag.2017.08.008

González-Teruel, J. D., Ruiz-Abellon, M. C., Blanco, V., Blaya-Ros, P. J., Domingo, R., & Torres-Sánchez, R. (2022). Prediction of Water Stress Episodes in Fruit Trees Based on Soil and Weather Time Series Data. *Agronomy*, *12*(6), Article 6. https://doi.org/10.3390/agronomy12061422

Gorthi, S. S., & Rastogi, P. (2010). Fringe projection techniques: Whither we are? *Optics and Lasers in Engineering*, *48*(ARTICLE), 133–140.

Graaff, R., Koelink, M. H., Mul, F. F. M. de, Zijlstra, W. G., Dassel, A. C. M., & Aarnoudse, J. G. (1993). Condensed Monte Carlo simulations for the description of light transport. *Applied Optics*, *32*(4), 426–434. https://doi.org/10.1364/AO.32.000426

Groenhuis, R. A. J., Ferwerda, H. A., & Ten Bosch, J. J. (1983). Scattering and absorption of turbid materials determined from reflection measurements 1: Theory. *Applied Optics*, *22*(16), 2456. https://doi.org/10.1364/AO.22.002456

Gwanpua, S. G., Jabbar, A., Zhao, M., Heyes, J. A., & East, A. R. (2018). Investigating the potential of dual temperature storage as a postharvest management practice to mitigate chilling injury in kiwifruit. *International Journal of Refrigeration*, *86*, 62–72. https://doi.org/10.1016/j.ijrefrig.2017.12.004

Habibi, F., Serrano, M., Zacarías, L., Valero, D., & Guillén, F. (2021). Postharvest Application of 24-Epibrassinolide Reduces Chilling Injury Symptoms and Enhances Bioactive Compounds Content and Antioxidant Activity of Blood Orange Fruit. *Frontiers in Plant Science*, *12*. https://www.frontiersin.org/articles/10.3389/fpls.2021.629733

Haishi, T., Koizumi, H., Arai, T., Koizumi, M., & Kano, H. (2011). Rapid Detection of Infestation of Apple Fruits by the Peach Fruit Moth, Carposina sasakii Matsumura, Larvae Using a 0.2-T Dedicated Magnetic Resonance Imaging Apparatus. *Applied Magnetic Resonance*, *41*(1), 1–18. Scopus. https://doi.org/10.1007/s00723-011-0222-8

Hale, G. M., & Querry, M. R. (1973). Optical Constants of Water in the 200-nm to 200-µm Wavelength Region. *Applied Optics*, *12*(3), 555–563. https://doi.org/10.1364/AO.12.000555

Hall, L. D., Evans, S. D., & Nott, K. P. (1998). Measurement of textural changes of food by MRI relaxometry. *Magnetic Resonance Imaging*, *16*(5–6), 485–492. https://doi.org/10.1016/S0730-725X(98)00116-7

Hallett, I. C., Macrae, E. A., & Wegrzyn, T. F. (1992). Changes in Kiwifruit Cell Wall Ultrastructure and Cell Packing During Postharvest Ripening. *International Journal of Plant Sciences*, *153*(1), 49–60. https://doi.org/10.1086/297006

Hallett, I. C., & Sutherland, P. W. (2005). Structure and Development of Kiwifruit Skins. *International Journal of Plant Sciences*, *166*(5), 693–704. JSTOR. https://doi.org/10.1086/431232

Harker, F. R., Carr, B. T., Lenjo, M., MacRae, E. A., Wismer, W. V., Marsh, K. B., Williams, M., White, A., Lund, C. M., Walker, S. B., Gunson, F. A., & Pereira, R. B. (2009). Consumer liking for kiwifruit flavour: A meta-analysis of five studies on fruit quality. *Food Quality and Preference*, *20*(1), 30–41. https://doi.org/10.1016/j.foodqual.2008.07.001

Harker, F. R., & Hallett, I. C. (1994). Physiological and Mechanical Properties of Kiwifruit Tissue Associated with Texture Change during Cool Storage. *Journal of the American Society for Horticultural Science*, *119*(5), 987–993. https://doi.org/10.21273/JASHS.119.5.987

Hashim, N., Janius, R. B., Abdul, R., Osman, A., Shitan, M., & Zude, M. (2014). *CHANGES OF BACKSCATTERING PARAMETERS DURING CHILLING INJURY IN BANANAS*. *9*, 12.

Hashim, N., Pflanz, M., Regen, C., Janius, R. B., Abdul Rahman, R., Osman, A., Shitan, M., & Zude, M. (2013). An approach for monitoring the chilling injury appearance in bananas by means of backscattering imaging. *Journal of Food Engineering*, *116*(1), 28–36. https://doi.org/10.1016/j.jfoodeng.2012.11.018

Haskell, R. C., Svaasand, L. O., Tsay, T.-T., Feng, T.-C., McAdams, M. S., & Tromberg, B. J. (1994). Boundary conditions for the diffusion equation in radiative transfer. *JOSA A*, *11*(10), 2727–2741. https://doi.org/10.1364/JOSAA.11.002727

Hass, R., Munzke, D., Vargas Ruiz, S., Tippmann, J., & Reich, O. (2015). Optical monitoring of chemical processes in turbid biogenic liquid dispersions by Photon Density Wave spectroscopy.

Analytical and Bioanalytical Chemistry, *407*(10), 2791–2802. https://doi.org/10.1007/s00216-015-8513-9

Hedstrom, C. S., Shearer, P. W., Miller, J. C., & Walton, V. M. (2014). The Effects of Kernel Feeding by Halyomorpha halys (Hemiptera: Pentatomidae) on Commercial Hazelnuts. *Journal of Economic Entomology*, *107*(5), 1858–1865. https://doi.org/10.1603/EC14263

Hertog, M. L. A. T. M., Jeffery, P. B., Gwanpua, S. G., Lallu, N., & East, A. (2016). A mechanistic model to describe the effects of time, temperature and exogenous ethylene levels on softening of kiwifruit. *Postharvest Biology and Technology*, *121*, 143–150. https://doi.org/10.1016/j.postharvbio.2016.08.002

Hewett, E. W., Kim, H. O., & Lallu, N. (1999). POSTHARVEST PHYSIOLOGY OF KIWIFRUIT: THE CHALLENGES AHEAD. *Acta Horticulturae*, *498*, 203–216. https://doi.org/10.17660/ActaHortic.1999.498.23

Ho, Q. T., Verboven, P., Verlinden, B. E., Schenk, A., Delele, M. A., Rolletschek, H., Vercammen, J., & Nicolaï, B. M. (2010). Genotype effects on internal gas gradients in apple fruit. *Journal of Experimental Botany*, *61*(10), 2745–2755. https://doi.org/10.1093/jxb/erq108

Holt, C. C. (2004). Forecasting seasonals and trends by exponentially weighted moving averages. *International Journal of Forecasting*, *20*(1), 5–10. https://doi.org/10.1016/j.ijforecast.2003.09.015

Holz, M., & Chen, S. H. (1978). Quasi-elastic light scattering from migrating chemotactic bands of Escherichia coli. *Biophysical Journal*, *23*(1), 15–31. https://doi.org/10.1016/S0006-3495(78)85429-0

Hu, D., Fu, X., He, X., & Ying, Y. (2016). Noncontact and Wide-Field Characterization of the Absorption and Scattering Properties of Apple Fruit Using Spatial-Frequency Domain Imaging. *Scientific Reports*, *6*(1), Article 1. https://doi.org/10.1038/srep37920

Ishimaru, A. (1978). *Wave propagation and scattering in random media* (Vol. 2). Academic press New York.

Jabbar, A. (2014). *Accelerated fruit libraries to predict storage potential of 'Hayward' kiwifruit grower lines*. 205.

Jabbar, A., & East, A. R. (2016). Quantifying the ethylene induced softening and low temperature breakdown of 'Hayward' kiwifruit in storage. *Postharvest Biology and Technology*, *113*, 87–94. https://doi.org/10.1016/j.postharvbio.2015.11.002

Jabbar, A., East, A. R., Jones, G., Tanner, D. J., & Heyes, J. A. (2014). Modelling batch variability in softening of 'Hayward' kiwifruit from at-harvest maturity measures. *Postharvest Biology and Technology*, *90*, 7–14. https://doi.org/10.1016/j.postharvbio.2013.11.008

Jacquez, J. A., & Kuppenheim, H. F. (1955). Theory of the Integrating Sphere. *JOSA*, *45*(6), 460–470. https://doi.org/10.1364/JOSA.45.000460

Janjai, S., Lamlert, N., Mahayothee, B., Bala, B., Haewsungcharoen, M., Nagle, M., Leis, H., & Müller, J. (2008). Finite Element Simulation of Drying of Longan Fruit. *Drying Technology*, *26*, 666–674. https://doi.org/10.1080/07373930802046088

Jiang, Y., Li, C., & Takeda, F. (2016). Nondestructive Detection and Quantification of Blueberry Bruising using Near-infrared (NIR) Hyperspectral Reflectance Imaging. *Scientific Reports*, *6*(1), Article 1. https://doi.org/10.1038/srep35679

Kader, A. A. (2002). *Postharvest technology of horticultural crops, 3rd ed.* (Vol. 3311). University of California Agriculture and Natural Resources.

Kader, A. A., & Rolle, R. S. (2004). *The role of post-harvest management in assuring the quality and safety of horticultural produce* (Vol. 152). Food & Agriculture Org.

Kemsley, E. K., Tapp, H. S., Binns, R., Mackin, R. O., & Peyton, A. J. (2008). Feasibility study of NIR diffuse optical tomography on agricultural produce. *Postharvest Biology and Technology*, *48*(2), 223–230. https://doi.org/10.1016/j.postharvbio.2007.10.014

Khoiruddin, A. A. (2015). Linear Profilometry: A low cost 3D acquisition system. *2015 IEEE/SICE International Symposium on System Integration (SII)*, 783–788. https://doi.org/10.1109/SII.2015.7405079

Kim, H. O., Hewett, E. W., & Lallu, N. (1999). THE ROLE OF ETHYLENE IN KIWIFRUIT SOFTENING. *Acta Horticulturae*, *498*, 255–262. https://doi.org/10.17660/ActaHortic.1999.498.29

Kim, S., & Schatzki, T. F. (2000). Apple watercore sorting system using x-ray imagery: I. Algorithm development. *Transactions of the American Society of Agricultural Engineers*, *43*(6), 1695–1702. Scopus. https://doi.org/10.13031/2013.3070

Kratsch, H. A., & Wise, R. R. (2000). The ultrastructure of chilling stress. *Plant, Cell & Environment*, *23*(4), 337–350. https://doi.org/10.1046/j.1365-3040.2000.00560.x

Kwiatkowski, D., Phillips, P. C. B., Schmidt, P., & Shin, Y. (1992). Testing the null hypothesis of stationarity against the alternative of a unit root: How sure are we that economic time series have a unit root? *Journal of Econometrics*, *54*(1), 159–178. https://doi.org/10.1016/0304-4076(92)90104-Y

Lai, P.-H. L., Bailey, D., East, A., Gwanpua, S.-G., & Heyes, J. (2019). Methodology of extracting microtopography of kiwifruit skin using fringe projection. *2019 IEEE International Instrumentation and Measurement Technology Conference (I2MTC)*, 1–5. https://doi.org/10.1109/I2MTC.2019.8826813

Lakowicz, J. R., Laczko, G., Gryczynski, I., Szmacinski, H., Wiczk, W., & Johnson, M. L. (1989). Frequency-domain fluorescence spectroscopy; principles, biochemical applications and future developments. *Berichte Der Bunsengesellschaft Für Physikalische Chemie*, *93*(3), 316–327. https://doi.org/10.1002/bbpc.19890930321

Lallu, N., Searle, A. N., & Macrae, E. A. (1989). An investigation of ripening and handling strategies for early season kiwifruit (Actinidia deliciosa cv Hayward). *Journal of the Science of Food and Agriculture*, *47*(4), 387–400. https://doi.org/10.1002/jsfa.2740470402

Lammertyn, J., Dresselaers, T., Van Hecke, P., Jancsók, P., Wevers, M., & Nicolaï, B. M. (2003). MRI and x-ray CT study of spatial distribution of core breakdown in 'Conference' pears. *Magnetic Resonance Imaging*, *21*(7), 805–815. https://doi.org/10.1016/S0730-725X(03)00105-X

Langerholc, J. (1982). Beam broadening in dense scattering media. *Applied Optics*, *21*(9), 1593–1598. https://doi.org/10.1364/AO.21.001593

Lara, J. R., Kamiyama, M., Hernandez, G., Lewis, M., & Hoddle, M. S. (2018). Laboratory assessment of feeding injury and preference of brown marmorated stink bug, *Halyomorpha halys* Stål (Hemiptera: Pentatomidae), for *Actinidia chinensis* var. *deliciosa* 'Hayward' (Zespri® Green) and *Actinidia chinensis* var. *chinensis* 'Zesy002' (Zespri® SunGold). *New Zealand Entomologist*, *41*(1), 12–24. https://doi.org/10.1080/00779962.2018.1438758

Lara, J. R., Kamiyama, M. T., Hernandez, G., Nay, J., & Hoddle, M. S. (2017). Assessment of Feeding Acceptance and Injury of Kerman Pistachios, Pistacia vera, by Brown Marmorated Stink Bug (Hemiptera: Pentatomidae). *Journal of Insect Science*, *17*(5), 106. https://doi.org/10.1093/jisesa/iex084

Lee, C., & Landgrebe, D. A. (1993). Feature extraction based on decision boundaries. *IEEE Transactions on Pattern Analysis and Machine Intelligence*, *15*(4), 388–400. https://doi.org/10.1109/34.206958

Li, H., Pidakala, P., Billing, D., & Burdon, J. (2016). Kiwifruit firmness: Measurement by penetrometer and non-destructive devices. *Postharvest Biology and Technology*, *120*, 127–137. https://doi.org/10.1016/j.postharvbio.2016.06.007

Li, M., Landahl, S., East, A. R., Verboven, P., & Terry, L. A. (2019). Optical coherence tomography—A review of the opportunities and challenges for postharvest quality evaluation. *Postharvest Biology and Technology*, *150*, 9–18. https://doi.org/10.1016/j.postharvbio.2018.12.005

Li, M., Pullanagari, R. R., Pranamornkith, T., Yule, I. J., & East, A. R. (2017). Quantitative prediction of post storage 'Hayward' kiwifruit attributes using at harvest Vis-NIR spectroscopy. *Journal of Food Engineering*, *202*, 46–55. https://doi.org/10.1016/j.jfoodeng.2017.01.002

Li, M., Pullanagari, R., Yule, I., & East, A. (2022). Segregation of 'Hayward' kiwifruit for storage potential using Vis-NIR spectroscopy. *Postharvest Biology and Technology*, *189*, 111893. https://doi.org/10.1016/j.postharvbio.2022.111893

Li, M., Rivera, S., Franklin, D., Nowak, E., Hallett, I., Kolenderska, S., Urbańska, M., Vanholsbeeck, F., & East, A. (2021). Use of optical coherence tomography and light microscopy for characterisation of mechanical properties and cellular level responses of 'Centurion' blueberries during weight loss. *Journal of Food Engineering*, *303*, 110596. https://doi.org/10.1016/j.jfoodeng.2021.110596

Li, M., Verboven, P., Buchsbaum, A., Cantre, D., Nicolaï, B., Heyes, J., Mowat, A., & East, A. (2015). Characterising kiwifruit (Actinidia sp.) near skin cellular structures using optical coherence tomography. *Postharvest Biology and Technology*, *110*, 247–256. https://doi.org/10.1016/j.postharvbio.2015.08.021

Liu, D., Guo, W., Li, Q., & Xie, D. (2019a). Effect of a plant growth regulator on optical properties of kiwifruit during growth in wavelength range of 950-1650 nm. *Postharvest Biology and Technology*, *156*, 110918. https://doi.org/10.1016/j.postharvbio.2019.05.019

Liu, D., Guo, W., Li, Q., & Xie, D. (2019b). Relationship of the bulk optical properties in 950–1650 nm wavelength range with internal quality and microstructure of kiwifruit during maturation. *Biosystems Engineering*, *184*, 45–54. https://doi.org/10.1016/j.biosystemseng.2019.05.005

López D., Y. Y., Martínez-García, A., & Gómez S., J. (2017). Apple quality study using fringe projection and colorimetry techniques. *Optik*, *147*, 401–413. https://doi.org/10.1016/j.ijleo.2017.08.069

Lu, R. (2007). Nondestructive measurement of firmness and soluble solids content for apple fruit using hyperspectral scattering images. *Sensing and Instrumentation for Food Quality and Safety*, *1*(1), 19. https://doi.org/10.1007/s11694-006-9002-9

Lu, R., & Peng, Y. (2005). Assessing Peach Firmness by Multi-Spectral Scattering. *Journal of Near Infrared Spectroscopy*, *13*(1), 27–35. https://doi.org/10.1255/jnirs.454

Lu, R., & Peng, Y. (2006). Hyperspectral Scattering for assessing Peach Fruit Firmness. *Biosystems Engineering*, *93*(2), 161–171. https://doi.org/10.1016/j.biosystemseng.2005.11.004

Lu, R., Van Beers, R., Saeys, W., Li, C., & Cen, H. (2020). Measurement of optical properties of fruits and vegetables: A review. *Postharvest Biology and Technology*, *159*, 111003. https://doi.org/10.1016/j.postharvbio.2019.111003

Lu, Y., Saeys, W., Kim, M., Peng, Y., & Lu, R. (2020). Hyperspectral imaging technology for quality and safety evaluation of horticultural products: A review and celebration of the past 20-year progress. *Postharvest Biology and Technology*, *170*, 111318. https://doi.org/10.1016/j.postharvbio.2020.111318

Ludwick, D., Morrison, W. R., III, Acebes-Doria, A. L., Agnello, A. M., Bergh, J. C., Buffington, M. L., Hamilton, G. C., Harper, J. K., Hoelmer, K. A., Krawczyk, G., Kuhar, T. P., Pfeiffer, D. G., Nielsen, A. L., Rice, K. B., Rodriguez-Saona, C., Shearer, P. W., Shrewsbury, P. M., Talamas, E. J., Walgenbach, J. F., … Leskey, T. C. (2020). Invasion of the Brown Marmorated Stink Bug (Hemiptera: Pentatomidae) into the United States: Developing a National Response to an Invasive Species Crisis Through Collaborative Research and Outreach Efforts. *Journal of Integrated Pest Management*, *11*(1), 4. https://doi.org/10.1093/jipm/pmaa001

Luo, Z., Li, D., Du, R., & Mou, W. (2015). Hydrogen sulfide alleviates chilling injury of banana fruit by enhanced antioxidant system and proline content. *Scientia Horticulturae*, *183*, 144–151. https://doi.org/10.1016/j.scienta.2014.12.021

Lurie, S., & Crisosto, C. H. (2005). Chilling injury in peach and nectarine. *Postharvest Biology and Technology*, *37*(3), 195–208. https://doi.org/10.1016/j.postharvbio.2005.04.012

Lurie, S., Vanoli, M., Dagar, A., Weksler, A., Lovati, F., Eccher Zerbini, P., Spinelli, L., Torricelli, A., Feng, J., & Rizzolo, A. (2011). Chilling injury in stored nectarines and its detection by time-resolved reflectance spectroscopy. *Postharvest Biology and Technology*, *59*(3), 211–218. https://doi.org/10.1016/j.postharvbio.2010.10.005

Ma, C., Feng, L., Pan, L., Wei, K., Liu, Q., Tu, K., Zhao, L., & Peng, J. (2020). Relationships between optical properties of peach flesh with firmness and tissue structure during storage. *Postharvest Biology and Technology*, *163*, 111134. https://doi.org/10.1016/j.postharvbio.2020.111134

Ma, T., Xia, Y., Inagaki, T., & Tsuchikawa, S. (2021). Non-destructive and fast method of mapping the distribution of the soluble solids content and pH in kiwifruit using object rotation near-infrared hyperspectral imaging approach. *Postharvest Biology and Technology*, *174*, 111440. https://doi.org/10.1016/j.postharvbio.2020.111440

Ma, Y., Xu, Y., Yan, H., & Zhang, G. (2021). On-line identification of silkworm pupae gender by short-wavelength near infrared spectroscopy and pattern recognition technology. *Journal of Near Infrared Spectroscopy*. https://doi.org/10.1177/0967033521999745

Macrae, E. A., Lallu, N., Searle, A. N., & Bowen, J. H. (1989). Changes in the softening and composition of kiwifruit(Actinidia deliciosa) Affected by Maturity at Harvest and Postharvest Treatments. *Journal of the Science of Food and Agriculture*, *49*(4), 413–430. https://doi.org/10.1002/jsfa.2740490404

MacRae, E. A., Stec, M. G. H., & Triggs, C. M. (1990). Effects of postharvest treatment on the sensory qualities of kiwifruit harvested at different maturities. *Journal of the Science of Food and Agriculture*, *50*(4), 533–546. https://doi.org/10.1002/jsfa.2740500411

MacRae, E., Quick, W. P., Benker, C., & Stitt, M. (1992). Carbohydrate metabolism during postharvest ripening in kiwifruit. *Planta*, *188*(3). https://doi.org/10.1007/BF00192797

MacRae, E., Redgwell, R., & Wegrzyn, T. (1990). The whens and hows of fruit softening. *NZ Kiwifruit*, 15–17. Scopus.

Magwaza, L. S., Ford, H. D., Cronje, P. J. R., Opara, U. L., Landahl, S., Tatam, R. P., & Terry, L. A. (2013). Application of optical coherence tomography to non-destructively characterise rind breakdown disorder of 'Nules Clementine' mandarins. *Postharvest Biology and Technology*, *84*, 16–21. https://doi.org/10.1016/j.postharvbio.2013.03.019

Magwaza, L. S., & Opara, U. L. (2015). Analytical methods for determination of sugars and sweetness of horticultural products—A review. *Scientia Horticulturae*, *184*, 179–192. https://doi.org/10.1016/j.scienta.2015.01.001

Marquet, P., Bevilacqua, F. P., Depeursinge, C. D., & Haller, E. B. de. (1995). Determination of reduced scattering and absorption coefficients by a single charge-coupled-device array measurement, part I: Comparison between experiments and simulations. *Optical Engineering*, *34*(7), 2055–2063. https://doi.org/10.1117/12.204798

Martelli, F., Del Bianco, S., & Ismaelli, A. (2009). *Light propagation through biological tissue and other diffusive media: Theory, solutions, and software*. CERN Document Server; Society of Photo-Optical Instrumentation Engineers. https://cds.cern.ch/record/2109284

McAtee, P. A., Richardson, A. C., Nieuwenhuizen, N. J., Gunaseelan, K., Hoong, L., Chen, X., Atkinson, R. G., Burdon, J. N., David, K. M., & Schaffer, R. J. (2015). The hybrid non-ethylene and ethylene ripening response in kiwifruit (Actinidia chinensis) is associated with differential regulation of MADS-box transcription factors. *BMC Plant Biology*, *15*(1), 304. https://doi.org/10.1186/s12870-015-0697-9

McCarthy, M. J., Zion, B., Chen, P., Ablett, S., Darke, A. H., & Lillford, P. J. (1995). Diamagnetic susceptibility changes in apple tissue after bruising. *Journal of the Science of Food and Agriculture*, *67*(1), 13–20. https://doi.org/10.1002/jsfa.2740670103

McCollum, T. G., D'Aquino, S., & McDonald, R. E. (1993). Heat Treatment Inhibits Mango Chilling Injury. *HortScience*, *28*(3), 197–198. https://doi.org/10.21273/HORTSCI.28.3.197

McGlone, V. A., Abe, H., & Kawano, S. (1997). Kiwifruit Firmness by near Infrared Light Scattering. *Journal of Near Infrared Spectroscopy*, *5*(2), 83–89. https://doi.org/10.1255/jnirs.102

McGlone, V. A., & Jordan, R. B. (2000). Kiwifruit and apricot firmness measurement by the non-contact laser air-puff method. *Postharvest Biology and Technology*, *19*(1), 47–54. https://doi.org/10.1016/S0925-5214(00)00068-5

McGlone, V. A., & Kawano, S. (1998). Firmness, dry-matter and soluble-solids assessment of postharvest kiwifruit by NIR spectroscopy. *Postharvest Biology and Technology*, *13*(2), 131–141. https://doi.org/10.1016/S0925-5214(98)00007-6

Meglinski, I. V., Buranachai, C., & Terry, L. A. (2010). Plant photonics: Application of optical coherence tomography to monitor defects and rots in onion. *Laser Physics Letters*, *7*(4), 307–310. https://doi.org/10.1002/lapl.200910141

Melado-Herreros, A., Muñoz-García, M.-A., Blanco, A., Val, J., Fernández-Valle, M. E., & Barreiro, P. (2013). Assessment of watercore development in apples with MRI: Effect of fruit location in the canopy. *Postharvest Biology and Technology*, *86*, 125–133. https://doi.org/10.1016/j.postharvbio.2013.06.030

Mendoza, F., Lu, R., & Cen, H. (2012). Comparison and fusion of four nondestructive sensors for predicting apple fruit firmness and soluble solids content. *Postharvest Biology and Technology*, *73*, 89–98. https://doi.org/10.1016/j.postharvbio.2012.05.012

Mills, L. (2004). Overseas travel-the kiwifruit journey continues. *The Orchardist, November*, *42*.

Mohammed, Y., & Verhey, J. F. (2005). A finite element method model to simulate laser interstitial thermo therapy in anatomical inhomogeneous regions. *BioMedical Engineering OnLine*, *4*(1), 2. https://doi.org/10.1186/1475-925X-4-2

Mohsenin, N. N. (1986). *Physical Properties of Plant and Animal Materials: Structure, Physical Characteristics, and Mechanical Properties*. Gordon and Breach.

Murata, N., & Nishida, I. (1990). Lipids in relation to chilling sensitivity of plants. *Chilling Injury of Horticultural Crops*, 181–199.

Nardozzaa, S., Halletta, I. C., Mccartneyb, R., Richardsonc, A. C., Macraea, E. A., Costad, G., & Clearwaterb, M. J. (2011). *Concentration between Actinidia*.

Nicolaï, B. M., Defraeye, T., De Ketelaere, B., Herremans, E., Hertog, M. L. A. T. M., Saeys, W., Torricelli, A., Vandendriessche, T., & Verboven, P. (2014). Nondestructive Measurement of Fruit and Vegetable Quality. *Annual Review of Food Science and Technology*, *5*(1), 285–312. https://doi.org/10.1146/annurev-food-030713-092410

Nicolaï, B. M., Verlinden, B. E., Desmet, M., Saevels, S., Saeys, W., Theron, K., Cubeddu, R., Pifferi, A., & Torricelli, A. (2008). Time-resolved and continuous wave NIR reflectance spectroscopy to predict soluble solids content and firmness of pear. *Postharvest Biology and Technology*, *47*(1), 68–74. https://doi.org/10.1016/j.postharvbio.2007.06.001

Nieuwenhuizen, N. J., Chen, X., Pellan, M., Zhang, L., Guo, L., Laing, W. A., Schaffer, R. J., Atkinson, R. G., & Allan, A. C. (2021). Regulation of wound ethylene biosynthesis by NAC transcription factors in kiwifruit. *BMC Plant Biology*, *21*(1), 411. https://doi.org/10.1186/s12870-021-03154-8

Olatunji, J. R., Love, R. J., Shim, Y. M., & East, A. R. (2019). A shape equation for Hayward Kiwifruit. *International Journal of Food Properties*, *22*(1), 371–382. https://doi.org/10.1080/10942912.2019.1584631

Ou-Yang, H., Stamatas, G., & Kollias, N. (2004). Spectral Responses of Melanin to Ultraviolet A Irradiation. *Journal of Investigative Dermatology*, *122*(2), 492–496. https://doi.org/10.1046/j.0022-202X.2004.22247.x

Chen, M. J. McCarthy, & R. Kauten. (1989). NMR for Internal Quality Evaluation of Fruits and Vegetables. *Transactions of the ASAE*, *32*(5), 1747–1753. https://doi.org/10.13031/2013.31217

Park, Y. S., Jung, S. T., & Gorinstein, S. (2006). Ethylene treatment of 'Hayward' kiwifruits (Actinidia deliciosa) during ripening and its influence on ethylene biosynthesis and antioxidant activity. *Scientia Horticulturae*, *108*(1), 22–28. https://doi.org/10.1016/j.scienta.2006.01.001

Parkin, K. L., Marangoni, A., Jackman, R. L., Yada, R. Y., & Stanley, D. W. (1989). Chilling Injury. A Review of Possible Mechanisms. *Journal of Food Biochemistry*, *13*(2), 127–153. https://doi.org/10.1111/j.1745-4514.1989.tb00389.x

Patterson, K. J., & Currie, M. B. (2011). OPTIMISING KIWIFRUIT VINE PERFORMANCE FOR HIGH PRODUCTIVITY AND SUPERIOR FRUIT TASTE. *Acta Horticulturae*, *913*, 257–268. https://doi.org/10.17660/ActaHortic.2011.913.33

Peirs, A., Scheerlinck, N., Touchant, K., & Nicolaï, B. M. (2002). PH—Postharvest Technology. *Biosystems Engineering*, *81*(3), 305–311. https://doi.org/10.1006/bioe.2001.0040

Peng, Y., & Lu, R. (2006). Improving apple fruit firmness predictions by effective correction of multispectral scattering images. *Postharvest Biology and Technology*, *41*(3), 266–274. https://doi.org/10.1016/j.postharvbio.2006.04.005

Pesis, E., Ackerman, M., Ben-Arie, R., Feygenberg, O., Feng, X., Apelbaum, A., Goren, R., & Prusky, D. (2002). Ethylene involvement in chilling injury symptoms of avocado during cold storage. *Postharvest Biology and Technology*, *24*(2), 171–181. https://doi.org/10.1016/S0925-5214(01)00134-X

Pickering, J. W., Prahl, S. A., Wieringen, N. van, Beek, J. F., Sterenborg, H. J. C. M., & Gemert, M. J. C. van. (1993). Double-integrating-sphere system for measuring the optical properties of tissue. *Applied Optics*, *32*(4), 399–410. https://doi.org/10.1364/AO.32.000399

Pifferi, A., Torricelli, A., Bassi, A., Taroni, P., Cubeddu, R., Wabnitz, H., Grosenick, D., Möller, M., Macdonald, R., Swartling, J., Svensson, T., Andersson-Engels, S., van Veen, R. L. P., Sterenborg, H. J. C. M., Tualle, J.-M., Nghiem, H. L., Avrillier, S., Whelan, M., & Stamm, H. (2005). Performance assessment of photon migration instruments: The MEDPHOT protocol. *Applied Optics*, *44*(11), 2104. https://doi.org/10.1364/AO.44.002104

Pifferi, A., Torricelli, A., Taroni, P., Comelli, D., Bassi, A., & Cubeddu, R. (2007). Fully automated time domain spectrometer for the absorption and scattering characterization of diffusive media. *Review of Scientific Instruments*, *78*(5), 053103. https://doi.org/10.1063/1.2735567

Pilz, M., Honold, S., & Kienle, A. (2008). Determination of the optical properties of turbid media by measurements of the spatially resolved reflectance considering the point-spread function of the camera system. *Journal of Biomedical Optics*, *13*(5), 054047. https://doi.org/10.1117/1.2983675

Postelmans, A., Aernouts, B., & Saeys, W. (2018). Estimation of particle size distributions from bulk scattering spectra: Sensitivity to distribution type and spectral noise. *Optics Express*, *26*(12), 15015. https://doi.org/10.1364/OE.26.015015

Prahl, S. A., Gemert, M. J. C. van, & Welch, A. J. (1993). Determining the optical properties of turbid media by using the adding–doubling method. *Applied Optics*, *32*(4), 559–568. https://doi.org/10.1364/AO.32.000559

Pyke, N. B., Hopkirk, G., Alspach, P. A., & Cooper, K. M. (1996). Variation in harvest and storage quality of fruit from different positions on kiwifruit vines. *New Zealand Journal of Crop and Horticultural Science*, *24*(1), 39–46. https://doi.org/10.1080/01140671.1996.9513933

Qin, J., & Lu, R. (2005). Hyperspectral diffuse reflectance for determination of the optical properties of milk and fruit and vegetable juices. *Optical Sensors and Sensing Systems for Natural Resources and Food Safety and Quality*, *5996*, 59960Q.

Qin, J., & Lu, R. (2008). Measurement of the optical properties of fruits and vegetables using spatially resolved hyperspectral diffuse reflectance imaging technique. *Postharvest Biology and Technology*, *49*(3), 355–365. https://doi.org/10.1016/j.postharvbio.2008.03.010

Qing, Z., Ji, B., & Zude, M. (2007). Predicting soluble solid content and firmness in apple fruit by means of laser light backscattering image analysis. *Journal of Food Engineering*, *82*(1), 58–67. https://doi.org/10.1016/j.jfoodeng.2007.01.016

Redgwell, R. J., Melton, L. D., & Brasch, D. J. (1992). Cell Wall Dissolution in Ripening Kiwifruit (Actinidia deliciosa). *Plant Physiology*, *98*(1), 71–81.

Redgwell, R. J., & Percy, A. E. (1992). Cell wall changes during on-vine softening of kiwifruit. *New Zealand Journal of Crop and Horticultural Science*, *20*(4), 453–456. https://doi.org/10.1080/01140671.1992.10418064

Reynolds, L., Johnson, C., & Ishimaru, A. (1976). Diffuse reflectance from a finite blood medium: Applications to the modeling of fiber optic catheters. *Applied Optics*, *15*(9), 2059–2067. https://doi.org/10.1364/AO.15.002059

Rice, K. B., Bergh, C. J., Bergmann, E. J., Biddinger, D. J., Dieckhoff, C., Dively, G., Fraser, H., Gariepy, T., Hamilton, G., Haye, T., Herbert, A., Hoelmer, K., Hooks, C. R., Jones, A., Krawczyk, G., Kuhar, T., Martinson, H., Mitchell, W., Nielsen, A. L., … Tooker, J. F. (2014). Biology, Ecology,

and Management of Brown Marmorated Stink Bug (Hemiptera: Pentatomidae). *Journal of Integrated Pest Management*, *5*(3), 1–13. https://doi.org/10.1603/IPM14002

Richardson, A. C., Boldingh, H. L., McAtee, P. A., Gunaseelan, K., Luo, Z., Atkinson, R. G., David, K. M., Burdon, J. N., & Schaffer, R. J. (2011). Fruit development of the diploid kiwifruit, Actinidia chinensis 'Hort16A'. *BMC Plant Biology*, *11*(1), 182. https://doi.org/10.1186/1471-2229-11-182

Ritenour, M. A., Crisosto, C. H., Garner, D. T., Cheng, G. W., & Zoffoli, J. P. (1999). Temperature, length of cold storage and maturity influence the ripening rate of ethylene-preconditioned kiwifruit. *Postharvest Biology and Technology*, *15*(2), 107–115. https://doi.org/10.1016/S0925-5214(98)00074-X

Rojas, A. m., Delbon, M., Marangoni, A. g., & Gerschenson, L. n. (2002). Contribution of Cellular Structure to the Large and Small Deformation Rheological Behavior of Kiwifruit. *Journal of Food Science*, *67*(6), 2143–2148. https://doi.org/10.1111/j.1365-2621.2002.tb09517.x

Rowe, P. (2015). *Optical Techniques for Fruit Firmness Assessment* [Thesis, University of Waikato]. https://researchcommons.waikato.ac.nz/handle/10289/9208

Schaare, P. N., & Fraser, D. G. (2000). Comparison of reflectance, interactance and transmission modes of visible-near infrared spectroscopy for measuring internal properties of kiwifruit (Actinidia chinensis). *Postharvest Biology and Technology*, *20*(2), 175–184. https://doi.org/10.1016/S0925-5214(00)00130-7

Schoeman, L., Williams, P., du Plessis, A., & Manley, M. (2016). X-ray micro-computed tomography (µCT) for non-destructive characterisation of food microstructure. *Trends in Food Science & Technology*, *47*, 10–24. https://doi.org/10.1016/j.tifs.2015.10.016

Schröder, R., & Atkinson, R. G. (2006). KIWIFRUIT CELL WALLS: TOWARDS AN UNDERSTANDING OF SOFTENING? *New Zealand Journal of Forestry Science*, 18.

Schroeder, R., Virgin-Harris, T., Beresford, M. K., & Hallett, I. (2018). Kiwifruit texture – a pilot study. *Acta Horticulturae*, 171–176. https://doi.org/10.17660/ActaHortic.2018.1218.23

Seifert, B., Zude, M., Spinelli, L., & Torricelli, A. (2015). Optical properties of developing pip and stone fruit reveal underlying structural changes. *Physiologia Plantarum*, *153*(2), 327–336. https://doi.org/10.1111/ppl.12232

Sevillano, L., Sanchez-Ballesta, M. T., Romojaro, F., & Flores, F. B. (2009). Physiological, hormonal and molecular mechanisms regulating chilling injury in horticultural species. Postharvest technologies applied to reduce its impact. *Journal of the Science of Food and Agriculture*, *89*(4), 555–573. https://doi.org/10.1002/jsfa.3468

Shahbandeh, M. (2022). *Global leading kiwi producing countries 2020*. Statista. https://www.statista.com/statistics/812434/production-volume-of-leading-kiwi-producing-countries/

Shahin, M. A., Tollner, E. W., McClendon, R. W., & Arabnia, H. R. (2002). Apple classification based on surface bruises using image processing and neural networks. *Transactions of the American Society of Agricultural Engineers*, *45*(5), 1619–1627. Scopus. https://doi.org/10.13031/2013.11047

Shumway, R. H., & Stoffer, D. S. (2017). *Time Series Analysis and Its Applications: With R Examples*. Springer International Publishing. https://doi.org/10.1007/978-3-319-52452-8

Simonenko, G. V., Denisova, T. P., Lakodina, N. A., & Tuchin, V. V. (2000). Measurement of an optical anisotropy of biotissues. *Coherence Domain Optical Methods in Biomedical Science and Clinical Applications IV*, *3915*, 152–157. https://doi.org/10.1117/12.384167

Spichtig, S., Hornung, R., Brown, D. W., Haensse, D., & Wolf, M. (2009). Multifrequency frequency-domain spectrometer for tissue analysis. *Review of Scientific Instruments*, *80*(2), 024301. https://doi.org/10.1063/1.3082024

Spinelli, L., Rizzolo, A., Vanoli, M., Grassi, M., Zerbini, P. E., Pimentel, R., & Torricelli, A. (2012). Optical properties of pulp and skin in brazilian mangoes in the 540–900 nm spectral range: Implication for non-destructive maturity assessment by time-resolved reflectance

spectroscopy. *International Conference of Agricultural Engineering, CIGR-AgEng2012, Valencia (Spain)*.

Stec, M. G. H., Hodgson, J. A., Macrae, E. A., & Triggs, C. M. (1989). Role of fruit firmness in the sensory evaluation of kiwifruit (Actinidia deliciosa cv Hayward). *Journal of the Science of Food and Agriculture*, *47*(4), 417–433. https://doi.org/10.1002/jsfa.2740470404

Suckling, D. M., Mazzoni, V., Roselli, G., Levy, M. C., Ioriatti, C., Stringer, L. D., Zeni, V., Deromedi, M., & Anfora, G. (2019). Trapping Brown Marmorated Stink Bugs: "The Nazgûl" Lure and Kill Nets. *Insects*, *10*(12), Article 12. https://doi.org/10.3390/insects10120433

Sun, D.-W. (2010). *Hyperspectral Imaging for Food Quality Analysis and Control*. Elsevier.

Sun, X., Sun, Z., Zhou, T., Hu, D., Sun, T., Yang, Z., & Zhou, G. (2022). Optical characterization of liquid phantoms in 500–1000 nm using an improved single integrating sphere system. *Infrared Physics & Technology*, *127*, 104386. https://doi.org/10.1016/j.infrared.2022.104386

Taglienti, A., Massantini, R., Botondi, R., Mencarelli, F., & Valentini, M. (2009). Postharvest structural changes of Hayward kiwifruit by means of magnetic resonance imaging spectroscopy. *Food Chemistry*, *114*(4), 1583–1589. https://doi.org/10.1016/j.foodchem.2008.11.066

Tavarini, S., Degl'Innocenti, E., Remorini, D., Massai, R., & Guidi, L. (2008). Antioxidant capacity, ascorbic acid, total phenols and carotenoids changes during harvest and after storage of Hayward kiwifruit. *Food Chemistry*, *107*(1), 282–288. https://doi.org/10.1016/j.foodchem.2007.08.015

Thomas, D., & Duguid, G. (2004). Optical coherence tomography—A review of the principles and contemporary uses in retinal investigation. *Eye*, *18*(6), Article 6. https://doi.org/10.1038/sj.eye.6700729

Tian, S., Wang, J., & Xu, H. (2022). Firmness measurement of kiwifruit using a self-designed device based on acoustic vibration technology. *Postharvest Biology and Technology*, *187*, 111851. https://doi.org/10.1016/j.postharvbio.2022.111851

Tuchin, V. V. (2007). A Clear Vision for Laser Diagnostics (Review). *IEEE Journal of Selected Topics in Quantum Electronics*, *13*(6), 1621–1628. https://doi.org/10.1109/JSTQE.2007.911313

Valero, C., Barreiro, P., Ruiz-Altisent, M., Cubeddu, R., Pifferi, A., Taroni, P., Torricelli, A., Valentini, G., Johnson, D., & Dover, C. (2005). Mealiness Detection in Apples Using Time Resolved Reflectance Spectroscopy. *Journal of Texture Studies*, *36*(4), 439–458. https://doi.org/10.1111/j.1745-4603.2005.00026.x

Van Beers, R., Aernouts, B., León Gutiérrez, L., Erkinbaev, C., Rutten, K., Schenk, A., Nicolaï, B., & Saeys, W. (2015). Optimal Illumination-Detection Distance and Detector Size for Predicting Braeburn Apple Maturity from Vis/NIR Laser Reflectance Measurements. *Food and Bioprocess Technology*, *8*(10), 2123–2136. https://doi.org/10.1007/s11947-015-1562-4

Van Beers, R., Aernouts, B., Watté, R., Schenk, A., Nicolaï, B., & Saeys, W. (2017). Effect of maturation on the bulk optical properties of apple skin and cortex in the 500–1850 nm wavelength range. *Journal of Food Engineering*, *214*, 79–89. https://doi.org/10.1016/j.jfoodeng.2017.06.013

Vangdal, E., Eccher Zerbini, P., Vanoli, M., Rizzolo, A., Lovati, F., Torricelli, A., & Spinelli, L. (2011). Detecting internal physiological disorders in stored plums (Prunus domestica L.) by time-resolved reflectance spectroscopy. *IV International Conference Postharvest Unlimited 2011 945*, 197–203.

Vanoli, M., Rizzolo, A., Zerbini, P. E., Spinelli, L., & Torricelli, A. (2010). Non-destructive detection of internal defects in apple fruit by time-resolved reflectancespectrscopy. *Environmentally Friendly and Safe Technologies for Quality of Fruit and Vegetables*, 20–26.

Vanoli, M., Zerbini, P. E., Spinelli, L., Torricelli, A., & Rizzolo, A. (2009). Polyuronide content and correlation to optical properties measured by time-resolved reflectance spectroscopy in 'Jonagored' apples stored in normal and controlled atmosphere. *Food Chemistry*, *115*(4), 1450–1457. https://doi.org/10.1016/j.foodchem.2009.01.081

Verboven, P., Nemeth, A., Abera, M. K., Bongaers, E., Daelemans, D., Estrade, P., Herremans, E., Hertog, M., Saeys, W., Vanstreels, E., Verlinden, B., Leitner, M., & Nicolaï, B. (2013). Optical

coherence tomography visualizes microstructure of apple peel. *Postharvest Biology and Technology*, *78*, 123–132. https://doi.org/10.1016/j.postharvbio.2012.12.020

Verroens, P., Verlinden, B. E., Sauviller, C., Lammertyn, J., De Ketelaere, B., & Nicolaï, B. M. (2006). TIME SERIES ANALYSIS OF CAPSICUM ANNUUM FRUIT PRODUCTION CULTIVATED IN GREENHOUSE. *Acta Horticulturae*, *718*, 97–104. https://doi.org/10.17660/ActaHortic.2006.718.10

Walsh, K. B., Blasco, J., Zude-Sasse, M., & Sun, X. (2020). Visible-NIR 'point' spectroscopy in postharvest fruit and vegetable assessment: The science behind three decades of commercial use. *Postharvest Biology and Technology*, *168*, 111246. https://doi.org/10.1016/j.postharvbio.2020.111246

Wang, C. Y. (1989). Chilling injury of fruits and vegetables. *Food Reviews International*, *5*(2), 209–236. https://doi.org/10.1080/87559128909540850

Wang, C. Y. (1994). *Chilling Injury of Tropical Horticultural Commodities*. *29*, 986–988. https://doi.org/10.21273/HORTSCI.27.6.569a

Wang, L. (1995). MCML—Monte Carlo modeling of light transport in multi-layered tissues. *Computer Methods and Programs in Biomedicine*, *47*(2), 131–146. https://doi.org/10.1016/0169-2607(95)01640-F

Wang, W., Li, C., & Gitaitis, R. D. (2014). Optical properties of healthy and diseased onion tissues in the visible and near-infrared spectral region. *Transactions of the ASABE*, *57*(6), 1771–1782. Scopus. https://doi.org/10.13031/trans.57.10815

Wang, Z., Künnemeyer, R., McGlone, A., & Burdon, J. (2020). Potential of Vis-NIR spectroscopy for detection of chilling injury in kiwifruit. *Postharvest Biology and Technology*, *164*, 111160. https://doi.org/10.1016/j.postharvbio.2020.111160

Wang, Z., Künnemeyer, R., McGlone, A., Sun, J., & Burdon, J. (2020). Comparison of a dual-laser and a Vis-NIR spectroscopy system for detection of chilling injury in kiwifruit. *Postharvest Biology and Technology*, 111418. https://doi.org/10.1016/j.postharvbio.2020.111418

Wang, Z., Van Beers, R., Aernouts, B., Watté, R., Verboven, P., Nicolaï, B., & Saeys, W. (2020). Microstructure affects light scattering in apples. *Postharvest Biology and Technology*, *159*, 110996. https://doi.org/10.1016/j.postharvbio.2019.110996

Ward, C., & Courtney, D. (2013). Chapter One - Kiwifruit: Taking Its Place in the Global Fruit Bowl. In M. Boland & P. J. Moughan (Eds.), *Advances in Food and Nutrition Research* (Vol. 68, pp. 1–14). Academic Press. https://doi.org/10.1016/B978-0-12-394294-4.00001-8

Watkins, C. B., Bramlage, W. J., & Cregoe, B. A. (1995). Superficial Scald of `Granny Smith' Apples is Expressed as a Typical Chilling Injury. *Journal of the American Society for Horticultural Science*, *120*(1), 88–94. https://doi.org/10.21273/JASHS.120.1.88

Watkins, C., & Harman, J. (1981). Use of penetrometer to measure flesh firmness of fruit. *Orchardist of New Zealand*.

Watté, R., Aernouts, B., Beers, R. V., & Saeys, W. (2015). Robust metamodel-based inverse estimation of bulk optical properties of turbid media from spatially resolved diffuse reflectance measurements. *Optics Express*, *23*(21), 27880–27898. https://doi.org/10.1364/OE.23.027880

Weng, Y., Wang, X., Hua, J., Wang, H., Kang, M., & Wang, F.-Y. (2019). Forecasting Horticultural Products Price Using ARIMA Model and Neural Network Based on a Large-Scale Data Set Collected by Web Crawler. *IEEE Transactions on Computational Social Systems*, *6*(3), 547–553. https://doi.org/10.1109/TCSS.2019.2914499

Wieme, J., Mollazade, K., Malounas, I., Zude-Sasse, M., Zhao, M., Gowen, A., Argyropoulos, D., Fountas, S., & Van Beek, J. (2022). Application of hyperspectral imaging systems and artificial intelligence for quality assessment of fruit, vegetables and mushrooms: A review. *Biosystems Engineering*, *222*, 156–176. https://doi.org/10.1016/j.biosystemseng.2022.07.013

Wills, R., & Golding, J. (2016). *Postharvest: An introduction to the physiology and handling of fruit and vegetables, 6th edition*. UNSW Press.

Xiangwei Chen. (2012). Spectroscopic determination of soluble solids content of 'Qinmei' kiwifruit using partial least squares. *AFRICAN JOURNAL OF BIOTECHNOLOGY*, *11*(10). https://doi.org/10.5897/AJB11.3177

Zang, X., Zu, Y., Zhang, T., Xia, K., Song, Y., Wang, Y., Dong, X., & Tan, M. (2017). Dynamic Water Mobility in Sea Cucumber (Stichopus japonicas) During Drying Process Assessed by LF-NMR and MRI in situ. *International Journal of Food Engineering*. https://doi.org/10.1515/ijfe-2016-0360

Zapponi, L., Morten, M., Chiesa, S. G., Angeli, G., Borri, G., Mazzoni, V., Sofia, M., & Anfora, G. (2022). Brown marmorated stink bug (Halyomorpha halys) feeding damage determines early drop in olive crops. *Journal of Applied Entomology*, *146*(6), 791–795. https://doi.org/10.1111/jen.13018

Zespri International. (2022). *Zespri Annual report 2021/2022*.

Zhang, M., Li, C., & Fan, S. (2017). Optical Properties of Healthy and Bruised Blueberry Tissues in the Near-Infrared Spectral Region. *2017 Spokane, Washington July 16 - July 19, 2017*. 2017 Spokane, Washington July 16 - July 19, 2017. https://doi.org/10.13031/aim.201700423

Zhao, J. M. (2017). *Development of a mathematical model for 'Hayward' kiwifruit softening in the supply chain: A thesis presented in partial fulfilment of the requirements for the degree of Doctor of Philosophy in Food Technology at Massey University, New Zealand: Vol. Doctor of Philosophy (PhD)* [Doctoral, Massey University]. http://hdl.handle.net/10179/12434

Zhao, J. M., Bronlund, J. E., & East, A. R. (2015). Effect of Cooling Rate on Kiwifruit Firmness and Rot Incidence in Subsequent Storage. *Acta Horticulturae*, *1079*, 313–318. https://doi.org/10.17660/ActaHortic.2015.1079.38

Zhou, Y., Wu, D., Hui, G., Mao, J., Liu, T., Zhou, W., Zhao, Y., Chen, Z., & Chen, F. (2018). Loquat Bruise Detection Using Optical Coherence Tomography Based on Microstructural Parameters. *Food Analytical Methods*, *11*(10), 2692–2698. https://doi.org/10.1007/s12161-018-1246-6

Zude, M., Herold, B., Roger, J.-M., Bellon-Maurel, V., & Landahl, S. (2006). Non-destructive tests on the prediction of apple fruit flesh firmness and soluble solids content on tree and in shelf life. *Journal of Food Engineering*, *77*(2), 254–260. https://doi.org/10.1016/j.jfoodeng.2005.06.027

Zude-Sasse, M., Hashim, N., Hass, R., Polley, N., & Regen, C. (2019). Validation study for measuring absorption and reduced scattering coefficients by means of laser-induced backscattering imaging. *Postharvest Biology and Technology*, *153*, 161–168. https://doi.org/10.1016/j.postharvbio.2019.04.002

Zulkifli, N., Hashim, N., Harith, H. H., & Mohamad Shukery, M. F. (2020). Finite element modelling for fruit stress analysis—A review. *Trends in Food Science & Technology*, *97*, 29–37. https://doi.org/10.1016/j.tifs.2019.12.029

Zuo, J., Wang, Q., Zhu, B., Luo, Y., & Gao, L. (2016). Deciphering the roles of circRNAs on chilling injury in tomato. *Biochemical and Biophysical Research Communications*, *479*(2), 132–138. https://doi.org/10.1016/j.bbrc.2016.07.032

Appendix I. Supplement data

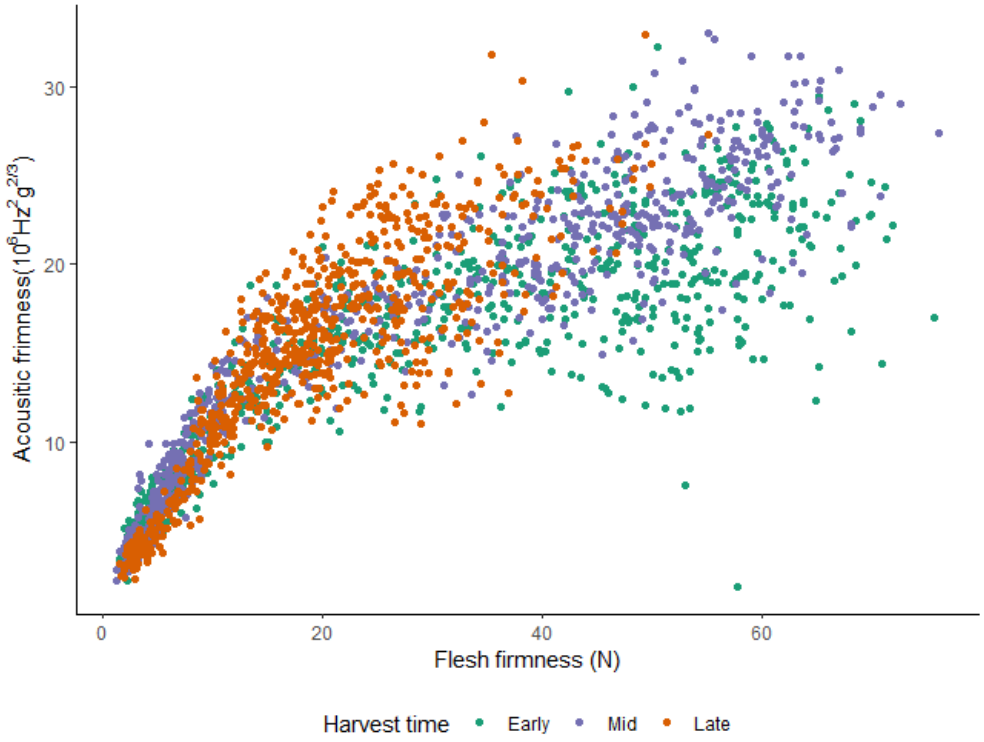

Figure I.1. 'Hayward' kiwifruit flesh firmness and acoustic firmness [measured by AWETA AFS (AWETA International Ltd., Nootdrop, Holland)] correlation scatter plot